Summer 8-2022

Utilization of Finite Element Analysis Techniques for Adolescent Idiopathic Scoliosis Surgical Planning

Michael A. Polanco
Old Dominion University, michael.polanco@gmail.com

Recommended Citation

UTILIZATION OF FINITE ELEMENT ANALYSIS TECHNIQUES FOR

ADOLESCENT IDIOPATHIC SCOLIOSIS SURGICAL PLANNING

by

Michael A. Polanco

B.S. May 2007, The Pennsylvania State University
M.S. December 2013, Old Dominion University

A Dissertation Submitted to the Faculty of
Old Dominion University in Partial Fulfillment of the
Requirements for the Degree of

DOCTOR OF PHILOSOPHY

MECHANICAL ENGINEERING

OLD DOMINION UNIVERSITY
August 2022

Approved by:

Sebastian Bawab (Director)

Stacie Ringleb (Member)

Michel Audette (Member)

Gene Hou (Member)

ABSTRACT

UTILIZATION OF FINITE ELEMENT ANALYSIS TECHNIQUES FOR ADOLESCENT IDIOPATHIC SCOLIOSIS SURGICAL PLANNING

Michael A. Polanco
Old Dominion University, 2022
Director: Dr. Sebastian Bawab

Adolescent Idiopathic Scoliosis, a three-dimensional deformity of the thoracolumbar spine, affects approximately 1-3% of patients ages 10-18. Surgical correction and treatment of the spinal column is a costly and high-risk task that is consistently complicated by factors such as patient-specific spinal deformities, curve flexibility, and surgeon experience. The following dissertation utilizes finite element analysis to develop a cost-effective, building-block approach by which surgical procedures and kinematic evaluations may be investigated. All studies conducted are based off a volumetric, thoracolumbar finite element (FE) model developed from computer-aided design (CAD) anatomy whose components are kinematically validated with in-vitro data. Spinal ligament stiffness properties derived from the literature are compared for kinematic assessment of a thoracic functional spinal unit (FSU) and benchmarked with available in-vitro kinematic data. Once ligament stiffness properties were selected, load sharing among soft tissues (e.g., ligaments and intervertebral disc) within the same FSU is then assessed during individual steps of a posterior correction procedure commonly used on scoliosis patients. Finally, the entire thoracolumbar spine is utilized to mechanically induce a mild scoliosis profile through an iterative preload and growth procedure described by the Hueter-Volkmann law. The mild scoliosis model is then kinematically compared with an asymptomatic counterpart. The thoracic

deformation exhibited in the mild scoliosis model compared well with available CT datasets.

Key findings of the studies confirm the importance of appropriately assigning spinal ligament properties with traditional toe and linear stiffness regimes to properly characterize thoracic spine FE models. Stiffness properties assigned within spinal FE models may also alter how intact ligaments and intervertebral discs respond to external loads during posterior correction procedures involving serial ligament removal, and thus can affect any desired post-surgical outcomes. Lastly, the thoracolumbar spine containing mild scoliosis experiences up to a 37% reduction in global range of motion compared to an asymptomatic spine, while also exhibiting larger decreases in segmental axial rotations at apical deformity levels. Future studies will address kinematic behavior of a severe scoliosis deformity and set the stage for column-based osseoligamentous load sharing assessments during surgical procedures.

ACKNOWLEDGMENTS

First off, I would like to graciously acknowledge Dr. Sebastian Bawab. After years of resisting from doing a doctorate, he was one of the few who knew I was capable of pursuing such a degree and persuaded me to go for it. Above all, he passed on valuable technical and life knowledge I will carry over for many years and never gave up on me while I persevered to produce good quality work for this dissertation.

I would like to also thank my committee members, Dr. Stacie Ringleb, Dr. Michel Audette, and Dr. Gene Hou for their time, patience, and support in fine-tuning this dissertation and serving on my committee. A special thanks also goes to Dr. Rumit Kakar for his valuable insight on spine biomechanics, and to Dr. James Bennett at Children's Hospital of the King's Daughters for helping guide this work.

A special thanks is extended to Dr. Tony Dean for helping me to build confidence and maturity during my years at ODU. Many thanks also to the SMART Scholarship program for funding my efforts to get my dissertation completed.

I would also like to thank the Harrington family for their unwavering love and friendship; to Gina, Nick, Alexis, Giovanni, Javi, and mom for their love and continued words of encouragement. Lastly, thanks to my father, retired Command Master Chief Tony Polanco, who instilled in me and my siblings that a good education is the best pathway to prosperity.

TABLE OF CONTENTS

LIST OF TABLES

LIST OF FIGURES

CHAPTER 1

INTRODUCTION

1.1 Overview of Spinal Anatomy

The spinal column serves as the central support structure for the human body. The spine can be described as serving three primary functions: protecting the spinal cord from potential injury and trauma, supporting the weights of the head, trunk, limbs, and miscellaneous weights lifted, and facilitating motion between the head, trunk, and pelvis. The human spine contains a total of 33 individual vertebrae, consisting of 7 cervical (C1-C7), 12 thoracic (T1-T12), 5 lumbar (L1-L5), 5 Sacral (S1-S5), and 4 in the coccyx region that are responsible for controlling movement of the torso, upper and lower extremities (Figure 1-1). The spine undergoes most of its growth before adolescence (American Association of Neurological Surgeons (AANS)) but appears to achieve steady-state geometry around 14 or 15 years old (Dougherty, 2014). The length of the spine can also dictate the motion of a person. However, it is their individual components, namely the Intervertebral Disc, ligaments, facets, and muscles, which control the motion and make stability of the spine possible. This section will break the spine down into their individual components and the functions.
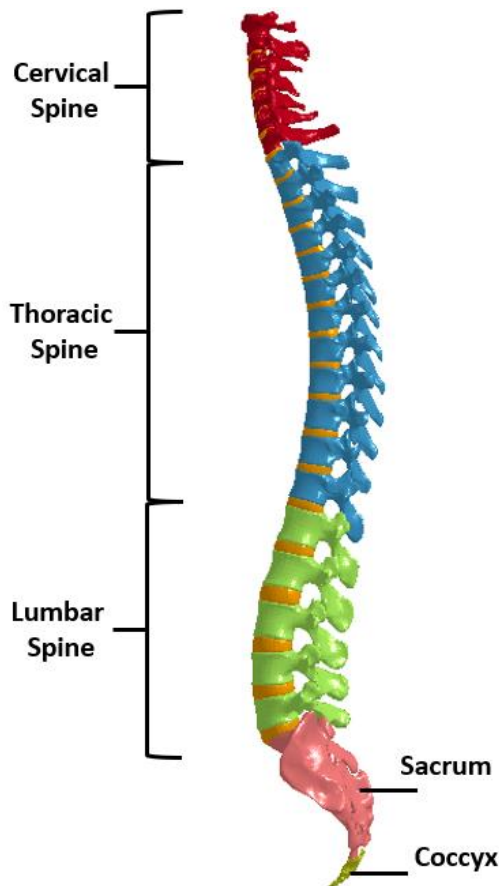
Figure 1-1: Regions of spinal column.

1.1.1 VERTEBRAE AND INTERVERTEBRAL DISC

The smallest anatomical entity one considers for biomechanical evaluation is the functional spinal unit, consisting of two vertebrae and an intervertebral disc (Figure 1-2). The vertebrae serve a primary role of supporting the spinal cord, nerve roots, head and neck (Williams et al., 1995). They facilitate motion of the upper body largely due to their inertial properties and presence of facet joints (Wachowski et al., 2009; Sharma et al., 1995). The vertebrae generally consist of cancellous bone, or sponge tissue, that is reinforced and enveloped by a layer of cortical bone, which provides a path for compressive loads to be transmitted throughout the spinal column. They contain

protrusions such as the transverse and spinous processes which serve as foundations to link neighboring vertebrae to each other through ligament attachments and articular cartilage placements. Descending caudally along the spinal column, vertebrae gradually increase in size; as a result, larger vertebrae in the lumbar spine are able to bear larger loads and strengths compared to those superiorly situated in the spine (e.g., ~2 kilonewtons in the cervical spine versus ~8 kilonewtons at L4) (White and Panjabi, 1990).
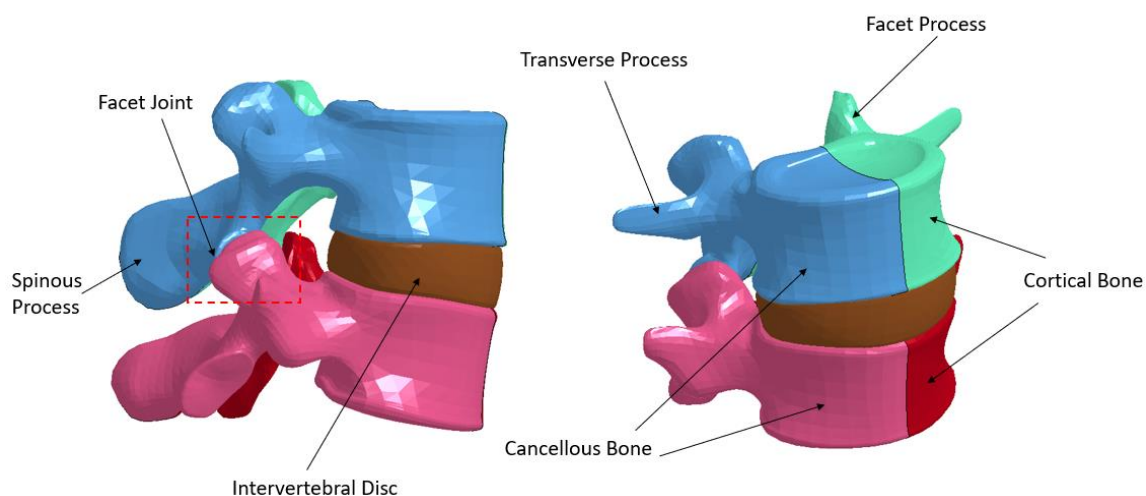
Figure 1-2: Functional Spinal Unit: A pair of vertebrae and an Intervertebral Disc.

The endplate serves as a bond between the intervertebral disc and adjacent vertebrae. The endplate typically consists of two layers: cartilage, which adheres to the intervertebral disc, and porous bone, which is positioned between the cartilaginous endplate and vertebra. Mechanically, the endplate sustains the intervertebral disc during compression. In the adolescent and younger populations, an epiphyseal plate, or cartilage layer, is

present where the endplate is located in adults (Lotz et al., 2013). It is here where spinal growth occurs throughout the spinal column. Up until approximately age 18, the epiphyseal plate progressively thins until closure is initiated and growth ceases, forming the endplate bone and cartilage layers.

The intervertebral disc (IVD), shown in Figure 1-3, is another important component of the spine that provides movement and load support. The IVD connects vertebral bodies and helps sustain the spine during compression, allowing for compressive loads up to three times the weight of a human trunk. The IVDs vary in thickness throughout the vertebral column. They are thinnest at the upper thorax but maintain uniform thickness throughout its length within the entire thoracic column. The IVDs are thickest within the lumbar region but increase in thickness along the posteroanterior direction. The IVD thicknesses largely determine the convexity (cervical, lumbar) and concavity (thoracic) of the anterior spine. Together with the vertebrae, they form individual joints to facilitate smooth, yet flexible, mobility. It supports axial rotation through shear loading and coronal and sagittal motion through compression. The intervertebral disc consists of three components: annulus fibrosus, the annulus fibers, and the nucleus pulposus.

The annulus fibrosus is a viscoelastic fibrocartilaginous soft tissue that is situated as the outer core of the intervertebral disc. It consists of mainly type I and type II cross-hatched collagen fibers, generally oriented 30° from the horizontal and provides the disc with tensile strength (Schroeder et al., 2006) and embedded within ring-shaped laminates layered concentrically around the disc. The cross-hatched fibers are responsible for the torsional stability of the disc under axial rotation and shearing. The annulus fibrosus also

maintains and secures the shape of the nucleus pulposus. This is a gel-like incompressible material positioned in the center of the intervertebral disc, consisting of approximately 80% water, protein, and an independent blood supply within the first 20 years of a person's life (Goodmurphy, 2005) giving the disc its incompressible capability as well as the ability to function like a shock absorber.

Over time, discs degenerate and have consequentially been linked to back pain in older patients (Urban et al., 2003). This degeneration has driven an abundance of research questions pertaining to the lumbar spine, serving as the foundation for load support within the spine. It is known that the disc geometrically varies along the spinal column, but geometric differences have shown that its parameters, such as disc height, can affect spinal mobility and segmental stiffness (Meijer et al., 2011).
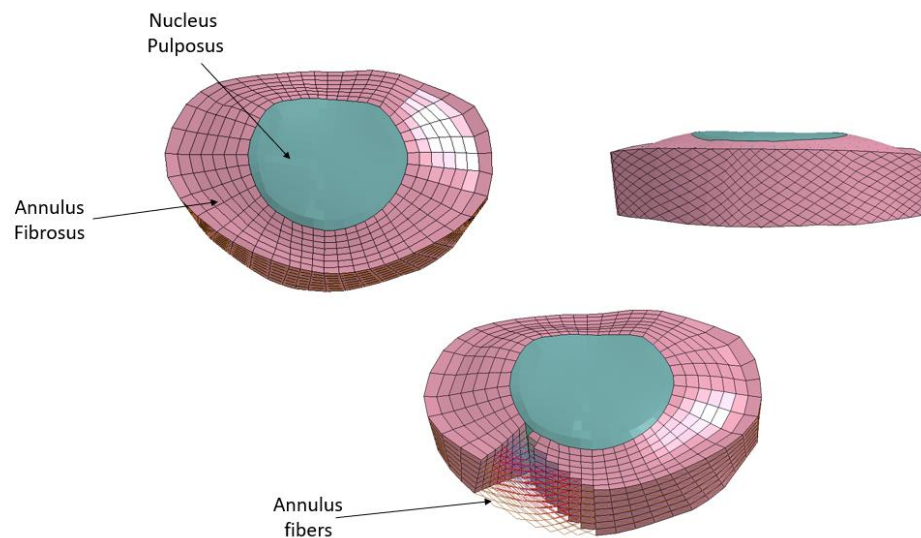
Figure 1-3: Intervertebral Disc.

1.1.2 FACET JOINTS

The facet joints, highlighted in dotted red in Figure 1-2, are primarily responsible for tri-planar rotations throughout the spinal column (e.g., flexion/extension, lateral bending, and axial rotation). They prevent large extension and axial rotations from taking place (Sharma et al., 1995). The facets consist of two articular surfaces bilaterally positioned and surrounded by two capsular ligamentous connections. Each cartilage surface is often lubricated due to the presence of synovial fluid. The facets are integral in helping to facilitate transfer loads and kinematic constraints throughout the spine and are said to transfer between 3 and 25% of compressive loads transmitted throughout the spine (Jaumard et al., 2011).

Facet orientations will dictate the quantitative loads each is capable of bearing (Sharma et al., 1995). The cervical spine has a shallower angle sagittally (approximately 45°), but no angle coronally. The thoracic spine contains a typical yet steeper facet orientation of approximately 60° sagittally and a medial orientation of approximately 20° from the coronal plane. The lumbar spine contains a purely vertical orientation sagittally, while having a more medial facet orientation of approximately 45°.

Due to their important role in kinematic facilitation, the facet joints have been a source of interest in understanding etiology of spinal pathologies. For example, their role in the causation of degenerative lumbar scoliosis has been previously investigated (Wang et al., 2016), as asymmetric degeneration through imbalance in forces within each facet joint leads to vertebral rotations, continually progressing a deformed curve. The facet joint has also been a subject of surgical procedures, such as facetectomies, to alleviate pressure between inferior and superior facet processes in spines with scoliosis (Ponte et

al., 2015) or lumbar stenosis (Ahuja et al., 2020). By alleviating pressure following a facetectomy, more flexibility may be gained within spinal segments of interest. However, removal of the facet can create instability in extension, particularly in the lumbar spine (Sharma et al., 1995). Likewise, removal of more than 30% of a facet may create rotational instability in a segment and exacerbate degeneration of adjacent anatomy like the intervertebral disc (Ahuja et al., 2020) as a result of load transfer.

C4-C5
(θ = 45°; φ = 0°)

T7-T8
(θ = 60°; φ = 20°)

L4-L5
(θ = 90°; φ = 45°)
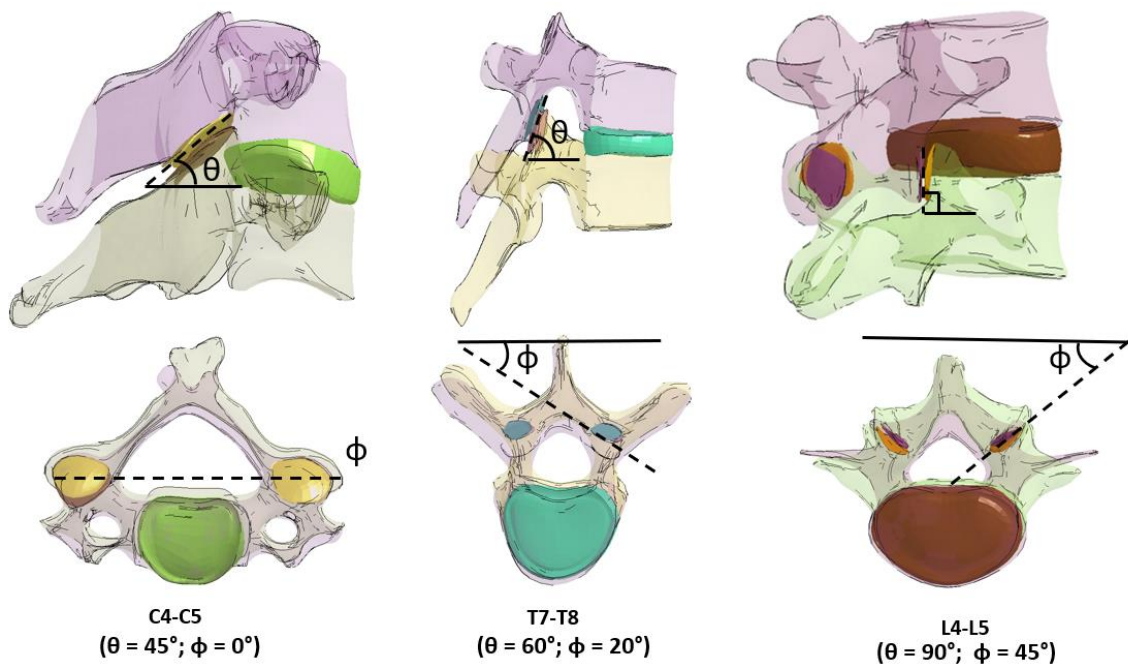
Figure 1-4: Facet joints and typical orientations in the cervical, thoracic, and lumbar spinal regions.

1.1.3 LIGAMENTS

Spinal ligaments are viscoelastic bands of tissue that allow for intactness and stability of the spine while controlling motion of spinal joints through tensile behavior.

They generally consist of a mix of collagen fibers embedded in a ground substance matrix, primarily of water (Hortin, 2015). The wet weight of the matrix can be up to 70%, while the dry weight can range up to 80% due to the fibrous content. Tensile stresses are highest in the direction of the fibers and become weaker as a function of fiber orientation. Due to the fibrous interaction with water and proteins, ligaments are considered either anisotropic (Hortin, 2015) and depend on applied load direction for a response, or viscoelastic as they exhibit hysteretic responses pertaining to creep and stress relaxation (Troyer, 2011). As a result, ligaments do not offer compression stiffness.

As highlighted in Figure 1-5, sets of ligaments are present throughout the spine and each serves a different function in providing stability and limits to rotational motion. As highlighted in Table 1-4, the geometric variation of these ligaments along the vertebral column as well as their can complicate how they are characterized on an intervertebral basis. Namely, the cross-sectional areas and effective lengths of spinal ligaments are necessary to properly derive stiffness characteristics; however, due to their small sizes they can be difficult to measure. The measurement methods for geometric ligament parameter values have varied. Earlier studies make use of a micrometer to measure ligament rest lengths (Chazal et al., 1985), while more recent studies used imaging slices to obtain effective length measurements (Pintar et al., 1992; Yoganandan et al., 2000). Early efforts have attempted to measure ligament thicknesses using micrometers and pressure-based dial displacement gauge (Tkaczuk, 1968); however, care was needed to avoid any effects of creep to not compromise the measurements obtained from each sample. Chazal et al. (1985) used a palpator to take cross sectional measurements along the length of specific ligaments through amplifier tracing on paper

and used the lowest value as reference for stress measurements. The few studies conducted in the last 30 years utilized digital imaging to determine cross sectional areas. Pintar et al. (1992) used digitized axial images of lumbar intervertebral ligaments combined with ligament boundary projection to determine cross-sectional dimensions; Yoganandan et al. (2000) used a similar technique using a cryostat with cervical ligaments. Troyer (2011) utilized a combination of microscopes and digital cameras to acquire images of small (e.g.,: anterior longitudinal ligament) and large (e.g.,: ligamentum flavum) ligament cross-sections while employing digital image software to obtain quantitative area values.

Table 1-1 shows that the geometric composition of the ligaments and the fibrous orientations throughout the spinal column vary greatly, which ultimately affects the movement and stability of the spine (Williams et al., 1995) as well as the strength of each individual ligament. Knowledge of this information is crucial in understanding the behavior of the spine at different regions as well as accurately characterizing the anatomy in a computer model for clinical assessments. Due to the intervertebral variation of ligament composition, the ability to characterize the anatomy for an entire spinal column can prove challenging. The composition of ligaments can vary on a patient-specific basis due to degree of hydration, age, and fibrous content (Hortin, 2015; Panjabi et al., 1991). As a result, characterizing ligament stiffness has produced wide variations. During in-vitro testing, bone-ligament-bone specimens are typically utilized for tensile testing, preserving their original attachments from the harvested subject. Because ligaments are viscoelastic in nature, they are often preconditioned (Ebrahimi et al., 2019; Mattucci et al., 2012; Yoganandan et al., 2000) prior to tensile testing. The purpose of

preconditioning is to overcome the time or history dependent behavior of the ligament due to viscoelasticity, thus enforcing a tensile steady-state response of the ligament and is applied cyclically using a strain level far below damage, typically no more than 10% (Mattucci et al., 2012).
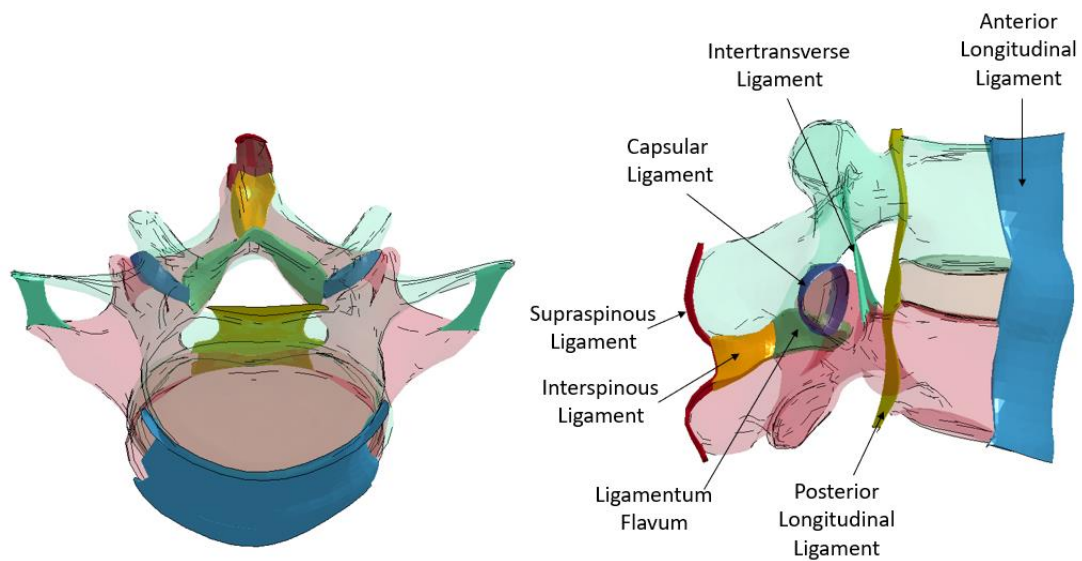
Figure 1-5: Ligament nomenclature.

Table 1-1: Intervertebral Spinal ligaments.

Ligament Type	Geometric Description	Function
Anterior Longitudinal Ligament (ALL)	ALL is positioned at the anterior spinal column, extending from the cervical to lumbar regions. The ligament becomes broader in the caudal direction, and thicker and narrow in the thoracic versus the lumbar and cervical regions. Its fibers can span between two and four vertebrae	Help keep the vertebrae intact, through firm connections to the intervertebral discs. Provide shearing resistance to prevent disc slipping. Limits spinal extension
Posterior Longitudinal Ligament (PLL)	PLL is positioned at the posterior region of each vertebra, extending from the cervical to lumbar regions. It is of uniform width in the cervical and thoracic regions, but everywhere else, it becomes rugged and narrow over the vertebrae before widening over the intervertebral discs. Its fibers can span up to four vertebral levels	Help keep the vertebrae intact, through firm connections to the intervertebral discs. Posterior attachment reinforces annulus fibrosus. Provide shearing resistance to prevent disc slipping. Limits spinal flexion
Ligamentum Flavum (LF)	LF is positioned in the posterior portion of the vertebrae, to connect vertebral arches of subsequent vertebrae. Known as a yellow ligament, it attaches to the vertebral lamina, and become thicker caudally.	Limit flexion. The elasticity of the ligament, due to high elastin fibers, allow for smooth motion of the vertebral column
Interspinous Ligament (ISL)	ISL is positioned along the spinal column between the spinous processes of adjacent vertebrae. They become thicker as one descends the spinal column.	Limits flexion of the spinal column
Supraspinous Ligament (SSL)	SSL is in the posterior of the spine. It connects the apices of the vertebral spinous processes and terminates in the lumbar region. Some fibers span as much as three and four vertebrae, more important fibers connect spinous processes of adjacent vertebrae	Limits flexion of the spinal column, helps maintain the head's upright position
Intertransverse Ligament (ITL)	ITL is placed between the transverse processes of the spine, blending with adjacent muscles of the back	Limit lateral bending of the spine
Capsular Ligament (CL)	CL surrounds facet joints for mechanical reinforcement	Limits extension and hyperflexion

1.1.4 RIB CAGE

The anatomy of the thoracic spine is made unique through the presence of the rib cage. Consistent of 12 ribs, the main function of the thorax is to allow for rib motion during respiration (Williams, 1995). The function is facilitated by the costal cartilage positioned at the anterior end of the ribs (Williams, 1995) While the anterior portion consists of upper 7 ribs being attached to the sternum via costal cartilage (with ribs 8-10 attached to the 7th layer of costal cartilage and 2 free floating ribs), the posterior region of the thorax is connected to the vertebral column through costovertebral joints. They consist mainly of costotransverse, capsular, radiate, and intra-articular ligaments (Table 1-2) connected to the vertebral bodies and transverse processes of each vertebra throughout the thoracic region, providing reinforced stiffness relative to the cervical and thoracic spine (Williams, 1995; Anderson et al., 2009). To facilitate expansion and contraction of the rib cage, intercostal muscles are positioned between the ribs. Figure 1-7 shows a depiction of the thorax and costovertebral joints.

The rib cage is said to contribute up to 78% stiffness of the thoracic spine (Mannen et al., 2015; Watkins et al., 2005) while it can limit flexion/extension Range of Motion (RoM) by 40%, lateral bending by 35%, and axial rotation by 31% (Watkins et al., 2005). Little understanding remains regarding the mechanics of the thoracic spine with a rib cage. However, clinical interest has recently picked up in examining the thoracic spine to assess feasibility of treatments such as rib shortening for Adolescent Idiopathic Scoliosis (AIS) (Grealou et al., 2002) and decompression procedures (Healy et al., 2014; Lubelski et al., 2014). The corrective surgical application for AIS will require

knowledge about the rib cage in anticipation of the forces the surgeon will need to apply

in the operating room.
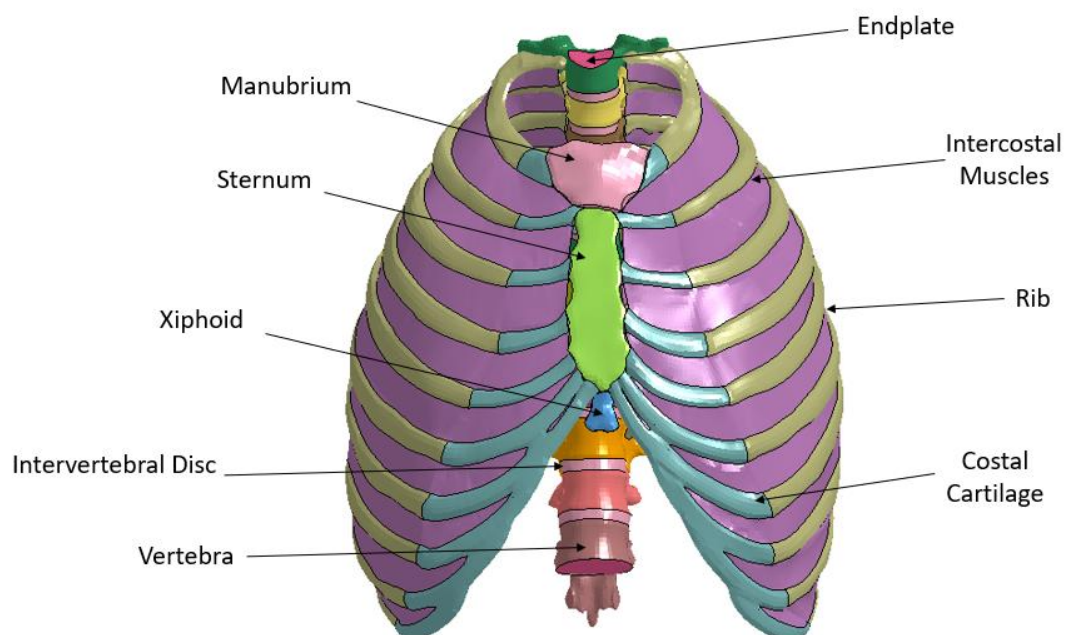
Figure 1-6: Thorax (thoracic spine with ribcage).
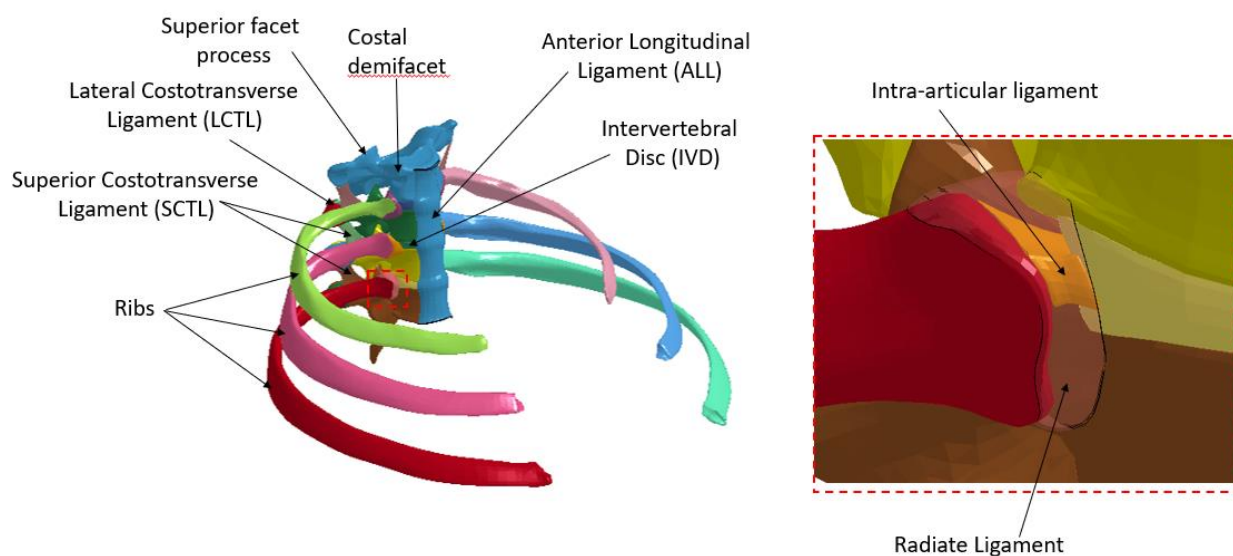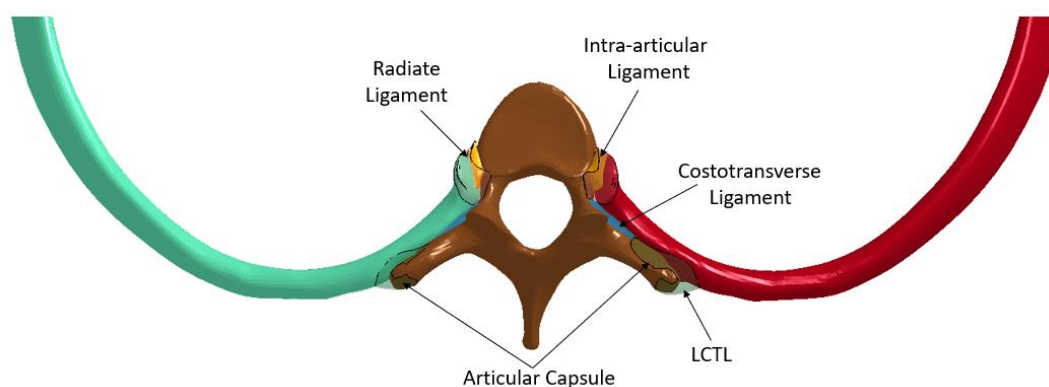
Figure 1-7: Costovertebral joints.

Table 1-2: Costovertebral ligaments.

Joint Type	Ligament Type	Description
Costotransverse Joint	Superior Costotransverse Ligament (SCTL)	The SCTL provides a longitudinal connection between the ribcage and adjacent transverse processes. It consists of both anterior and posterior fibers, which run from the rib neck to the anterior and inferior transverse process borders respectively. They are found between T1 and T10.
	Lateral Costotransverse Ligament (LCTL)	The LCTL provides a lateral connection between the rib tubercle and the outermost transverse process tips on each vertebra. It surrounds an articular capsule which facilitates contact between the rib and transverse process They exhibit a presence between T1 and T10.
	Costotransverse Ligament (CTL)	The CTL consists of dense, elastic fibers bilaterally connecting ribs to the transverse process, and positioned between the LCTL and the rib head. They stretch when the ribs rotate ventrally and contract during dorsal rib rotation.
Costocentral Joint	Intra-articular Ligament	The intraarticular ligament provides a secondary attachment between the rib head and adjacent vertebrae, which facilitates a bilateral connection of the ribcage to intervertebral discs along the spinal column.

Table 1-2 continued.

	Radiate Ligament	The Radiate ligament surrounds the intraarticular ligament and upper and lower cavities within the rib head. They are present between T1 and T12. With the exceptions of T1 and T10-T12, they provide attachments to two successive vertebrae and an intervertebral disc versus one vertebra for aforementioned levels.

1.2 KINEMATICS

1.2.1 RANGE OF MOTION

The Range of Motion (RoM) is a commonly utilized variable in the biomechanics field to assess kinematic behavior of anatomic joints. RoM has been measured in a variety of biomechanics studies, such as assessing the effect of removing anatomic components such as ligaments & facets (Sharma et al., 1995; Little and Adam, 2011b), effects of joint pathologies such as scoliosis (Wilke et al., 2015), and spine degeneration (Wang et al., 2016) or the effects of post-surgical treatments through spinal fusions (Healy et al., 2014). Deviations from RoM may point to specific pathologies, such as disc degeneration (Park et al., 2013), while increases in RoM may point to rotational instability in the segment (Sharma et al., 1995). Individual segments within the spine column vary in RoM depending on the spinal region (Table 1-5). Motion magnitudes within the three planes are driven by anatomical features such as disc height (Meijer et al., 2011), facet orientation, and musculature (White & Panjabi 1990). In the thoracic spine, the position of the costovertebral joint relative to each disc helps to reinforce the motion exerted within each segment. As a result, rotations within the upper and mid-

thoracic region are lowest in the sagittal and coronal planes. The measurement of RoM can vary depending on the standard being applied. The International Society of Biomechanics, for example, defines Euler rotation sequences based on the joint of interest (Wu et al., 2002). In an experimental sense, extracting the angles require a generated rotation matrix from marker data, which could then be derived based on the sequence defined for a joint. For the spine specifically, the sequence is sagittal, axial, and coronal rotation.

Table 1-3: RoM per spinal region (Values taken from White and Panjabi, 1990).

	Flexion/Extension	One Side Lateral Bending	One Side Axial Rotation
Cervical	5°-29°	0°-20°	0°-10°
Thoracic	3°-8° (T1-T10); 4-20 (T10-T12)	4°-7° (T1-T10); 3°-13° (T10-T12)	14° (T1); 2°-12° (T2-T12);
Lumbar	5°-21°	2°-12°	0°-3°

1.2.2 INSTANTANEOUS CENTER OF ROTATION

The instant center of rotation (ICoR) is a physiological variable describing qualitative joint movement within a plane. It offers one perspective of three typically offered through an instantaneous axis of rotation, which depicts the quality of tri-planar movement of a joint in space but is usually sufficient if motion data along one plane is desired. The ICoR offers clinical insight regarding potential pathologies of the spine that cannot be offered by simply comparing with the RoM (Bogduk, 1995) in comparison with healthy subjects. It may also be utilized to understand how surgical treatments, such as fusion in the cervical spine (Anderst et al., 2013), may improve or exacerbate mobility

compared to other treatments that could be available to resolve the pathology. The ICoR is generally depicted by a load-dependent path within the joint and can be deciphered through a sequence of radiographs which depict its movement within a plane. By taking two points along a rigid body during movement, one may use a perpendicular bisector to determine where the ICoR is located at any point during the applied load.

Recent efforts have demonstrated that the paths taken by ICoR vary depending on the assessment method, (e.g., in-vivo (muscle activation) or in-vitro (external moment)) (Rockenfeller et al., 2021) and may have implications on how the effects of different treatments are interpreted. It has been shown that, anatomically, the ICoR has a dependence on the biomechanical function of ligaments (Naserkhaki et al., 2018), facet forces (Schmidt et al., 2008), and IVDs (Liebsch et al., 2020a) during joint movement. Thus, in the context of an FE model, it becomes crucial to accurately characterize the anatomy such that the ICoR behaves physiologically realistic. As such, it may also be representative of moment arm origins for muscles and ligaments in determining the greatest contributors behind the ICoR behavior, which is important as the physiological behavior of ICoR depicted in the FE model may affect stresses depicted in a spinal column.
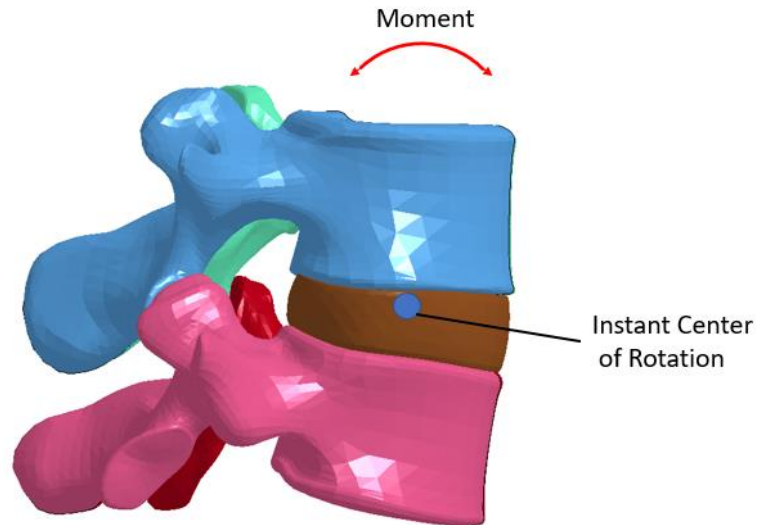
Figure 1-8: Instant center of rotation.

1.3 SCOLIOSIS

1.3.1 OVERVIEW

Scoliosis is a three-dimensional clinical condition that is characterized by deformity of the thoracic and lumbar spines. A scoliotic spine is typically deformed in an 'S' or a 'C' shape within the coronal plane and decreased curvature in the sagittal plane. The American Association of Neurological Surgeons states that scoliosis affects between six and nine million Americans per year. Scoliosis is often treated and classified based on when it occurs in the patient's lifespan (birth vs. old age) as well as its form of causation. Table 1-4 lists the different types of scoliosis patients are commonly diagnosed with, as well as their region of occurrence and causes behind the deformity.

Table 1-4: Main Types of Scoliosis Deformities.

Type of Scoliotic Deformity	Who is affected?	Causation	Forms of Treatment
Congenital (AANS)	1 in 10,000 newborns	Birth defect, such as undeveloped vertebrae	Spinal Fusion, Growing Rod
Neuromuscular (AANS)	Usually children and adolescents	Disorders of the brain, spinal cord	Spinal Fusion, wheelchair modification
Degenerative [2,3]	Aging population	Disc and facet joint degeneration	Nutrition, Physical therapy, spinal fusion
Idiopathic	Usually teenagers going through puberty	Unclear	Bracing, Surgery with correction rods

Adolescent Idiopathic Scoliosis (AIS) constitutes the most common form of scoliosis, occurring in approximately 80% of idiopathic scoliosis patients (Wang et al., 2014) The term 'idiopathic' denotes that there is no known cause for the deformity. The condition affects approximately 1%-3% of adolescents aged 10-18 (Menger and Sin, 2022). On average, the onset of scoliosis occurs between the ages of 12 and 14 (Riseborough and Davies, 1973) just as spinal growth is beginning to slow down (Dougherty, 2014). It is also a disease that is more likely to strike females, showing prevalence of a deformity up to 7 times compared to males, increasing directly with the Cobb deformity (Salmingo, 2013; Konieczny et al., 2013). Unlike other forms of scoliosis, the causation behind idiopathic scoliosis remains unclear. A few research studies have speculated on the causation behind idiopathic scoliosis, including asymmetrical loading in the spine as governed by the Hueter-Volkmann law (Stokes and Liable, 1990; Modi et al., 2008) which states that bone growth is stunted in areas of high

intervertebral pressure while growth accelerates once that pressure is released, causing unbalanced growth usually during puberty. Some have theorized genetics as a cause, as approximately 30% of patients diagnosed with AIS have family history associated with their condition (AANS). Other potential causes include low levels of leptin during puberty (Matusik et al., 2000). The deformity lies primarily within the thoracic spine, often extending into the lumbar region of the spine.

The discomfort level scoliosis patients are forced to endure can be taxing as the deformity progresses. The sagittal and frontal balance of the patient can be affected (AANS), as exhibited by physical and cosmetic deformities such as pelvic crest asymmetry, which creates body tilting, virtual leg length discrepancies, and the hip and shoulder appearing higher between one side and the other. Due to stiffer muscles in scoliosis patients, they have also been shown to stiffen the ankle joints (Mahaudens and Detrembleur, 2015). In severe cases of deformation, shifting of the spine and rib cage can lead to deformation and malfunction of the lungs and heart (Mayurama and Takeshita, 2008) affecting respiration of the patient.

Diagnosing scoliosis is generally performed to monitor and assess the progression of the deformed spine. It initially can be assessed using non-invasive techniques such as the Adams forward bend test (Senkoylu et al. 2021), where any present rib humps in the spine could be measured using a scoliometer. The option for monitoring progression of spinal deformity is given using imaging techniques such as X-rays or more modern techniques such as EOS, which allows for low-dose radiation imaging of the spine, as shown in Figure 1-9. Examination of radiographs (i.e.: X-rays, MRI scans, etc) can point

to the severity of the deformation through a Cobb angle measurement (Reamy and Slakey, 2001). This metric is assessed from the coronal plane, as shown in Figure 1-10.

(a) Coronal view   (b) Sagittal view
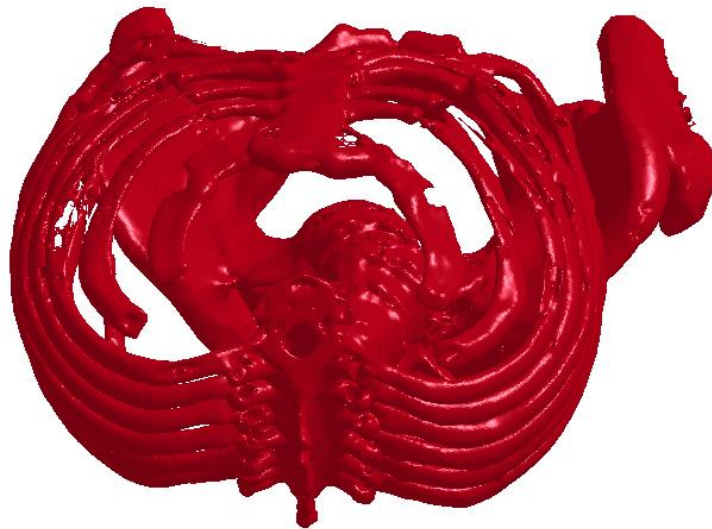
(c) Transverse view

Figure 1-9: Coronal, sagittal, and transverse images of a spine with AIS.
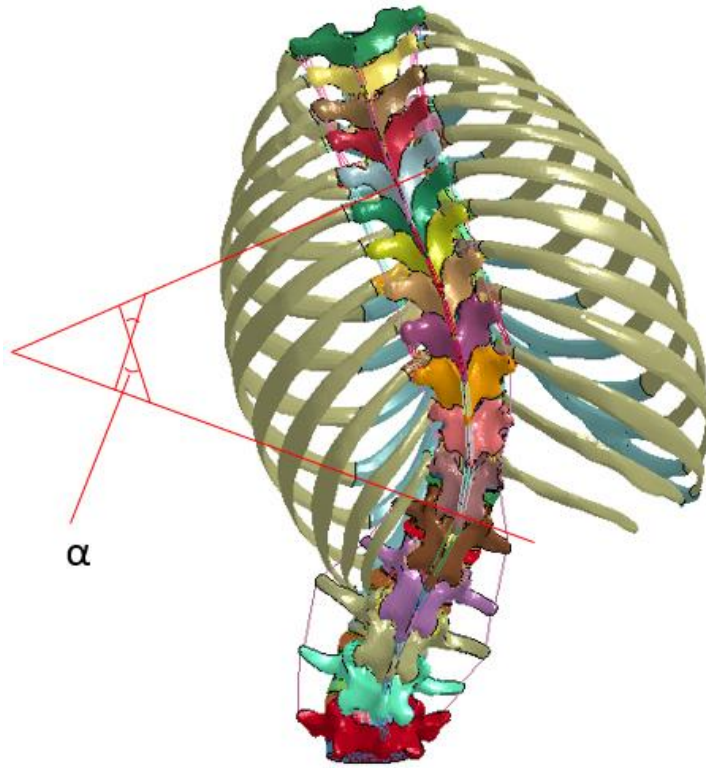
Figure 1-10: Scoliotic spine with Cobb Angle α.

The choice of treatment depends on the severity of the deformity. Generally, a spine is not considered scoliotic until it has reached a Cobb angle of at least 10 degrees. The North American Spine Society has listed standards for deciding the type of treatment a patient with AIS would receive, as seen in Table 1-5. For example, a Cobb angle of at least 20 degrees, would require bracing to fix the deformity. Bracing is typically used as a mechanism to prevent a deformity from developing further, even though it may not correct the spine (Bilgic et al., 2010). If the Cobb angle exceeds 40 degrees, usually the patient will require surgery to correct the spine. Typical surgical techniques incorporate hardware such as pedicle screws and distraction rods to bring the spine back to nominal shape, either through anterior (Shah et al., 2013), posterior (Kim et al., 2012), or

anteroposterior (Fairhurst et al., 2009) fusions. The procedure generally consists of the surgeon retrofitting a pair of distraction rods around the concave and convex portions of the deformity, secured to the spine by pedicle screws. The corrective forces are anchored by the screws and the rods after the surgeon has applied compression on said hardware (Salmingo, 2013; Fairhurst et al., 2009).

Table 1-5: Scoliotic treatment forms based on spinal deformity.

Cobb Angle range	Recommended treatment
0°-20°	Observe deformity progression
20°-25°	Brace if progression documented, and substantial growth progresses
25°-30°	Brace if progressive and deformity progresses
30°-40°	Brace if deformity progresses
40°-50°	Brace if deformity progresses vs. surgery
>50°	Surgery

Guidelines tailored to AIS exist to help surgeons in identifying the most appropriate treatment and fusion, or instrumented vertebral levels, possible based on the curvature on the spine. The Lenke classification system (Lenke et al., 2003) provides a widely accepted and modernized methodology for surgical planning based on coronal and sagittal spinal deformity and identifying whether or not they have an effect on spinal flexibility. As shown in Table 1-6, the procedure for identifying the curve includes three steps. The first step classifies the coronal deformity in the proximal thoracic (PT), main thoracic (MT), and/or thoracolumbar/lumbar regions (Numbers 1-6). For this, the structural criteria is assessed based on the degree of deformity in both the coronal and sagittal planes and identified as either minor or major. Next, the deformity of the lumbar

spine is classified by drawing a vertical line from the sacrum through the lumbar spine and assessing how the vertebrae are positioned with respect to the line. The degree of deformity increases with letter (A for negligible, B for touching apical body, C for apex not crossing the line). Lastly, the degree of sagittal deformity is assessed and assigned either a minus (-) sign (kyphosis < 10°), an N (10°≤ kyphosis angle ≤ 40°), or a plus (+) sign (kyphosis angle > 40°). A curve, for example, could be given the classification Lenke Type 1A+ for a curve with mainly thoracic deformity, no coronal lumbar deformity, and significant kyphosis deformity.

Table 1-6: The Lenke Classification System for AIS.

Table 1-6-1: Step 1: Classifying the coronal curve type.

Curve Type	Proximal Thoracic	Main Thoracic	Thoracolumbar/Lumbar	Description
1	Non-structural	Structural*	Non-structural	Main Thoracic (MT)
2	Structural+	Structural*	Non-structural	Double Thoracic (DT)
3	Non-structural	Structural*	Structural+	Double Major (DM)
4	Structural+	Structural^	Structural^	Triple Major (TM)
5	Non-structural	Non-structural	Structural*	Thoracolumbar/Lumbar (TL/L)
6	Non-structural	Structural+	Structural*	Thoracolumbar/Lumbar-Main Thoracic (TL/L-MT)

*Major curve-largest coronal (Cobb) measurement, +Minor curve-remaining structural curves, ^In Type 4, either MT or TL/L can be considered the major curve.

Table 1-6-2: Step 2: Classifying structural criteria for curve deformity.

Structural Deformity Criteria for Minor Curves		Apex Criteria	
Region	Criteria	Region	Location of Apex
Proximal Thoracic	Cobb angle ≥ 25°, T2-T5 kyphosis ≥ 20°	Thoracic	T2 to T11-T12 IVD
Main Thoracic	Cobb angle ≥ 25°, T10-L2 kyphosis ≥ 20°	Thoracolumbar	T12 to L1
Thoracolumbar/Lumbar	Cobb angle ≥ 25°, T10-L2 kyphosis ≥ 20°	Lumbar	L1-L2 IVD to L4

Table 1-6-3: Step 3: Classifying the Lumbar & Sagittal Cobb angle.

Lumbar Deformity Profile		Sagittal Profile (T5-T12)	
Lumbar Spine Modifier	Center Sacral Vertical Line to Lumbar Apex	Thoracic Sagittal Modifier	Cobb Angle
A	Between pedicles	-(hypokyphosis)	≤ 10°
B	Touches apical bodies	N (normal kyphosis)	10°- 40°
C	Completely medial	+ (hyperkyphosis)	≥ 40°

Among surgical experts there are varying opinions on the best techniques to correct the spine in a way that increases its flexibility during surgery. Those that favor the anterior approach to spinal correction rely on disc removal to increase spinal flexibility, less soft tissue dissection and a lower fusion level of the spine is often required for correction (Betz et al., 1999; Huitema et al., 2014). Those that favor posterior-based approaches typically used the techniques for kyphotic corrections have become popular for scoliosis treatment in recent years due to the ability of the surgeon to increase column

flexibility through osteotomy techniques (Sangiorgio et al., 2013; Pizones et al., 2015) as well as advances in instrumentation technology that allow for more effective column corrections (Vigneswaren et al., 2015). There is also less risk to damage of vital organs such as the heart and lungs one would face during an anterior surgery. Regardless of the surgical method used, it is estimated that 20% of idiopathic scoliosis patients that undergo surgery experience some degree of post-surgical mechanical complications (Weiss et al., 2008). These include susceptibility to pedicle screw pullout, correction rod failure, and infection (Barton et al., 2017). Post-surgical complications often lead surgeons to perform the operation again to restore correction to the spinal region in question. Understanding the complications that arise after surgery is currently an area being examined among researchers.

1.3.2 PONTE OSTEOTOMY

The Ponte osteotomy is a posterior-based correction procedure applied to scoliosis patients, offering treatment of sagittal-based deformities. Its original purpose was to reduce posterior column length in spines with increased convexity, or kyphosis, through ligamentous posterior release. The steps of the corrective procedure are as follows: the spinous ligaments are removed (e.g., interspinous and supraspinous ligaments) along with the spinous processes. Next, a bilateral inferior facetectomy is performed to release the pressure exerted through axial rotations. If the flexibility is deemed insufficient for the surgeon, they move towards resection of the ligamentum flavum. Finally, if more flexibility is needed, a bilateral superior facetectomy is conducted. The Ponte osteotomy has gained interest in the surgical community for its ability to produce increased

correction to the scoliotic spine. A study of 191 adolescent patients with Lenke Type 1A or 1B scoliosis curves had their Cobb deformities compared pre-and post-surgery (Samdani et al., 2015). After 2 years, those who underwent a Ponte osteotomy saw greater coronal correction to their spines versus those who did not undergo a Ponte osteotomy for spinal correction (67% vs. 62%), as well as slight increase in T5-T12 kyphosis angles.

1.3.3 TREATMENT COSTS

The costs of treating scoliosis in children is rising and can be attributed to a number of factors. First, the number of children seeking treatment accounts for the largest quantity of all musculoskeletal deformity clinical visits, over 850,000 per year (Agency for Healthcare Research and Quality, 2011). The mean hospital charges for surgical treatment of AIS have increased almost threefold between 1997-2012 (Vigneswaren et al., 2015), from $55,495 to $177,176 respectively, while the average cost of a hospital stay for a scoliosis patient is $92,000, five times the national average (Agency for Healthcare Research and Quality, 2011). The posterior and anteroposterior surgical methods currently contribute the most to the rise in costs, at approximately $175,000 and $250,000 respectively in 2012 (Vigneswaren et al., 2015) due to an increase in instrumentation required for fusion and post-surgical complication rates in patients, which was the greatest at 37.1%. Approximately 29,000 adolescents undergo scoliosis surgery annually (Nochesko et al., 2015). Given these alarming trends, there is a need to answer clinical questions that enhance treatment and understanding of scoliosis biomechanics.

1.4 FINITE ELEMENT ANALYSIS AS A TOOL FOR SURGICAL PLANNING

The finite element method (FEM) is a commonly utilized numerical-based procedure that solves a series of differential equations to provide approximate answers to engineering-based questions that are otherwise time consuming to manually resolve. FEM has been employed as a powerful tool designed to assist in resolving questions pertinent to clinical treatment and obtain data that would prove either difficult or unethical to collect either experimentally (e.g., in-vitro) or from live subjects (e.g., in-vivo). The method is preferred for its capability in accurately representing patient-specific material and geometric heterogeneities along the spinal column to objectively predict kinematics and stress-strain distributions among vertebrae and attached soft tissues (e.g., ligaments and IVD) under complex loading.

The degree to which anatomical details have been introduced into FE models of the spine are highly variable, yet dependent on the clinical study. Further complicating the matter is that the basis for all FE models may be dependent on subject demographics such as age, gender, and preexisting condition of the anatomy. To validate the biomechanical behavior of an FE model requires comparison between one or more variables from in-vivo or in-vitro experiments. The methods necessary to achieve model validation may also vary depending on the FE program as well as the A functional spinal unit (FSU), consisting of two vertebrae and one IVD, is the most basic FE model utilized to answer basic clinical questions about variables influencing pathology (Rohlmann et al., 2006a; Meijer et al., 2011), effects of various treatments such as spinal implants (Coogan et al., 2016) and surgical destabilization (Little and Adam, 2011b), or anatomic characterizations pertinent to an FE model such as with facets (Kumaresan et al., 1998;

Ahuja et al., 2020) or spinal ligaments (Naserkhaki et al., 2018). The lessons learned from an FSU model can be further applied towards validation and development of larger FE models of the spine.

Some previous research investigating scoliosis using FE model techniques have characterized thoracic and lumbar spines using one-dimensional beam elements and joints to represent vertebrae, ligaments, and the IVDs respectively. Their utilization has been employed in scoliosis induction (Villemure et al., 2002), rib shortening and lengthening (Carrier et al., 2004), and kinematic validation efforts with radiographic motion in-vivo (Lafon et al., 2010). The main deficiency behind this methodology is the turnaround time necessary to assign proper geometric and material properties to each spinal segment to ensure proper biomechanical behavior of each FE model. This requires knowledge of anatomic dimensions as well as rotational stiffness of each segment, which may be variable by patient and by segment (White and Panjabi, 1990).

Due to an enhancement in computational power, a gradual migration towards three-dimensional volumetric FE models is being performed for clinical scoliosis investigations. Volumetric FE models offer a more realistic representation of vertebrae and IVDs and eliminate the need to manually account for geometric nonlinearity. They also allow for further detail within each component to be explicitly modeled. These components include: cortical and cancellous bones in the vertebrae, facet joints, endplates, and the annulus fibrosus, fibers and nucleus pulposus of the IVD. A main advantage volumetric FE models offer is the ability to predict critical stress and strains, which may indicate sources of pain in scoliotic spines (Wang et al., 2016) or the effect of implanted rods to maintain spinal correction (Agarwal et al., 2014).

To generate volumetric patient-specific anatomy, scanners are typically employed to obtain radiographic images of a patient, such as a CT scan or an X-ray, within three anatomic planes. From these images, a segmentation procedure is employed which maps the images from the radiographs into a computer-aided design (CAD) format that may subsequently be used as a platform for finite element analysis. This method is preferred among researchers as clinical investigations may be more focused on specifically resolving questions pertinent to the patient and potentially others within their demographic. Clinical questions applied in the general sense are utilized from publicly available CAD models. For example, some have utilized publicly available CAD models from digital atlases for FE spinal studies (Lv et al., 2018; Cahill et al., 2012).

In the scoliosis arena, 3D FE models have been utilized to understand the effects of post-surgical treatment. Cahill et al. (2012) utilized a FE model of a C6-T12 spine without a ribcage to understanding how kyphotic curves may be inhibited post-scoliosis surgery using a transition rod. The study focused only on applying sagittal moments and displacements, as well as removing the spinous ligaments separately, while assessing the differences in IVD pressure as well as screw stress and pullout force in both scenarios. While they determined that having the spine intact with a transition rod reduced force overall, the study did not consider the effect of the ribcage, which may have altered the results reported.

Volumetric FE models have also been utilized for investigating scoliosis etiology. Shi et al. (2011) utilized a series of volumetric thoracolumbar FE models to understand the difference in loading patterns on the progression of scoliosis over time. Using scoliosis curves with different Lenke classifications, the Hueter-Volkmann law was

employed to induce scoliosis over a period of 2-3 years pseudo time. They found that the greater the lateral deformity, the more pronounced the Cobb angle was, where those profiles with no initial lateral deformity did not see a change in Cobb angle. Most recently, Zhang et al. (2021) utilized a scoliotic lumbar spine with a 43° Cobb angle to investigate load distribution along the lumbar spinal column during movement. They determined the greatest stress values in the disc to be along the concave sides and on the most superior vertebra. The latter study did not consider the thoracic spine, and the study by Shi et al. did not incorporate a ribcage. There was also no kinematic data for scoliotic spines available to validate the study by Zhang et al.

Obtaining biomechanical data on adolescents is difficult, especially in-vitro, due to the smaller number of subjects to choose from compared to the adult population. Due to changes in spinal anatomy that occur from birth to adulthood, it is simply not sufficient to linearly scale down from an adult to match the morphology of a younger spine. Thus, researchers often had to make assumptions regarding estimations on geometric and material properties. Meijer (2011) generated an entire thoracolumbar FE model for AIS studies. Using adult vertebrae as the basis for the studies, they were scaled through a computer program to match average dimensions concurrent with a 10-year-old adolescent and positioned to match a Cobb angle of 32°, while maintaining material properties appropriate for an adult. The focus of the thesis was primarily to assess the effects of different anatomic parameters throughout the spinal column either removed or varied in a computational model and their implications on patient-specific surgical planning. Hadagali (2014) outlined a methodology for constructing a subject-specific thoracic FE model of an adolescent for scoliosis surgical planning. Using segmented anatomy of a 10-

year-old, scale factors were proposed for appropriate loading regimes from available in-vitro adult data, and material properties to introduce into the FE model, taken primarily from interpolation curves generated by Liu and Kang (2002), which was based on the state-of-the-art literature review on computer models for children at the time. Jebaseelan et al. (2012) examined the sensitivity of the material properties for a juvenile lumbar spine FE model to external moments. By increasing and decreasing the elastic moduli between components of the vertebral column by 25% in each direction, they assessed the changes in stresses in each component. Changes to stresses were more pronounced when modulus values were decreased.

As scoliosis is a deformity that involves both the thoracic and lumbar spines, the gaps in literature present an opportunity to examine the biomechanics of the thoracic spine. Where most of the literature has focused on understanding behavior of the cervical and lumbar spine regions, the same level of focus has not been reciprocated to the thoracic spine. Owing to column reinforcement due to the presence of a ribcage, as well as size differences in the vertebrae and IVDs, it becomes important to understand how to develop a thoracolumbar FE model to best fit the morphology of the thoracic and lumbar spines alike. Despite the lack of data to validate adolescent and scoliotic FE models, one may still benefit in the steps taken to develop a detailed thoracolumbar FE model on the road to a patient-specific surgical planning platform for AIS.

1.5 SPECIFIC AIMS

Objective: Develop a platform by which finite element analysis techniques may be adapted towards patient-specific scoliosis surgical planning.

SPECIFIC AIM 1: Assess and compare the kinematic behavior of a thoracic spine functional spinal unit through input of different intervertebral ligament stiffness properties.

HYPOTHESIS: Ligament properties exhibiting compliant toe and stiff linear regimes in their stiffness curves will improve kinematic behavior when compared with available in-vitro data.

SPECIFIC AIM 2: Apply a surgical procedure on a thoracic spine functional spinal unit to assess how load sharing among intact ligaments and the intervertebral disc change after ligaments are serially removed.

HYPOTHESIS: Sagittally, the load sharing percentage will increase towards posteroanterior ligaments while in axial rotation, most of the load will be transferred to the IVD after facets are removed.

SPECIFIC AIM 3: Assess different methods to incorporating the facet joint in a finite element model.

HYPOTHESIS: Incorporating increased compressibility through explicit modeling of synovial fluid will improve functional spinal unit kinematics, particularly in extension.

SPECIFIC AIM 4: Mechanically induce a mild scoliosis curve into an asymptomatic thoracolumbar FE model, and kinematically compare with an asymptomatic FE model.

HYPOTHESIS: The scoliotic FE model will behave stiffer as a result of vertebral axial rotations and reduced disc height in apical segments.

CHAPTER 2

DEVELOPMENT AND VALIDATION OF THE SPINAL FINITE ELEMENT MODEL

2.1 INTRODUCTION

The following chapter details the procedure implemented by which an osseoligamentous finite element (FE) model is developed and validated. A selection process between two computer-aided design (CAD) geometry spine models was implemented. Once a decision was made, the development procedure commenced beginning with the lumbar spine and validation of both a functional unit as well as the lumbar spine column compared with published data (e.g., in-vitro and FE model). Next, the thoracic spine and the ribcage were constructed using CAD geometry. Costovertebral joint configurations for the ribcage were also developed and validated using available in-vitro data. An attempt was made to validate the thoracic spine using published in-vitro data. In both instances, a mesh sensitivity study was completed to assess the optimal mesh size to utilize for subsequent biomechanical studies. The approach presented followed standard practices by which FE models are to be developed while implementing approaches to volumetric modeling of the thoracic spine, whose information is lacking in the literature.

2.2 CAD MODEL DIMENSION ASSESSMENT

To commence development of the finite element model, two versions of a CAD geometry model of the full spine were evaluated for potential utilization. The first was downloaded from the BodyParts3D anatomical database (Figure 2-1), (Mitsuhashi et al.,

2009). The BodyParts 3D CAD model was created using a hybridized approach where the anatomy of an adult human male was digitally reconstructed using MRI images. However, where detail was missing from the reconstructed anatomy either due to the segmentation or the image quality, a 3D editing program was utilized to supplement the necessary features using textbooks, digital atlases, and medical models. The second CAD model was drawn by an anatomist (Figure 2-2; CGHero, Manchester, UK), designed to be representative of the average adult. The primary difference between CAD models here was the presence of spinal ligaments in the latter versus the BodyParts 3D model. It is important to note that segmentation of patient-specific anatomy is a commonly used method to generate osseoligamentous geometry serving as a foundation for Finite Element models. Unfortunately, this iteration of the project did not readily possess the tools necessary for patient-specific reconstruction, prompting the use of CAD models for this study.

The total height of each CAD model was manually measured using Hypermesh (Altair Engineering, Troy, MI, USA) from the spinous process tips of C1 to L5, and from the spinous process tips of T1 to L5, to ensure comparability in measurements between the two (Table 2-1). Next, individual dimensions of each vertebra and intervertebral disc (IVD) were assessed in the thoracic and lumbar spinal columns, also using Hypermesh. All measurements taken were compared with literature values primarily acquired from published CT scan data (Busscher et al. 2010, Frost et al. 2019, Zhou et al. 2000; Yao et al. 2016) or textbooks (White and Panjabi, 1990). The image data obtained from Spineweb was utilized for manual measurements using a measure tool in 3D Slicer Version 4.10.2. By comparing key dimensions of both CAD models, the accuracy of the

anatomic input could be confirmed for utilization in the biomechanical studies conducted for this dissertation. Results are shown graphically in Figures 2-4 to 2-6 and further transcribed in Tables 2-2 to 2-3.

(a)Sagittal View   (b) Coronal View   (c) Axial View
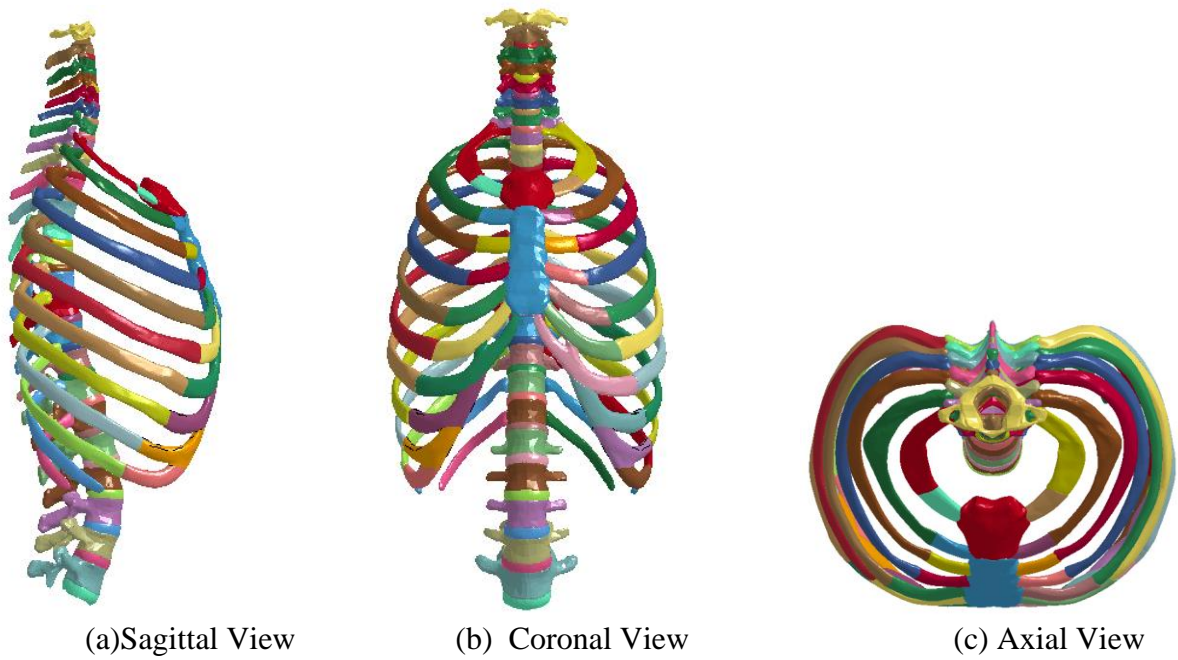
Figure 2-1: BodyParts3D CAD model. (a) Sagittal View. (b) Coronal View. (c) Axial View.

(a) Sagittal View   (b) Coronal View   (c) Axial View
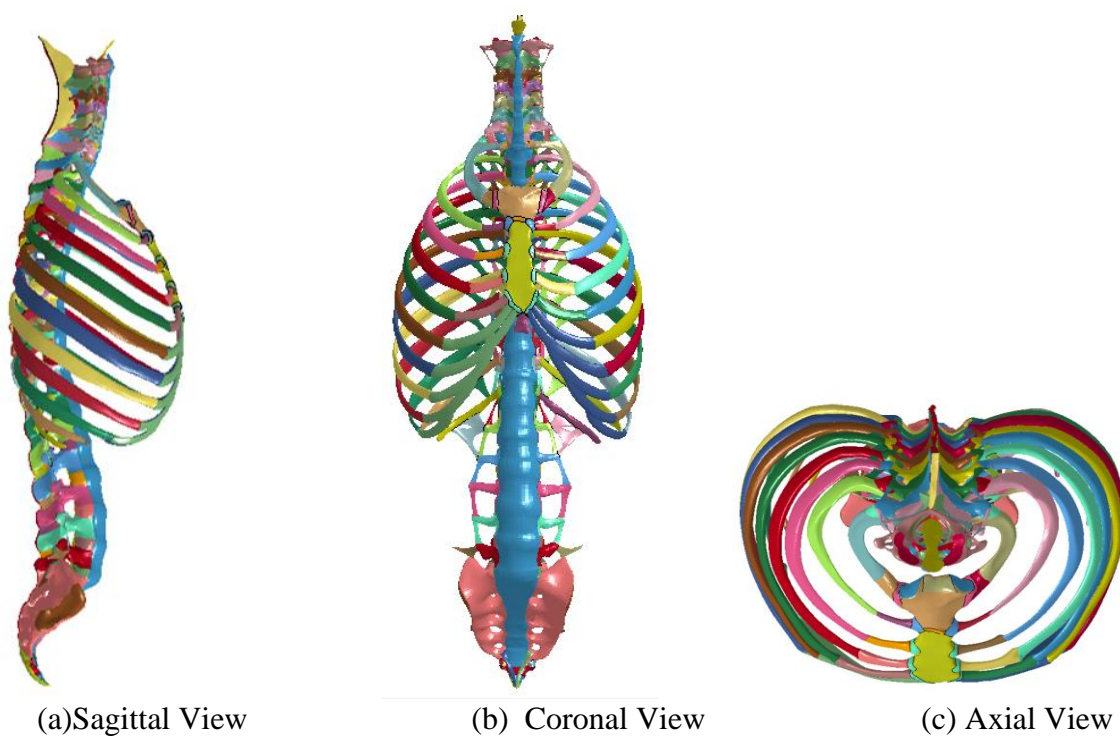
Figure 2-2: CGHero CAD model. (a) Sagittal View. (b) Coronal View. (c) Axial View.

(a)   (b)

(c)
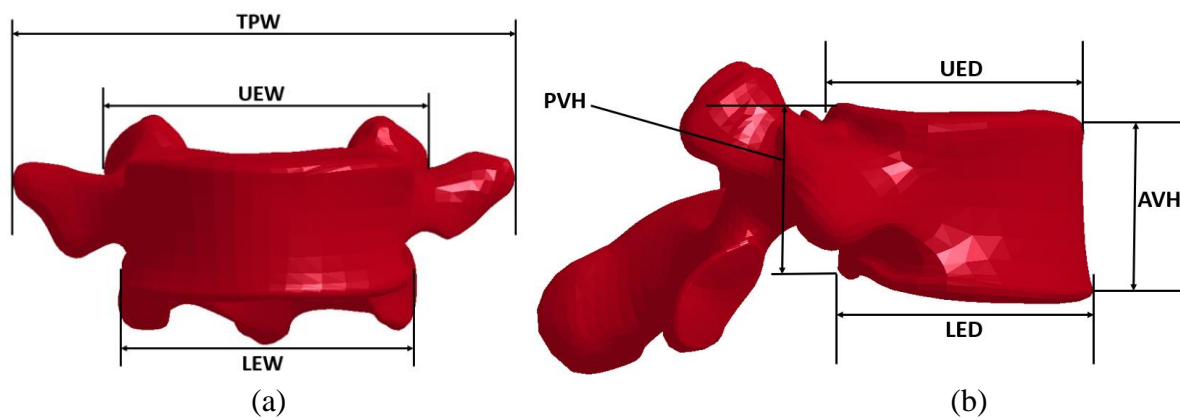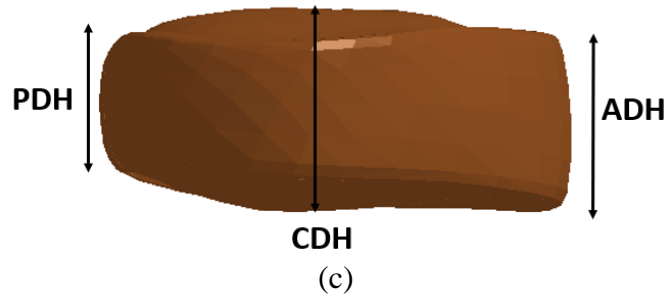
Figure 2-3: (a) Vertebral dimensions. (b) IVD dimensions; Abbreviations are as follows: TPW (Transverse Process width), UEW (Upper Endplate width), LEW (Lower Endplate width), UED (Upper Endplate depth), LED (Lower Endplate depth), PVH (Posterior Vertebral height), AVH (Anterior Vertebral height), PDH (Posterior Disc height), CDH (Center Disc height), ADH (Anterior Disc height).

Table 2-1: Measured lengths compared between CAD models.

Measured reference points	BodyParts3D	CGHero
C1 spinous process tip to L5 spinous process tip	537.989 mm	556.506 mm
T1 spinous process tip to L5 spinous process tip	422.388 mm	445.955 mm

Table 2-2: Quantitative vertebral dimensions, abbreviations referenced in Figure 2-3. All values are listed in mm. Quantitative thoracic anatomy is compared with White & Panjabi (1990).

		TPW	UEW	LEW	UED	LED	PVH	AVH
T1	BodyParts3D	73	27.1	28.5	16.5	16.9	14.1	13.7
	CGHero	80.3	25.3	27.9	15.1	15.6	17.6	14.4
	White and Panjabi (1990)	**75.3**	**24.5**	**27.8**	**18.5**	**19.7**	**14.1**	**N/A**
T2	BodyParts3D	68.8	27.1	29.5	17.1	16.7	14.8	16.3
	CGHero	67.4	27.6	28.2	15.3	16.6	17.6	15.1
	White and Panjabi (1990)	**69.4**	**24.9**	**27.4**	**19.6**	**21.6**	**15.6**	**N/A**
T3	BodyParts3D	62.8	27.5	26.9	19.6	21.1	17.3	17
	CGHero	67.6	24	26.4	17.6	18.7	19	16.8

Table 2-2 continued.

	White and Panjabi (1990)	**60.8**	**24.6**	**25.9**	**22.7**	**23.3**	**15.7**	**N/A**
T4	BodyParts3D	69.4	26	26.1	20.1	21.1	17.3	18.1
	CGHero	62.1	25.5	26.6	19	19.1	18.3	16.5
	White and Panjabi (1990)	**56.9**	**24.5**	**26.0**	**23.3**	**24.5**	**16.2**	**N/A**
T5	BodyParts3D	69.9	26.4	25	22.8	25.1	18.1	17.5
	CGHero	63.7	25.2	27	20.8	20.4	17.7	16.2
	White and Panjabi (1990)	**61.1**	**24.9**	**27**	**24.3**	**25.8**	**16.2**	**N/A**
T6	BodyParts3D	70.8	27.9	29.3	24.2	26	18.7	18
	CGHero	63.2	26.3	29.2	21.2	20.8	20.5	18
	White and Panjabi (1990)	**61.3**	**26.2**	**28.2**	**26**	**26.9**	**17.4**	**N/A**
T7	BodyParts3D	72	32.2	29	27.1	28.9	21.2	20
	CGHero	65.2	28.4	30.4	21.9	22	21	17.6
	White and Panjabi (1990)	**60.4**	**27.8**	**29.1**	**27.4**	**28.5**	**18.2**	**N/A**
T8	BodyParts3D	62.1	29	29.8	29	30.6	21.2	19.7
	CGHero	61.5	28.2	31.2	23.1	23.3	23.1	18.8
	White and Panjabi (1990)	**59.9**	**29.5**	**30.5**	**27.9**	**29.4**	**18.7**	**N/A**
T9	BodyParts3D	64.2	32	32.9	31.2	31.5	22.3	20.8
	CGHero	58.9	29.9	32.8	23.5	24.5	22.6	20.3
	White and Panjabi (1990)	**59.3**	**30.6**	**33**	**29.3**	**31**	**19.3**	**N/A**
T10	BodyParts3D	64.6	33	35	31.5	32.4	23.7	22.3
	CGHero	58.3	31.8	35	23.9	26	25.4	23.7
	White and Panjabi (1990)	**58.4**	**31.9**	**35.4**	**30.5**	**31.6**	**20.2**	**N/A**
T11	BodyParts3D	51.9	34.7	36.2	32.3	32.6	22.4	22
	CGHero	47.8	34.8	40.1	25	24.9	26.6	22.5
	White and Panjabi (1990)	**52.2**	**34.9**	**39.1**	**31.9**	**31.8**	**21.3**	**N/A**
T12	BodyParts3D	41.6	37	37.6	34.2	32.8	24.2	23.9
	CGHero	43.2	39.3	42	25.6	27.1	27.5	22.9
	White and Panjabi (1990)	**46.9**	**39**	**42.1**	**32.8**	**33.4**	**22.7**	**N/A**
L1	BodyParts3D	70.2	40	39.8	33.6	32.3	24.3	25.9
	CGHero	73.5	41	44	27.5	29.7	31.4	28.6
L2	BodyParts3D	77.8	38.7	41.5	33.8	32.9	22.8	28.1
	CGHero	89.4	43.6	46.5	30.5	31.1	32.4	28.8
L3	BodyParts3D	77.5	41.6	40.3	33.5	34.5	24.3	29

Table 2-2 continued.

	CGHero	110.4	45.8	49.8	31.2	30.7	30.8	29.7
L4	BodyParts3D	83.3	42.3	44.9	33.7	33.6	24.8	27.7
	CGHero	100.7	48.5	53.3	30.4	34.3	26.3	26.3
L5	BodyParts3D	98.6	46.1	44.9	36.1	39.1	21.9	27.5
	CGHero	90.3	51.3	51.8	31.4	34.1	22.4	24.6
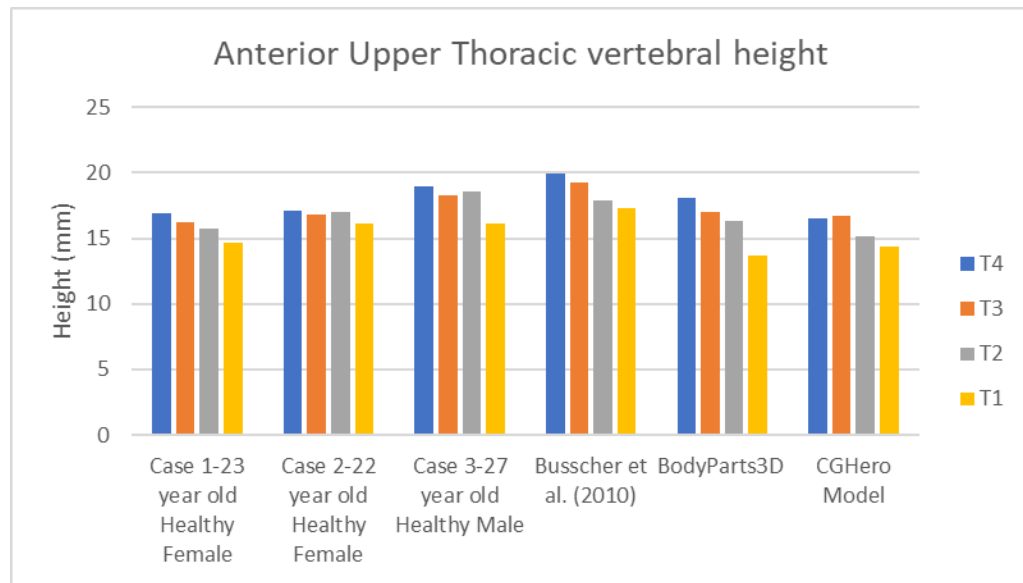
(a)
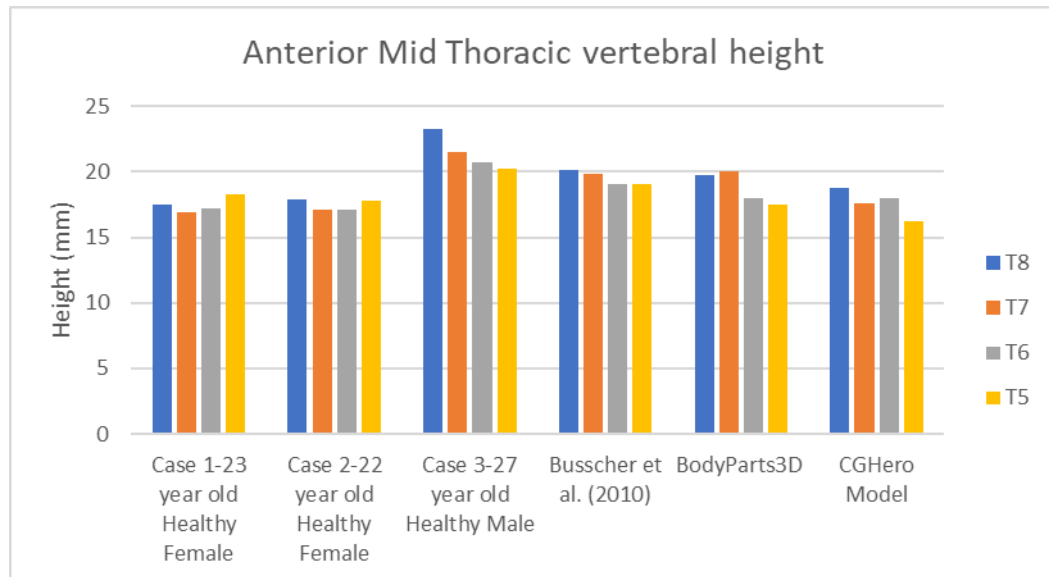
(b)
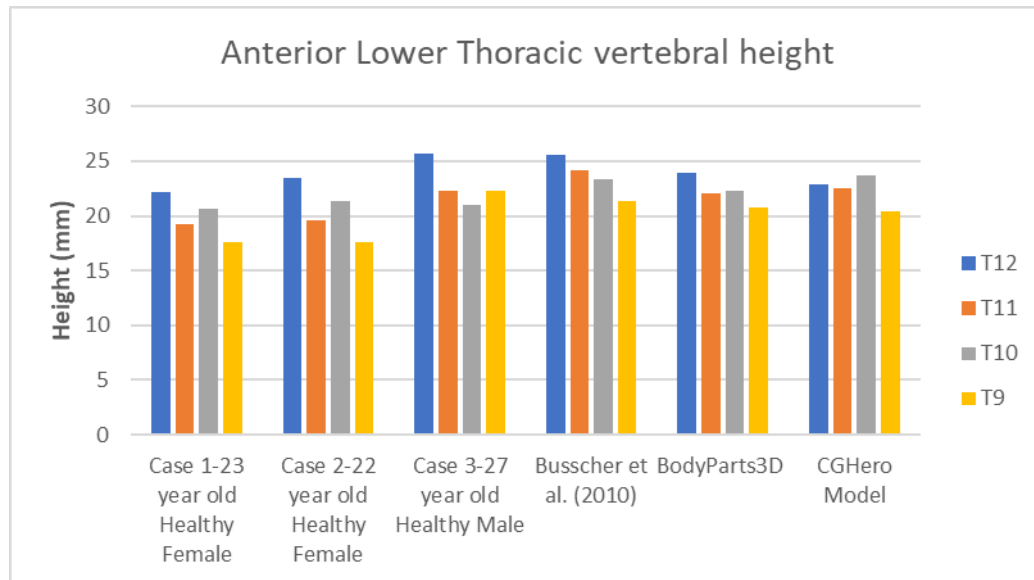
(c)
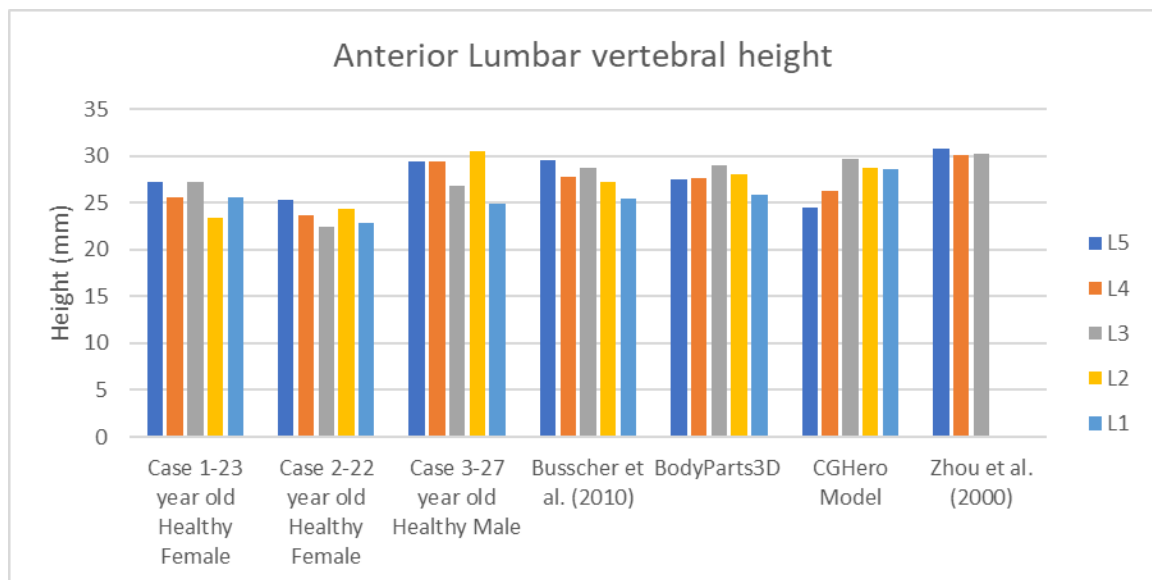
(d)

Figure 2-4: Anterior Vertebral Height (AVH) measurements compared with image data from various sources. (a) Anterior upper thoracic vertebral height. (b) Anterior mid thoracic vertebral height. (c) Anterior lower thoracic vertebral height. (d) Anterior lumbar vertebral height.
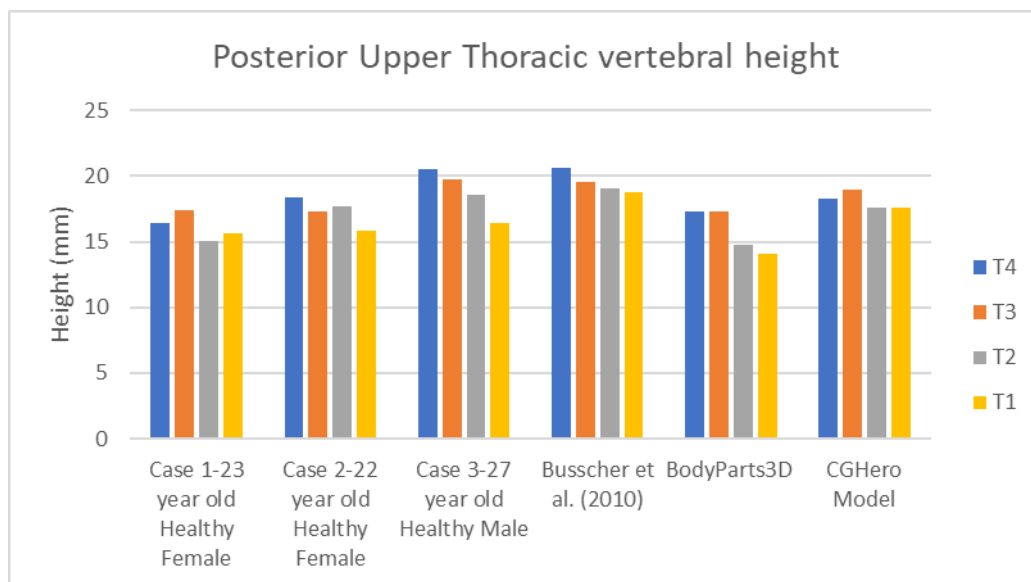
(a)
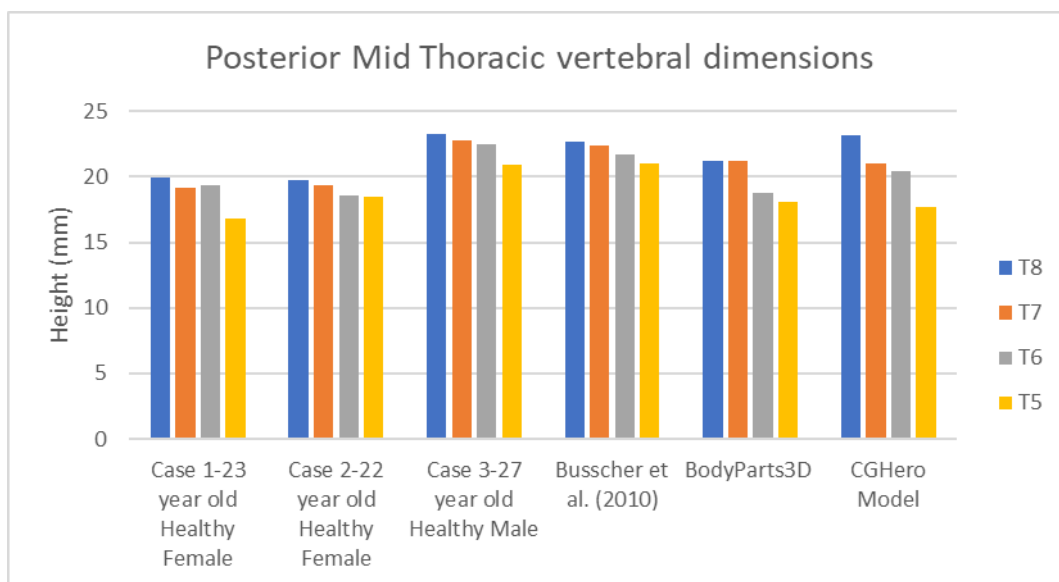
(b)
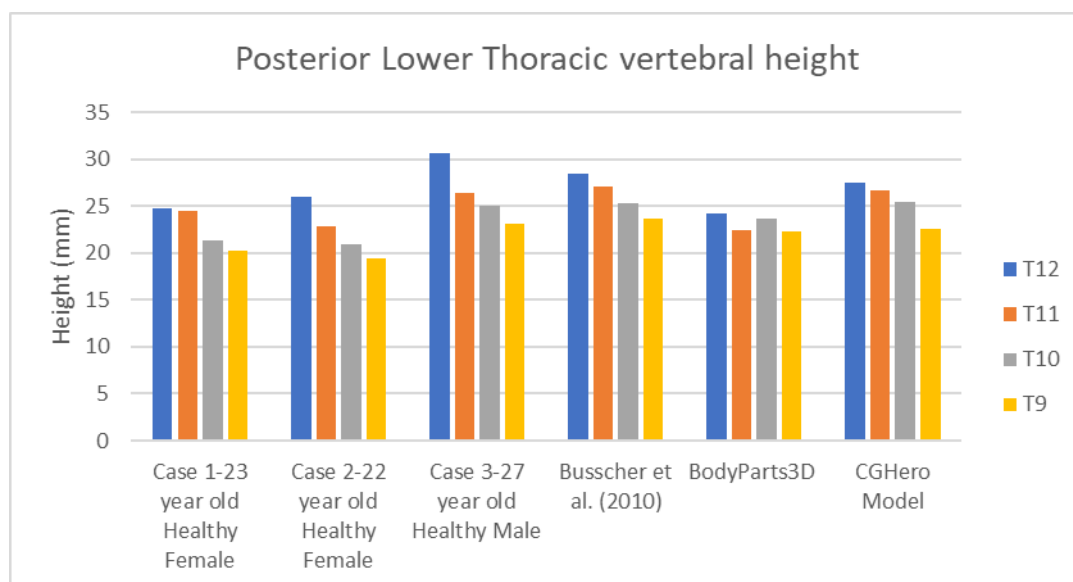
(c)
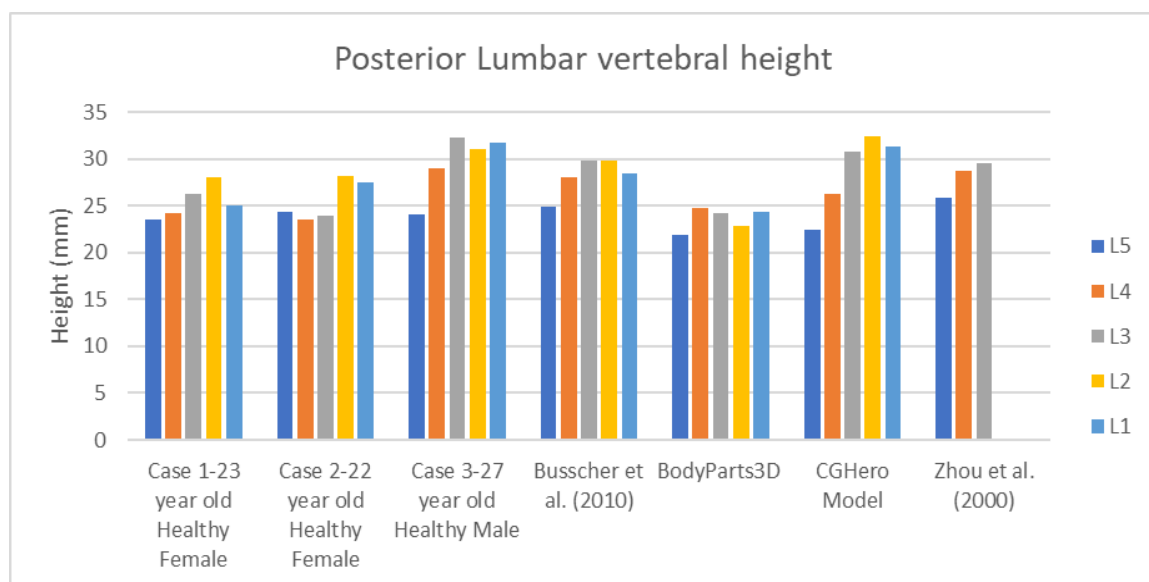
(d)

Figure 2-5: Posterior Vertebral Height (AVH) measurements compared with image data from various sources. (a) Posterior upper thoracic vertebral height. (b) Posterior mid thoracic vertebral height. (c) Posterior lower thoracic vertebral height. (d) Posterior lumbar vertebral height.

Table 2-3: IVD CAD model thickness measurements in mm within different spine regions compared with mean IVD thickness values from patients' CT images ages 20-79 (Fletcher et al., 2015). Abbreviations referenced in Figure 2-3.

		PDH	CDH	ADH	Mean
T1-T2	BodyParts3D	5.7	4.6	5.9	5.4
	CGHero	3.1	5.9	4.9	4.6
T2-T3	BodyParts3D	6	6.8	6.3	6.4
	CGHero	2.1	5.6	4.5	4.0
	Fletcher et al. (2015) Male	**3.5**	**4.3**	**2.9**	**N/A**
	Fletcher et al. (2015) Female	**3.0**	**4.5**	**2.7**	**N/A**
T3-T4	BodyParts3D	6	6.1	5.9	6.0
	CGHero	2.8	4.7	4.5	4.0
T4-T5	BodyParts3D	7.1	6.2	5.4	6.2
	CGHero	4.1	6	4.2	4.7
	Fletcher et al. (2015) Male	**3.1**	**4.1**	**2.7**	**N/A**
	Fletcher et al. (2015) Female	**2.9**	**4.1**	**2.6**	**N/A**
T5-T6	BodyParts3D	7.5	5.3	6.6	6.5
	CGHero	3.5	5.4	4.3	4.4
T6-T7	BodyParts3D	9.9	6.3	7.2	7.8
	CGHero	3.8	6	5.3	5
	Fletcher et al. (2015) Male	**3.8**	**4.6**	**3.9**	**N/A**
	Fletcher et al. (2015) Female	**3.5**	**4.6**	**3.4**	**N/A**
T7-T8	BodyParts3D	7.7	7.4	7.5	7.5
	CGHero	4.1	7	5.8	5.6
T8-T9	BodyParts3D	5.6	5.8	8.7	6.7
	CGHero	3.9	6.2	4.6	4.9
	Fletcher et al. (2015) Male	**3.9**	**5.1**	**4.9**	**N/A**
	Fletcher et al. (2015) Female	**3.7**	**5.2**	**4.2**	**N/A**
T9-T10	BodyParts3D	5.6	5.8	8.7	6.3
	CGHero	5.2	7	5.6	5.9
T10-T11	BodyParts3D	6.8	5.3	7.3	6.5
	CGHero	3.9	6.7	6.1	5.6
	Fletcher et al. (2015) Male	**3.7**	**5.9**	**5.4**	**N/A**

Table 2-3 continued.

	Fletcher et al. (2015) Female	3.8	6.1	5.1	N/A
T11-T12	BodyParts3D	7.2	5.2	8.4	6.9
	CGHero	3	7.1	5.1	5.1
T12-L1	BodyParts3D	8	6.7	8.1	7.6
	CGHero	2.8	7.4	7.3	5.9
L1-L2	BodyParts3D	5.8	8	9.8	7.8
	CGHero	4.3	8.2	8.6	7.0
L2-L3	BodyParts3D	6.5	10.5	11	9.3
	CGHero	7	13.1	12.2	10.8
L3-L4	BodyParts3D	5.5	5.1	11.8	7.5
	CGHero	6.6	14.5	12.2	11.1
L4-L5	BodyParts3D	10.3	11.9	8.6	10.3
	CGHero	8.3	13.9	12	11.4

(a)
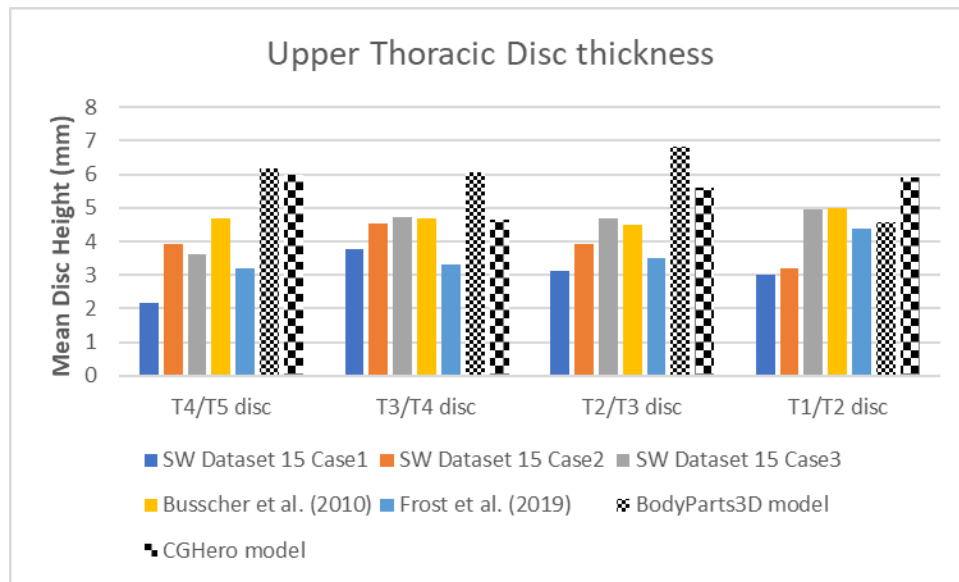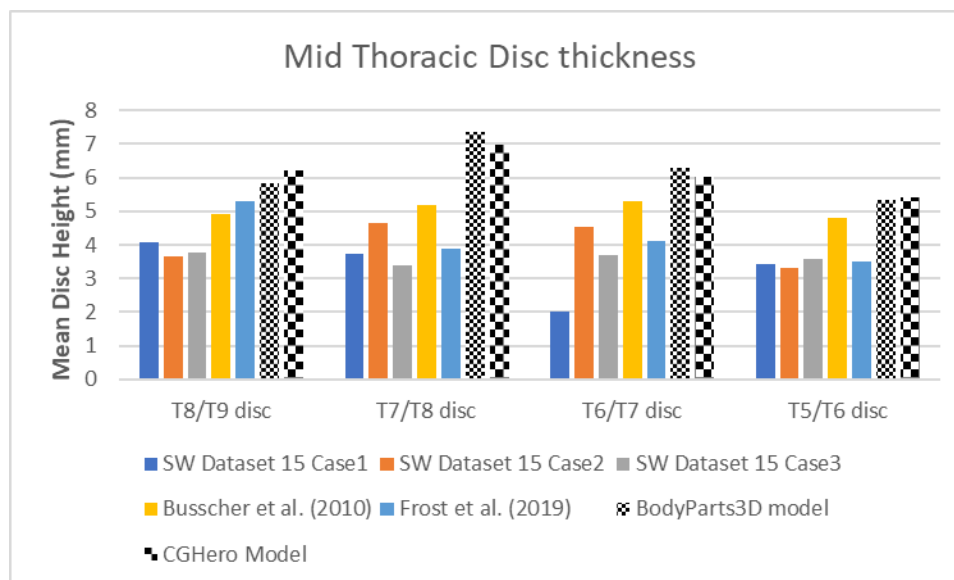
(b)
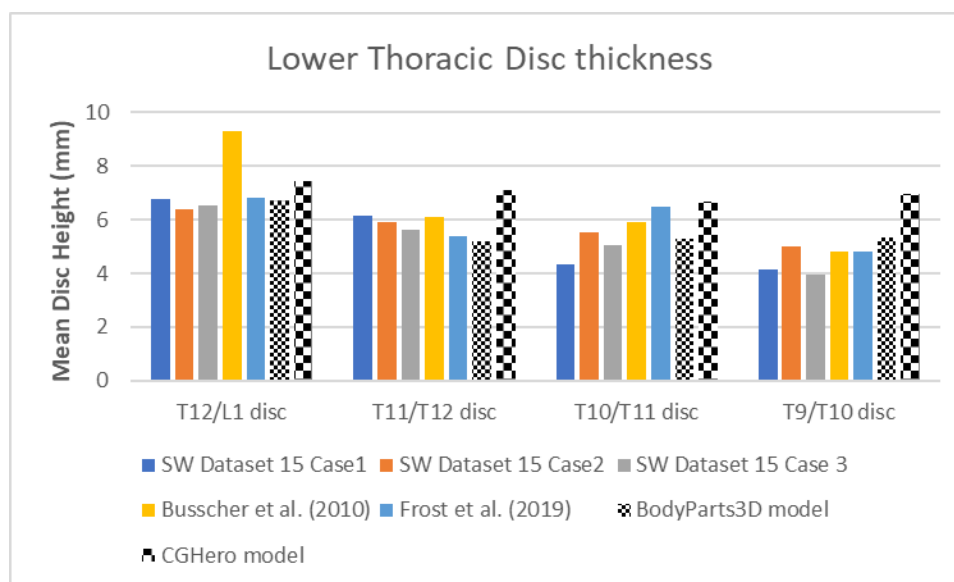
(c)
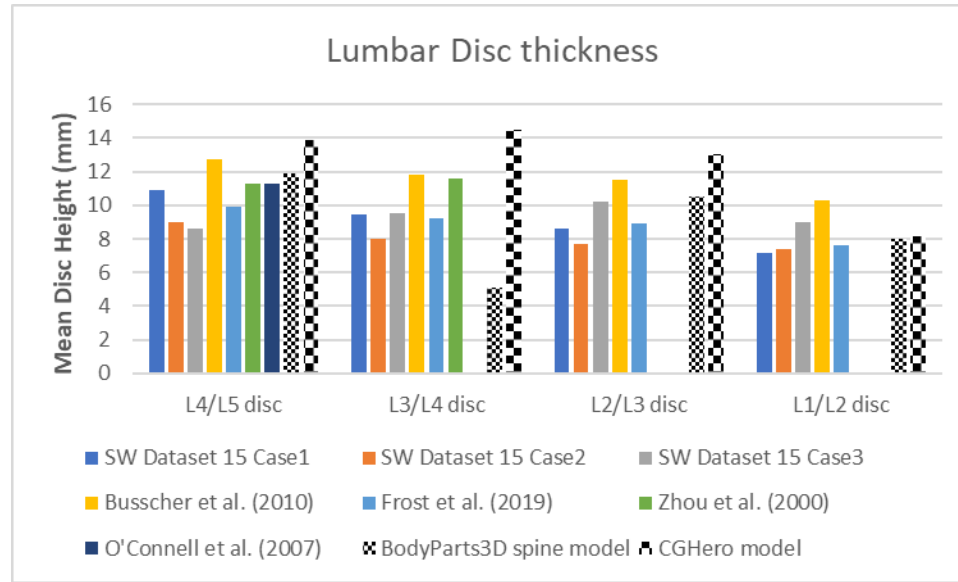
(d)

Figure 2-6: Mean IVD thickness. (a) Upper thoracic IVD thickness; (b). Mid thoracic IVD thickness; (c) Lower thoracic IVD thickness; (d). Lumbar IVD thickness.

2.3 INITIAL MESH SENSITIVITY ASSESSMENT

After dimensions were acquired on both CAD models, a mesh sensitivity analysis was then conducted, first, on a lumbar (L4-L5) functional spinal unit (FSU). Initially, the BodyParts3D CAD model was utilized for meshing as the CGHero model had not yet been discovered at the time of the study; the approach presented was utilized for self-guidance and verification of mesh, contact and anatomic material properties for the FE model. All functional unit model variations utilized the following anatomical entities: cortical bone, posterior elements, cancellous bone, IVD with annulus fibers, cartilaginous endplate, and intervertebral ligaments (Figures 7a-7g). To develop the functional unit model, the finite element meshing software Hypermesh (Altair Engineering, Troy, MI, USA) was utilized to tesselate all parts of the model appropriately. Both the cancellous bones and IVD were created using a mapping technique that referenced endplate surfaces

to extrude layers of elements through the thickness of all anatomy to create hexahedral elements. The posterior elements, consisting of the vertebral arch, pedicles, transverse and spinous processes, were meshed using tetrahedral elements due to the highly nonlinear geometric configuration. The cortical bone was meshed using quad and tria elements in the anterior and posterior portions of the vertebrae respectively; the cartilaginous endplate was meshed using quad elements. Material properties for all FSU counterparts were acquired from literature and summarized in Table 2-4. All annulus fibers were generated using a custom MATLAB script to position cable elements concentrically cross-hatched at diagonal faces of each element generated along the annulus fibrosus ground substance and scaled to reflect reduced stiffness from the outer to inner disc circumference (Table 2-5). Cross-sectional area values were calculated in conjunction with the length for all annulus fibers such that the total volume fraction of the fibers was approximately 16% of the annulus fibrosus ground substance volume. The product of the average cross-sectional fiber area and length per concentric layer were used to calculate fiber volume.

The lumbar FSU was meshed using three different element sizes: coarse (2.92mm), medium (2.13mm), and fine (1.52mm). Accordingly, the number of layers through the IVD thickness for each case was 3, 5, and 7 layers respectively. Both first and second order elements for all shell and solid elements in the model were considered for each mesh size highlighted; the utilization of second order elements adds more nodes to all elements and is generally considered to produce accurate solutions relative to first order elements. Further information for each model can be found in Table 2-7.

The intervertebral ligaments were characterized using cable elements which, by

proxy, only contain tensile stiffness; all were configured based on cross-sectional area data from the literature and initial unstretched lengths from the FE model. Information on the functional unit ligaments is listed in Table 2-6; stiffness properties are shown in Figure 2-9(a). A penalty contact algorithm between inferior and superior facet surfaces was configured with a contact thickness of 0.2mm for each surface. A moment of approximately 15 N-m was applied over a rigid body element, depicted in red in Figure 2-8(d), in flexion, extension, right lateral bending, and left axial rotation; by rotating in one direction coronally and axially, symmetry conditions were assumed within the functional unit models. All nodes on the inferior facet processes and endplate were fixed in all model runs. RoM was chosen as the output variable by utilizing kinematic data over the superior (L4) endplate and compared with published FE model data utilizing similar osseoligamentous material property characterization (Naserkhaki et al., 2018). LS-DYNA implicit v971 R10.1 was utilized for all analyses presented here.

(a)

(b)

(c)

Layer 8   Layer 1

(d)

(e)

SSL

ISL

LF

PLL

ALL

CL

(f)
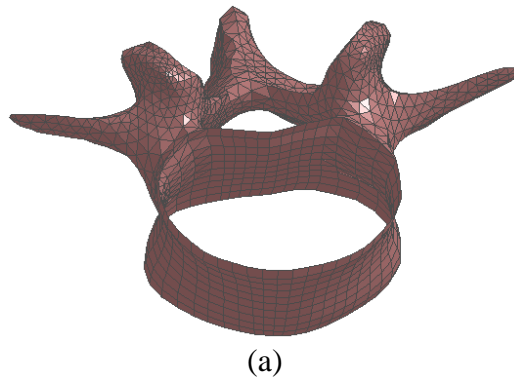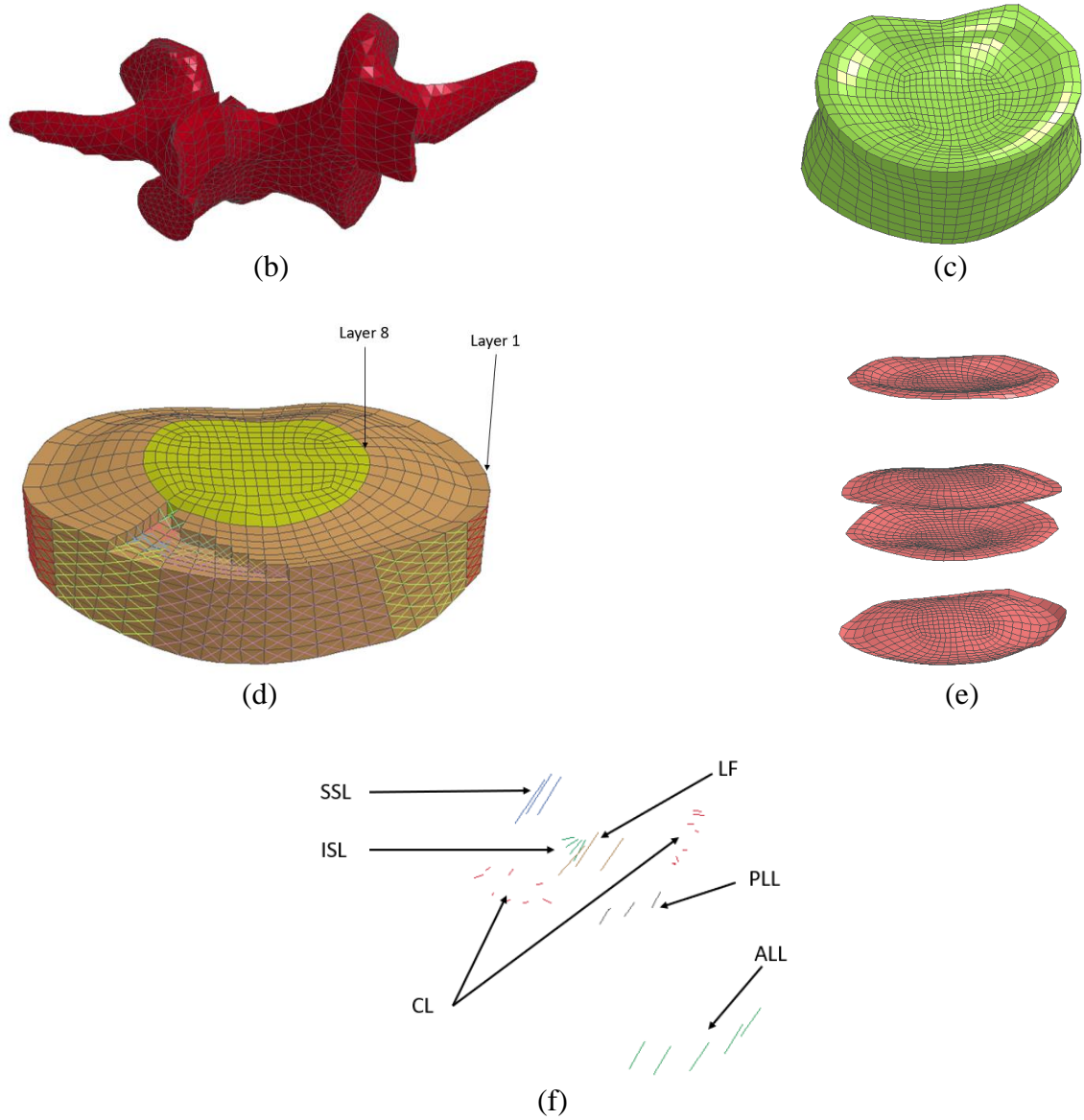
Figure 2-7: L4-L5 functional unit anatomy. (a) Cortical bone; (b) Posterior elements; (c) Cancellous bone; (d) IVD with annulus fibers (fiber colors denote different regions of the annulus fibrosus); (e) Cartilaginous endplate; (f) Intervertebral ligaments.

(a)   (b)   (c)

Moment applied

Fixed Boundary Conditions

(d)
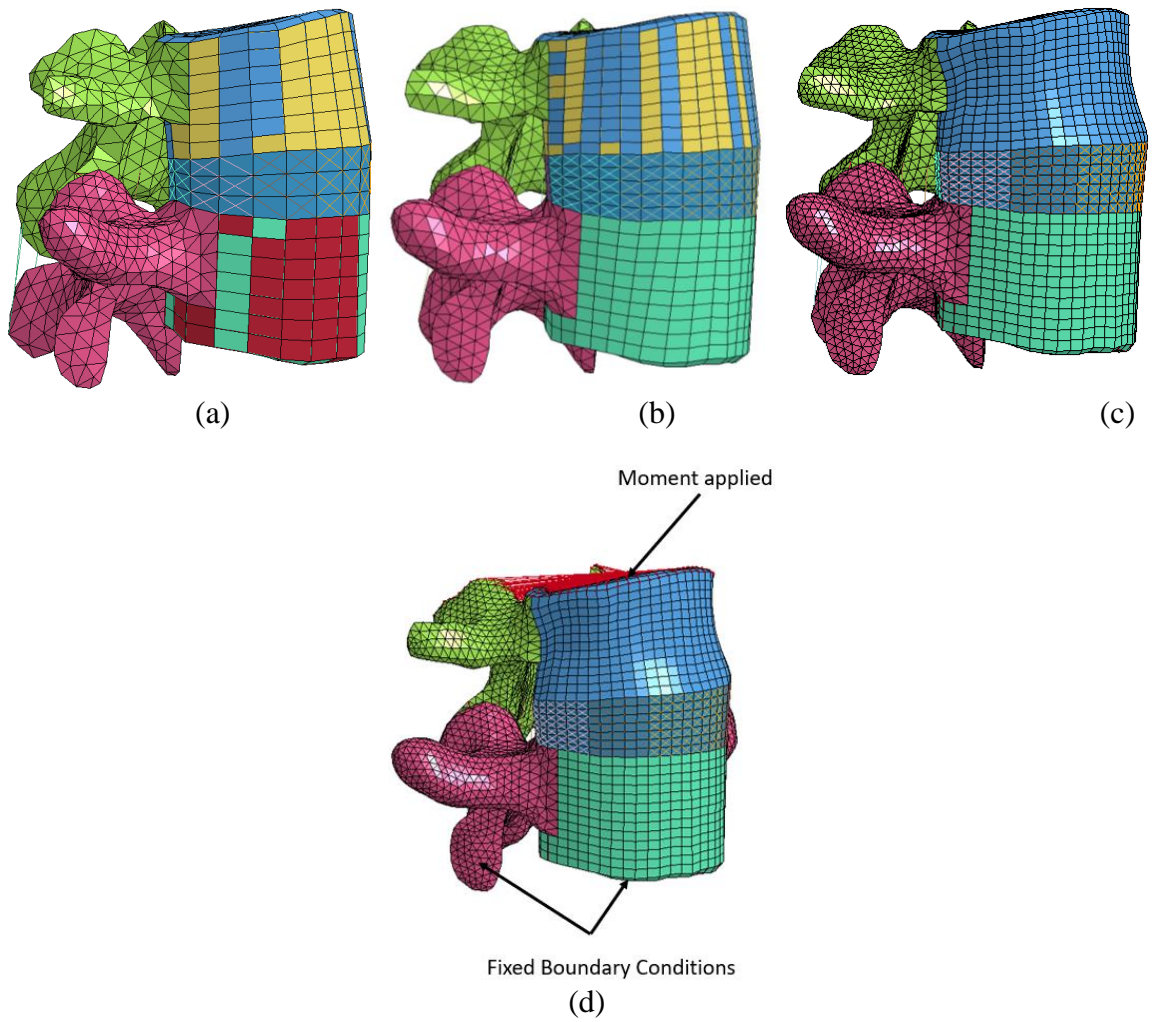
Figure 2-8: L4-L5 FSU with various discretized sizes. (a) Coarse mesh; (b) Medium mesh; (c) Fine mesh; (d) Load and boundary conditions.

(a) (b)
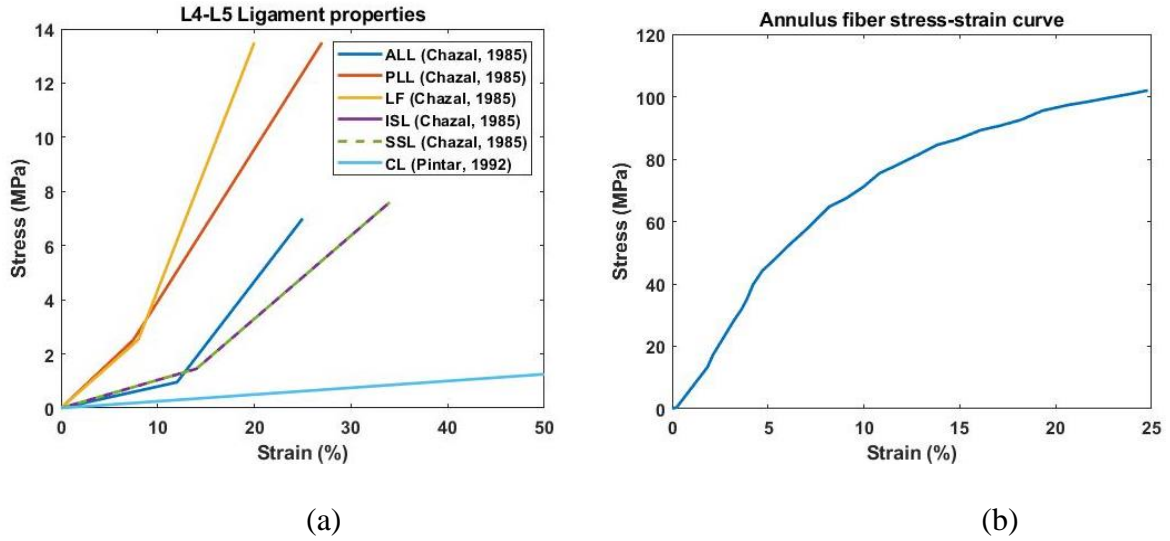
Figure 2-9: Intervertebral ligament properties. (a) Ligament stiffness properties; (b) Annulus fiber material property.

Table 2-4: Intervertebral joint properties.

Spinal Component	Material Property	Source
Cortical Bone	E=12 GPa, v=0.3, 1mm thickness	Naserkhaki et al., (2018)
Cancellous Bone	E=200 MPa, v=0.315	Naserkhaki et al., (2018)
Endplate	E=23.8 MPa, v=0.4, 1mm thickness	Schmidt et al., (2006)
Annulus Fibrosus	C10=0.18 MPa, C01=0.045 MPa, v=0.45 Mooney-Rivlin	Schmidt et al., (2006)
Nucleus Pulposus	C10=0.12 MPa, C01=0.03 MPa, v=0.499, Mooney-Rivlin	Schmidt et al., (2006)
Annulus Fibers	Nonlinear Stress-Strain curve, all material and geometric scale factors adjusted based on layer position	Shirazi-Adl et al., (1986)

Table 2-5: Annulus fiber geometric and material scale factors.

	Volumetric scale factors	Stress-strain scale factors
Layers 1 & 2 (outer circumference)	1	1
Layers 3 & 4	0.9	0.78
Layers 5 & 6	0.75	0.62
Layers 7 & 8 (inner circumference)	0.65	0.47

Table 2-6: Ligament initial length & quantity information.

	No. of cable elements per group	Average Initial lengths (mm)
Anterior Longitudinal Ligament (ALL)	5	14.21
Posterior Longitudinal Ligament (PLL)	3	8.53
Ligamentum Flavum (LF)	3	18.36
Capsular Ligament (CL)	8 (per side)	1.76
Interspinous Ligament (ISL)	4	8.83
Supraspinous Ligament (SSL)	3	20.36

Table 2-7: Mesh sensitivity model information.

	Total elements	Total nodes	No. of elements in IVD	No. of elements in vertebrae	No. of ligament/fiber elements
Coarse (1st order elements)	11,173	3,715	312	10,332	529
Medium (1st order elements)	25,130	11,201	1,580	21,565	1,985
Fine (1st order elements)	60,580	27,867	4,452	50,894	5,234

Table 2-7 continued.

Coarse (2nd order elements)	11,173	11,173	312	10,332	529
Medium (2nd order elements)	25,130	49,102	1,580	21,565	1,985
Fine (2nd order elements)	60,580	122,997	4,452	50,894	5,234

Table 2-8: Model computation times.

	Flexion	**Extension**	**Left Axial Rotation**	**Right Lateral Bending**
Coarse (1st order elements)	7 minutes	7 minutes	7 minutes	7 minutes
Medium (1st order elements)	29 minutes	33 minutes	33 minutes	30 minutes
Fine (1st order elements)	1 hour 55 minutes	1 hour 19 minutes	1 hour 20 minutes	2 hours 1 minute
Coarse (2nd order elements)	32 minutes	35 minutes	44 minutes	44 minutes
Medium (2nd order elements)	4 hours 57 minutes	4 hours 52 minutes	5 hours 24 minutes	5 hours 38 minutes
Fine (2nd order elements)	26 hours 57 minutes	26 hours 48 minutes	26 hours 41 minutes	43 hours 15 minutes
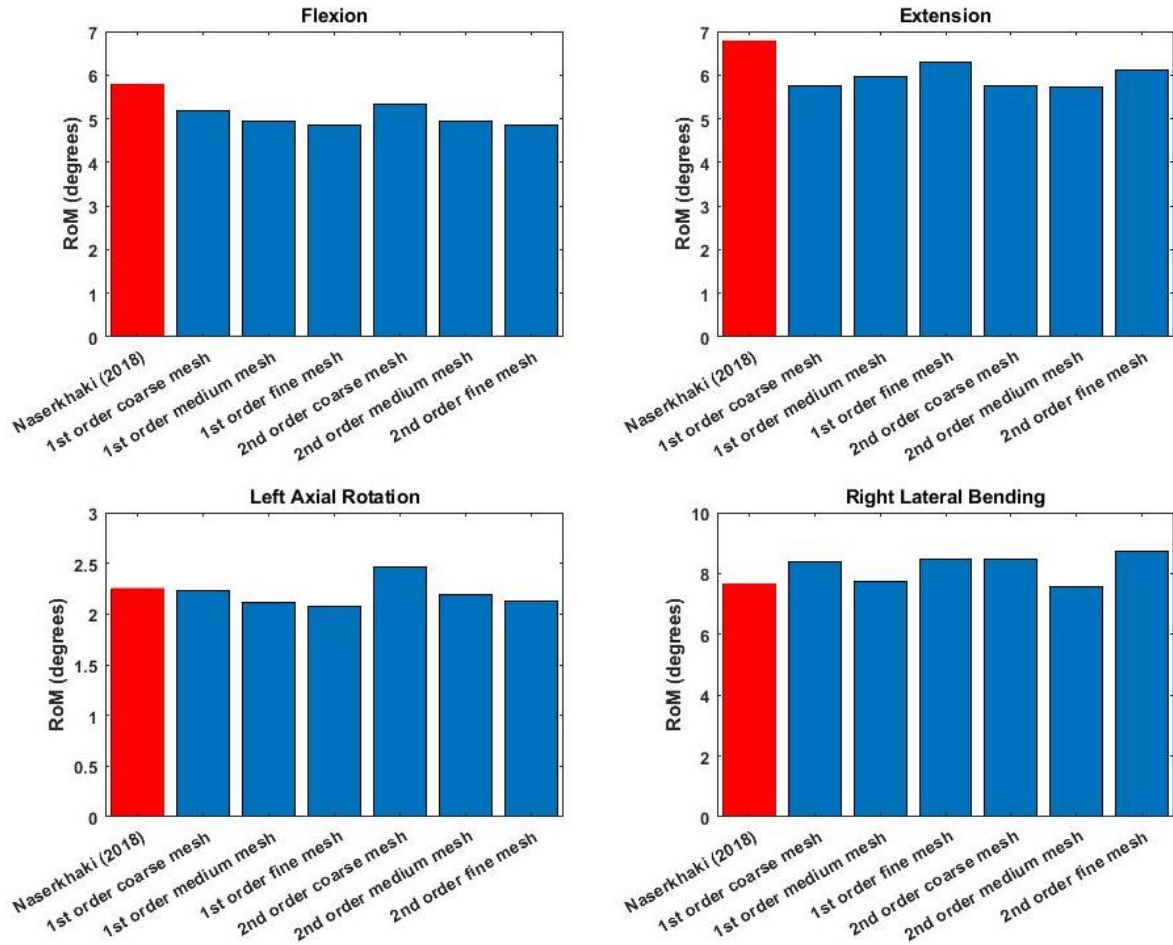
Figure 2-10: Mesh sensitivity results.

The RoM results presented are not seemingly dependent upon mesh size, however, they are overall are in line with the FE model data highlighted in red in Figure 2-10. Upon taking manual measurements of the spinal anatomy in the BodyParts3D CAD geometry, it was discovered that the IVD thickness pattern was not consistent as described for a typical IVD situated in the lumbar spine region. In other words, at L4-L5, the anterior thickness was smaller than the posterior and central measurements of the IVD; it has been demonstrated that the disc thickness (height) could affect the RoM of the spine as a primary driving factor of spinal movement (Meijer et al., 2011). As shown

in Figure 2-8, by adjusting the position of L4 to provide for a more tapered IVD, the RoM is more improved and in line with published data. However, the compromised position also readjusted the facet orientation and could further exacerbate spine kinematics in future analyses. Thus, the BodyParts3D geometry was not further considered and a migration to the CGHero CAD model was performed. However, this mesh sensitivity analysis, through material properties and boundary conditions employed within the FE model, provided a reference by which to further develop the finite element model of the spinal column.

2.4 LUMBAR SPINE MODEL DEVELOPMENT AND VALIDATION

Lumbar spine geometry from the CGHero CAD model was further developed for FE model validation. Two approaches were performed to verify and validate the setup of the FE model: utilization of an L4-L5 finite element model and an FE model of the full lumbar spine (L1-L5). Development of both osseoligamentous FE models also utilized Hypermesh using the same methodology and mesh configurations as described for the L4-L5 FE model developed using the BodyParts3D geometry. All elements were of the first order. All annulus fibers were generated using the same MATLAB program with a 16% volume fraction configured relative to the annulus fibrosus ground substance. The IVD for the lumbar spine model contained 7 layers through the thickness based on the results of the mesh study utilizing the BodyParts3D CAD geometry. A penalty contact surface algorithm with no initial gap was employed to model the facet joint. All ligaments utilized were configured using tension-only springs. Force-displacement stiffness curves (Figure 2-11(f)) were created based on stiffness equations customized for

toe, linear and yield regimes (Rohlmann et al., 2006b) and average unstretched ligament lengths in the FE model (Table 2-9). When developed, the functional unit contained 56,519 elements and 22,536 nodes with an average element edge length of 1.5mm. Utilizing the loading and boundary conditions highlighted in Figure 11(d), a 15 N-m moment was applied in flexion, extension, right lateral bending, and left axial rotation. Coronal and axial symmetry conditions were assumed by not adding left lateral bending and right axial rotation. As part of the validation procedure, in-vitro data was utilized at different load regimes (Heuer et al., 2007). Accordingly, the intertransverse ligament was not considered for this set of runs as it was not included in any specimens during in-vitro data acquisition. All rotations were calculated based on projection angles from translation data along the L4 superior endplate with respect to a local coordinate system. Maximum rotations of 6.3°, 5.1°, 8.4°, and 2.9° were recorded in flexion, extension, right lateral bending, and left axial rotation respectively. Taking rotations at the 2.5 N-m, 5 N-m, 7.5 N-m, and 10 N-m load steps per the in-vitro experiment, the functional unit was within range of all in-vitro rotations recorded for all functional unit specimens in the experiment (Figure 2-12).

Using the same mesh configurations as the functional unit as well as the same methodology to generate annulus fibers, the L1-L5 lumbar spine FE model was created. All IVDs in the lumbar column were constructed using 7 elements through the thickness. All ligament tension-only springs were customized to the average length of unstretched springs per group (Table 2-10) over the entire lumbar column and utilized to create force-displacement curves (Figure 2-13) for each set of ligaments. In total, there were 136,707 elements and 58,162 nodes; the average element edge length was approximately 1.6mm.

Full information regarding model size is found in Table 11. A 7.5 N-m external moment in flexion, extension, right lateral bending, and left axial rotation was applied on the L1 superior endplate while the L5 inferior endplate and facet processes were fixed. A minimum gap of zero was employed along all facet contact surfaces. Outputs from the model included global and intervertebral rotations based on projection data, calculated from translation data on all superior endplates. In addition, left and right facet joint contact forces are reported to verify the penalty contact algorithm settings employed throughout the FE model. For benchmark comparisons, the in-vitro data published in (Dreischarf et al., 2014) by way of (Rohlmann et al., 2001) for their finite element comparison study was utilized for an applied 7.5 N-m moment with no preload.

The global rotations (Figure 2-14) produced along the lumbar spine column amounted to 18.4°, 14.8°, 20.1°, and 6.2° in flexion, extension, right lateral bending, and left axial rotation respectively. The intervertebral RoM (Figure 2-15), which was summed up by rotations along respective planes, ranged from 2.5° to 3.5° in axial rotation (0.6%-40% difference), 7.5° to 8.9° in sagittal rotations (flexion and extension with a 0.7%-15.2% difference), and 8.1 to 10.8 in coronal rotations (left and right lateral bending with a 1.2%-26.6% difference). Facet joint forces (Figure 2-16) in extension ranged between 54 N in the L2-L3 right facet and 73 N in the L4-L5 left facet, with overall differences between published data and the model ranging between 0.8% and 42.3%. In left axial rotation, right facet joint forces ranged between 74 N in L4-L5 and 114 N in L1-L2; overall percent differences between 19.2% and 45.8% were present between the model and publication. Finally, right lateral bending rotations produced between 13 and 50 Newtons in the L4-L5 right facet and L1-L2 left facet respectively,

resulting in overall differences ranging between 11% and 37%. No facet forces were recorded in flexion, which agrees with the publication (Du et al., 2016); in addition, the opposing facets in axial rotation and lateral bending did not register any forces, thus are not shown in the presented graphs.

(a)   (b)   (c)

(d)   (e)

(f)
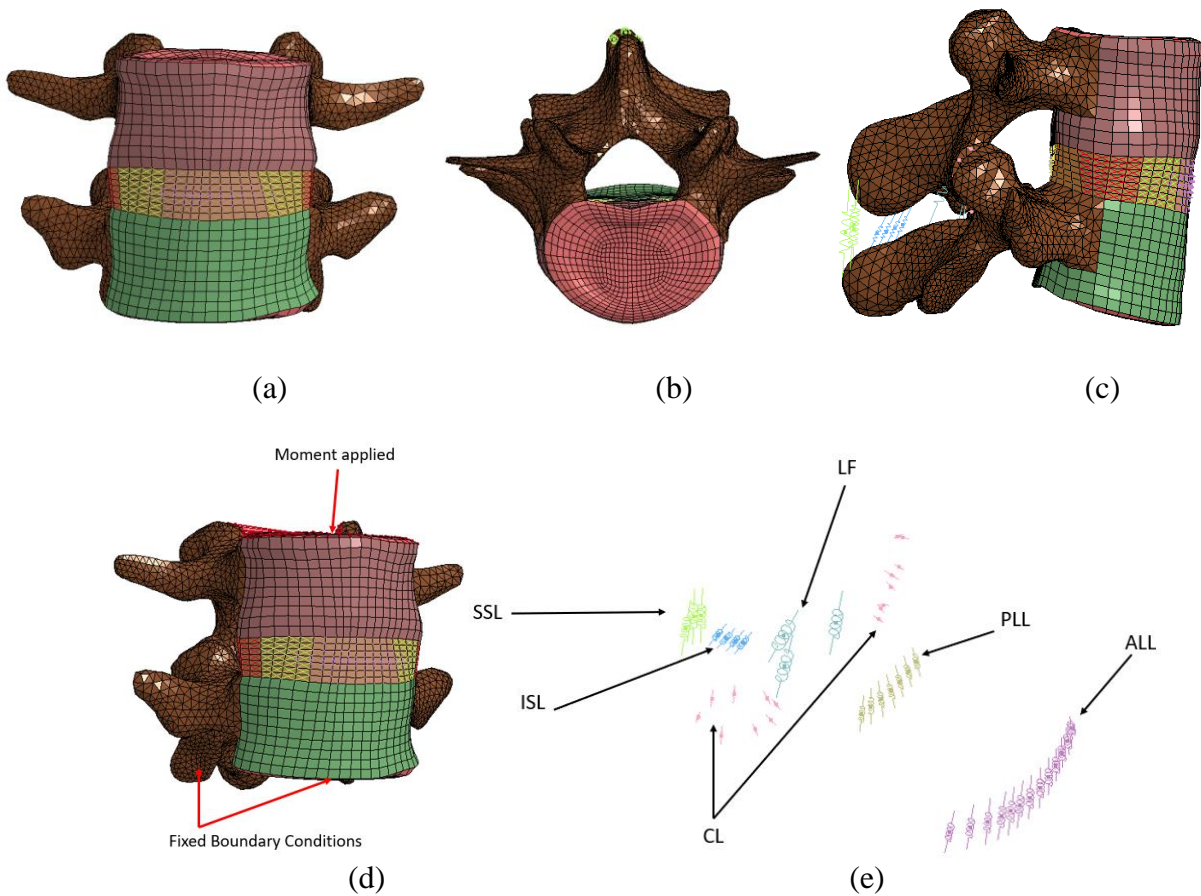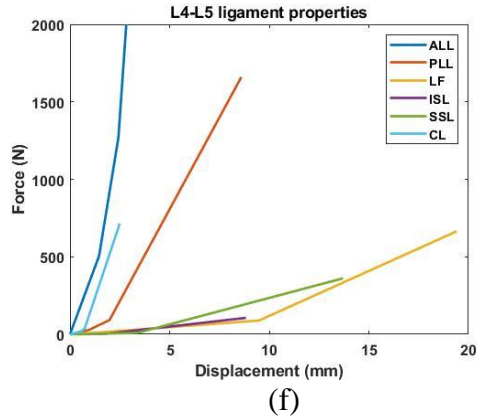
Figure 2-11: L4-L5 CGHero functional unit FE model. (a) Coronal view; (b) Axial view; (c) Sagittal view; (d) Boundary conditions applied; (e) Ligament labels; (f) Intervertebral ligament properties.

Table 2-9: L4-L5 ligament information in CGHero FE model.

	No. of ligaments per group	Average Initial lengths (mm)
Anterior Longitudinal Ligament (ALL)	13	11.957
Posterior Longitudinal Ligament (PLL)	7	8.605
Ligamentum Flavum (LF)	3	19.376
Capsular Ligament (CL)	8 (per side)	2.502
Interspinous Ligament (ISL)	4	8.834
Supraspinous Ligament (SSL)	3	13.733
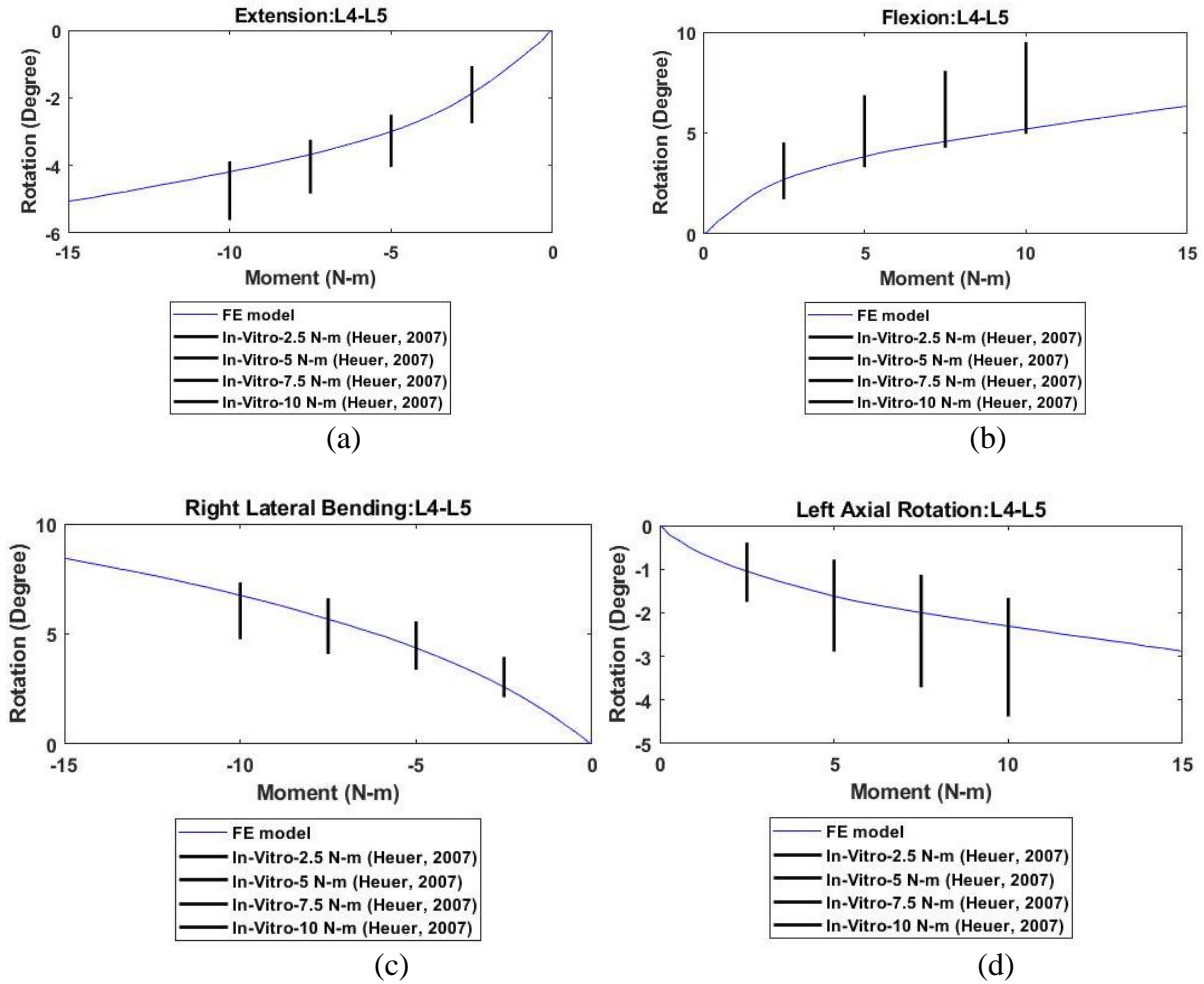
Figure 2-12: L4-L5 comparison with in-vitro data. (a) Extension; (b) Flexion; (c) Right lateral bending; (d) Left Axial Rotation.

Table 2-10: L1-L5 ligament information from CG Hero FE model.

	No. of ligaments per group per segment	Average Initial lengths (mm)				
		L1-L2	L2-L3	L3-L4	L4-L5	Average (L1-L5)
Anterior Longitudinal Ligament (ALL)	13	10.376	14.203	13.514	11.957	12.513
Posterior Longitudinal Ligament (PLL)	7	5.839	9.335	7.37	8.605	7.787
Ligamentum Flavum (LF)	3	26.282	26.654	20.817	18.709	23.116

Table 2-10 continued.

Capsular Ligament (CL)	8 (per side)	2.834	3.726	3.285	2.526	3.093
Interspinous Ligament (ISL)	4	8.683	7.715	5.574	6.65	7.155
Supraspinous Ligament (SSL)	3	19.36	17.14	12.691	14.538	15.932
Intertransverse Ligament (ITL)	1 (per side)	26.566	26.767	29.423	24.602	26.839

Table 2-11: L1-L5 lumbar spine FE model size information.

Component	No. of elements	No. of nodes	Element configuration
Cortical Bone	21,188	11,574	3 & 4 noded tria and quads
Cancellous Bone	27,600	31,625	8-noded hexahedron
Posterior elements	47,039	13,290	4 noded tetrahedron
Cartilaginous Endplate	5,520	5,750	4 noded quads (1mm thickness)
Annulus Fibrosus	8,624	11,264	8-noded hexahedron
Annulus Fibers	19,712	11,264	Cable elements
Nucleus Pulposus	6,832	8,544	8-noded hexahedron

(a)   (b)
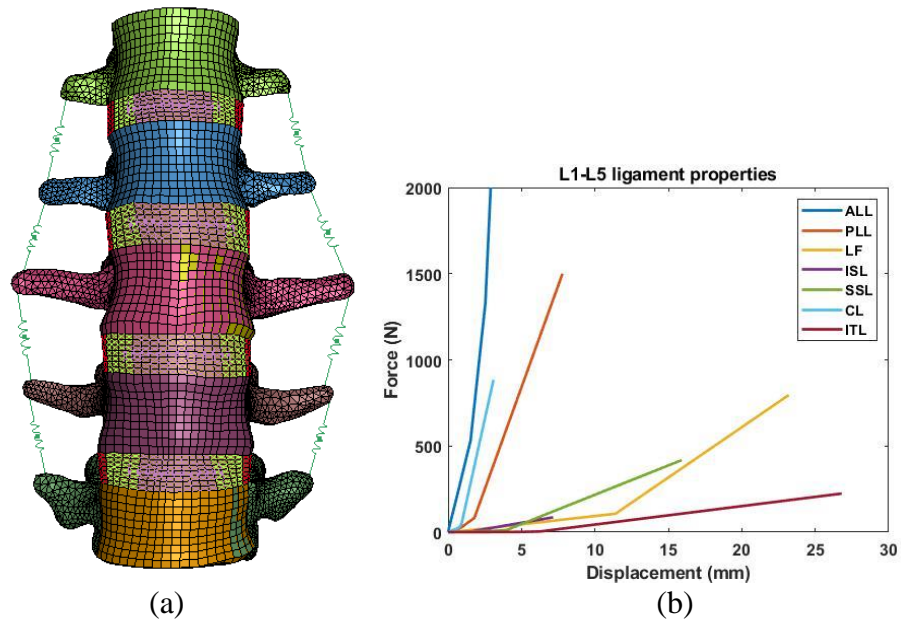
Figure 2-13: (a) Lumbar spine FE model; (b) Lumbar spine ligament stiffness properties
(Rohlmann et al., 2006b).

(a)   (b)

(c)
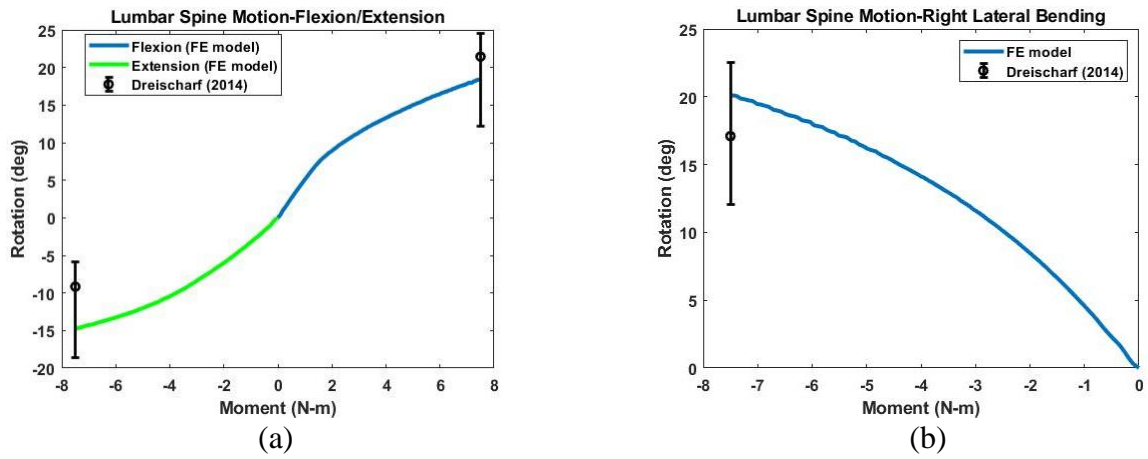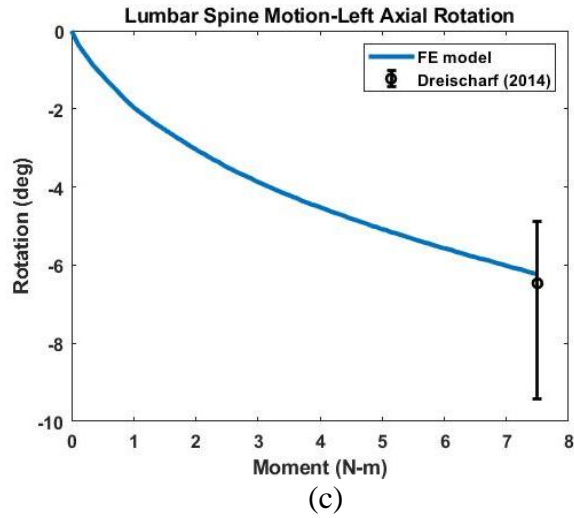
Figure 2-14: Lumbar spine FE model kinematic behavior compared with publication data. (a) Flexion/Extension; (b) Right lateral bending; (c) Left axial rotation.

(a) Flexion/Extension   (b) Left/Right lateral bending   (c) Left/Right axial rotation
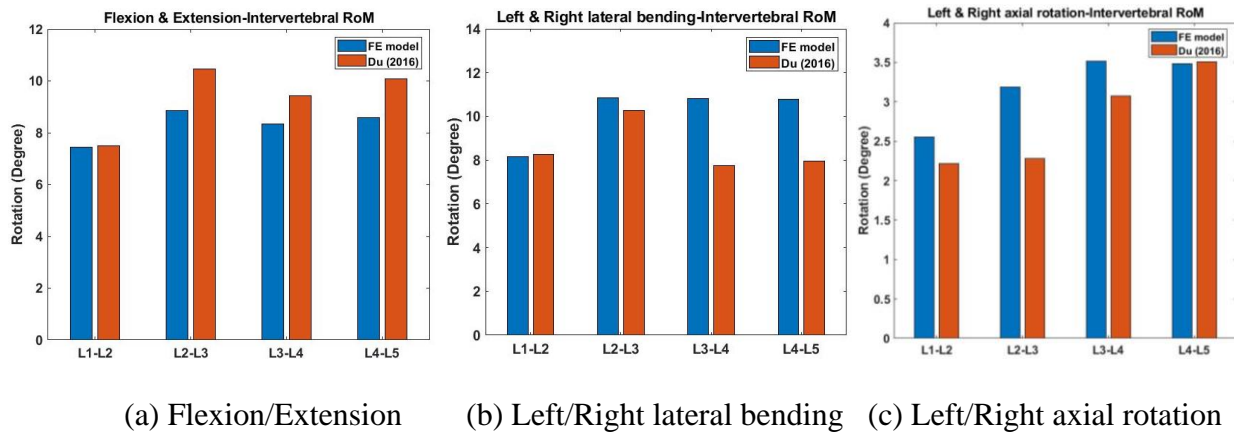
Figure 2-15: Intervertebral RoM compared with Du et al. (2016). (a) Extension; (b) Right lateral bending; (c) Left axial rotation.

(a)Extension	(b) Right Lateral Bending	(c) Left axial rotation
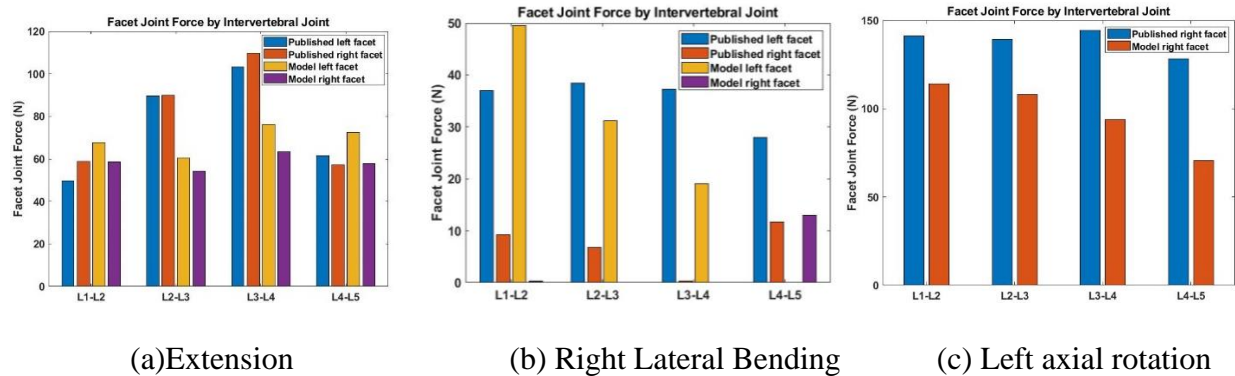
Figure 2-16: Facet joint forces compared with Du et al. (2016). (a) Extension; (b) Right lateral bending; (c) Left axial rotation.

2.5 THORACIC MESH SENSITIVITY ANALYSIS

To assess an optimum mesh size suitable for subsequent computational analyses of the spine, a mesh sensitivity analysis was conducted for a T7-T8 functional unit finite element (FE) model. Six different mesh configurations were prescribed within the model (Figure 2-17; Table 2-12). Three configurations (coarse, medium, and fine) utilized a varied mesh size of both the vertebrae, rib sections, and intervertebral disc (IVD). The element layer quantity through the IVD thickness was set to 2, 3, and 6 respectively. The second three solely focused on mesh variance of the IVD in the thickness direction at 4, 5, and 6 elements, while maintaining the medium-sized mesh of the vertebrae, as much of the deformation was expected to take place within the IVD. Using LS-DYNA SMP R971 R10.1 (Livermore Software Technology, Livermore, CA), two series of quasi-static analyses were conducted to assess mesh convergence. A pure moment of 7.5 N-m was applied on the endplate and superior facet processes for T7 in flexion, extension, right lateral bending, and left axial rotation and the T8 inferior endplate and facet processes were fixed (Figure 2-18). Range of Motion (RoM) data, global and IVD (Annulus

Fibrosus and Nucleus Pulposus) strain energies, and global strain energy are reported. All analyses assumed a run time of 300ms using a 3.4 GHz Intel-core processor with 4 CPUs. To ensure quasi-static conditions, the run time was chosen based on kinetic energy being approximately 7 orders of magnitude lower relative to the total energy throughout all analyses. The CV joints with partial rib sections and contact algorithms were excluded from the analyses to eliminate influence from contact forces that would interfere with mesh-dependent deformations produced in the analyses. Material properties for the vertebrae and IVD can be found in Table 2-4. Intervertebral ligaments were present in all analysis runs to maintain stability; stiffness properties were generated using the same methodology outlined in the manuscript. Ligament stiffness properties utilized for all model runs are found in Figure 2-19.

Overall, the model cases considered show a significant dependence on the mesh size of the vertebrae, and both functional unit kinematics and computation time (Table 2-13) remained negligible when vertebral mesh size was constant but the element layers through the IVD thickness varied. The discrepancies exhibited in strain energy convergence trends could be attributed to the load case imposed on each model. Rotations partially compress or shear specific regions of the IVD depending on how the superior vertebra is loaded. The higher deformations of a highly refined annulus fibrosus relative to the nucleus pulposus may have also contributed to the significant increase in run time between the medium and fine mesh cases, particularly in extension and right lateral bending. The medium mesh case with 3 IVD layers was thus chosen since, compared with the most refined mesh case presented, it exhibited the lowest percent difference overall and most results of all variables were within 10% (Figure 2-20).
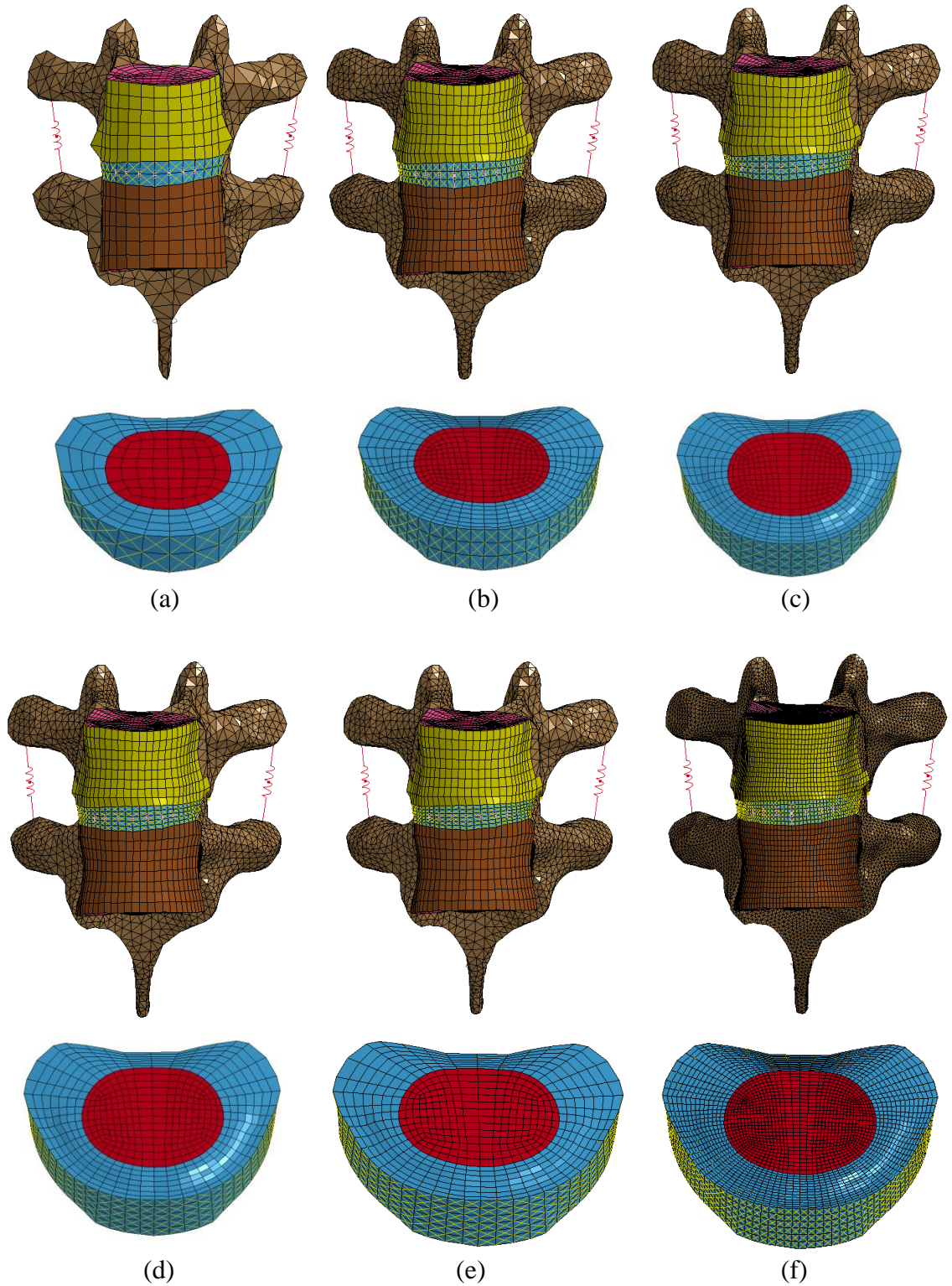
Figure 2-17: Functional unit model mesh configurations and IVDs for sensitivity analyses. (a) Coarse mesh; (b) Medium mesh with 3 elements through IVD thickness; (c) Medium mesh with 4 elements through IVD thickness; (d) Medium mesh with 5 elements through IVD thickness; (e) Medium mesh with 6 elements through IVD thickness; (f) Fine mesh.
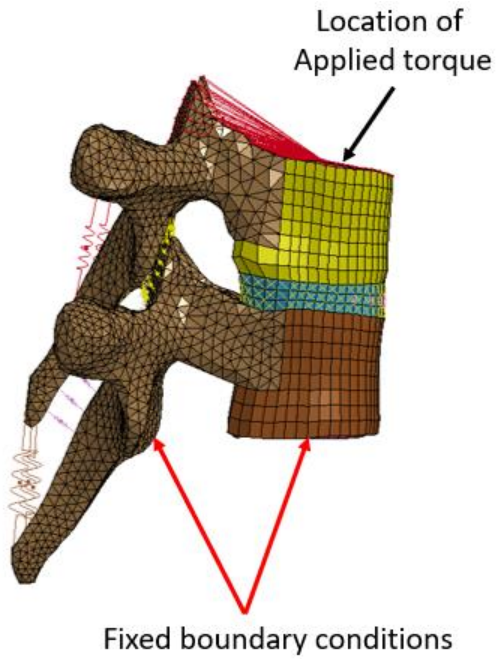
Figure 2-18: T7-T8 Functional Unit model setup for rotational motion.
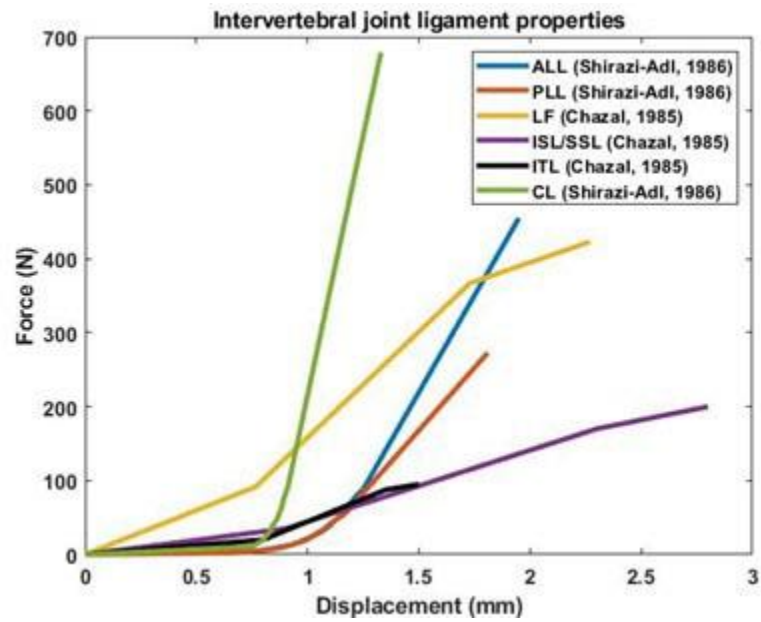
Figure 2-19: Intervertebral Ligament properties.

Table 2-12: Mesh sensitivity FE model details.

Mesh model configuration	No. of elements/No. of nodes (entire model)	No. of elements/No. of nodes (IVD)	Average element mesh size (Vertebrae)	Average element mesh size (IVD)
Coarse mesh	6,859/2,134	792/507	2.25mm	2.01mm
Medium mesh with 3 elements through IVD thickness	33,708/15,023	3,768/2,300	1.31mm	1.09mm
Medium mesh with 4 elements through IVD thickness	35,472/15,693	5,024/2,875	1.31mm	1.07mm
Medium mesh with 5 elements through IVD thickness	36,728/16,268	6,280/3,450	1.31mm	1.06mm
Medium mesh with 6 elements through IVD thickness	37,984/16,843	7,536/4,025	1.31mm	1.04mm
Fine mesh	211,752/106,243	29,088/15,771	0.67mm	0.55mm

(a)

(b)

(c)

(d)

(e)
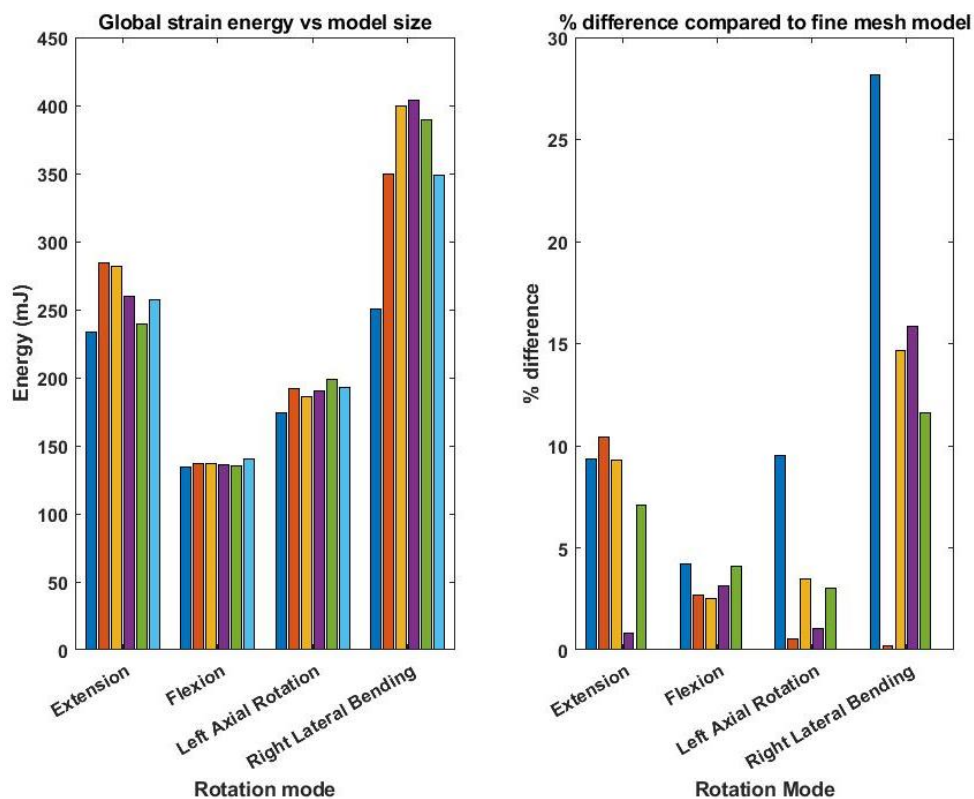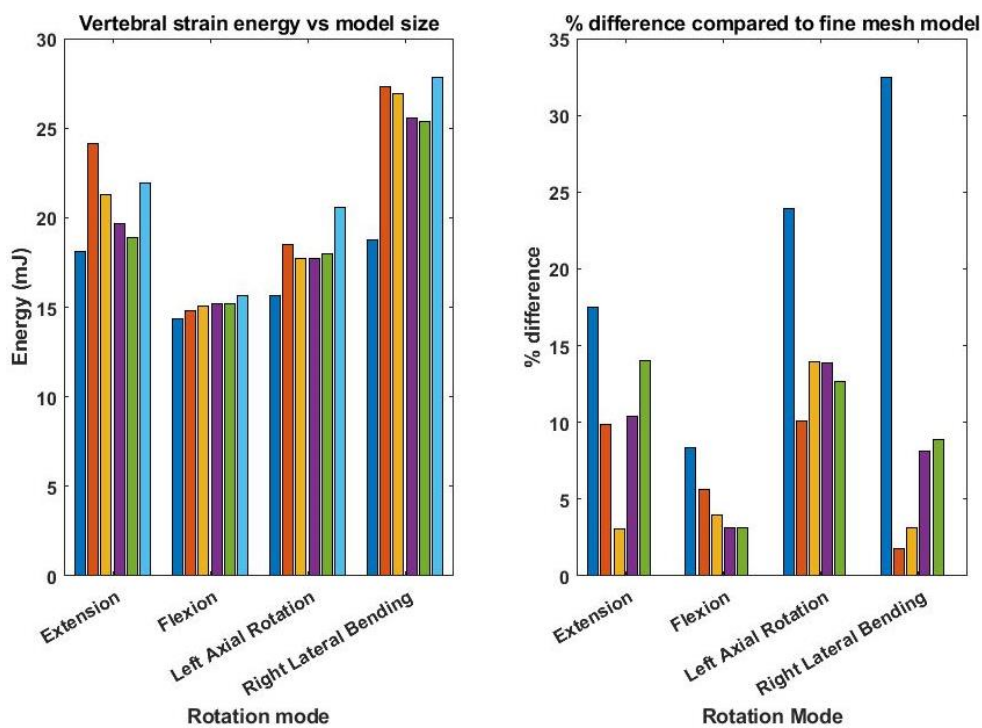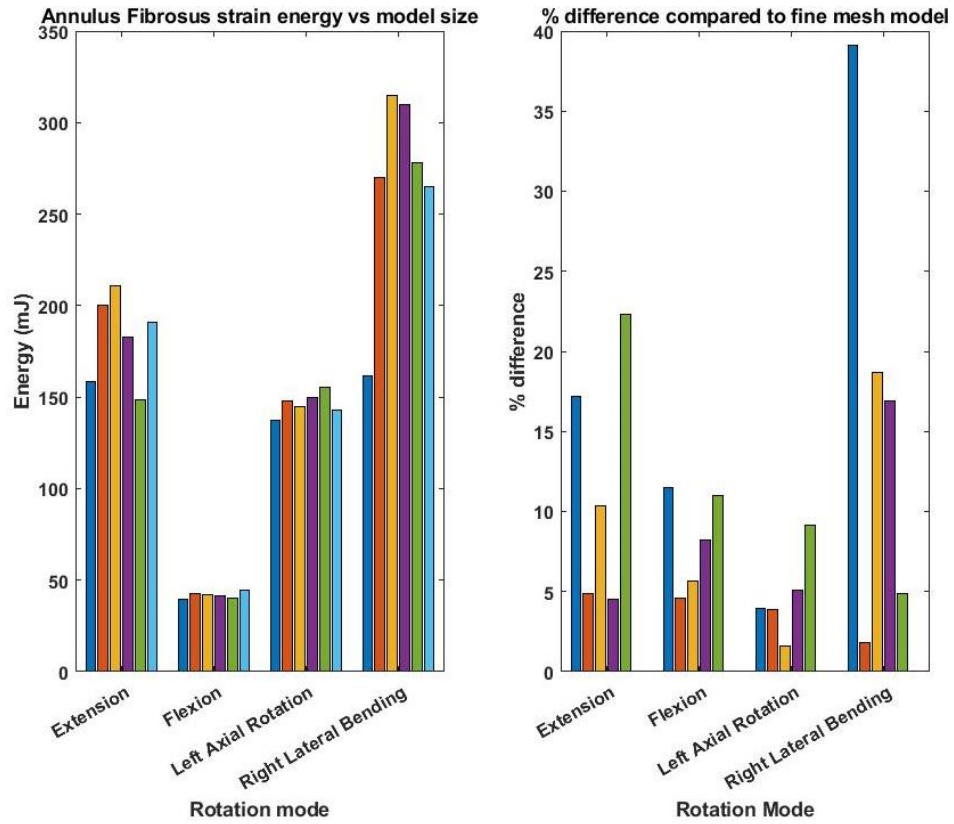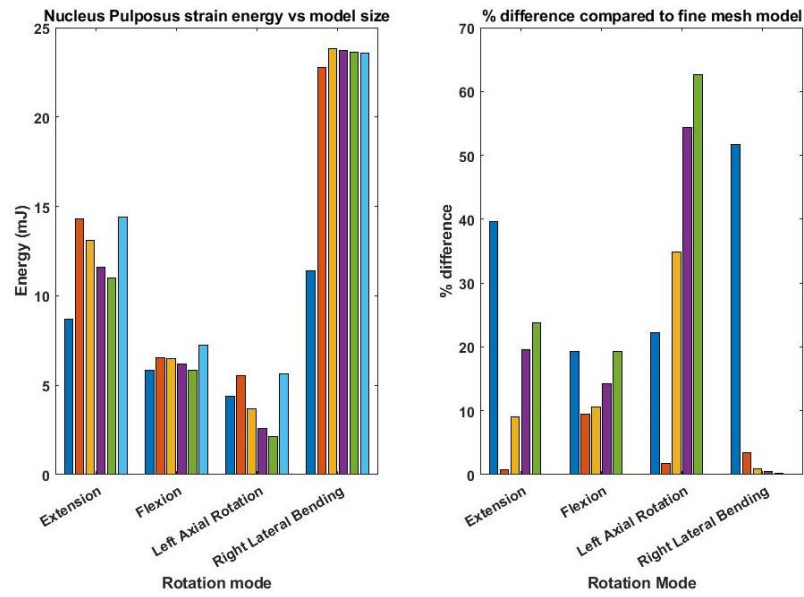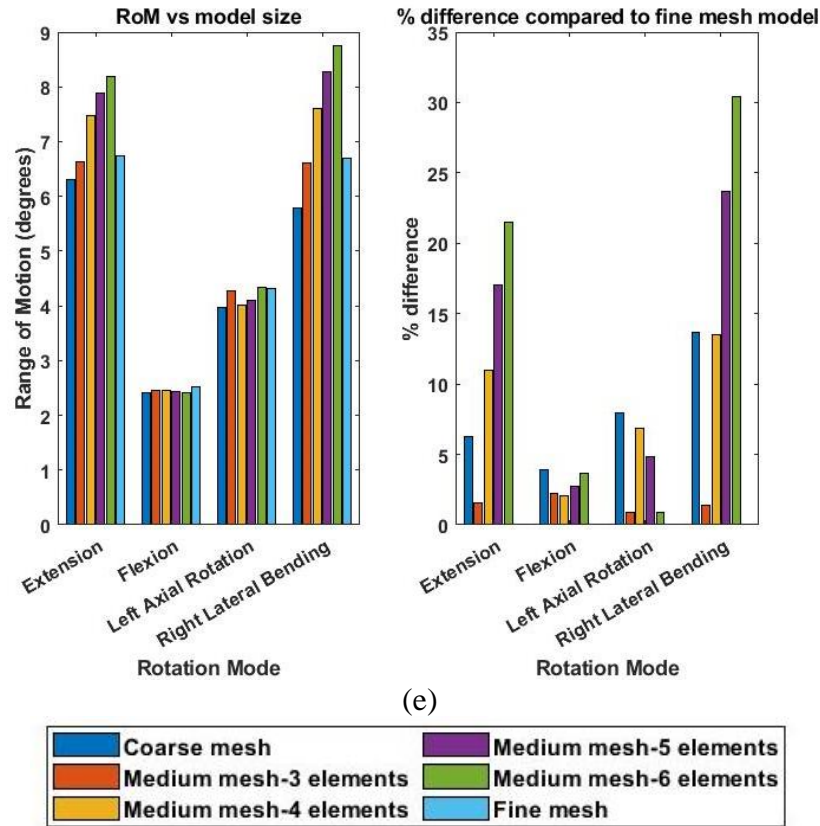
Figure 2-20: Mesh sensitivity results and percent differences from fine mesh model. (a) Global strain energy; (b) Vertebral strain energy; (c) Annulus Fibrosus strain energy; (d) Nucleus Pulposus strain energy; (e) Functional unit rotational RoM.

Table 2-13: Computation times for all runs in HH:MM:SS format.

	Extension	**Flexion**	**Left AR**	**Right LB**
Coarse mesh	00:00:53	00:00:49	00:00:55	00:03:18
Medium mesh - 3 elements through IVD thickness	00:22:33	00:06:32	00:08:57	00:34:28
Medium mesh - 4 elements through IVD thickness	00:20:53	00:06:12	00:10:02	00:41:11
Medium mesh - 5 elements through IVD thickness	00:15:56	00:06:06	00:12:32	00:37:26

Table 2-13 continued.

Medium mesh - 6 elements through IVD thickness	00:13:03	00:06:02	00:13:34	00:40:49
Fine mesh	06:41:15	02:07:31	02:45:25	15:14:48

2.6 RIBCAGE FE MODEL DEVELOPMENT

The ribcage included with the CGHero model was meshed utilizing a combination of sweep and mapping methods along the geometric surfaces of each anatomical component. Each component included: ribs, intercostal muscles, costal cartilage, manubrium, sternum, and xiphoid. A description of all model size components is listed in Table 2-14. To connect each component of the ribcage, the intercostal muscles were directly connected via their nodes to each rib cranially and caudally situated relative to each other. The costal cartilage was also directly connected through their nodes to each adjacent rib on one end. Where meshes were not congruent with one another, a tied surface algorithm, through LS-DYNA v971 R10.1, was utilized to tie the costal cartilage to the sternum, manubrium, and xiphoid, and the sternum, manubrium, and xiphoid together. The rest of the ribcage was connected to the main spinal column through costovertebral joints, made up of a group of ligaments and contact surfaces along each rib. The next section highlights the costovertebral joint configuration in greater detail.
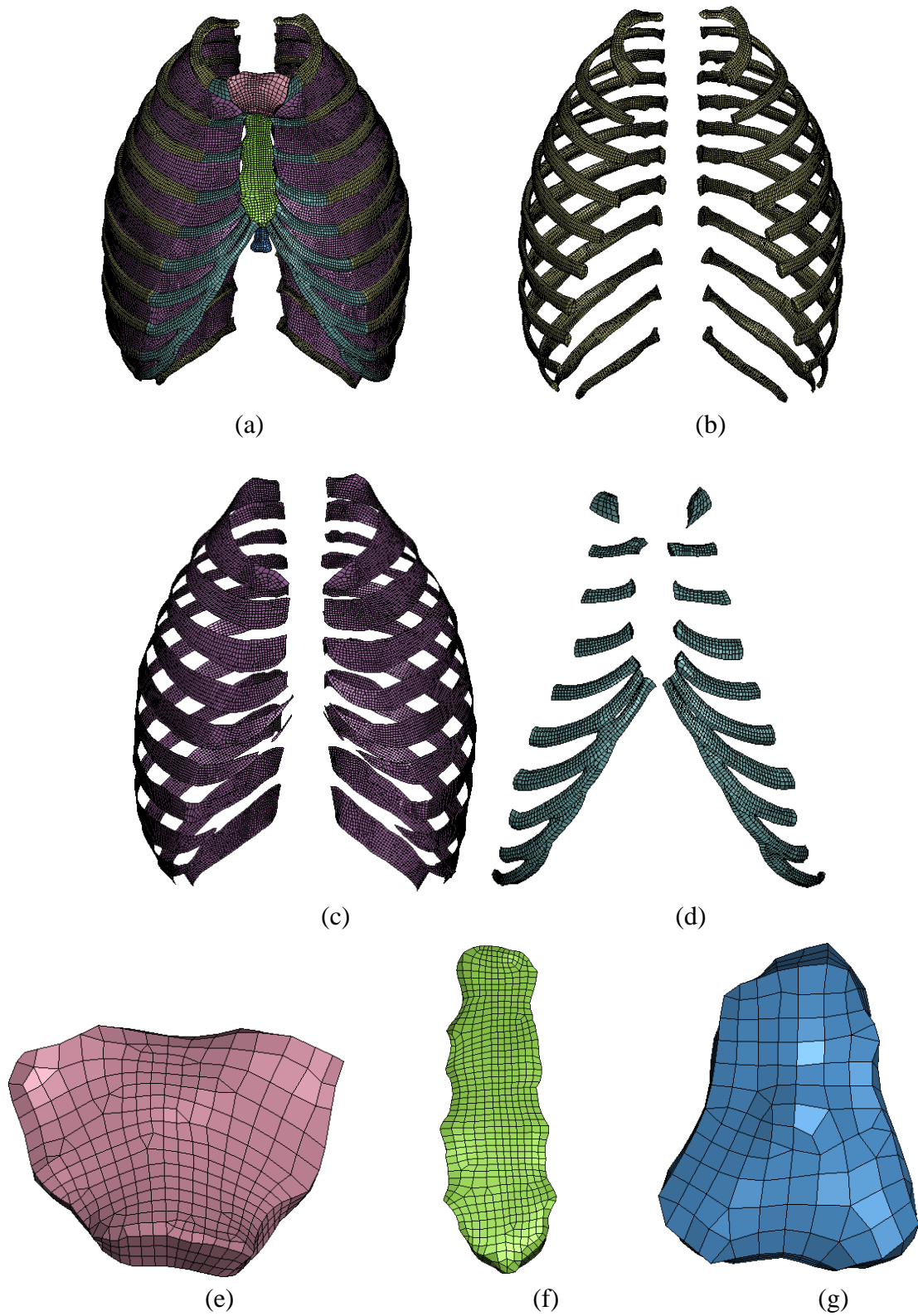
Figure 2-21: Ribcage and its components. (a) Full ribcage (b) Ribs; (c) Intercostal muscles. (d) Costal cartilage. (e) Manubrium. (f) Sternum. (g) Xiphoid.

Table 2-14: Ribcage component model size.

Component	No. of elements	No. of nodes	Element configuration
Full ribcage	67,658	83,661	
Ribs	36,778	52,912	8-noded hexahedron
Intercostal muscles	22,642	25,079	3 & 4 noded tria and quads
Costal cartilage	5,400	7,740	8-noded hexahedron
Manubrium	783	1,116	8-noded hexahedron
Sternum	1,740	2,520	8-noded hexahedron
Xiphoid	315	480	8-noded hexahedron

2.7 COSTOVERTEBRAL JOINT MODEL AND VALIDATION

The costovertebral (CV) joint is responsible for connecting and reinforcing the ribcage to the thoracic spinal column, whose attachments are made through two subjoints: the costocentral joint, which bilaterally connects each rib head to adjacent vertebrae and IVDs, and the costotransverse joint, which bilaterally connects each rib tubercle to the adjacent transverse processes. The ligament labels and their contact surfaces are found in Figures 22d-e. To validate the CV joint properties and configuration, its kinematic behavior needed to be benchmarked through existing in-vitro data. Validation was conducted using in-vitro kinematic data based on the experiment conducted by Duprey et al. (2010). Three intact configurations were utilized for validation: T1-T2-R2, T5-T6-R6, and T9-T10-R10, to cover the upper, mid, and lower thoracic regimes of the spine respectively. An aluminum rod 0.25 inches in diameter was coupled to the ribs with a 0.1 N-m torque was applied in torsion (+Mx) along the rod and torques of ±0.5 N-m applied in cranial-caudal (±My) and ventral-dorsal (±Mz) directions. The cranial-caudal and ventral-dorsal moment magnitudes were calculated based on the

product of the moment arm, or rod length, and the appropriate normal force. A penalty contact algorithm was employed on contact surfaces corresponding to the costocentral and costotransverse joints with constant contact thicknesses on opposing sides and minimum gap of zero along the contact surfaces. Available ligament stiffness properties (Aira et al., 2019) were employed for each costovertebral joint configuration described here are plotted in Figures 25a-c for the upper, middle, and lower thoracic spine regions respectively; for T9-T10-R10, the intra-articular ligament was not present. For all configurations, the fixed boundary conditions (Figure 22(a)) were employed to represent the potting of the FSU. All kinematic data was read in a local coordinate system (Figure 22(c)) at the joint center. Moment-rotation data from each FE model was calculated for each configuration.

Moment-rotation corridor equations (Equations 2-1 to 2-6) derived from the experimental data in (Duprey et al., 2010) was utilized as benchmarks for all moment-rotation responses. The R2 rib rotated along all directions were within the in-vitro corridors (Figure 2-23a-c). The R6 rib was largely within all corridors; however, rotation about the caudal (+My) direction exhibited slightly stiffer behavior compared to the largest corridor (Figures 2-23d-f). The R10 rib was within the corridor under torsion (+Mx), however, was compliant and stiff in the cranial and caudal directions respectively, and compliant in the dorsal (+Mz) direction (Figures 2-23g-i).

$$\text{For moment about local x axis (Mx):}$$

$$\text{Mx\_1}(\theta) = 0.0012*\theta^3 - 0.0085*\theta^2 + 0.0388*\theta \quad \text{(Equation 2-1)}$$
$$\text{Mx\_2}(\theta) = -0.0002*\theta^3 + 0.001*\theta^2 + 0.0022*\theta \quad \text{(Equation 2-2)}$$

For moment about local y axis (My):

$$My\_1(\theta) = 0.0018*\theta^3 + 0.0116*\theta^2 + 0.0578*\theta \quad \text{(Equation 2-3)}$$
$$My\_2(\theta) = -0.0115*\theta^3 + 0.001*\theta^2 + 0.0022*\theta \quad \text{(Equation 2-4)}$$

For moment about local z axis (Mz):

$$Mz\_1(\theta) = 0.0031*\theta^3 + 0.006*\theta^2 + 0.2071*\theta \quad \text{(Equation 2-5)}$$
$$Mz\_2(\theta) = 0.0028*\theta^3 + 0.0037*\theta^2 + 0.0348*\theta \quad \text{(Equation 2-6)}$$

(a)

(b)

(c)

(d)   (e)
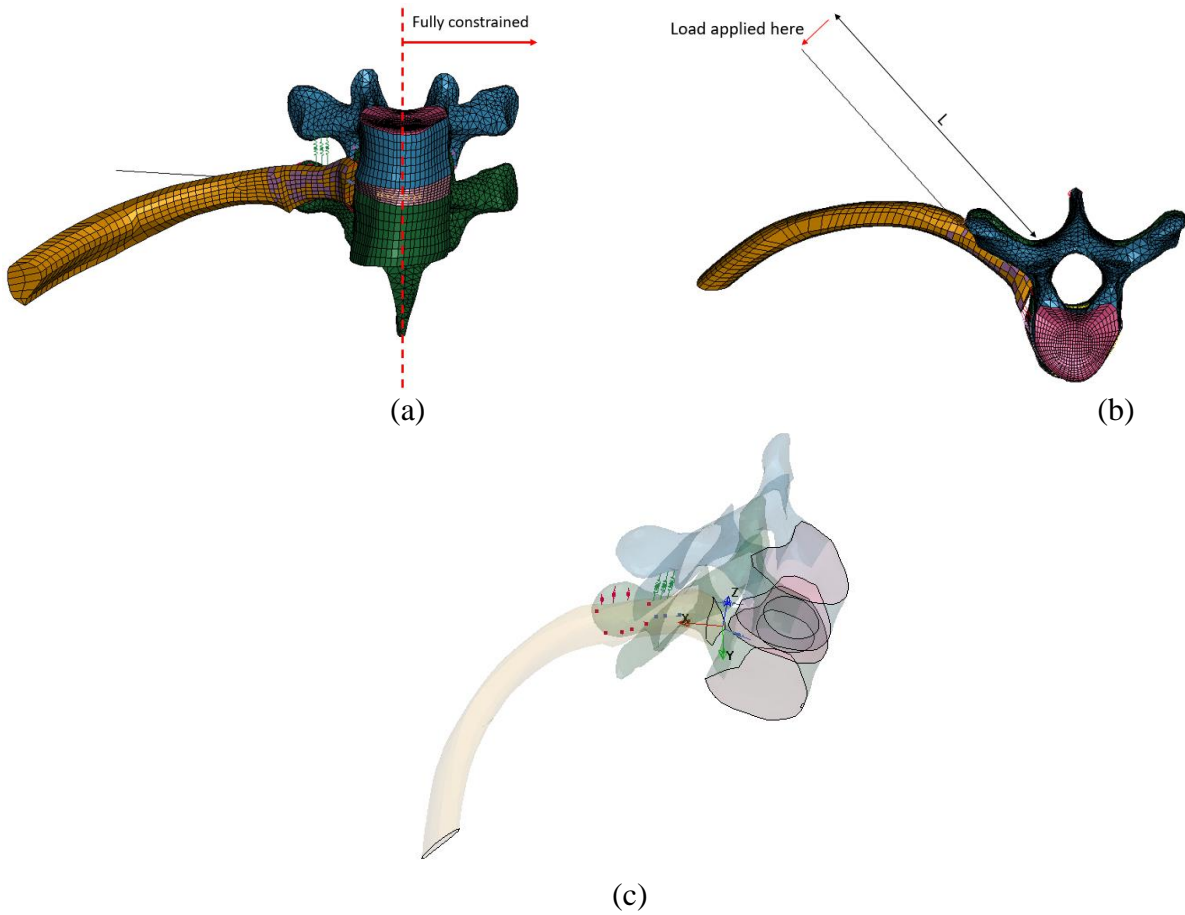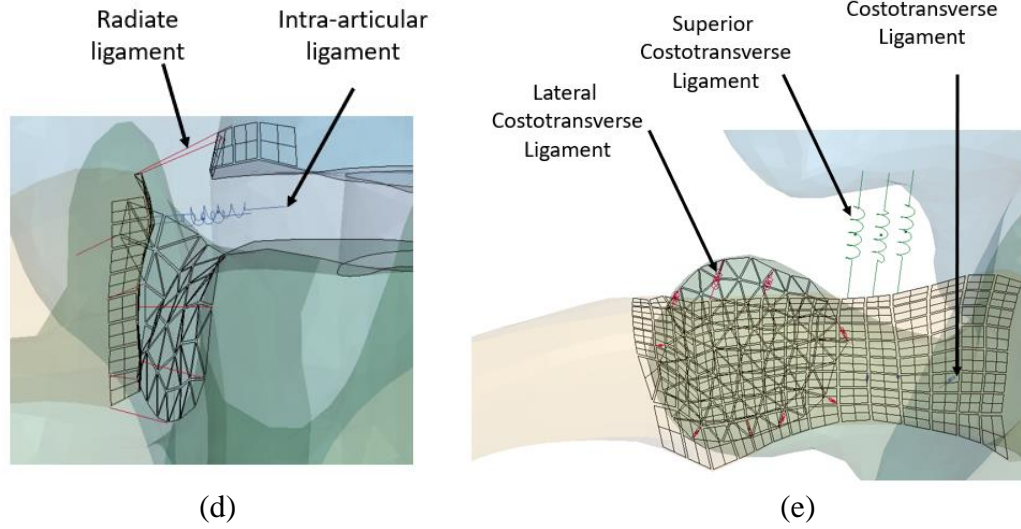
Figure 2-22: T5-T6-R6 specimen. (a) Functional unit constraints. (b) Load application on the rod relative to origin. (c) Local coordinate system used for kinematic reference. (d) Costocentral joint with contact surfaces. (e) Costotransverse joint with contact surfaces.

(a)   (b)

(c)

(d)

(e)

(f)

(g)

(h)

(i)
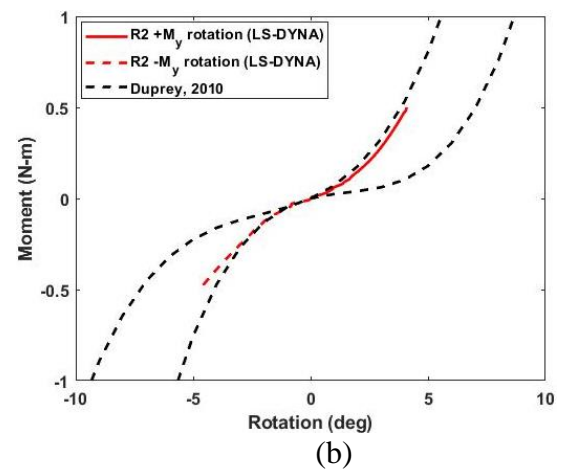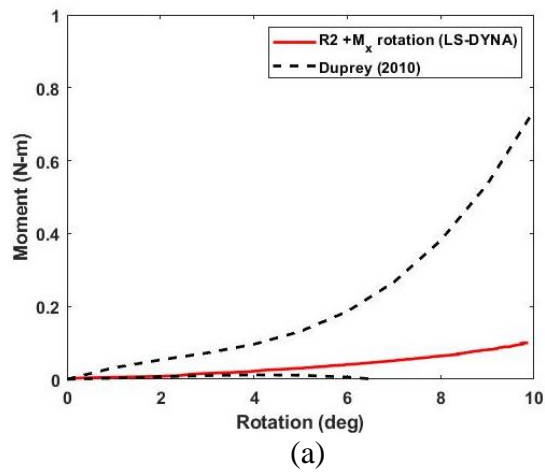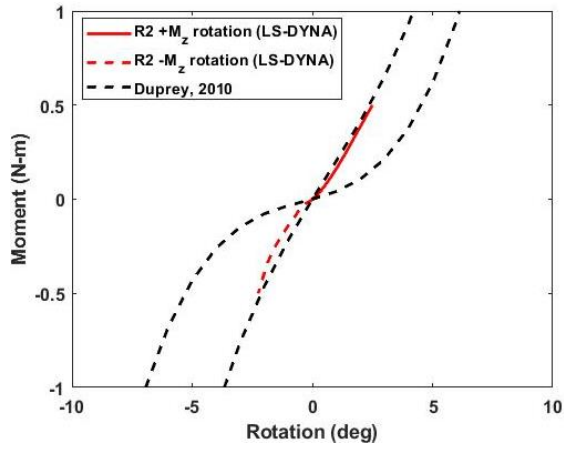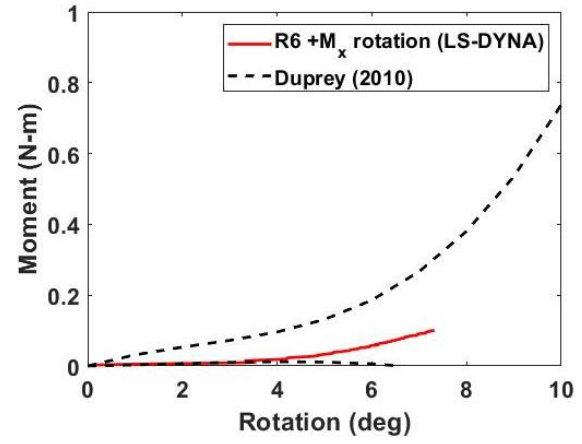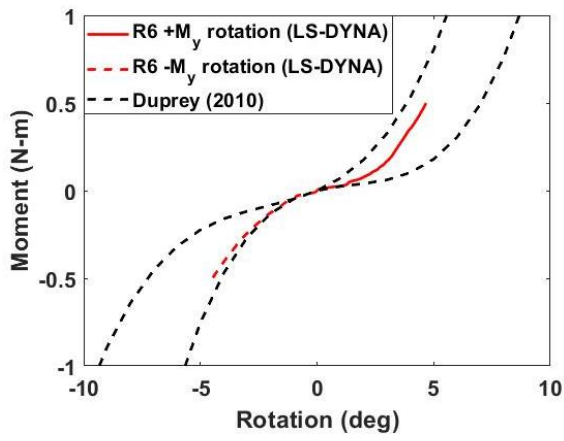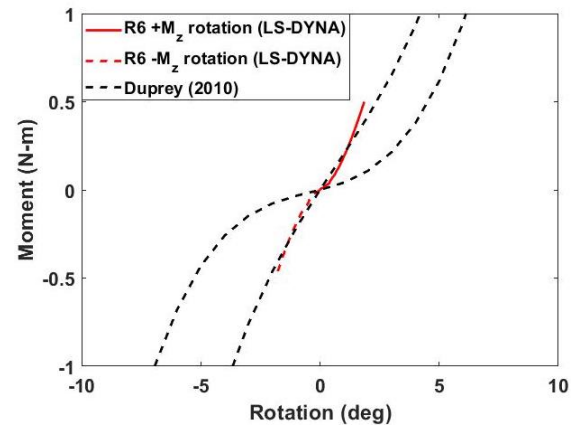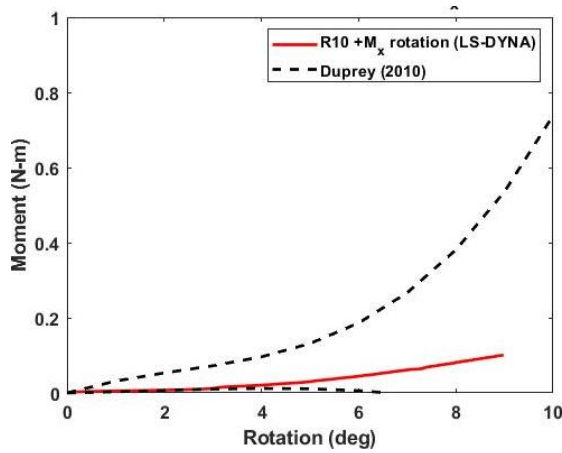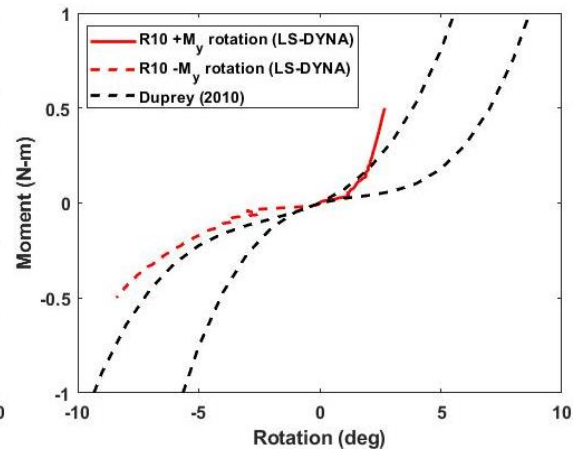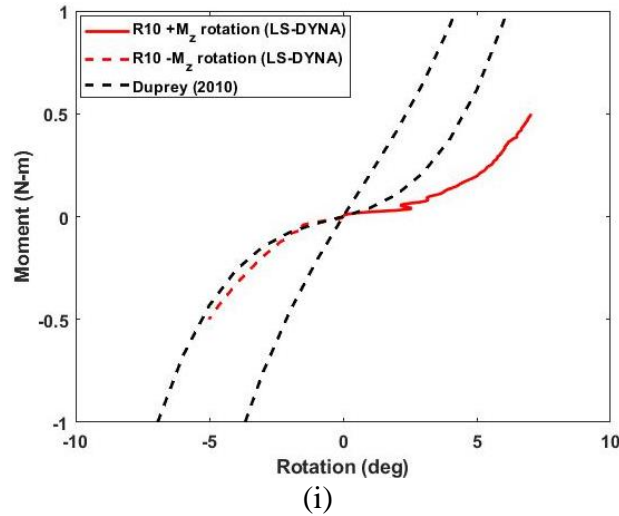
Figure 2-23: Costovertebral joint stiffness responses vs. in-vitro data corridors. (a) R2-Mx. (b) R2-My. (c) R2-Mz. (d) R6-Mx. (e) R6-My. (f) R6-Mz. (g) R10-Mx. (h) R10-My. (i) R10-Mz.

2.8 THORACIC SPINE FE MODEL VALIDATION

Finally, the kinematics of the full thoracic spine with ribcage were analyzed. Using the CGHero CAD geometry described earlier in this section, the vertebrae between T1 and T12 were meshed using a solid map extrusion between each vertebra's superior and inferior cartilaginous endplates to generate hexahedral elements for the cancellous bone, while the posterior elements were generated using tetrahedral elements. Like the cancellous bone, all IVDs were meshed using a solid map extrusion between the inferior and superior cartilaginous endplates of the vertebrae positioned above and below them. Symmetric geometry within each IVD was ensured by mirroring one half of the disc about the sagittal plane centered along each disc (Figures 2-24a-h). The annulus fibrosus of the disc was meshed using 8 layers concentrically while the number of layers in the thickness direction varied between three (T1-T9) and four (T10-T12) based on the optimum mesh size determined by the sensitivity study described previously. The

intervertebral ligament material and geometric properties utilized force-displacement curves based on scaled stress-strain curves from the literature (Figure 2-25) using initial unstretched lengths and cross-sectional ligament areas as scale factors. All intervertebral and costovertebral ligament properties were consistently applied throughout specific spinal regions (e.g., T1-T4, T5-T8, and T9-T12). Facet contact thicknesses were configured with an initial minimum gap of 0.5mm through a surface penalty contact algorithm. All costovertebral joint contact surfaces employed no initial minimum gaps within the same contact surface algorithms. Tied surface conditions within ribcage components were maintained as previously described. The final thoracic spine model with ribcage contained 274,895 elements and 167,100 nodes. A breakdown of the model size of each component within the spinal column is located in Table 2-15; details regarding ribcage model size were previously described in Table 2-14. Material properties for the spinal column and ribcage are documented in Tables 2-4 and 2-16 respectively, while intervertebral and costovertebral ligament properties can be found in Tables 2-17 and 2-18 respectively.

An external torque of 5 N-m was quasi-statically applied along the T1 superior endplate and facet processes while keeping the inferior endplate and facet processes at T12 fixed. Rotations in flexion, extension, left and right lateral bending, and left and right axial rotations were imposed. Translation data was collected at the T1 spinous process tip to convert to flexion, extension, and left and right lateral bending rotations, and collected at the T1 superior endplate to convert to left and right axial rotation based on vector projection. The global in-plane rotations were compared with available in-vitro data (Mannen,et al., 2015; Healy et al., 2014) collected from thoracic cadavers with ribcages

intact under the same boundary conditions. The presented results show separate rotations in flexion and extension, as well as a summation of rotations in flexion/extension, left and right lateral bending, and left and right axial rotation. As shown in Figure 26, rotations of 6.3° in flexion, 13.1° in extension, 18.1° in left and right lateral bending, and 28.8° in left and right axial rotation were calculated from the FE model. All rotations are within the standard deviations established within the benchmarked results, establishing the validity of all material properties and boundary conditions set within the FE model.

(a)　　　　　(b)　　　　　(c)　　　　　(d)

(e)

(f)

(g)

(h)
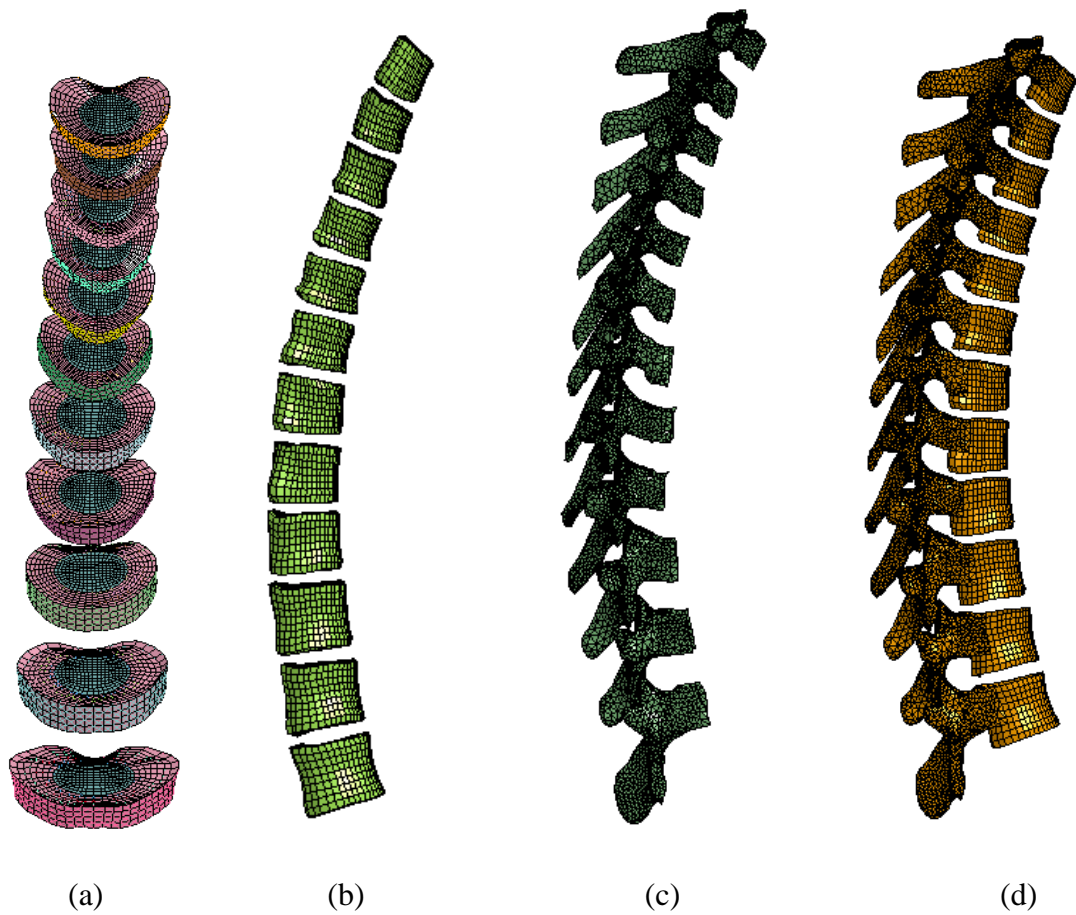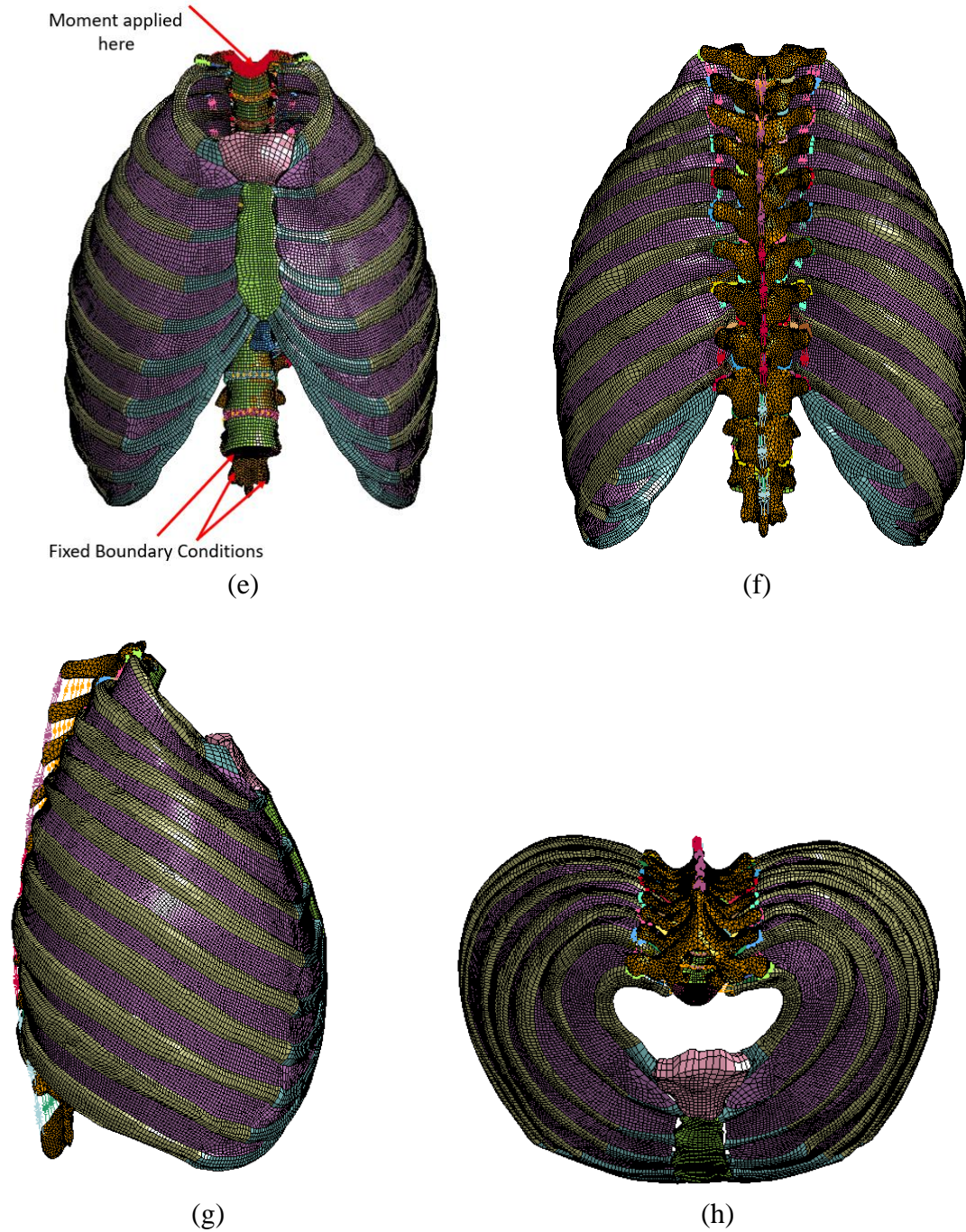
Figure 2-24: Thoracic Spine column (T1-T12) with ribcage FE model. (a) IVDs. (b) Cancellous bone. (c) Posterior elements. (d) Cortical bone. (e) FE model-anterior view with boundary conditions. (f) FE model-posterior view. (g) FE model-sagittal view. (h) FE model-axial view.

Table 2-15: Thoracic spine FE model size information.

Component	No. of elements	No. of nodes	Element configuration
Cortical Bone	34,478	19,047	3 & 4 noded tria and quads
Cancellous Bone	49,680	58,650	8-noded hexahedron
Posterior elements	65,242	19,810	4 noded tetrahedron
Cartilaginous Endplate	13,248	13,800	4 noded quads (1mm thickness)
Annulus Fibrosus	11,088	16,544	8-noded hexahedron
Annulus Fibers	23,544	16,544	Cable elements
Nucleus Pulposus	8,784	12,549	8-noded hexahedron

Table 2-16: Thoracic spine ribcage material properties (refer to Table 2-4 for vertebral and IVD material properties).

Component	Material properties	Source
Ribs	E=12 GPa, v=0.35	Schlager et al. (2018)
Intercostal muscles	E=1.03 MPa, v=0.3 (3mm thickness)	Kindig et al. (2015)
Costal cartilage	E=23.8 MPa, v=0.45	Meijer (2011)
Manubrium, Sternum, & Xiphoid	E=2.5 GPa, v=0.3	Jansova et al. (2015)

Table 2-17: Thoracic column intervertebral ligament information.

	T1-T4		T5-T8		T9-T12	
	No. of ligaments per group	Avg. length (mm)	No. of ligaments per group	Avg. length (mm)	No. of ligaments per group	Avg. length (mm)
Anterior Longitudinal Ligament (ALL)	5	4.58	7	4.8	13	6.65
Posterior Longitudinal Ligament (PLL)	3	3.51	3	4.07	7	4.5

(a)

(b)

(c)

Figure 2-25: Intervertebral & Costovertebral ligament stiffness properties utilized in the thoracic spine FE model. (a) T1-T4. (b) T5-T8. (c) T9-T12.
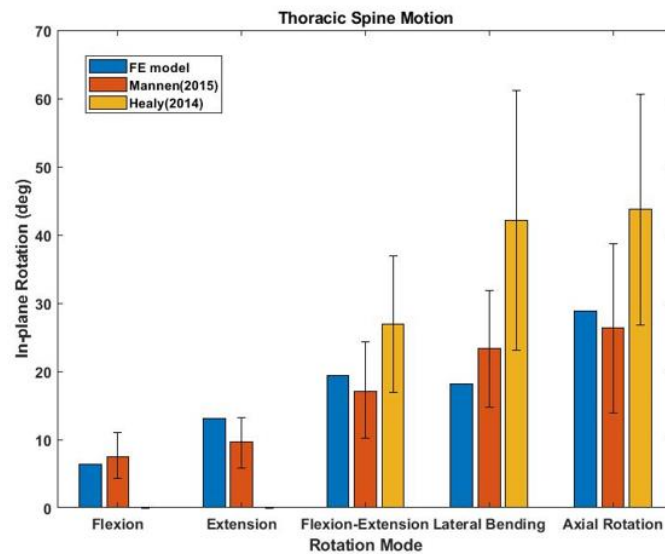
Figure 2-26: Global FE model rotations compared with existing in-vitro data.

2.9 DISCUSSION AND CONCLUSIONS

The developed FE model did not utilize patient-specific anatomy due to initial lack of resources necessary (e.g., image scanner, radiographs) to reconstruct and convert to a custom CAD model. Thus, an effort was taken to verify the precision of key anatomic dimensions within both the BodyParts3D and CGHero CAD models compared where possible with adult anatomic data in the literature prior to their utilization. Detailed vertebral dimensions compared with White and Panjabi (1990) more closely matched with the BodyParts3D model, however, when comparing the thickness, or height of both the vertebrae and the IVD, the CGHero CAD dimensions were more closely aligned with various sources. More attention was paid to the IVD dimensions as they are an important driver behind spine kinematics. The detailed morphology compared with Fletcher et al., (2015) found that the trends and thickness values in the posterior, center, and anterior disc regions were more aligned with the CGHero CAD model compared with the BodyParts3D CAD model. The study by Fletcher et al. documented thoracic IVD data for males and females ages 20-79. Since the mean center disc thickness was reported and not broken down into age demographics, all disc thickness variables had the mean values reported. However, the anterior and posterior dimensions, which were broken down by age, did not deviate by more than 0.7mm overall from the 20-29 age group sampled, which is the closest demographic to adolescents. In addition, the L4-L5 disc within the BodyParts3D had a thin anterior thickness dimension relative to the posterior, which could lead to lower rotations and make initial validation of the model difficult, as shown in the initial mesh sensitivity efforts for L4-L5. Both factors drove the decision to pivot to the CGHero CAD model.

A mesh sensitivity study is an essential part of determining the optimum mesh parameters necessary for obtaining accurate solutions while keeping the computation run times low. The run times were selected since they were sufficient to ensure quasi-static conditions which, in LS-DYNA, requires the kinetic energy of the model to be low compared to the strain energy (Livermore Software Technology, 2003). Accordingly, strain energy, which is defined by half the product of stress and strain of a deformable body at any given time, was chosen along with RoM as variable for comparison among mesh configurations for the T7-T8 model as had been done in previous mesh sensitivity studies (Ayturk and Puttlitz 2011). Differences in the mesh sensitivity results, while primarily attributable to the mesh size, may have also been slightly affected by the modification to the annulus fiber configuration; a decrease in mesh size led to an increase in fibers while decreasing both the overall lengths and cross-sectional areas to ensure a 16% volume relative to the annulus fibrosus (ground substance and fibers). However, choosing the FE model containing a medium mesh size with three elements through the IVD thickness produced a reconciliation between results produced by more refined FE mesh models and computational time.

Validation of an FE model compared to specific in-vivo or in-vitro experimental conditions is an important part of developing a model to accurately answer pertinent clinical questions. Ligament property selection, while scarce in the literature, was tantamount to achieving proper kinematic behavior compared to available in-vitro data for the lumbar spine FE models of the L4-L5 FSU and spinal columns. The intervertebral ligament properties documented in Rohlmann et al., (2006b) in conjunction with proper IVD morphology, helped produce a kinematic response in three anatomic planes that

matched well with available in-vitro data for the lumbar spine. Though the properties were seemingly derived from earlier studies aimed at calibrating FE models of the lumbar spine, no data could be readily found on the original demographics of the patient that formed the basis for the ligament properties. However, since the ligament properties were properly characterized by exhibiting toe and linear characteristics aiding in good agreement with in-vitro data, the decision was made to employ these properties for future analyses. The intervertebral RoM and facet joint forces were compared the pure moment model results from (Du et al., 2016) since they employed a facet joint initial contact gap of 0.1mm, which was lower relative to values utilized by other researchers (Mengoni, 2021). The segments in which facet joint forces and RoM were close in value or disparate varied and could be due to the explicit modeling of facet cartilage along different segments in their model, versus pure contact surfaces modeled here. Due to the level of closeness of some segments' results, the penalty contact setting was deemed acceptable for this exercise.

Ligament stiffness properties for the costovertebral joint were difficult to obtain, as researchers have previously simplified it to a spherical joint without ligamentous connections to the adjacent spinal column (Kindig et al., 2015; Schlager et al., 2018). Only the stiffness properties derived by Aira et al., 2019 could be found for these ligaments and were thus utilized. Since nonlinear properties were not documented, a kinematic validation with existing in-vitro data needed to be performed. While the properties exhibit effective elastic stiffnesses as opposed to a traditional sigmoidal curve, most of the moment-rotation responses from the FE model were within the standard deviation established by the response corridors. The discrepancies between the FE model

response and in-vitro response, particularly in R10, could be tied to the changing rib head orientation relative to the adjacent spinal column, which affects when the rib engages in contact with the vertebrae. However, the compliance exhibited in the cranial-caudal rotations presented in this model is not unlike the responses seen within R10 specimens tested in the same rotation directions; it is unclear as to why the compliance was exhibited in the test. Nonetheless, the costovertebral joint configuration was deemed valid for further use.

Development of the thoracic spine FE model required utilization of material properties from various sources as overall documentation is scarce for modeling in this spinal region. As a result, the vertebral and IVD material properties as well as mesh settings employed for the lumbar spine were carried over to the thoracic region. The decision to analyze both costovertebral joints and divide ligament properties by upper, mid, and lower thoracic regions are based on the kinematic characteristics of the spine in those regions, dictated primarily by vertebral size, facet joint orientation, intervertebral disc height, and in-plane/coupled motion patterns (White and Panjabi, 1990; Fletcher et al., 2015; Busscher et al., 2009). The intervertebral ligament stiffness properties utilized were chosen based on available in-vitro kinematic data for spinal FSUs. Chapters 4 and 5 will go into further detail on the basis behind their utilization. Based on the available in-vitro data available for global motion for cadaveric spines containing ribcage, all constraints and material properties were deemed acceptable for further use.

Since in-vitro or in-vivo kinematic data for adolescents is currently lacking, the use of benchmarks based on adult cadaveric specimens was a compromise in kinematically validating the FE models constructed here, with the assumption that an

adolescent possesses more flexibility of their spines compared to an adult. Based on the kinematic performance of individual components, the setup described for the FE model is acceptable for further utilization in the subsequent studies to be summarized in this dissertation.

CHAPTER 3

A COMPARISON OF INTERVERTEBRAL LIGAMENT PROPERTIES UTILIZED IN A THORACIC SPINE FUNCTIONAL UNIT THROUGH KINEMATIC EVALUATION

3.1 ABSTRACT

Ligament properties in the literature are variable, yet scarce, but needed to calibrate computational models for spine clinical research applications. A comparison of ligament stiffness properties and their effect on the kinematic behavior of a thoracic functional spinal unit (FSU) is examined in this paper. Six unique ligament property sets were utilized within a volumetric T7-T8 finite element (FE) model developed using computer-aided design (CAD) spinal geometry. A 7.5 N-m moment was applied along three anatomical planes both with and without costovertebral (CV) joints present. Range of Motion (RoM) and Instantaneous Centers of Rotation (ICoR) were assessed for each property set and compared to published experimental data. Intact and serial ligament removal procedures were implemented in accordance with experimental protocol. The variance in both kinematic behavior and comparability with experimental data among property sets emphasizes the role nonlinear characterization plays in determining proper kinematic behavior in spinal FE models. Additionally, a decrease in RoM variation among property sets was exhibited when the model setup incorporated the CV joint. With proper assessment of the source and size of each ligament, the material properties considered here could be expanded and justified for implementation into thoracic spine clinical studies.

3.2 INTRODUCTION

Ligaments are fibrous bands of tissue that bind vertebral bodies and intervertebral discs together within a spinal column, restricting motion along the axial, coronal, and sagittal planes. The understanding of load distribution throughout the spinal column can assist clinicians in planning for treatment of musculoskeletal disorders. Surgical procedures such as the Ponte osteotomy (Samdani et al., 2015), involving the removal and re-sectioning of ligaments and facet joints, have gained interest in their ability to offer increased spinal column correction for kyphosis and scoliosis. Finite Element (FE) modeling can be utilized to answer clinical questions that cannot be easily answered from in-vitro experimentation or clinical practice. A model's ability to assist in surgical planning is contingent upon accurate characterization of ligaments and their benchmark with experimental data.

To date, there are limited in-vitro experimental studies that have examined the quasi-static mechanical stiffness of spinal ligaments situated throughout the spinal column (Chazal et al., 1985; Pintar et al., 1992; Myklebust et al., 1988; Nolte et al., 1990). These studies generally harvest ligament specimens with varied predetermined factors such as age of the cadaver (Neumann et al., 1992) and sample preparation procedures such as ligament preconditioning (Mattucci et al., 2012), which may play a role in the ligament tensile response. In addition, material and geometric properties for spinal ligaments remain limited while the data presented in literature varies. Tensile ligament properties were primarily published as in-vitro failure properties such as maximum load and displacement (Myklebust et al., 1988; Pintar et al., 1992), leaving out key information about the nonlinear deformation path that ligaments in toe, linear, and

yield regimes traditionally exhibited in tension (White and Panjabi 1990, p. 20-21). Some studies include information regarding the cross-sectional area and initial lengths of each ligament tested (Chazal et al., 1985; Yoganandan et al., 2000), helping to enhance model input and understanding of stiffness variation along the column. Unfortunately, the limited published data leaves researchers creating computational models based on their assumptions about ligament properties from previously conducted studies (Rohlmann et al., 2006b; Shirazi-Adl et al., 1986) or generate their own property sets through model calibration (Schmidt et al., 2007).

Kinematic validation of a model typically assesses the Range of Motion (RoM), or quantitative rotation, of a joint under specific loading conditions. However, the Instantaneous Center of Rotation (ICoR) has emerged in alternatively assessing motion quality (Anderst et al., 2013) as the RoM only provides information on end-range mobility. The ICoR between two adjacent vertebrae can provide specific information on pathological abnormalities (Bogduk et al., 1995) that may guide appropriate clinical treatments. The ICoR path can clinically be assessed through a sequence of radiographic images evaluating joint mobility. From a surgical planning perspective, ICoR behavior from specific procedures performed on symptomatic patients may be evaluated in a spinal FE model and compared with asymptomatic patients.

There is limited knowledge on the role ligaments play in the kinematic behavior in the thoracic spine. Previous FE studies on the lumbar spine have examined the effects of spinal ligament input properties (Naserkhaki et al., 2018) and morphological representation (Meijer, 2011; Zander et al., 2017) on the RoM of a spine model. Other studies assessed the ICoR within the lumbar spine and its relation to facet forces

(Schmidt et al., 2008) and ligament properties (Naserkhaki et al., 2018). Thus far, only one study has examined the ICoR on an FE model of a thoracic functional spinal unit (FSU) (Qiu et al., 2003). The thoracic spine uniquely differs due to morphological differences in ligament stiffness properties, disc dimensions, and facet orientations compared with other spinal regions that can affect its movement (White and Panjabi 1990, pp.9,20,22). Also, the presence of the ribcage through costovertebral (CV) joint connections between ribs and adjacent vertebrae provides stability to the thoracic column and up to 77% RoM reduction (Mannen et al., 2015). However, in-vitro studies that have examined FSU behavior in the thorax have done so both with (Wilke et al., 2017; Liebsch et al., 2020b) and without CV joints present (Wilke et al., 2020; Panjabi et al., 1984). This study assesses the suitability of intervertebral ligament properties on a thoracic spine FSU with and without CV joints using RoM and ICoR as variables for comparison.

3.3 METHODS

3.3.1 FE MODEL PREPARATION

An FE model (Figure 3-1) for a T7-T8 FSU was created utilizing Hypermesh (Altair Engineering Troy, MI) based on an anatomist-drawn computer-aided design (CAD) spine model representative of an average asymptomatic adult (CGHero Manchester, UK) and analyzed using LS-DYNA implicit SMP Version 971 R10.1 (Livermore Software Technology Livermore, CA). The FSU contained vertebral endplates and cortical bone characterized as Quad and Tria shells, respectively. The cancellous bone, encapsulated within the cortical bone, is characterized using hexahedral elements, and the vertebral arches characterized using tetrahedral elements. The

intervertebral disc (Figure 3-2), consisting of the nucleus pulposus and annulus fibrosus, were characterized using hexahedral elements. The nucleus pulposus area and volume made up approximately 37% and 40% of the disc's transverse cross-section and volume respectively (Newell et al., 2017) and was sized sagittally based on disc length ratios (Zhong et al., 2014) while being laterally centered. Disc thickness and area dimensions are shown in Table 3-1. Embedded within the annulus fibrosus were fibrous elements represented as cables for an 8 radial layer and 3 thickness layer composition. The material and geometric configuration of the annulus fibers followed that of (Shirazi-Adl et al., 1986) such that they constituted 16% of the total annulus fibrosus volume. To facilitate the incorporation of the CV joint, approximately 3 cm of the ribs bilaterally situated were included in the model and constrained through appropriate ligament attachments (Figure 3-1b). Null shell contact elements were incorporated over the rib to facilitate a frictionless penalty surface contact algorithm between it and the FSU (Figure 3-1c). Material properties for the aforementioned entities are listed in Tables 3-2 and 3-3, respectively. In total, the model contained 34,990 elements and 15,944 nodes. The average overall mesh size was approximately 1.33mm. Average mesh sizes for each part are documented in Table 3-2.

Six ligament property sets were initially designated and utilized from various sources (Chazal et al., 1985; Myklebust et al., 1988; Nolte et al., 1990; Cribb et al., 2020; Rohlmann et al., 2006b; Shirazi-Adl et al., 1986) (Figure 3-3). The choice to utilize these material properties stemmed from three considerations: whether properties existed specifically for ligaments in the thoracic region, if they were utilized in previous numerical studies of the thoracic spine (Little and Adam 2011), or if promising results

were obtained in previous studies using lumbar ligament material properties (Naserkhaki et al., 2018; Polanco et al., 2020). For a set that had properties for a ligament missing, they were substituted from a property set with available data for the ligament in question. The property sets formulated are highlighted in Table 3-4. Both intervertebral and CV entities were characterized using tension-only elements complemented by a force-displacement relationship derived for all intervertebral entities based on the geometric and material properties documented in the literature. If ligament stiffness properties were denoted by stress and/or strain, the strain was scaled by average undeformed ligament lengths (Table 3-5) to obtain displacement, while the stress was scaled by a constant cross-sectional area to obtain force if mentioned in the source. All stiffnesses were divided among the number of elements in the model for each ligament group (Tables 3-3 and 3-5). Due to low ligament forces typically imposed in pretension (e.g., < 10 N) (Meijer, 2011), all ligaments were left initially unstretched in all model runs. As with the CV joint, the facet capsules were characterized using a frictionless penalty surface contact algorithm with a 0.5mm minimum initial gap. This gap value is within range of those traditionally utilized in facet characterization through contact (Mengoni, 2021).

3.3.2 ANALYSIS PROCEDURES

Validation of the CV joint configuration was first conducted using in-vitro kinematic data based on the experiment conducted by Duprey et al., (2010). As depicted in Figure 3-4, an aluminum rod 0.25 inches in diameter was coupled to the R8 rib with torques of ±0.5 N-m applied in cranial-caudal ($\pm My$) and ventral-dorsal ($\pm Mz$) directions, while a 0.1 N-m torque was applied in torsion ($+Mx$) along the rod. Fixed boundary

conditions were employed to represent the potting of the FSU. All kinematic data was read in a local coordinate system at the joint center as described in the reference and seen in Figure 3-4a. Next, kinematic assessment was performed for each ligament property set with CV joints incorporated and compared with RoM data (Wilke et al., 2017). ITL connections were assumed to be present here with properties utilized from Chazal et al., (1985). With fixed boundary conditions imposed on the T8 inferior endplate and facet processes (Figure 3-1a), the FSU was rotated within 3 anatomical planes in flexion (+y), extension (-y), right lateral bending (+x) and left axial rotation (+z) using a pure moment of 7.5 N-m and no preload along a rigid body element on the T7 superior endplate guided by a local coordinate system. Per the recommendations of the Scoliosis Research Society (Stokes 1994), this coordinate system was positioned between the T7 superior and inferior endplates, with x and y in the anteroposterior and mediolateral directions respectively.

The role of each ligament in the FSU RoM was then individually assessed. Serial ligament removal for each property set was performed per the sequence described in Wilke et al., (2020) for their in-vitro experiment. To match the conditions of the specimens tested, the CV joints and ITLs were assumed to be absent; boundary conditions were the same as before. RoM in all three planes for the following configurations were assessed and compared with in-vitro data: Intact, Supraspinous Ligament (SSL) removed, Interspinous Ligament (ISL) removed, Ligamentum Flavum (LF) removed, Facet Capsule (FC) removed, Vertebral Arch (VA) removed, Posterior Longitudinal Ligament (PLL) removed, and Anterior Longitudinal Ligament (ALL) removed. All translational data was collected on nodes along the superior endplate and

converted to RoM through vector projection. The intact configuration from this study was also used as the basis for sagittal ICoR comparison in flexion and extension. Using confidence ellipses generated from in-vitro data (Panjabi et al., 1984), the ICoR was calculated every 0.1 N-m and compared for each ligament property set. The ICoR was found through a perpendicular bisector method documented by (Pearcy and Bogduk, 1988) based on the same nodal data and differential positions of T7.

Finally, to further investigate the suitability of lumbar ligament stiffness curves for thoracic ligaments, an assessment was conducted to assess the effect of scaling the stress in ligament stress-strain curves originally utilized for lumbar spine FE models by thoracic cross-sectional area values. The ligament Property Set 6 was chosen primarily due to larger differences between the thoracic and lumbar areas utilized to scale the stress to force (Table 3-6). Thoracic cross-sectional area values were chosen based on available data for mid-thoracic ligaments (e.g., T5-T8) tested during in-vitro experimentation and averaged per ligament group (Chazal et al., 1985). The stress-strain curves were then scaled by the averaged areas to reflect the dimensioning proper to the mid-thoracic spine region; the strain was maintained at the original scale. The stepwise removal procedure highlighted earlier was implemented for the FSU without CV joints. RoM at each step and average sagittal ligament displacements at maximum load (e.g., 7.5 N-m) were highlighted for this assessment.

Table 3-1: Intervertebral Disc Dimensions.

Anterior (mm)	Center (mm)	Posterior (mm)	Nucleus Pulposus Cross-Sectional Area (mm^2)	Nucleus Pulposus Volume (mm^3)	Transverse Disc Cross-Sectional Area (mm^2)	Disc Volume (mm^3)
5.9	6.9	4.8	352	1242	1049.5	3073

Table 3-2: Functional Unit Material Properties.

Spinal Component	Material Property	Source	Average Element Edge Length
Cortical Bone	E=12 GPa, v=0.3	Naserkhaki et al., 2018	1.42mm
Cancellous Bone	E=200 MPa, v=0.315	Naserkhaki et al., 2018	1.35mm
Rib	E=12 GPa, v=0.3	Schlager et al., 2018	1.83mm
Endplate	E=23.8 MPa, v=0.4, 1mm thickness	Schmidt et al., 2006	0.98mm
Annulus Fibrosus	C10=0.18 MPa, C01=0.045 MPa, v=0.45 Mooney-Rivlin	Schmidt et al., 2006	1.26mm
Nucleus Pulposus	C10=0.12 MPa, C01=0.03 MPa, v=0.499, Mooney-Rivlin	Schmidt et al., 2006	1.06mm
Annulus Fibers	Nonlinear Stress-Strain curve, all material and geometric scale factors adjusted based on layer position	Shirazi-Adl et al., 1986	N/A

Table 3-3: Costovertebral Joint Properties.

Spinal Component	Material Property	Source	Number of elements (on each side)
Lateral Costotransverse Ligament	Keff=126.5 N/mm	Aira et al., 2019	9
Superior Costotransverse Ligament	Keff=90.2 N/mm	Aira et al., 2019	3
Costotransverse Ligament	Keff=54.9 N/mm	Aira et al., 2019	6
Radiate Ligament	A=10mm^2, E=42.1 Mpa	Aira et al., 2019; Jiang et al., 1994	10
Intra-articular Ligament	Keff=20.9 N/mm	Aira et al., 2019	2

Table 3-4: Ligament property sets and their sources denoted by numerical ID in parentheses.

Property Set	ALL	PLL	LF	ISL	SSL	CL
1	(1)	(1)	(1)	(1)	(1)	(2)
2	(2)	(2)	(2)	(2)	(2)	(2)
3	(3)	(3)	(3)	(3)	(3)	(3)
4	(4)	(4)	(4)	(4)	(4)	(2)
5	(5)	(5)	(5)	(5)	(5)	(5)
6	(6)	(6)	(6)	(6)	(6)	(6)

(1)Chazal et al., 1985: human, in-vitro; (2) Myklebust et al., 1988: human, in-vitro; (3) Nolte et al., 1990: human, in-vitro, lumbar; (4) Cribb et al., 2020: porcine, in-vitro, lumbar; (5) Rohlmann et al., 2006b: model, lumbar; (6) Shirazi-Adl et al., 1986: model, lumbar.

Table 3-5: Average Model Ligament lengths.

Spinal Component	Average Length (mm)	Number of elements
Anterior Longitudinal Ligament (ALL)	5.36	7
Posterior Longitudinal Ligament (PLL)	4.929	3
Ligamentum Flavum (LF)	24.832	3
Interspinous Ligament (ISL)	5.541	4

Table 3-5 continued.

Supraspinous Ligament (SSL)	25.588	3
Capsular Ligament (CL)	2.799 (over both sides)	15 (on each side)
Intertransverse Ligament (ITL)	18.359 (over both sides)	1 (on each side)

Table 3-6: Lumbar & Thoracic cross-sectional area comparison. The intertransverse ligament was not included to ensure appropriate compatibility with experimental conditions.

Spinal Component	Lumbar cross-sectional areas (mm^2) (Shirazi-Adl et al., 1986)	Thoracic cross-sectional areas (mm^2) (Chazal et al., 1985)	% change in cross-sectional area
Anterior Longitudinal Ligament (ALL)	24	30	+25%
Posterior Longitudinal Ligament (PLL)	14	17	+21%
Ligamentum Flavum (LF)	75	24.75	-67%
Interspinous Ligament (ISL)	40	29.5	-26.3%
Supraspinous Ligament (SSL)	30	29.5	-1.7%
Capsular Ligament (CL)	36	36	0%
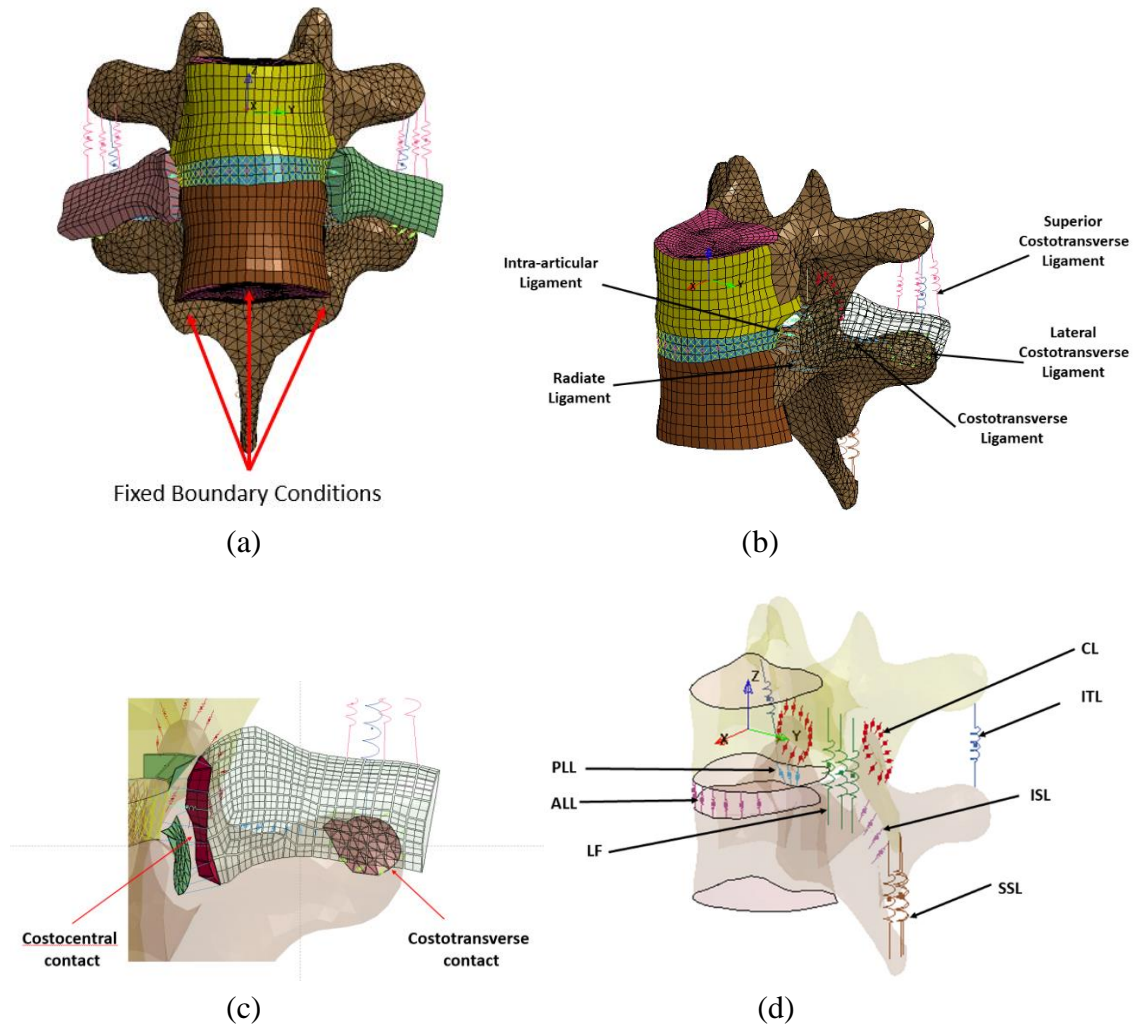
Figure 3-1: (a) T7-T8 Functional Unit with CV Joints; (b) CV joints display; (c) CV joint contact surface definitions; (d) Transparent display of Functional Unit with Intervertebral ligaments.
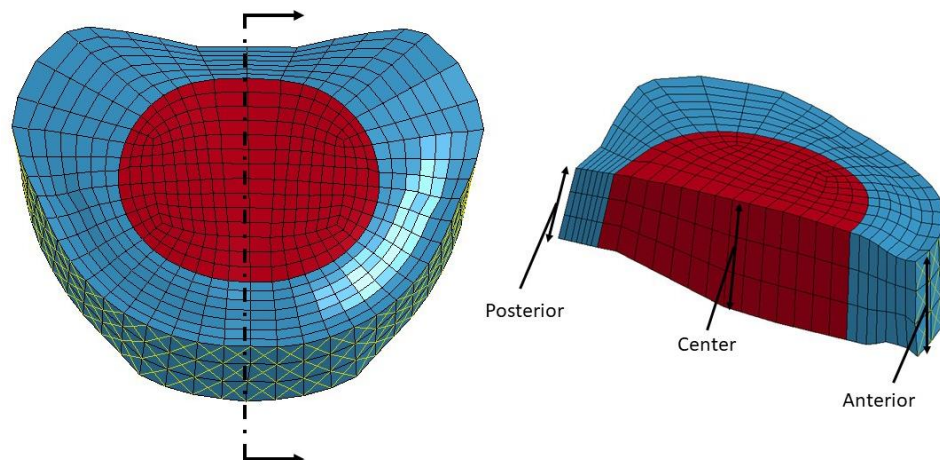
Figure 3-2: Intervertebral disc.
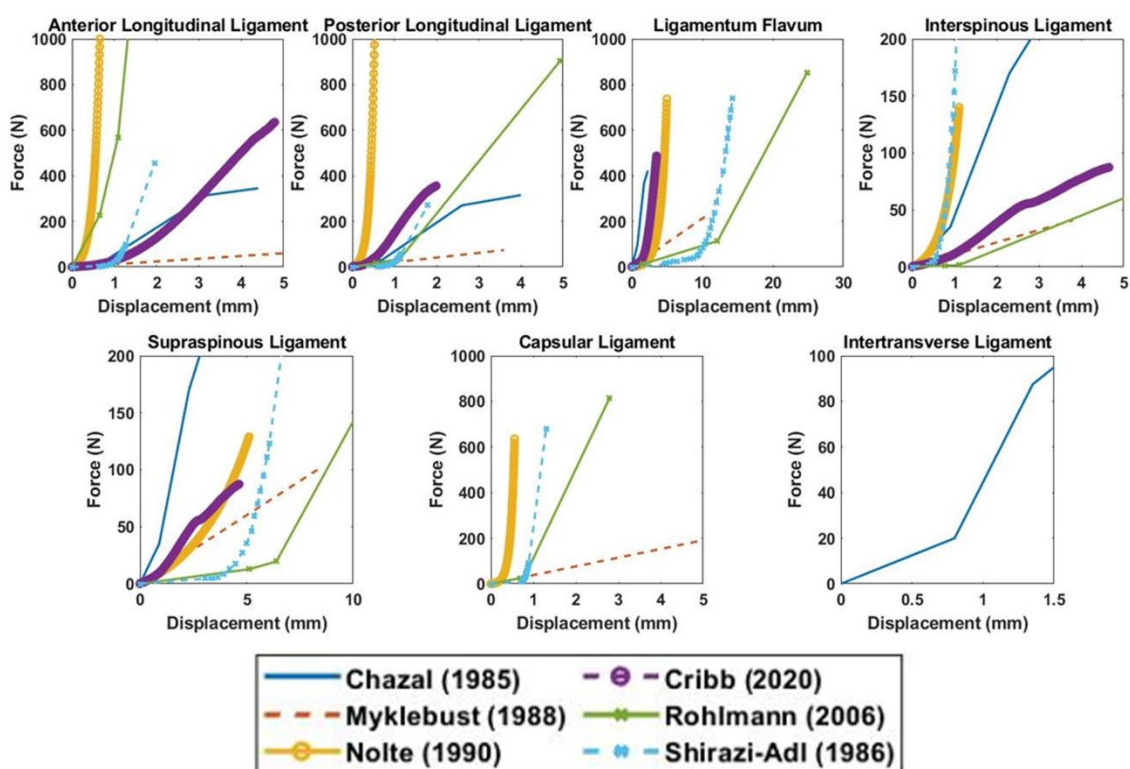
Figure 3-3: Ligament input properties and their sources. Capsular ligament properties were assigned to each individual facet except for properties derived from Myklebust (1988), who tested capsular ligaments bilaterally intact.
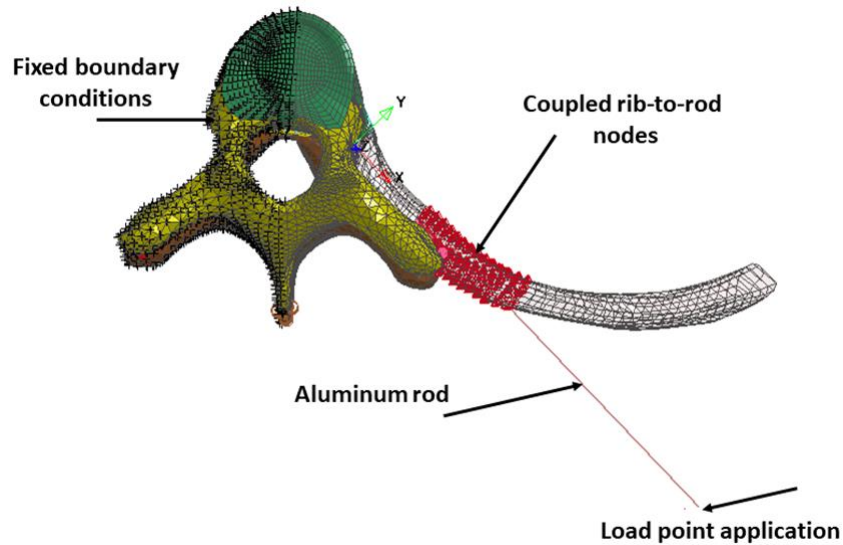
Figure 3-4: FE Model setup for CV joint validation.

3.4 RESULTS

3.4.1 MODEL VALIDATION-COSTOVERTEBRAL JOINT MECHANICS

The RoM of the rib was taken at applied moments of ± 0.1 N-m in all three planes and compared with average RoM data acquired from Duprey et al., (2010) and Lemosse et al., (1998). Overall, the model RoM is shown to be within range of the data shown in the bar graphs (Figures 4b-4d). Additionally, rib angular displacement for each direction was acquired using the trigonometric equations documented in Duprey et al., (2010). The model response was compared with the characteristic stiffness corridor and specimen responses derived from the in-vitro experimental results. The torsion and ventral-dorsal responses from the model are mostly within the corridor. While the caudal (-My) response lies within the corridor, the cranial (+My) response (Figure 3-4b) reveals stiffer behavior due to contact between the rib head and the vertebra with increasing torque. Though it has been shown that the CV joint is stiffer in the mid-thoracic region due to a

larger rib cross-section (Lemosse et al., 1998), differences in contact surface morphology between specimen and model vertebrae likely produced the discrepancy. Nonetheless, the CV ligament configuration was considered acceptable for application in subsequent analyses.

(a)   (b)   (c)
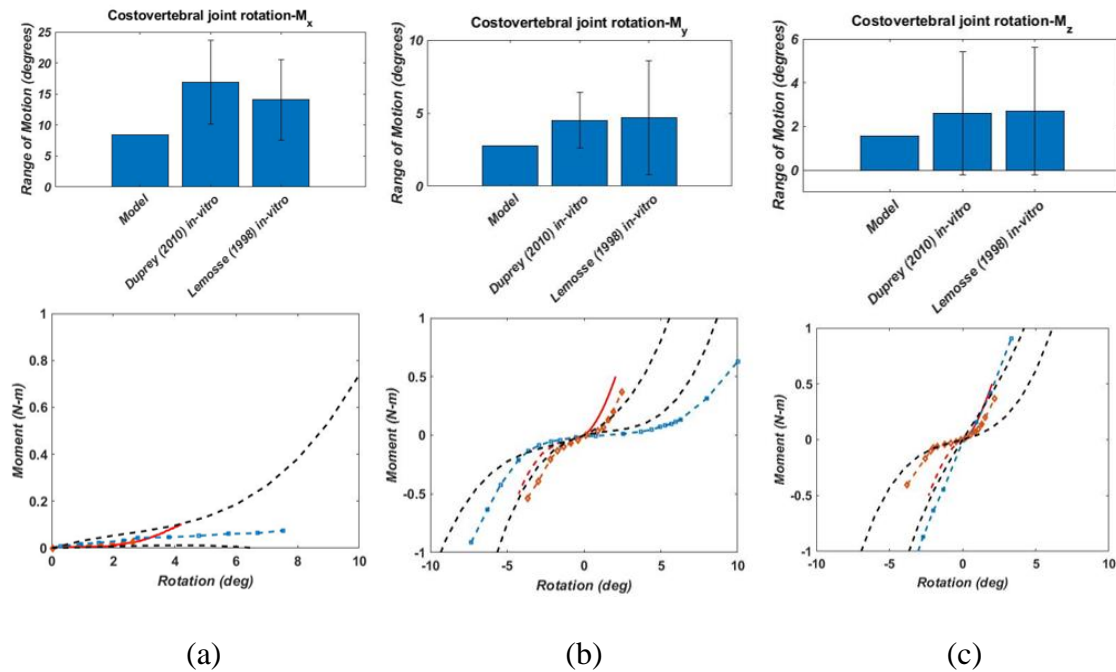
Figure 3-5(a)-(c): Costovertebral joint moment-angle comparisons with in-vitro data in torsion, Cranial-Caudal flexion, and Ventral-Dorsal flexion respectively.

3.4.2 RoM ASSESSMENTS WITH CV JOINTS

In flexion (Figure 3-6), the FSU RoM ranges between 2.1° and 2.7° while in extension, the RoM ranges between 4.7° and 7.3° at maximum load. In right lateral bending, the RoM among property sets ranges between 5.5° and 5.6°. In left axial rotation, the RoM among property sets assessed ranged between 3.2° and 5.0°, while the

FSU in right axial rotation 4.1° and 5.3°, all at maximum load. The comparison with in-vitro data (Wilke et al., 2017) was realized for a T7-T8 function unit with CV joints at maximum load. In accordance with coronal and axial rotational symmetry assumptions, only right lateral bending and left axial rotation results are reported here.
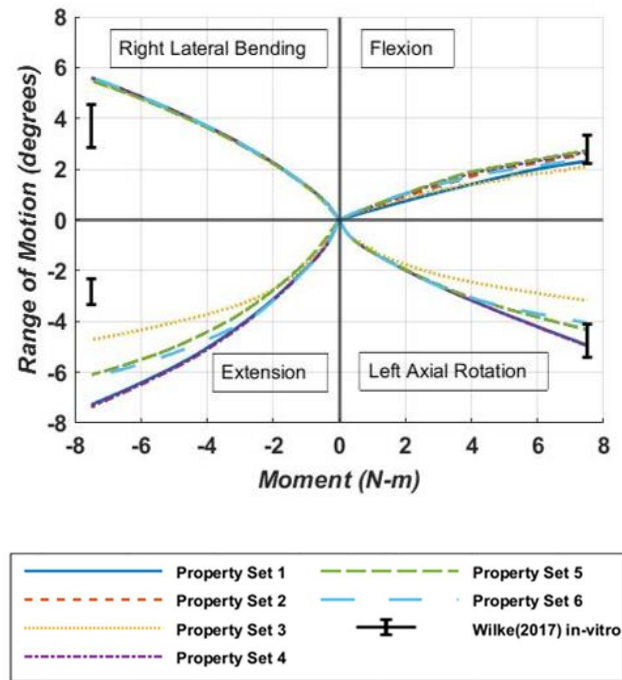
Figure 3-6: RoM plots in Flexion/Extension, Right Lateral Bending, and Left/Right Axial Rotation with CV joints and ITL incorporated.

3.4.3 RoM ASSESSMENTS DURING SERIAL LIGAMENT REMOVAL

Between the intact configuration and the final stage of ligament removal in flexion, the maximum RoM increased between approximately 106%-434% (Figure 3-6), while in extension, the RoM increased between 13%-88%. In right lateral bending and left axial rotation, the maximum RoM increased between approximately 2%-9% and 8%-74% respectively. The RoM increased gradually as ligament groups were removed,

leading to a converged RoM response in flexion, lateral bending, and axial rotation after PLL removal, and extension after ALL removal. Within removal steps, the greatest overall influence in RoM was seen when the facets were removed, having produced maximum increases of 1.3% in right lateral bending, 74% in left axial rotation, 45% in extension and 200% in flexion. Comparison of the intact configurations presents maximum RoM increases of 33% in right lateral bending, and 5% in left axial rotation, 11% in extension, and 93% in flexion when the CV joints and ITL are absent. Likewise, among Property Sets, the ranges at maximum load increase, resulting from an absent CV joint and ITL, by up to 440% in right lateral bending, 11% in left axial rotation, 236% in extension, and 394% in flexion.

(a)

(b)

(c)

(d)

(e)

(f)

(g)

(h)
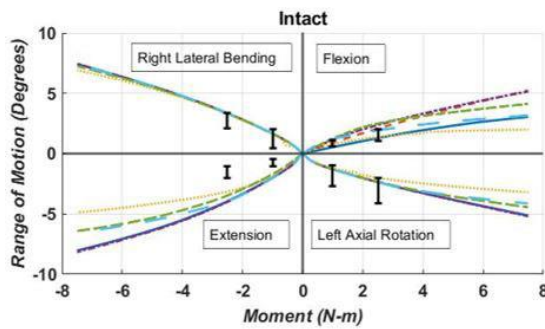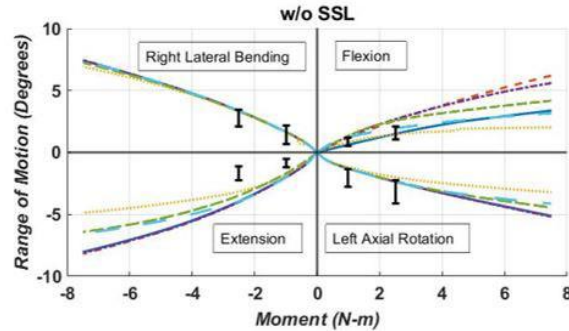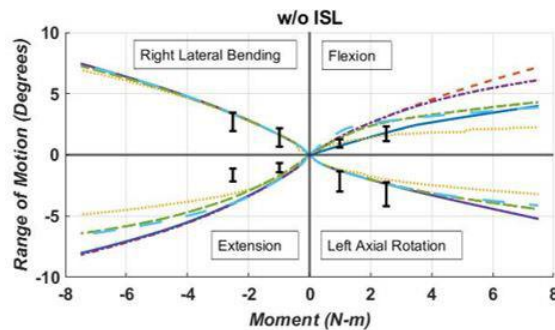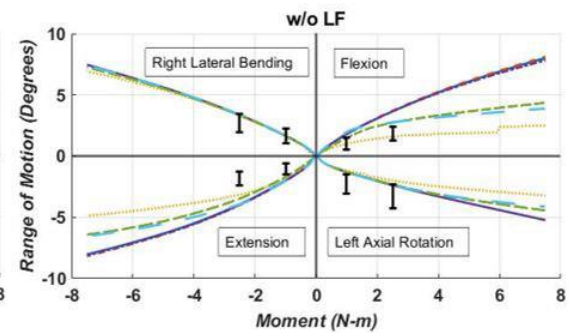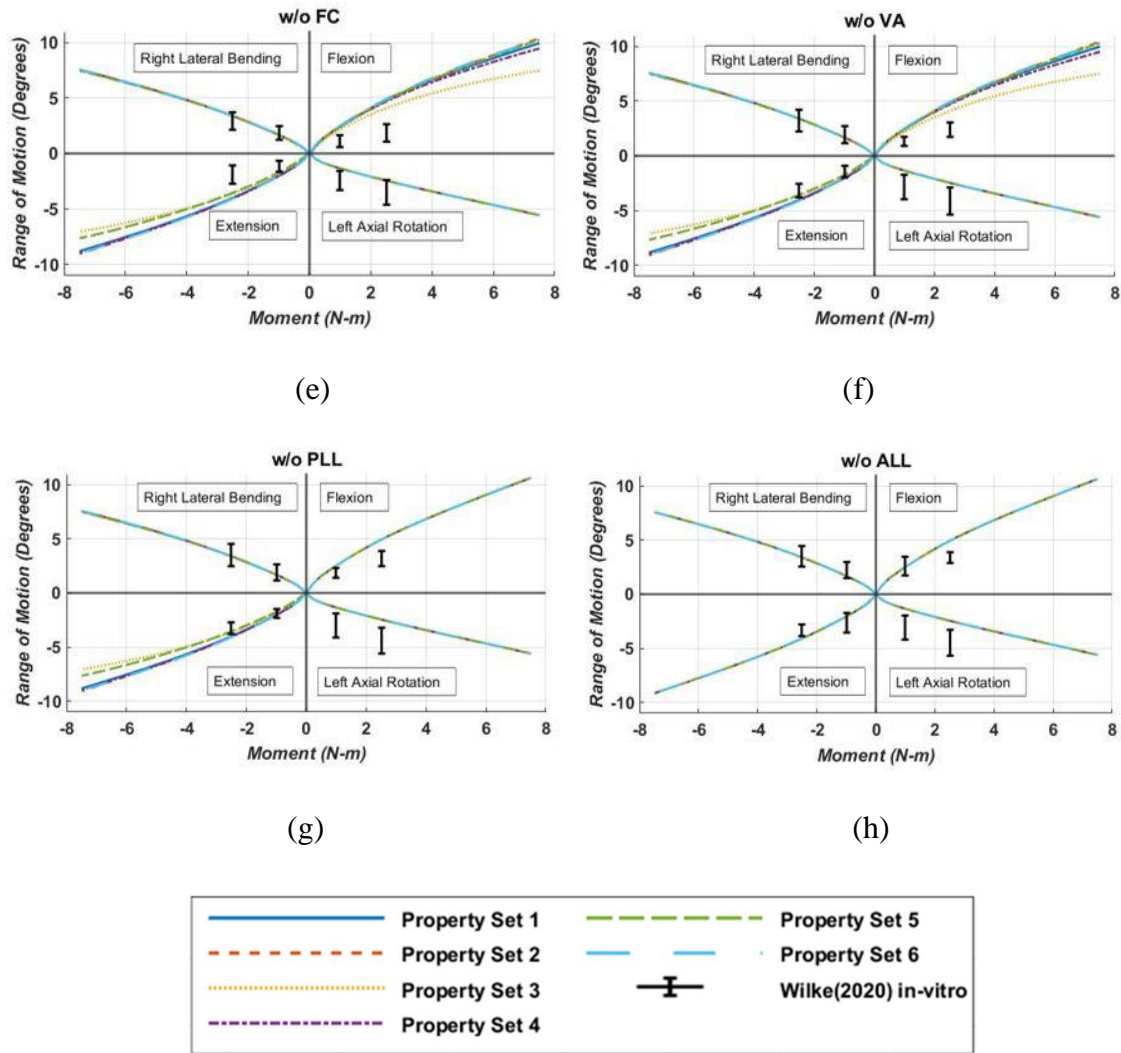
Figure 3-7: Functional unit RoM during serial ligament removal. (a) Intact configuration; (b) SSL removed; (c) ISL removed; (d) LF removed; (e) FC removed; (f) VA removed; (g) PLL removed; (h) ALL removed.

3.4.4 ICoR SAGITTAL BEHAVIORAL ASSESSMENTS

The ICoR (Figure 7) shifts anteroposteriorly between a net minimum of 0.03mm (Property Set 1) and a maximum of 2.43mm (Property Set 6). In the superior direction, the trace ranges between 1 mm (Property Set 5) and 4.43 mm (Property Set 1). Upon

moving circularly, at a minimum, extension produces 0.3 mm shifts (Property Set 6) and maximum shift of 0.57 mm posteroanterior (Property Set 3). In the inferior direction the trace ranges between 0.24 mm (Property Set 6) and 1.2 mm (Property Set 1). To assess the validity of ICoR behavior, all traces were compared with confidence ellipse equations derived from experimentation (Panjabi et al., 1984) for flexion and extension without CV joints. The ICoR at applied external moments in 1.5 N-m increments up to 7.5 N-m are highlighted, with the ICoR at all load steps highlighted by an open marker except for the last, highlighted as closed.
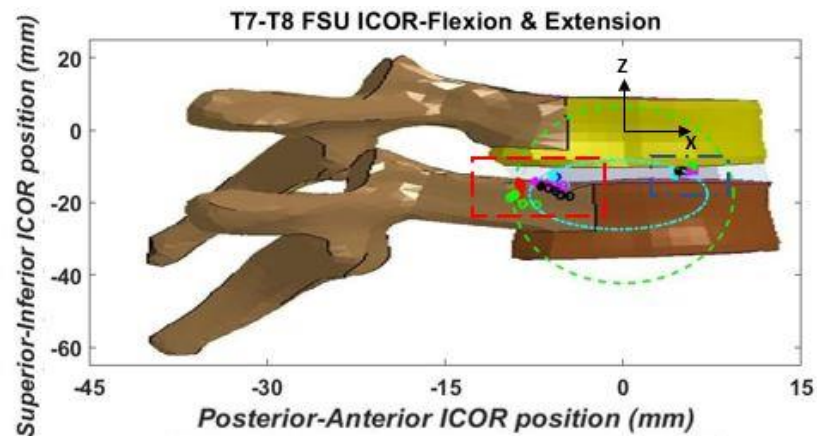
(a)
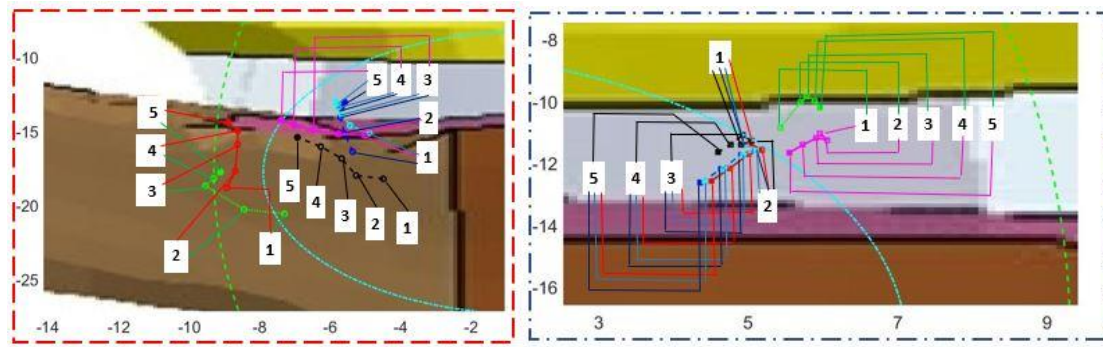
(b)   (c)

Figure 3-8: T7-T8 Functional Unit; axes denote the position of the vertebrae in space, with the origin denoting location of the local coordinate system. Numbers 1-5 denote the ICoR at various load steps: (1) 1.5 N-m, (2) 3 N-m, (3) 4.5 N-m, (4) 6 N-m, (5) 7.5 N-m. (a) Flexion & Extension ICoR traces superimposed over the T7-T8 vertebral geometry; (b) Closeup of ICoR traces in flexion; (c) Closeup of ICoR traces in extension.

3.4.5 THORACIC AND LUMBAR CROSS-SECTIONAL AREA COMPARISON

The RoM at each serial removal stage of ligament groups using thoracic cross-sectional areas as stress-strain scale factors were largely unchanged from lumbar scale factors. As shown in Figure X, the trends when all four rotations were imposed were very similar, with rotations between all configurations not seeing a difference in RoM by more than 2%, occurring with the configuration after the SSL removal. The average displacements within each ligament group generally grew as posterior ligaments were serially removed in flexion, with the most posterior ligaments stretching prior to their removal (e.g., SSL, ISL). The largest increase occurring with the PLL from 0.14mm to

0.83mm from the intact configuration to when the vertebral arches removed. Overall, when the thoracic cross-sectional areas are used to scale the stress-strains of each ligament, no ligament group sees a difference between applied lumbar and thoracic cross-sections more than approximately 5.3%, which occurred within the ISL group after the SSL was removed. The results reported for average displacement are shown only for the first six removal steps involving a posterior ligament in flexion or facet capsule in extension; extension only was dependent upon the facet capsule and ALL to resist motion.

(a)   (b)

(c)

(d)

(e)

(f)

(g) (h)
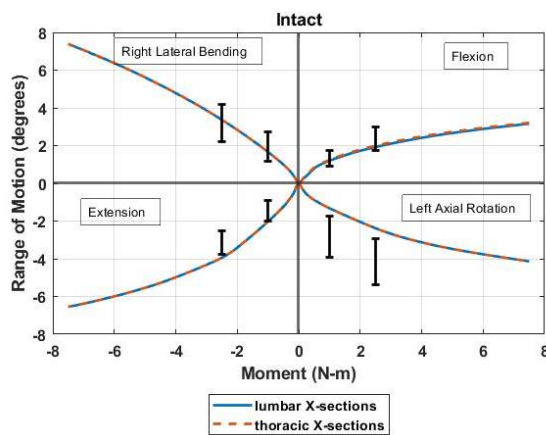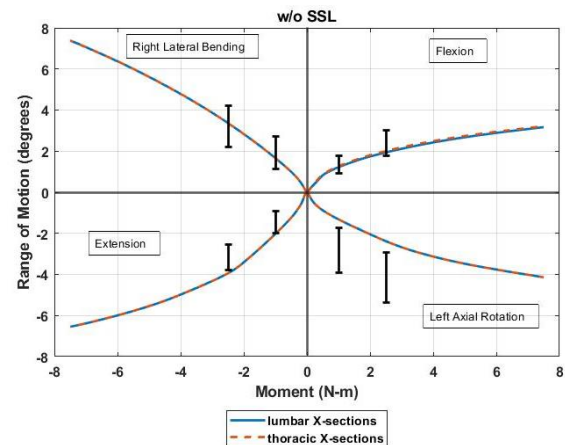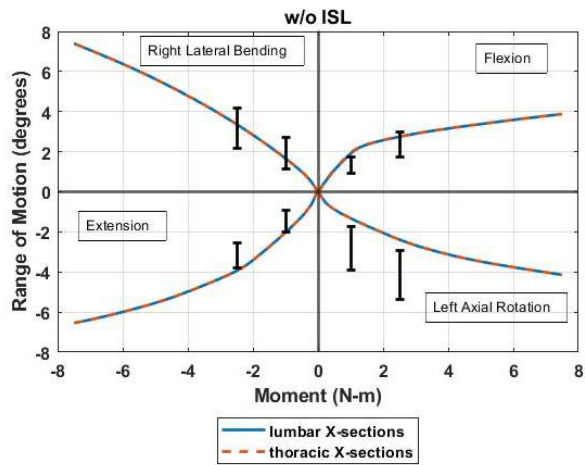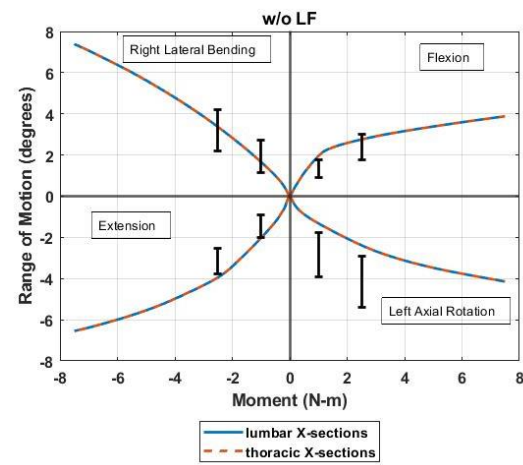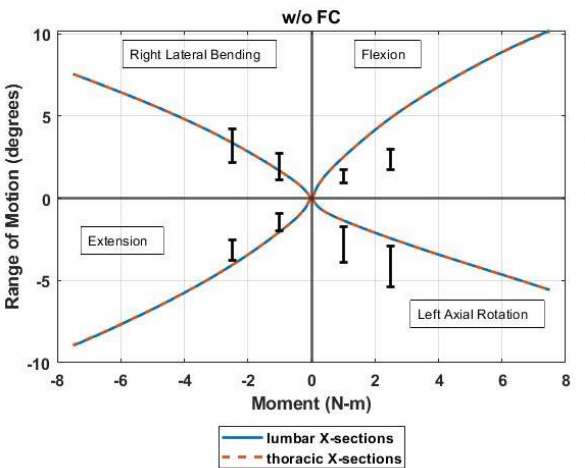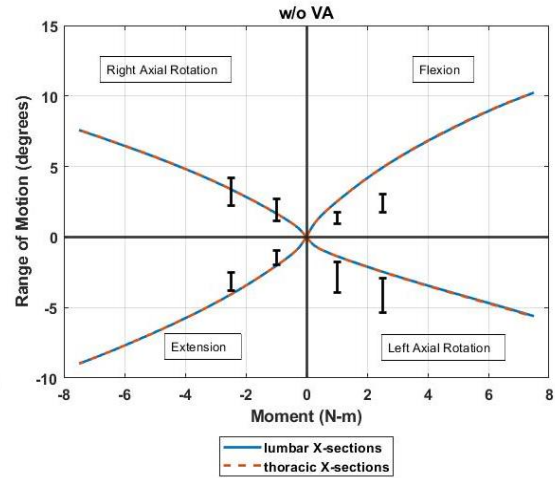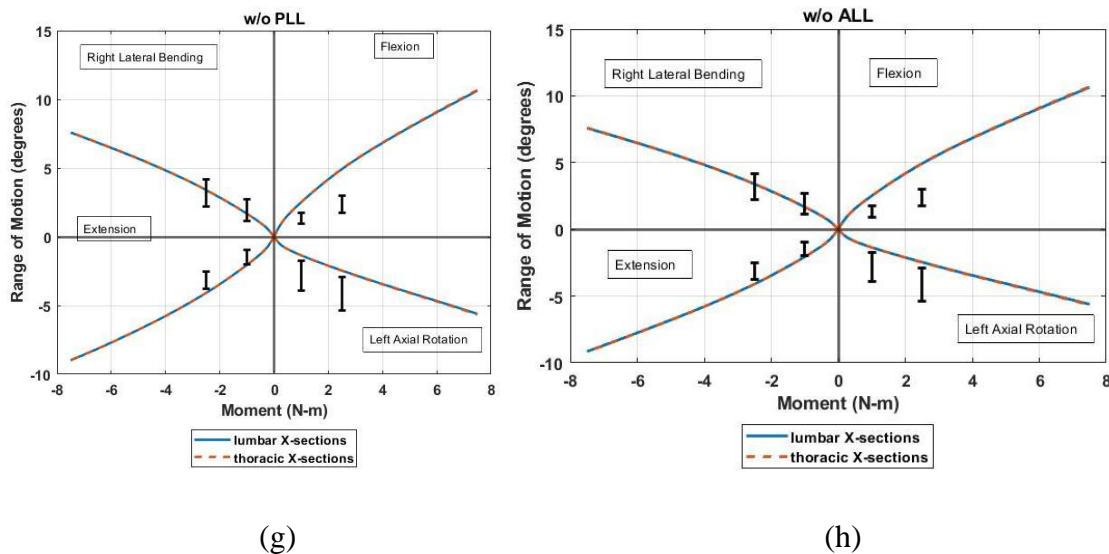
Figure 3-9: Functional unit RoM during serial removal comparing thoracic & lumbar ligament cross-sectional area scale factors. (a) Intact configuration; (b) SSL removed; (c) ISL removed; (d) LF removed; (e) FC removed; (f) VA removed; (g) PLL removed; (h) ALL removed.
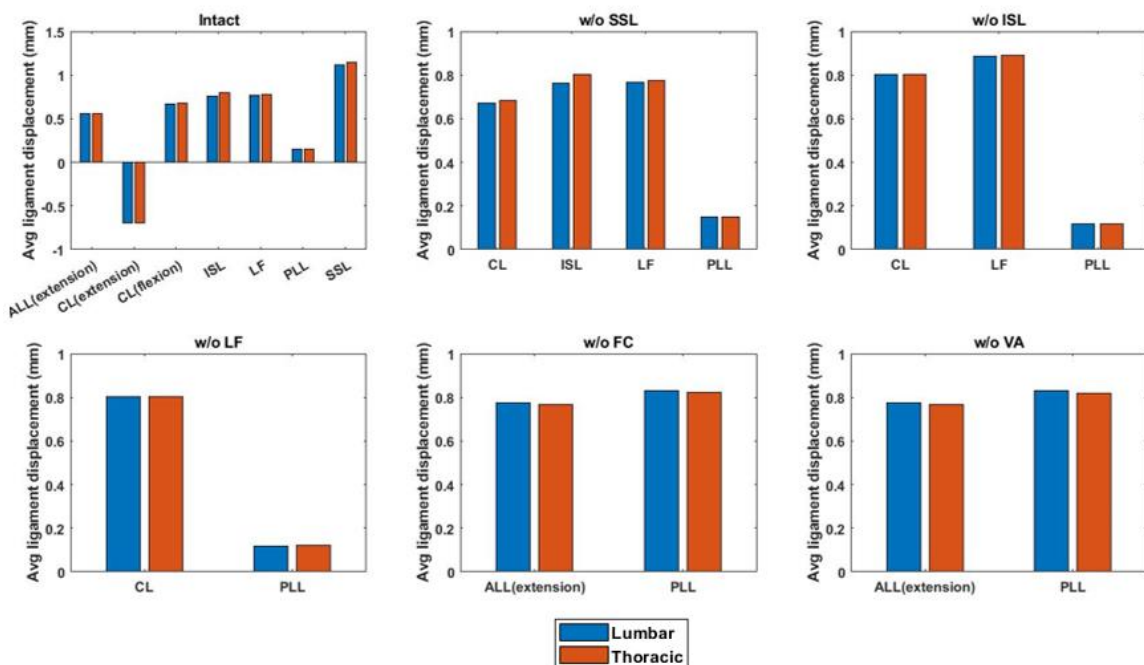
Figure 3-10: Average ligament displacements during serial removal procedure.

3.5 DISCUSSION

Kinematic behavior of a mid-thoracic FSU was assessed as a function of intervertebral ligament stiffness properties and compared with appropriate experimental data. To the authors' knowledge, a ligament property comparison for suitable use in a thoracic spine FE model has not been performed. The lack of ligament data in the literature forced a set of assumptions to be made regarding the material and geometric properties combinations utilized for the study. Only two sources examined (Chazal et al., 1985; Myklebust et al., 1988) contained quasi-static stiffness data for the thoracic spinal ligaments, with Property Set 2 being characterized linearly due to missing information regarding the toe to linear transition. Consequentially, the other property sets formulated in this study were obtained from the lumbar spine where material data are more abundant, following assumptions made in previous studies that have made use of lumbar ligament material properties for thoracic spine examination (Qiu et al., 2003; Little and Adam, 2011).

Utilizing an appropriate combination of ligament properties depends on clinical variables of interest and their comparability to experimental data for appropriate load regimes. Performing serial ligament removal through RoM assessment in an FSU, as recommended in previous publications (Heuer et al., 2007; Schmidt et al., 2007; Wilke et al., 2020), can help determine appropriate ligament properties for utilization in a model. The FSU RoM assessed from all six ligament property sets produced greater variability among the three rotations as the external moment increased, a result also seen in lumbar FE analyses (Naserkhaki et al., 2018). Greater RoM increase after facet removal, particularly in flexion, confirm their role as a stabilizer during hyperflexion and is in line

with observations seen in previous studies for the lumbar spine (Adams et al., 1980). The increases in RoM seen in lateral bending and axial rotation align with the same observation made in (Wilke et al., 2020) for the mid-thoracic FSU. Furthermore, a discontinuity in the kinematic response prior to facet removal in Property Set 3 is attributed to stiffer capsular ligament characterization; a shallower facet joint orientation in the thoracic spine relative to the lumbar spine may have contributed to the discontinuous behavior. Based on the importance of the facets as demonstrated by model kinematics, capsular ligament properties must carefully be chosen for compatibility with thoracic spine morphology.

The ICoR complements the ligament forces exerted for motion control through moment arm assessment. As a potential guide for clinical treatment, it has been recommended that for stresses and strains in an FE model to be accurately predicted, the center of rotation should not remain static and presupposed artificially (Shirazi-Adl et al., 1986; Schmidt et al., 2008; Little and Adam, 2011). By comparing with existing thoracic in-vitro data, insight is provided on how ICoR may behave as a function of ligament properties beyond an FSU and utilized within a spinal column FE model. The ligament property sets exhibiting more compliant toe regions (Property Sets 5 and 6) were within the flexion confidence ellipse established by (Panjabi et al., 1984), while sets with compliant ALL properties were within the confidence ellipse calculated for extension. The ICoR traces shift to the posterior as the external moment increased, reducing the moment arm for posterior ligaments. To the author's knowledge, the literature currently offers little information regarding ICoR in the thoracic region with CV joints; thus, the study was limited to comparing ICoR during sagittal rotations without CV joints per the

experimental conditions of (Panjabi et al., 1984). Also, ICoR is limited to planar kinematics and does not fully capture coupled rotations in three dimensions. Future work will investigate ICoR behavior in axial rotation and lateral bending as well as coupled rotation behavior along all three planes with the CV joint incorporated and intervertebral ligament properties varied.

The property sets exhibiting RoM within experimental error bounds were preferential to ligament characterization. All property sets utilized within the FSU matched experimental kinematic data to varying degrees. The onsets of the ligament toe and linear regions influenced the degree to which certain property sets matched the experimental RoM data, which produced either stiffer behavior (e.g., Property Set 3 in axial rotation) or compliant behavior (e.g., Property Set 5) relative to both the experiment and to other ligament properties evaluated. Property Set 2 contained mostly linear intervertebral ligament properties and produced relatively compliant behavior during serial ligament removal. However, the hyperelasticity of the intervertebral disc likely played a significant role in enhancing RoM response, emphasizing the importance of nonlinearity in soft tissue characterization for high load applications. This conclusion has been reported in previous studies where linear soft tissue properties were deemed valid for low load regimes in the cervical spine (Kumaresan et al., 1999) and explaining discrepancies between FE model and experimental data (Qiu et al., 2003).

This study was also the first to the authors' knowledge to compare the performance of porcine ligaments collected in-vitro with those harvested from human cadavers in an FE model utilizing human vertebrae. Porcine specimens are sometimes utilized as a suitable alternative for human clinical applications due to their

biomechanical and geometrical homogeneity (Sikoryn and Hukins, 1990), and ease of procurement relative to human cadavers. Additionally, evidence of their comparability with human RoM (Gillespie and Dickey, 2004) and similar collagen fibrous composition to human ligaments (Hukins et al., 1990) has been previously established. Their use in this study showed kinematic comparability with the FSU utilizing human data, suggesting that porcine data could be used as an acceptable substitute in the absence of human ligament data.

While ligaments are realistically three-dimensional (Weiss et al., 2005), the strain-rate dependent nature of ligaments is difficult to accurately characterize in commercial FE codes (Troyer et al., 2012). Consequentially, most clinical model studies have sufficiently simplified ligaments to one-dimensional entities. Using assumed attachments and geometric conversion factors such as unstretched length and cross-sectional area, their incorporation in this specific model led to compatibility with experimental data in most cases; however, as certain ligaments such as the PLL tend to be thicker but narrower in the thoracic spine, more complete ligament representations may have enhanced motion response kinematically, as evidenced by compliance in flexion relative to in-vitro data when the PLL was left intact (Wilke et al., 2020). Additionally, spinal flexibility is subject-specific and varies along the spinal column (White and Panjabi 1990, p. 107) likely due to key geometric features such as disc height and CV joint presence, which may affect the kinematic response influenced by specific intervertebral ligaments. Future work should investigate ligament behavior along various regions of the spine. Nonetheless, the results suggest that ligament material characteristics may be utilized regardless of the harvested spinal region with

consideration of load regimes appropriate for the spinal region of interest (Wilke et al., 1998) and appropriately scaling ligament dimensions such as cross-sectional area for the thoracic column.

Kinematic discrepancies from movements dependent on facet articulation presented a limitation to this study. Resistance was exhibited by capsular ligaments in these scenarios (e.g., extension), however, the use of a frictionless penalty contact algorithm may not sufficiently capture compression necessary to transmit loads through the facets. The latter is a common method by which facet joints have been historically modeled, where contact methods between cartilages vary greatly (Mengoni, 2021) and can affect key validation parameters such as facet forces and RoM (Zander et al., 2017). In addition, the facet joint realistically contains synovial fluid, an incompressible lubricant situated between two cartilage layers and theoretically prevents contact. To enhance facet incompressibility, its explicit modeling (Kumaresan et al., 1998) may be necessary in lieu of contact.

While an attempt was made to include the CV joint as part of this study, its absence in previous in-vitro experiments presented a challenge to the validation of key parameters. Literature has previously stated that computational models involving the thoracic spine should include the ribcage during its calibration process (Wilke et al., 2020) because of its ability to stabilize and stiffen the spine (Liebsch et al., 2020b; Mannen et al., 2015). Detailed non-linear ligament properties for the costovertebral joint are currently non-existent in the literature, thus effective linear stiffness properties supplemented by kinematic validation with in-vitro data (Aira et al., 2019; Duprey et al., 2010) were utilized. Rib section connections through the CV joint were employed in this

study to represent in-vitro thoracic specimen conditions (Wilke et al., 2017). While stiffer RoM and reduced variation were present with the inclusion of the CV joint, reinforcements are expected to become more pronounced when full rib sections are joined through costosternal connections (Liebsch et al., 2020b), representing a ribcage better and kinematically enhancing the FE model's applicability to clinical or in-vivo scenarios. As the long-term goal is to use a set of verified ligaments in tandem within the spinal column, this study represents a first step in determining the proper characterization of intervertebral ligaments based on thoracic kinematic behavior for future model studies incorporating surgical planning.

3.6 CONCLUSION

The study presented shows how various ligament stiffness properties may be utilized to adapt to finite element models of the human thoracic spine. Since ligament properties are scarce in the literature, assumptions related to the source and geometric parameters of each ligament group to derive property sets were utilized and their effect on functional unit kinematic behavior assessed. The key findings include: the utilization of ligament properties previously configured for use outside the human thoracic spine leads to favorable kinematic comparisons when assessing both RoM and ICoR. In addition, to utilize an appropriate set of properties, one must understand the physiological ranges of motion that specific spinal joints will undergo as they will influence the load regimes excised in various ligament groups. Most importantly, the user must consider the condition (e.g., healthy, symptomatic, etc) and demographics of the spine, such as the age, gender, and the species (e.g., human or animal) to decide the ligament properties most appropriate for their clinical studies.

CHAPTER 4

LOAD SHARING ASSESSMENT OF OSSEOLIGAMENTOUS STRUCTURES WITHIN A THORACIC SPINE SEGMENT DURING SURGICAL RELEASE

4.1 ABSTRACT

Spinal surgical procedures often require release of intervertebral discs and ligaments to optimally achieve postural correction on a patient-specific basis. In this paper, a T7-T8 Finite Element (FE) model is utilized to examine internal load sharing during resection steps performed in a Ponte osteotomy. The FE model was rotated bidirectionally along three anatomical planes using an externally applied moment. In each step, the Ranges of Motion (RoM), Instantaneous Centers of Rotation (ICR), and forces from ligaments, discs, facet, and costovertebral joints were calculated. The product of each component's force and the distance between the ICR and their position were used to calculate percent load sharing at the maximum moment magnitude. Removal of the facet joints accounts for overall significant increases in load sharing to the intervertebral disc, with maximum values reported in extension by approximately 18% and axial rotation by 16%. This study highlights key spine components whose kinematic influence may be considered to achieve desired surgical outcomes.

4.2 INTRODUCTION

Adolescent Idiopathic Scoliosis (AIS) is a three-dimensional deformity of the spine that affects approximately 2.5% of patients aged 10-18; approximately 10% of those patients will require surgical intervention to prevent progression of the deformity (Asher and Burton, 2006). Release procedures for spinal correction traditionally require

the removal of osseoligamentous (bone and ligaments) anatomy to achieve sufficient correction. The sequential steps that a surgeon performs for spinal correction and fusion depend upon experience level (Majdouline et al., 2009), the deformity profile and apex location (Lenke et al., 2003), and curve flexibility, which is influenced by soft tissue and vertebral morphology (He and Wong, 2018; Little and Adam, 2011a). Historically, anterior-based releases of the spinal column were done to help achieve correction. However, posterior-based spinal surgery has allowed for improved 3-column correction of the spine with procedures such as the Ponte osteotomy (Samdani et al., 2015).

In-vitro experiments that serially remove ligaments, facets (Heuer et al., 2007; Wilke et al., 2020), ribs, and costovertebral (CV) joints (Oda et al., 2002; Liebsch and Wilke, 2020) offer insight into spinal kinematics. However, experimental results do not provide information on load distribution changes within the spine following component removal. A load distribution assessment through Finite Element (FE) modeling may help surgeons understand how soft tissue components behave after serial release or vertebral fusions and could lead to improved patient outcomes. FE models of the spinal column have been utilized as a powerful non-invasive tool to answer surgical-based questions regarding scoliosis (Wang et al., 2014). Additionally, FE models can examine the biomechanical effects of non-surgical treatment options and surgical steps prior to implementation (Lafon et al., 2010; Vergari et al., 2015; Viviani et al., 1986).

Load distribution through FE analysis has been used to understand the role of ligaments and facets on rotational stability of the lumbar spine (Sharma et al., 1995) and the cervical spine (Panzer and Cronin, 2009) during release. Additionally, static equilibrium equations have been used to quantify and assess sagittal load sharing among

osseoligamentous entities in an intact lumbosacral spine (Naserkhaki et al., 2016). Yet, little is presently known about the load distribution of the thoracic spine during motion. The thoracic column is a common site for hyperkyphotic and scoliotic deformity and, because of the connections of the ribs to vertebrae via CV joints, this area of the spine is provided reinforcement and stability not seen in the cervical and lumbar regions. Kinematic and load distribution behavior of the thoracic column could be altered during component release. A study by Little and Adam (2011b) previously explored the effect of CV joint incorporation on the load distribution of posterior ligaments within a thoracic functional unit. However, their study was primarily guided by validating their FE model with in-vitro experimental data (Oda et al., 2002), focusing on anterior release procedures and fixing the axis of rotation about the mid-column according to experimental conditions.

As previously recommended (Little and Adam 2011b), loading must take place at an Instantaneous Center of Rotation (ICR) to accurately represent physiological joint motion as well as predict load distribution and deformations about the spinal column (Schmidt et al., 2008; Shirazi-Adl et al., 1986). In addition, the ICR may guide appropriate clinical treatments for symptomatic patients when used to assess spinal motion quality (Lee et al., 1997) and diagnose pathological abnormalities (Bogduk et al., 1995). The following study examines the effect of load distribution within the osseoligamentous components of a thoracic functional unit during posterior release and as a function of ICR.

4.3 METHODS

4.3.1 FE MODEL PREPARATION

A T7-T8 FE model (Figure 4-1a) was constructed from an anatomist-drawn computer aided design (CAD)-based spine model whose morphology is representative of an asymptomatic adult (CGHero Ltd., Manchester, UK). The T7-T8 segment was tessellated using Hypermesh (Altair Engineering, Troy, MI, USA). Both vertebrae consisted of superior and inferior endplates, represented by quadrilateral elements, cortical bone, represented by quadrilateral and triangular elements, and cancellous bone, represented by hexahedral elements. Both the vertebral arch and spinous process, which are connected posteriorly to the cancellous bone, were represented using tetrahedral elements. Material properties for all components were acquired from literature (Table 4-1). The intervertebral disc (IVD) components (Figure 4-1b), the annulus fibrosus and nucleus pulposus, were both represented using hexahedral elements. The transverse cross-sectional area and the volume of the nucleus pulposus relative to the intervertebral disc were approximately 37% and 40%, respectively. Complete dimensions can be found in Table 4-2. Fibers within the annulus fibrosus were represented using cables and configured such that their total volume equated to approximately 16% of the ground substance; geometric and material property scale factors for the fibers were configured (Shirazi-Adl et al., 1986) for the IVD containing 8 radial layers and 3 layers through the thickness. A frictionless penalty contact algorithm was employed to represent the facet capsule, using contact thickness values to facilitate a 0.5mm initial gap between superior and inferior facet processes. This algorithm was also employed on rib sections to

represent contact between the rib and the functional unit, facilitated by null contact elements over the ribs. In total, the FE model contains 34,990 elements and 15,944 nodes.

Seven intervertebral ligament groups (Table 4-3) were included within the functional unit configuration. Each ligament group's force-displacement properties (Figure 4-2) were derived from stress-strain curves by respectively using the cross-sectional area and the initial ligament lengths as scale factors. Cross-sectional areas documented for the mid-thoracic region were averaged and utilized for all ligaments; a cross-sectional area for the lumbar region was assumed for the capsular ligament due to absent data. The CV joint was also incorporated to bilaterally connect 3cm of rib to the functional unit. The CV joint consisted of two separate joint groups (Figure 4-1c): the Costocentral joint (CCJ), consisting of the Intra-articular and Radiate ligaments, which connect the rib head to the spinal column, and the Costotransverse joint (CTV), consisting of the Lateral Costotransverse, Superior Costotransverse and Costotransverse ligaments, which connect the ribs to adjacent transverse processes. Properties utilized are listed in Table 4-4.

4.3.2 ANALYSIS PROCEDURES

Quasi-static analyses on the functional unit were performed using LS-DYNA implicit SMP Version 971 R10.1 (Livermore Software Technology, Livermore, CA, USA). To validate the ligament property set utilized in this study, a stepwise ligament removal procedure was first simulated on the functional unit based on the experimental conditions from Wilke et al., (2020). Throughout the procedure, the unit was rotated in flexion, extension, right lateral bending, and left axial rotation. By including only one

half of rotations in the coronal and axial planes, symmetry behavior was assumed. Range of Motion (RoM) data during each step was collected from the T7 superior endplate using a local coordinate system set up per the Scoliosis Research Society recommendations (Stokes, 1994). A pure moment of ±2.5 N-m and no preload was employed for all cases. The T8 inferior endplate and facet processes were fixed. Per the experiment, the following configurations were analyzed sequentially: Intact, Supraspinous Ligament (SSL) removal, Interspinous Ligament (ISL) removal, Ligamentum Flavum (LF) removal, and Facet Joint (FJ) removal. The Facet Joint (FJ) in this manuscript refers to the capsular ligament and facet capsule combined. Based on specimen conditions during experimentation, the CV joint and ITL were excluded from this procedure. CV joint kinematics were previously validated (Polanco et al., 2021) in comparison with in-vitro data (Duprey et al., 2010; Lemosse et al., 1998).

Next, the resection procedure consistent with a Ponte osteotomy was implemented onto the functional unit model. Per the standard recommended moments to be applied to thoracic spine segments in-vitro (Wilke et al., 1998), a ±5 N-m pure moment with no preload was applied over the superior T7 endplate. The unit was rotated in flexion, extension, left and right lateral bending, and left and right axial rotation. For each rotation direction, five different configurations were assessed to represent the steps of the Ponte osteotomy as follows (Figure 4-3):

(1) all spine components intact,

(2) removal of the interspinous and supraspinous ligaments,

(3) bilateral inferior facetectomy,

(4) removal of the ligamentum flavum, and

(5) completion of the osteotomy across the superior facet.

During each analysis, the following assumptions were made: approximately two-thirds of each facet surface and all capsular ligaments were symmetrically removed by the bilateral inferior facetectomy. Secondly, because ligaments primarily control rotational behavior of the functional unit, bones serving as ligament attachments were not removed during each step of the osteotomy. Finally, as with the previous study, the T8 inferior endplate and facet processes were fixed. In each step, the RoM was calculated using vector projection along the superior endplate. The ICR trace along the rotational plane was calculated based on the perpendicular bisector method (Pearcy and Bogduk 1998). The ICR location (Figure 4) was used to find the moment arm for each spinal component and was multiplied by forces calculated in the analyses for all ligaments, intervertebral discs, and joints. Using Equation 1, rotational equilibrium was assumed in all cases to calculate the moment distribution for each component about the ICR. The moment distributions were calculated as percentages of the externally applied moment. Ligament, disc, and facet force information were also calculated.

$$\sum M_{ICR} = \overrightarrow{External\ Moment} + \sum\left(\overrightarrow{r_{(ICR-Ligament\ Position)}} \times \overrightarrow{Ligament\ Forces}\right) +$$

$$\sum\left(\overrightarrow{r_{(ICR-Joint\ Position)}} \times \overrightarrow{Joint\ Forces}\right) + \overrightarrow{Disc\ Moment} = 0$$

(Equation 4-1)

Table 4-1: Vertebral and Intervertebral disc material properties.

Spinal Component	Material Property	Source
Cortical Bone	E=12 GPa, v=0.3	Naserkhaki et al., 2018
Cancellous Bone	E=200 MPa, v=0.315	Naserkhaki et al., 2018
Endplate	E=23.8 MPa, v=0.4, 1mm thickness	Schmidt et al., 2006
Annulus Fibrosus	C10=0.18 MPa, C01=0.045 MPa, v=0.45 Mooney-Rivlin	Schmidt et al., 2006
Nucleus Pulposus	C10=0.12 MPa, C01=0.03 MPa, v=0.499, Mooney-Rivlin	Schmidt et al., 2006
Annulus Fibers	Nonlinear Stress-Strain curve, all material and geometric scale factors adjusted based on layer position	Shirazi-Adl et al., 1986

Table 4-2: Intervertebral Disc dimensions.

Anterior (mm)	Center (mm)	Posterior (mm)	Nucleus Pulposus Cross-Sectional Area (mm^2)	Nucleus Pulposus Volume (mm^3)	Transverse Disc Cross-Sectional Area (mm^2)	Disc Volume (mm^3)
5.9	6.9	4.8	352	1242	1049.5	3073

Table 4-3: Average model ligament lengths and cross-sectional areas.

Spinal Component	Average Length (mm)	Average Cross-Sectional Areas (mm^2)	Source
Anterior Longitudinal Ligament (ALL)	5.36	30	Chazal et al., 1985
Posterior Longitudinal Ligament (PLL)	4.929	17	Chazal et al., 1985
Ligamentum Flavum (LF)	24.832	26.7	Chazal et al., 1985

Table 4-3 continued.

Interspinous Ligament (ISL)	5.541	30	Chazal et al., 1985
Supraspinous Ligament (SSL)	25.588	30	Chazal et al., 1985
Capsular Ligament (CL)	2.799 (over both sides)	36	Shirazi-Adl et al., 1986
Intertransverse Ligament (ITL)	18.359 (over both sides)	1.85	Chazal et al., 1985

Table 4-4: Costovertebral Joint Properties.

Spinal Component	Material Property	Source
Lateral Costotransverse Ligament (LCTL)	Keff=126.5 N/mm	Aira et al., 2019
Superior Costotransverse Ligament (SCTL)	Keff=90.2 N/mm	Aira et al., 2019
Costotransverse Ligament (CTL)	Keff=54.9 N/mm	Aira et al., 2019
Radiate Ligament	A=10mm^2, E=42.1 MPa	Aira et al., 2019; Jiang et al., 1994
Intra-articular Ligament	Keff=20.9 N/mm	Aira et al., 2019

(a)   (b)

(c)

Figure 4-1: (a) T7-T8 Finite element model; (b) Intervertebral Disc with cross-section view; (c) Transparent axial view with ligaments and joints labeled.
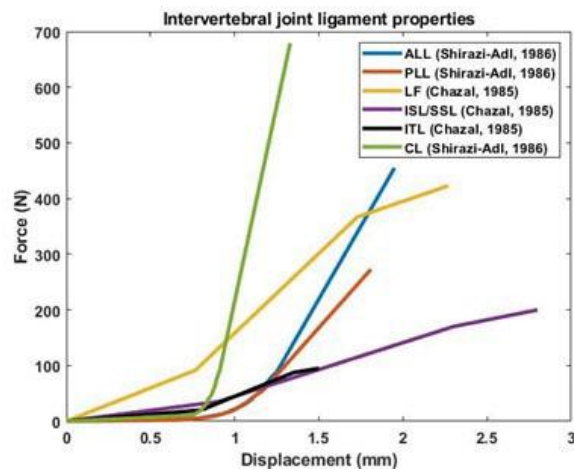
Figure 4-2: Ligament stiffness curves and their sources.
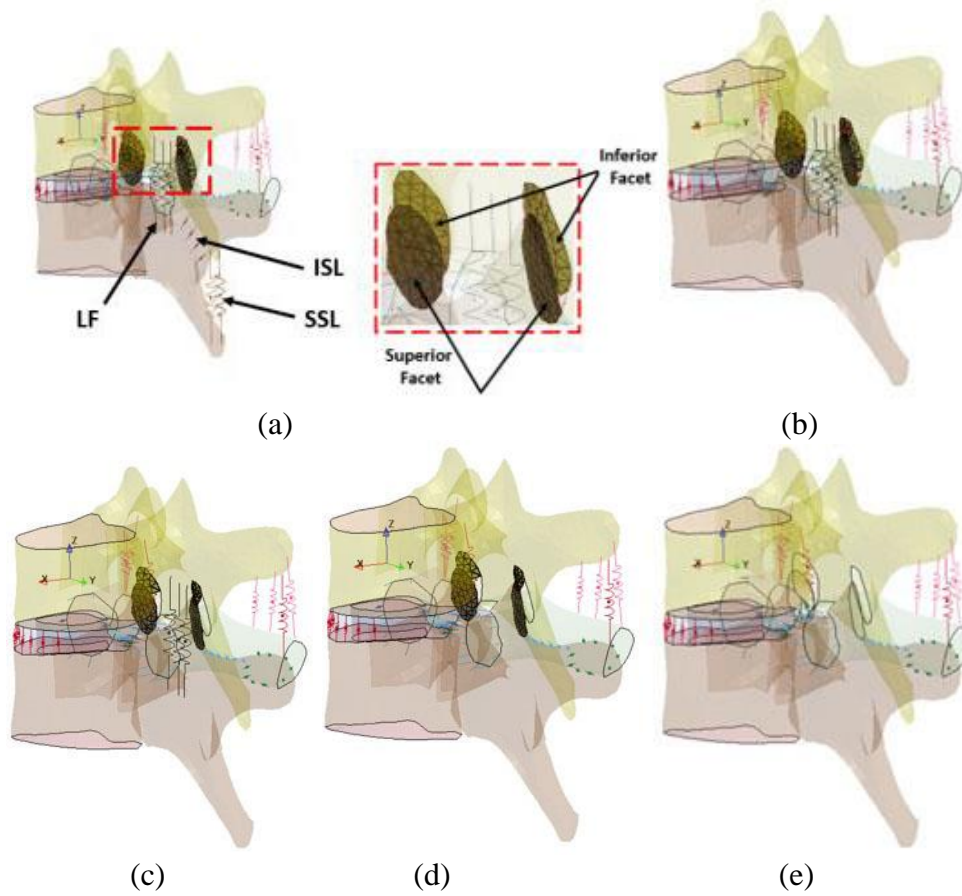
Figure 4-3: The five model configurations corresponding to the steps of a Ponte osteotomy: (a) Step 1: An intact configuration. Components removed in subsequent steps are labeled; (b) Step 2: Removal of the Spinous Ligaments (SSL and ISL); (c) Step 3: Bilateral inferior facetectomy; (d) Step 4: Ligamentum Flavum (LF) removal; (e) Step 5: Bilateral superior facetectomy.
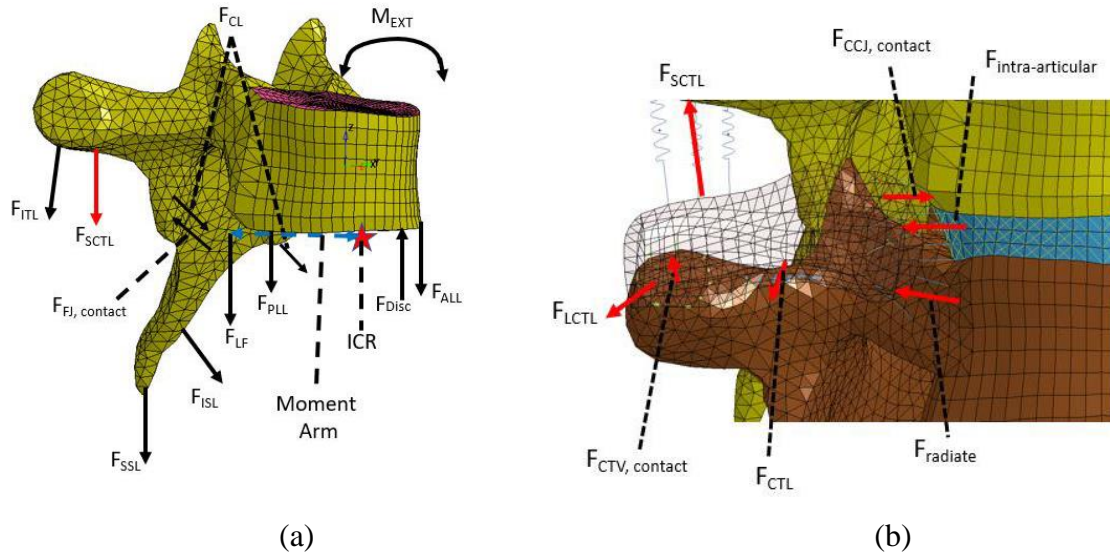
Figure 4-4: (a) Free-body diagram of intervertebral spine components with moment arm; (b) Free-body diagram of CV joint components (red arrow depiction).

4.4 RESULTS

4.4.1 FE MODEL VALIDATION-STEPWISE LIGAMENT REMOVAL

The largest increases in RoM relative to the preceding removal step (Figure 5) come after both the ligamentum flavum and the facet joint are removed in flexion, respectively at approximately 154% and 28% at 1 N-m and 50% and 77% at 2.5 N-m. Negligible increases in overall RoM were seen within removal steps exercised in extension, right lateral bending, and left axial rotation; the maximum was 3.7% after facet removal in extension. The extension modes were compliant compared to the experimental data; however, most of the ligament removal steps in flexion, right lateral bending and left axial rotation were within range of the data highlighted from the experiment. Since most of the RoM data was within range of the experimental data, the ligament properties were deemed acceptable for further use.
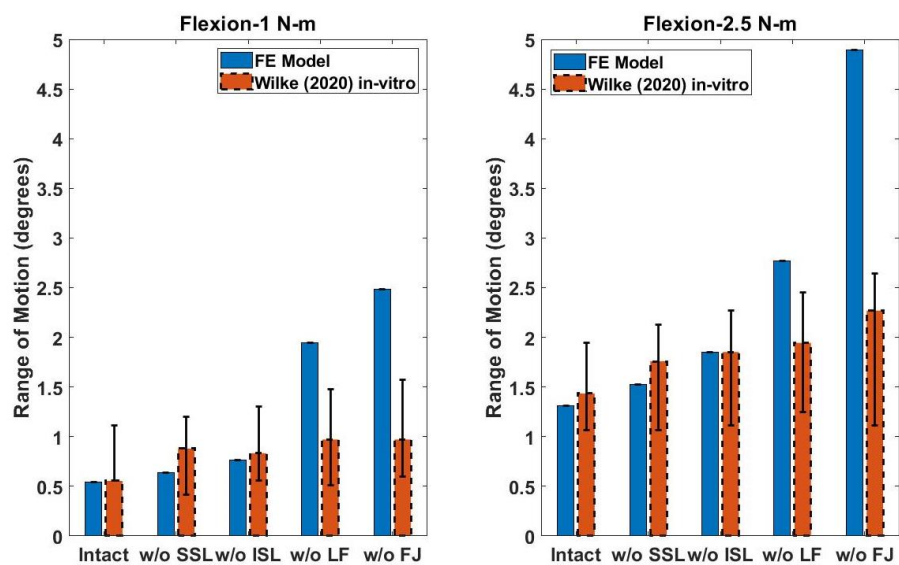
(a)
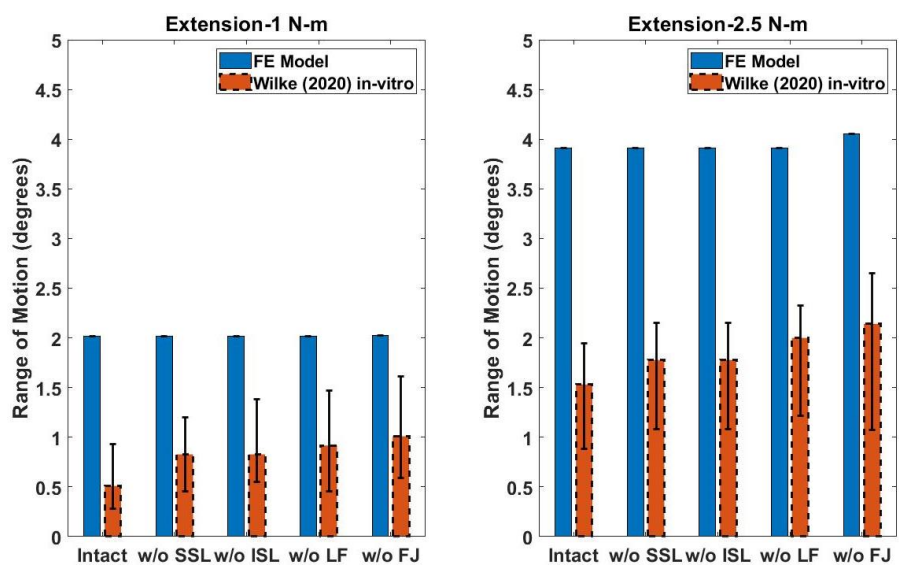
(b)
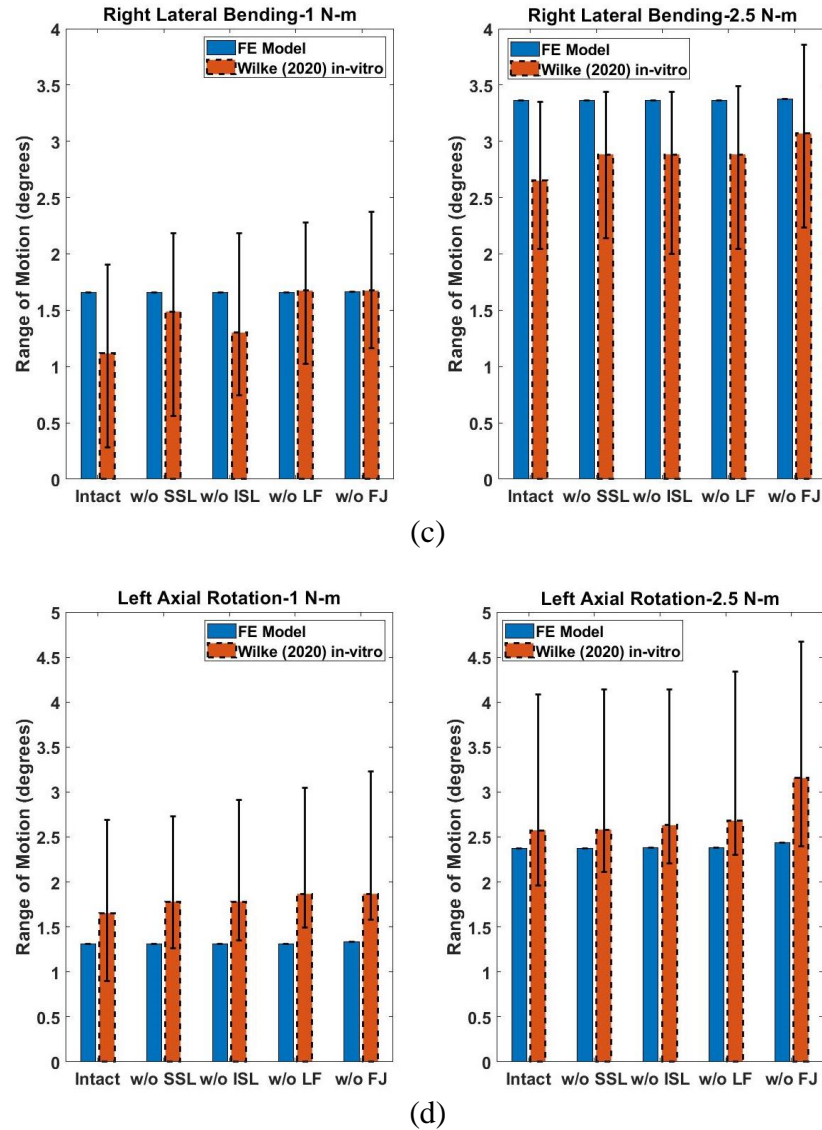
Figure 4-5: Stepwise ligament removal. (a) Flexion; (b) Extension; (c) Right Lateral Bending; (d) Left Axial Rotation.

4.4.2 RoM AND ICR KINEMATIC ASSESSMENT

Next, the functional unit with both the ITL and the CV joint incorporated were rotated along the three anatomical planes. To check the validity of the RoM data, the flexibility coefficient (ratio of rotation to applied moment) for all rotations were calculated for the intact configuration at the applied moment of 5 N-m. The coefficients

(Figure 6a) derived from the FE model were approximately 0.52 and 1.04 for flexion and extension, 0.69 for both left and right axial rotation, and 0.877 and 0.872 for left and right lateral bending respectively. Compared to the average coefficients reported (Panjabi and White 1976), the extension, lateral bending, and left axial rotations exhibit compliance, while the right axial rotation and flexion modes respectively match or exhibit slightly stiffer behavior.

The RoM (Figures 4-6b-4-6d) increase during serial ligament removal in flexion amounted to approximately 18%, 1.4%, and 11.9% for the spinous ligament, bilateral inferior facetectomy, and ligamentum flavum removal stages, respectively. No change was seen after the bilateral superior facetectomy was conducted. After the inferior facets were removed, RoM increased in extension by 16%, in left axial rotation by 12.1%, in right axial rotation by 10.7% and in left lateral bending by 2.5%. Following the bilateral superior facetectomy, a 0.8% increase in RoM was seen in right lateral bending. When the superior facets were removed, the RoM overall showed no more than a 1.5% increase; the maximum increase took place in right axial rotation.

In flexion (Figure 4-7a), at the maximum applied moment, the removal of the spinous ligaments shifts the ICR anteriorly by 0.97mm and superiorly by 3.72mm. In the same circumstance, after the bilateral inferior facetectomy, the ICR is shifted anteriorly by 0.27mm and superiorly by 1.14mm. After the ligamentum flavum is removed, the ICR shifts 2mm anteriorly and 0.82mm superiorly. No changes were seen after the bilateral superior facetectomy. In extension after the bilateral inferior facetectomy, anterior and inferior ICR shifts of 0.11mm and 0.71mm were respectively observed. In extension after the bilateral superior facetectomy, superior direction ICR shifts of 0.23mm were

observed; a negligible shift in the anterior direction was observed. The ICR position in left and right lateral bending (Figure 7b) overall see a negligible shift upon all steps and directions in ligament removal (less than 0.1mm). In left and right axial rotation (Figure 4-7c), the ICR experiences a 0.23mm shift in the medial and lateral directions, respectively, after spinous ligament removal. After the bilateral inferior facetectomy is simulated, a shift occurs by 0.17mm laterally and 0.65mm anteriorly in left axial rotation, and 0.13mm medially and 1mm anteriorly in right axial rotation. After the bilateral superior facetectomy is simulated; a shift of 0.24mm and 0.09mm respectively occur medially and anteriorly in left axial rotation, and a shift of 1.49mm and 0.63mm respectively occur medially and anteriorly in right axial rotation.

(a)

(b)

(c)   (d)
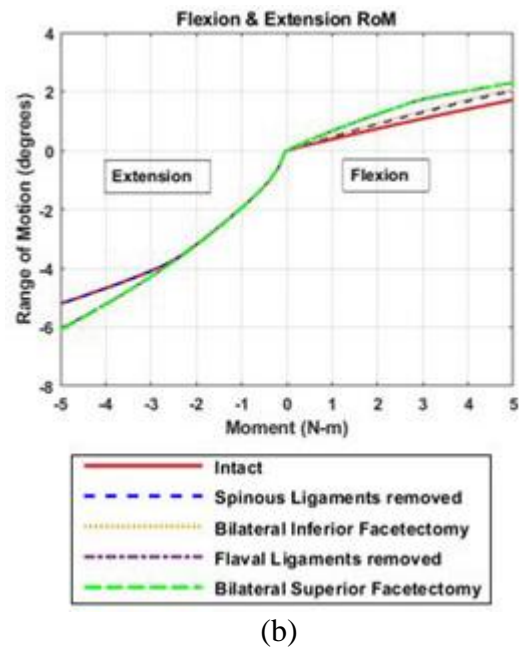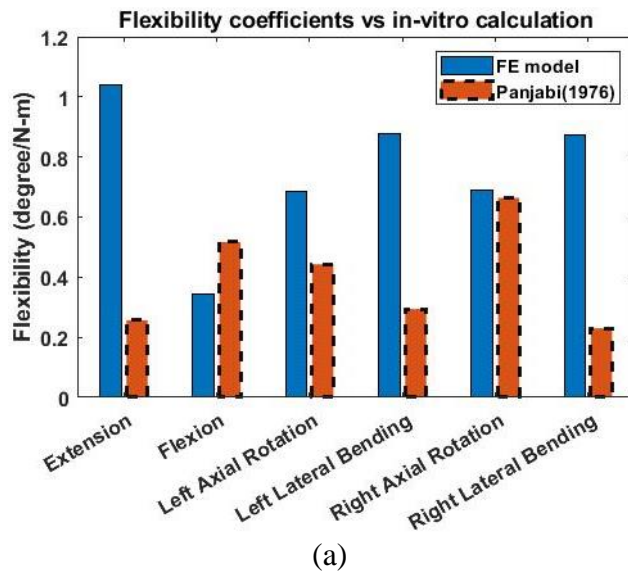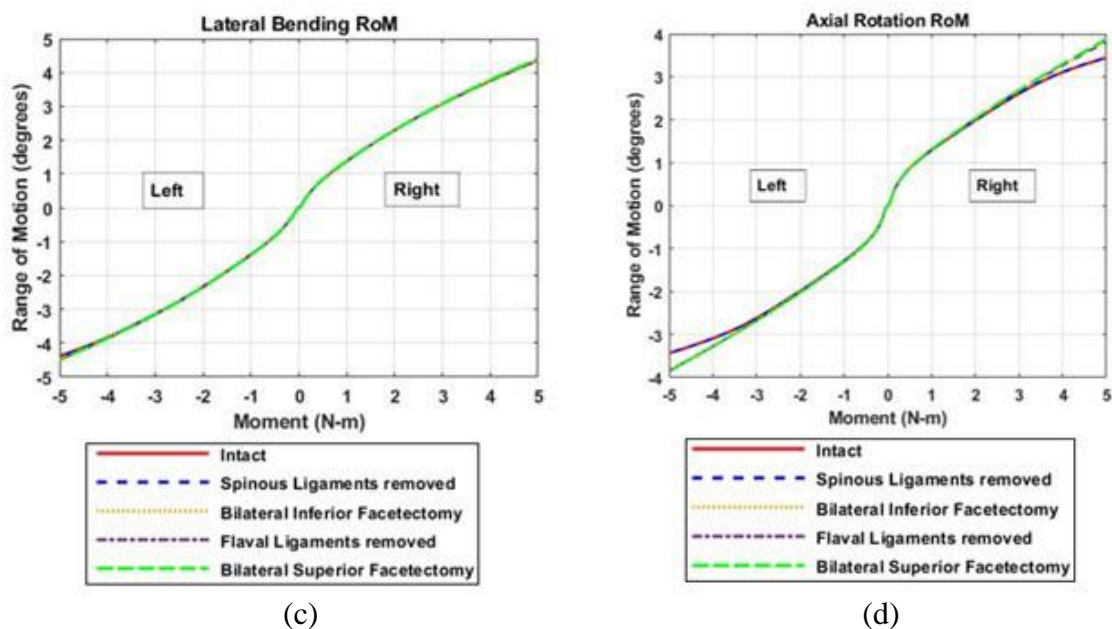
Figure 4-6: (a) Compliance coefficients for intact functional unit compared with Panjabi (1976); (b) Flexion-Extension RoM; (c) Left-Right Lateral Bending RoM; (d) Left-Right Axial Rotation RoM.

(a)

(b)

(c)
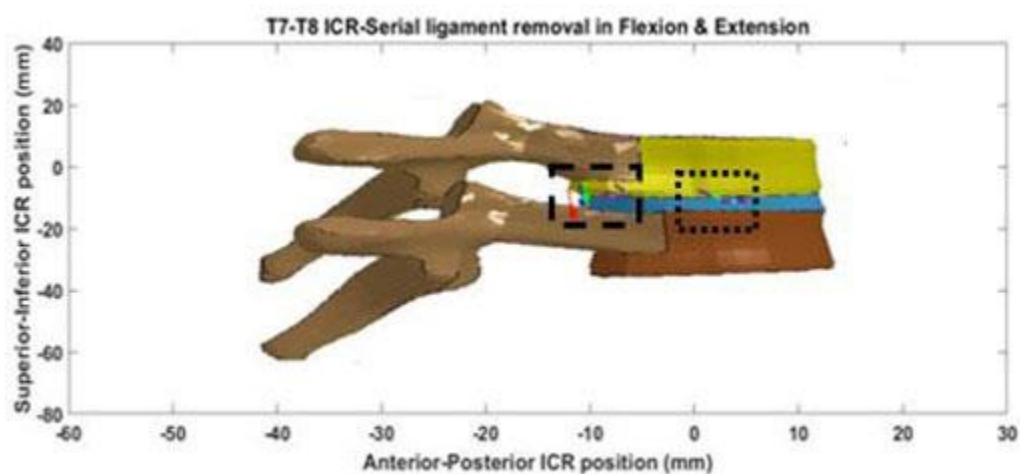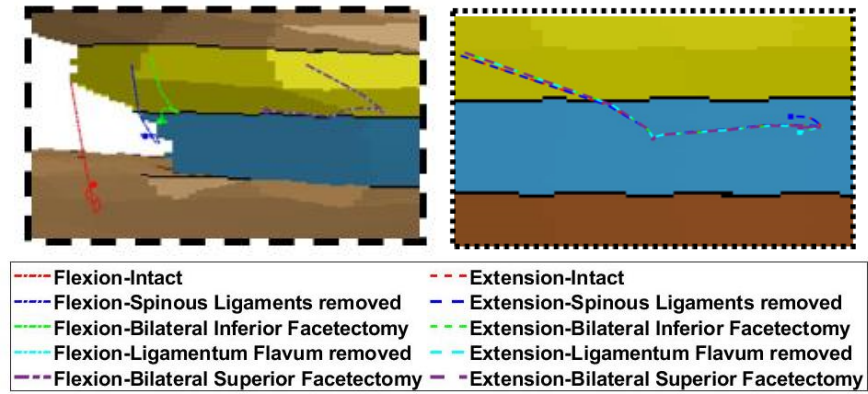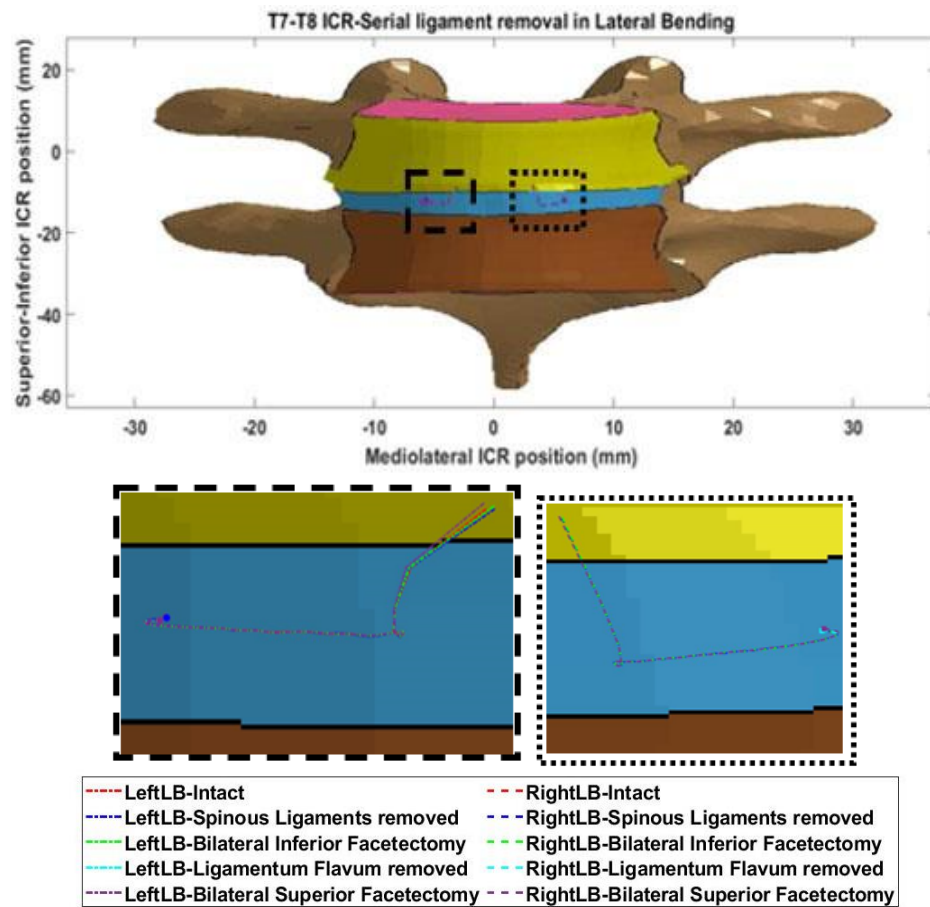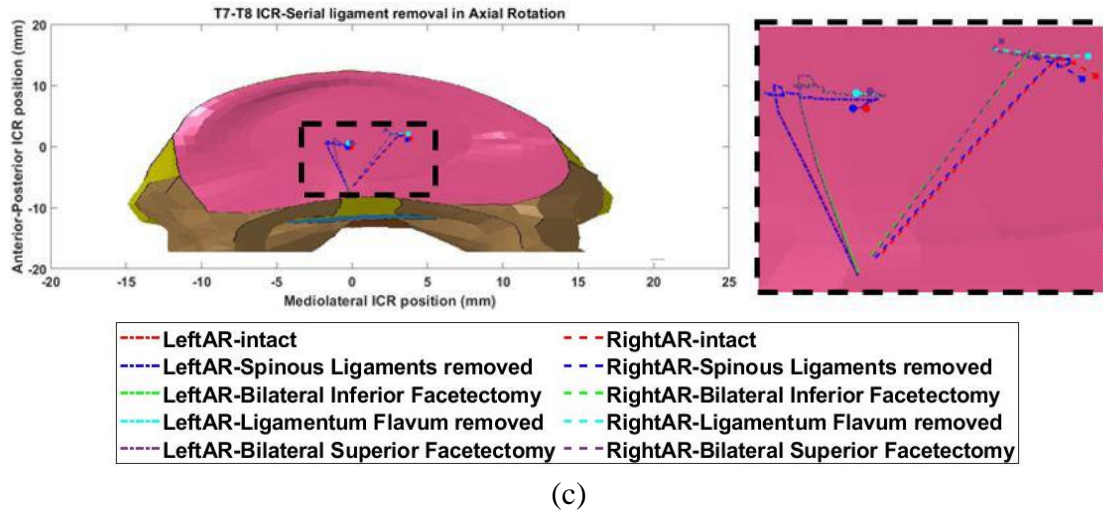
Figure 4-7: ICR traces with solid markers depicting the rotation center at maximum load. (a) Flexion-Extension; (b) Left-Right Lateral Bending; (c) Left-Right Axial Rotation.

4.4.3 FUNCTIONAL UNIT LOAD DISTRIBUTION

4.4.3.1 FLEXION AND EXTENSION

In flexion (Table 4-5), 56% of the total load is initially borne by posterior ligaments, however, approximately 76% of the total load at the maximally applied moment were carried by the IVD, ITL, and the LF, at approximately 44%, 17%, and 16% load distribution respectively; the spinous ligaments bore approximately 18%. When the spinous ligaments were removed, the total load distribution among the 3 components accounted for approximately 92% of the total load. The largest overall increase in load distribution occurred when the ligamentum flavum was removed, leading to a 19.4% increase in the amount of load borne by the intertransverse ligament.

In extension, approximately 88% of the total load at maximum applied moment is borne by the facet joint and intervertebral disc. However, load redistribution is only seen when the bilateral inferior and superior facetectomies are conducted, increasing by

approximately 17% and 0.5% respectively within the intervertebral disc; meanwhile, load distribution in the facets drop respectively by 21% and 0.4%. The CCJ and CTV showed an increase of approximately 1.6% and 2.4%, respectively, in load distribution after the bilateral inferior facetectomy was conducted. The absence of compression stiffness within both spinous ligaments and the ligamentum flavum create negligible change in the load distribution following removal. Sagittal ligament force counterparts at each removal stage are listed in Table 4-6.

Table 4-5: Load distribution percent by spine component at maximum sagittal moment (5 N-m).

		ALL	CCJ	CTV	FJ	IVD	ITL	LF	ISL	SSL	PLL
Intact	Flexion	0	0.05	4.2	1.9	43.9	16.7	15.6	8.6	9.1	0
	Extension	0.42	4.2	7.5	22.2	65.7	0	0	0	0	0
ISL & SSL removed	Flexion	0	0.62	4.7	3.2	48.6	22.1	20.8	0	0	0
	Extension	0.42	4.2	7.5	22.2	65.6	0	0	0	0	0
Bilateral Inferior Facetectomy	Flexion	0	1	4.6	0	48.5	24.1	21.8	0	0	0
	Extension	0.47	5.8	9.9	0.4	83.5	0	0	0	0	0
LF removed	Flexion	0	1.4	5.8	0	47.3	45.5	0	0	0	0
	Extension	0.47	5.8	9.9	0.4	83.5	0	0	0	0	0
Bilateral Superior Facetectomy	Flexion	0	1.5	5.8	0	47.3	45.5	0	0	0	0
	Extension	0.47	5.7	10.0	0	83.8	0	0	0	0	0

Table 4-6: Ligament forces (Newtons) calculated at maximum sagittal moment (5 N-m).

		ALL	CCJ	CTV	FJ	ITL	LF	ISL	SSL	PLL
Intact	Flexion	0	6.6	11.3	6.5	33.5	48.8	14.2	13.4	0
	Extension	3.5	14.2	11.8	37.1	0	0	0	0	0
ISL & SSL removed	Flexion	0	9.3	12.9	10.3	43.3	62.9	0	0	0
	Extension	3.5	14.2	12	37.1	0	0	0	0	0
Bilateral Inferior Facetectomy	Flexion	0	11.6	12.9	0	46.9	65.2	0	0	0
	Extension	4	20.1	15.7	9.7	0	0	0	0	0
LF removed	Flexion	0	12.7	15.9	0	82.4	0	0	0	0
	Extension	4	20.1	15.7	9.7	0	0	0	0	0
Bilateral Superior Facetectomy	Flexion	0	13	15.9	0	82.4	0	0	0	0
	Extension	4	19.6	15.8	0	0	0	0	0	0

4.4.3.2 LEFT AND RIGHT LATERAL BENDING

In left lateral bending (Table 4-7), approximately 79% of the load distribution is borne by the IVD intact and experiences an increase in load bearing to approximately 82% after the bilateral inferior facetectomy is conducted, due to the left facet bearing only 2.5% of the total load prior to removal. Negligible load by the facet is borne during subsequent steps. The right ITL bears approximately 7.6% of total load with negligible distribution change during release. In right lateral bending, the IVD bears approximately 70% of the load distribution intact and increases by approximately 3% after the bilateral superior facetectomy is simulated. The left ITL bears approximately 6% of total load and negligibly changes throughout release. Load borne by the right CCJ bears approximately 12-13%, driven by contact between the rib head and T7. The distributions of the other CV joint components are not as variable between left and right lateral bending, bearing less than 7% total load overall. Coronal ligament force counterparts at each removal stage are listed in Table 4-8.

Table 4-7: Load distribution percent by spine component at maximum coronal moment (5 N-m).

		CCJ-Left	CCJ-Right	CTV-Left	CTV-Right	FJ-Left	FJ-Right	ITL-Left	ITL-Right	IVD
Intact	Left	2.8	0.47	3.6	3.5	2.5	0	0	7.6	79.4
	Right	0.28	12.6	2.5	6.8	0	1.4	6.2	0	70.2
ISL & SSL removed	Left	2.8	0.47	3.7	3.5	2.5	0	0	7.6	79.4
	Right	0.28	12.6	2.5	6.8	0	1.4	6.2	0	70.2
Bilateral Inferior Facetectomy	Left	3.1	0.44	4.1	3.4	0	0	0	7.2	81.6
	Right	0.28	12.6	2.5	6.8	0	1.4	6.2	0	70.2
LF removed	Left	3.1	0.44	4.1	3.4	0	0	0	7.2	81.6
	Right	0.28	12.6	2.5	6.8	0	1.4	6.2	0	70.1
Bilateral Superior Facetectomy	Left	3.1	0.44	4.1	3.4	0	0	0	7.2	81.6
	Right	0.32	11.7	2.6	6.3	0	0	6.1	0	73.1

Table 4-8: Ligament forces (Newtons) calculated at maximum sagittal moment (5 N-m).

		CCJ-Left	CCJ-Right	CTV-Left	CTV-Right	FJ-Left	FJ-Right	ITL-Left	ITL-Right
Intact	Left	6.9	4.3	4.9	8.4	7.6	0	0	16.1
	Right	2.3	32.7	5.3	9.7	0	5.1	13	0
ISL & SSL removed	Left	6.9	4.3	4.9	8.4	7.6	0	0	16.1
	Right	2.3	32.7	5.3	9.7	0	5.1	13	0
Bilateral Inferior Facetectomy	Left	7.8	4.1	5.6	8.1	0	0	0	15.3
	Right	2.3	32.6	5.3	9.7	0	5.1	13	0
LF removed	Left	7.8	4.1	5.6	8.1	0	0	0	15.3
	Right	2.3	32.7	5.3	9.7	0	5.1	13	0
Bilateral Superior Facetectomy	Left	7.8	4.1	5.6	8.1	0	0	0	15.3
	Right	2.4	30.3	5.3	9	0	0	12.8	0

4.4.3.3 LEFT AND RIGHT AXIAL ROTATION

In left axial rotation (Table 4-9), approximately 64% of the load distribution is borne by the intervertebral disc in the intact model and increases to approximately 76% and 79% after the bilateral inferior and superior facetectomies are respectively conducted. The left and right FJ bear approximately 14% and 3.6% total load respectively prior to the inferior facet removal, then drop to zero and 1.4% respectively following the bilateral inferior facetectomy. The CV joint components bear no more than 6.4% of the total load prior to facet removal, seen by the left CTV, which experiences an approximately 1.5% maximum increase. In right axial rotation, approximately 67% load distribution is borne by the IVD; this increases to approximately 79% and 83% respectively after the bilateral inferior and superior facetectomies. As with the left axial rotation, the change in load distribution is evidenced by the left and right FJ bearing approximately 14% and 6% load respectively prior to removal. After the bilateral inferior facetectomy stage the load distribution on the left and right FJ drop to 4.6% and zero respectively. The CV joint components see a maximum increase of 1.9% load distribution by the left CTV after facet removal; however, prior to facet removal, the components bear no more than approximately 6%. The load borne by the left and right ITL was small in comparison throughout all removal steps, seeing less than 2% throughout the entire procedure. A small load sharing percentage of approximately 0.64% is borne by the ISL in right axial rotation prior to removal. Axial ligament force counterparts at each removal stage are listed in Table 4-10. Intervertebral disc stresses and annulus fiber forces generated during all six rotations are highlighted in transverse views in Figures 4-8 and 4-9 respectively.

Table 4-9: Load distribution percent by spine component at maximum axial moment (5 N-m).

		CCJ-Left	CCJ-Right	CTV-Left	CTV-Right	FJ-Left	FJ-Right	ISL	ITL-Left	ITL-Right	IVD
Intact	Left	1.7	3.6	6.4	6	14.1	3.6	0	0	0.97	63.7
	Right	0.92	6	2	2.8	14.4	5.8	0.64	0.42	0	67.1
ISL & SSL removed	Left	1.7	3.6	6.4	5.9	14.2	3.6	0	0	0.98	63.7
	Right	0.95	6	2.1	2.8	14.3	6.1	0	0.63	0	67.2
Bilateral Inferior Facetectomy	Left	2.2	4	7.9	6.6	0	1.4	0	0	1.6	76.4
	Right	1.1	7.5	4	3.1	4.6	0	0	1.1	0	78.5
LF removed	Left	2.2	4	7.9	6.6	0	1.4	0	0	1.6	76.4
	Right	1.1	7.5	4.1	3.1	4.6	0	0	1.1	0	78.4
Bilateral Superior Facetectomy	Left	2.1	4.1	7.6	5.7	0	0	0	0	1.6	78.9
	Right	1.4	6.4	5.2	2.8	0	0	0	1.1	0	83.2

Table 4-10: Ligament forces (Newtons) calculated at maximum axial moment (5 N-m).

		CCJ-Left	CCJ-Right	CTV-Left	CTV-Right	FJ-Left	FJ-Right	ISL	ITL-Left	ITL-Right
Intact	Left	6.2	10.2	8.5	8.9	27.7	9.2	0	0	1.1
	Right	4.8	17.2	4	3.7	28.6	9.5	1.4	0.47	0
ISL & SSL removed	Left	6.2	11.9	8.5	8.7	27.8	9.3	0	0	1.1
	Right	4.9	17.3	4.1	3.7	28.2	10.1	0	0.7	0
Bilateral Inferior Facetectomy	Left	8.2	12.8	10.4	9.5	0	3.4	0	1.8	0
	Right	5.4	20.6	6.5	4	17.9	0	0	1.2	0
LF removed	Left	8.2	12.8	10.4	9.5	0	3.4	0	1.8	0
	Right	5.4	20.6	6.4	4	17.8	0	0	1.2	0
Bilateral Superior Facetectomy	Left	8.2	11.7	10	9.6	0	0	0	1.8	0
	Right	6.2	17.4	7.7	3.5	0	0	0	1.2	0

Figure 4-8: Intervertebral Disc stresses at each stage of the Ponte osteotomy in all six rotations. Transverse view is depicted.
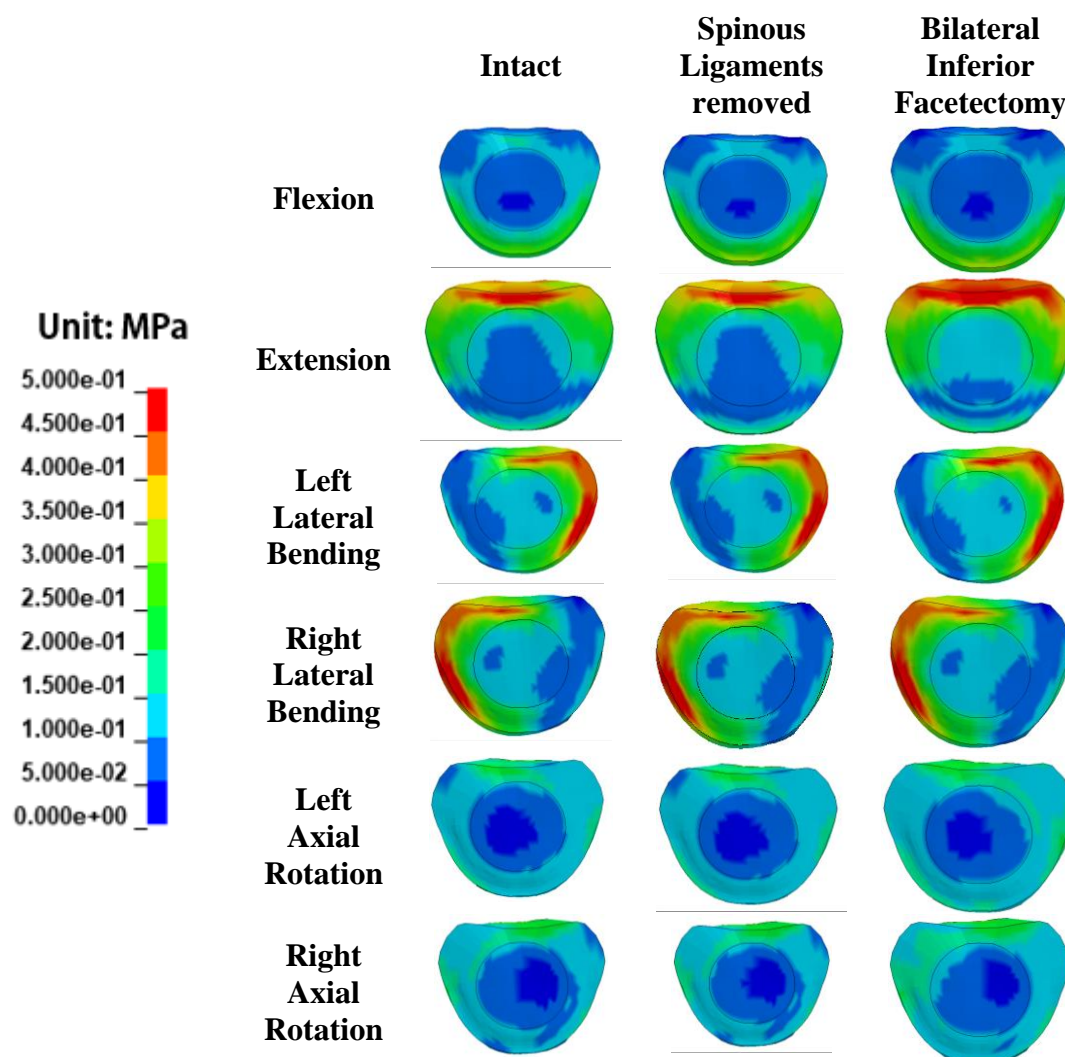
Figure 4-8 continued.
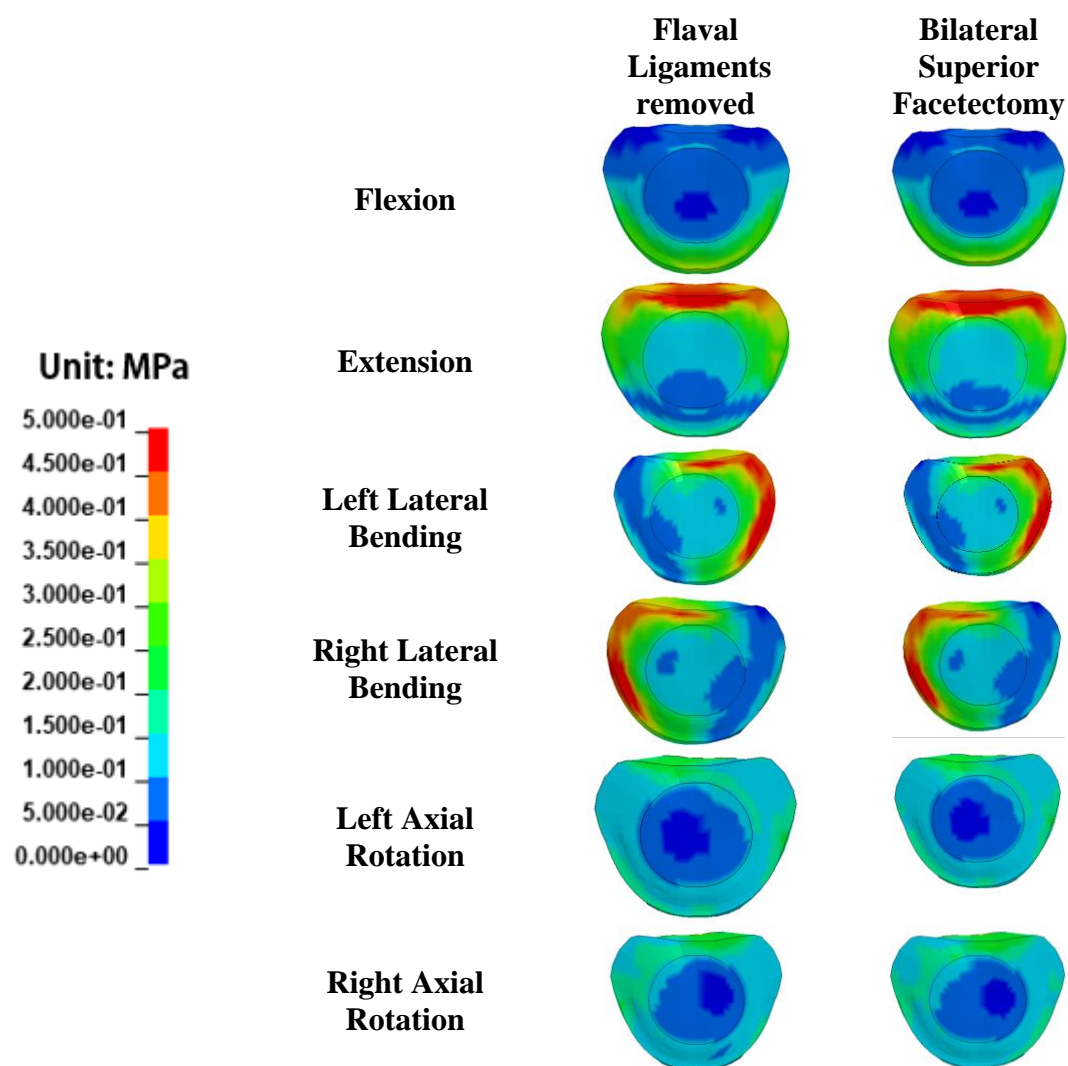
Figure 4-9: Axial force distribution among annulus fibers. Transverse view is depicted.
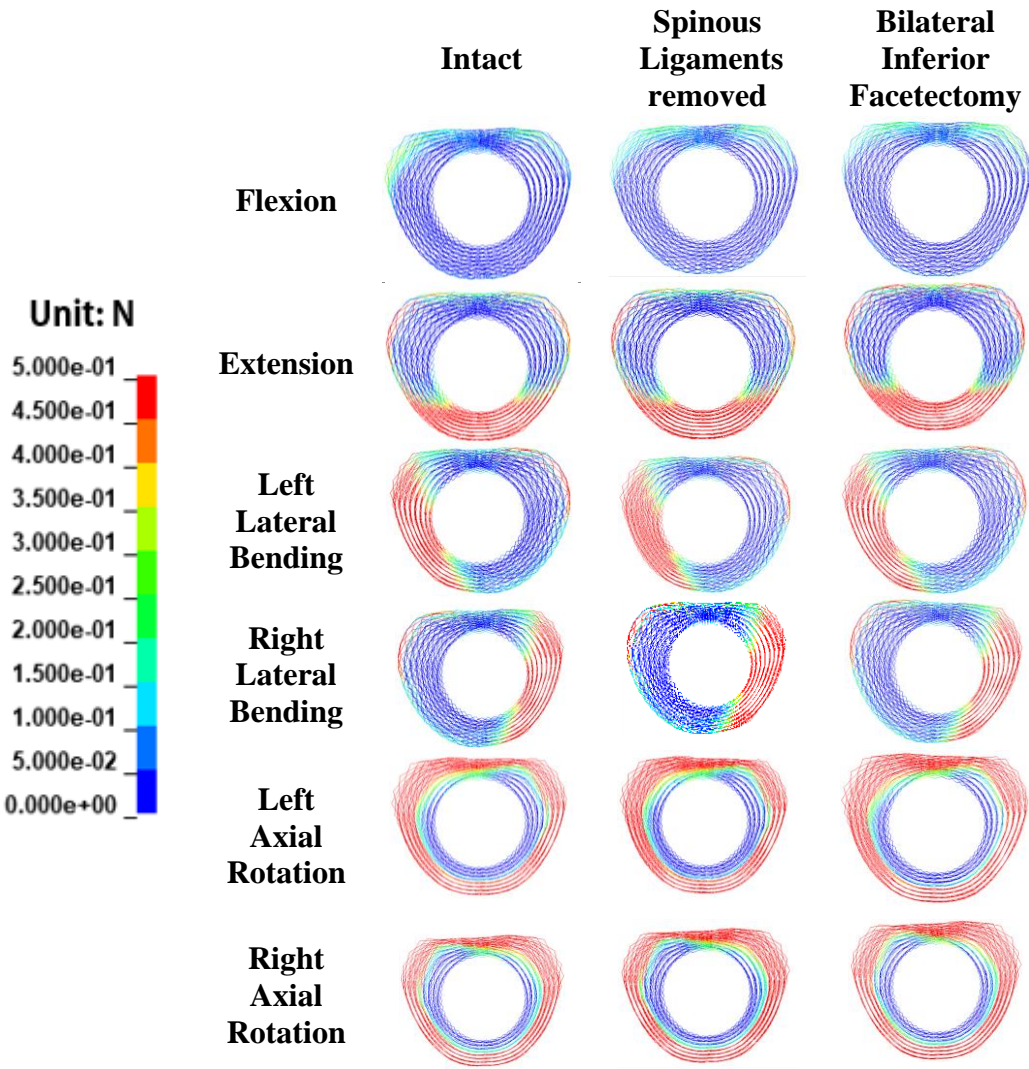
Figure 4-9 continued.
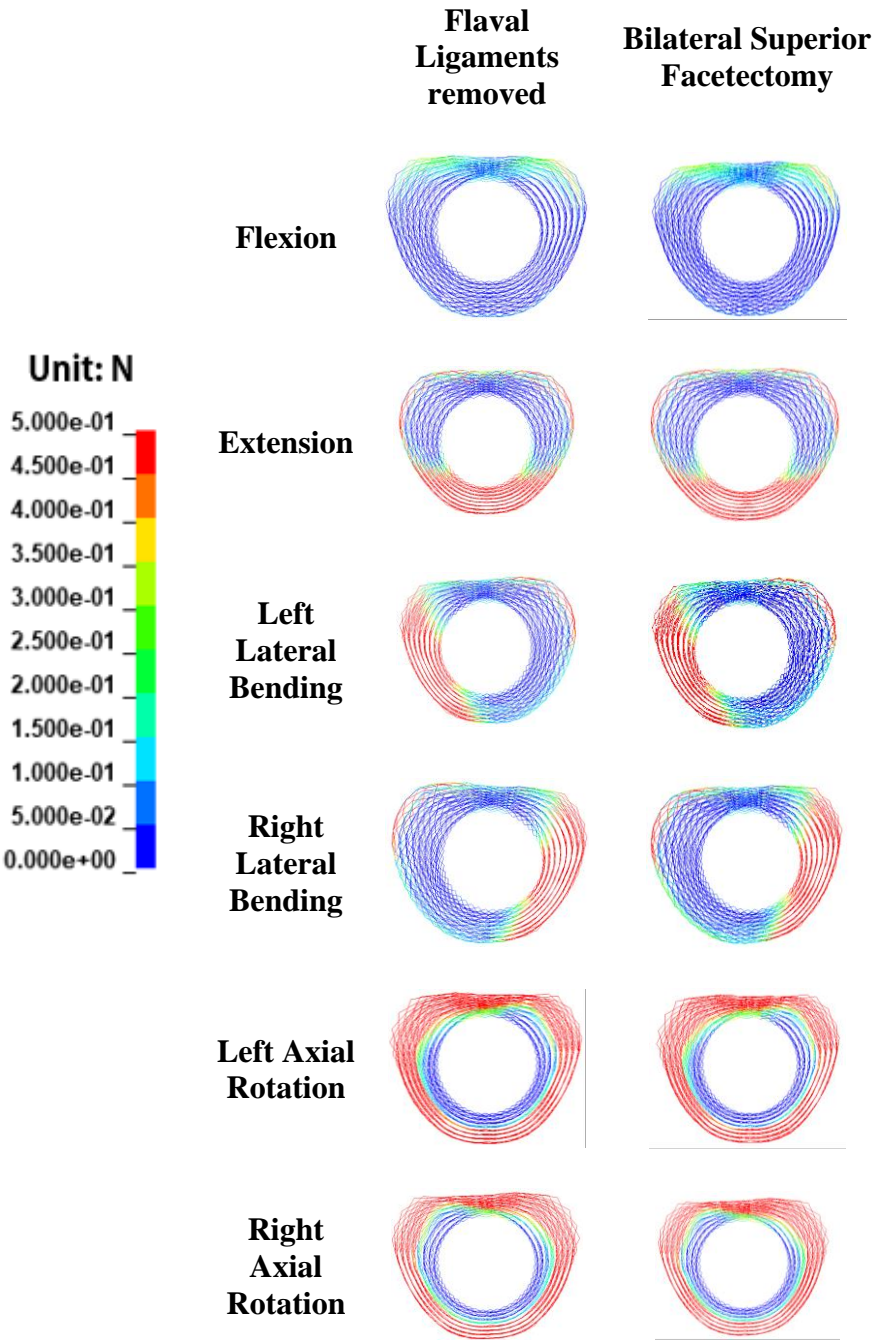
4.5 DISCUSSION

Patient-specific surgical planning can be a challenging feat due to variability in symptomatic profiles. The nonlinearities of vertebral geometry and wide-ranging characterization of soft tissue (Wang et al., 2014; Lafon et al., 2010) can affect clinical decisions on how to optimally address spinal deformities. Posterior correction procedures such as the Ponte osteotomy (Samdani et al., 2015; Ponte et al., 2018) have gained interest within the surgical community because of their superior correction outcomes. However, the ideal goal of a surgical procedure is to minimize the resection steps to achieve desired correction and, in turn, reduce the risk of intraoperative (e.g., blood loss) and post-operative complications (e.g., screw pullout). In a Ponte osteotomy, the surgeon typically resections spinal ligaments and facet joints at the apex of a spinal deformity. More aggressive techniques, such as a Pedicle Subtraction osteotomy (Bridwell, 2006) or Vertebral Column resectioning (Papadopoulos et al., 2015), may be required to obtain necessary correction for patients with large kyphoscoliotic curves. The load distribution study presented here can help surgeons make informed clinical decisions that will improve long-term patient outcomes.

To ensure that the FE model was accurately functioning, it was validated with experimental data pertinent to the clinical conditions being examined. Accordingly, the experimental sequence outlined (Wilke et al., 2020) was abridged to include only the key components to be sectioned for this study. The functional unit movements in right lateral bending and left axial rotation were largely within the experimental RoM highlighted in the study; the facet joint removal produced the only significant change in the sequence as it was one of the few components active in resisting joint movement. It also explains the

consistency in motion when the other components were removed. In extension and in flexion, upon release of the ligamentum flavum and facet joints, the compliance in the rotational response relative to the experiment may be explained respectively by anterior and posterior longitudinal ligaments that are thicker relative to other spinal regions. Although cross-sectional area values for these ligaments are used and evenly distributed to characterize nonlinear spring stiffness, very little data exists listing the thickness or width dimensions of the ligament. As a result, such ligaments may be better represented using two-dimensional or three-dimensional formulations.

To the authors' knowledge, the study is the first to make use of the ICR for thoracic posterior release. In flexion, the anterior shift of the ICR position during each resection step agrees with clinical observations regarding posterior release (Ponte et al., 2018). A significant shift in ICR position and RoM upon spinous ligament removal confirms their importance in spinal column stabilization, whose resistance is driven by the moment arm and posterior positioning (Sharma et al., 1995). Previous in-vitro (Wilke et al., 2020) and FE model (Little and Adam, 2011b) studies did not draw that conclusion potentially due to the lower moment magnitudes applied (2.5 and 2 Nm versus 5 Nm), consequentially affecting the strain seen from those ligaments. In addition, the high load bearings of the ligamentum flavum and intertransverse ligaments could be attributed to high thickness and stiffness characterizations present within the thoracic spine (White and Panjabi 1990, p.20,22-23). As such, removal of the ligamentum flavum contributed to a significant ICR shift and RoM. Except for flexion, where most load sharing took place within the posterior ligaments, the study confirms the load bearing significance of the intervertebral disc throughout all rotations and resection steps. The CV joint, overall,

did not contribute significantly to the load distribution of the functional unit, possibly due to the open bilateral configuration of the ribs. With an intact ribcage configuration present, however, the RoM could behave stiffer (Liebsch and Wilke, 2020).

Though their removal did not shift the ICR as significantly in flexion, the role facet joints play in bearing load in extension, lateral bending, and axial rotation is confirmed by the findings of this study (Wilke et al., 2020; Panzer and Cronin, 2009). Furthermore, significant shifts in kinematic behavior were exhibited after the inferior and superior facets were removed, particularly in axial rotation. As a result of the capsular ligament being absent following the bilateral inferior facetectomy, the absence of load distribution alternates based on the rotation direction, supplemented by contact between the superior and remaining inferior facets. The inferior facet removal saw more correction overall as most of the facet is removed, and smaller correction amounts after the superior facets were removed. This finding agrees with the results from the in-vitro study by Holewijn et al., (2015). The final step in the Ponte osteotomy may be utilized on a scoliosis patient to achieve further correction if residual pressure between inferior and superior facets complicates the surgery. Thus, an FE model with scoliosis may predict greater correction following removal of the superior facets. The setup for the bilateral inferior facetectomy was driven by general practice of removing the inferior facet up to the transverse process bottom during a Ponte osteotomy (Ponte et al., 2018). However, the amounts of the facet left upon release may vary based on surgeon experience and facet orientation.

The behavior of the functional unit intact compared sufficiently well in flexion and axial rotation with the calculated stiffness coefficients (Panjabi and White, 1976).

However, compliance in extension and lateral bending is observed, which is consistent with rotations utilizing the facet joints to resist motion. Historically, facet joints have been modeled utilizing available contact algorithms in FE codes; the methods in which facets have been modeled vary greatly (Mengoni, 2021) and could affect key parameters such as RoM and facet joint forces (Zander et al., 2017). The nonzero moment percentages reported for the facets indicate they engage in contact; however, the penalty algorithm alone may fail to sufficiently capture facet joint mechanics, which is realistically a fluid-solid interaction between synovial fluid and cartilage layers. Thus, to enhance facet modeling, parameters such as contact gaps and facet capsule characterization should be explored thoroughly; such parameters may affect load distributions calculated in spine models. Explicit representation of the synovial fluid may also be needed to enhance facet incompressibility.

The load distribution findings presented assume that the FE model moves within a plane and that negligible coupling takes place. Future work may investigate the effects of out-of-plane coupling on load distribution within the spinal column. In addition, the load distribution behavior is valid for the provided set of ligament properties and the sectioning sequence applied for a Ponte osteotomy. Both spinal flexibility and deformity are known to vary on a patient-specific basis (Lafon et al., 2010; Lamarre et al., 2009); thus, the load distribution behavior may be altered based on the patient or the section sequence a surgeon decides to perform. Examining load distribution using patient-specific FE meshes could also provide better estimations of surgical outcomes (Tapp et al., 2021). Lastly, the load distribution presented was valid for one mid-thoracic segment. As intervertebral stiffness varies throughout the spinal column (Panjabi and White,

1976), load distribution within different regions of the spine should be investigated as it can influence the level of surgical correction achievable.

4.6 CONCLUSION

A load distribution assessment has been performed on a FE model of a thoracic functional unit for potential application to surgical planning. Ligament properties were chosen and utilized based on available in-vitro data, qualitative descriptions of ligaments within the thoracic spine, and comparability with available experimental data. The simulated posterior release, through kinematic and load distribution changes, highlight components, like the intervertebral disc and facet joints, that are crucial to stabilization during serial removal. Also emphasized is the importance of moment arm, through the ICR, in determining the resistance levels that components exert during segmental rotation. A surgeon may collectively utilize these variables to achieve desired post-surgical outcomes while decreasing risk for their patients.

CHAPTER 5

ANALYSIS OF VARIOUS APPROACHES TO MODELING THE FACET JOINT IN THE THORACIC SPINE

5.1 ABSTRACT

Representation of the facet joint capsule in finite element models of the spine is varied yet is necessary to accurately capture intervertebral movement and load transfer along the spinal column. Six distinct approaches to modeling the facet capsule were implemented into a T7-T8 finite element model: two approaches consisted of explicitly representing synovial fluid layers sandwiched in between capsules attached to the facet processes, another approach utilized the explicit representation of facet capsule with synovial fluid modeled by frictionless surface penalty contact, and the last approach represented the facet capsule through shells purely through frictionless penalty contact using three different initial gap values. For each approach, the functional unit was rotated along three anatomical planes and compared with available in-vitro data. In some rotations, such as extension, facet capsule model approaches incorporating explicit representation of the synovial fluid led to improved kinematic behavior in comparison to configurations relying on frictionless penalty contact to model the synovial fluid, while use of the penalty surface algorithm led to good behavior in flexion and left axial rotation compared with in-vitro data. However, due to longer finite element model run times associated with explicit solver analyses involving fluids, explicit modeling of the synovial fluid may not always be a practical alternative to facet joint representation and may be best represented using contact algorithm parameters or nonlinear material models that best capture articulation and compressibility of the facet joint.

5.2 INTRODUCTION

The facet joints are crucial anatomical entities in the spinal column whose primary purpose is to stabilize the spine providing mobile constraints along three anatomic planes. Situated bilaterally within each vertebra, their angular orientations relative to the three anatomic planes vary within each spinal region and help dictate how vertebrae move relative to each other (White and Panjabi, 1990). Each joint consists of articular capsules and capsular ligaments attached to facet processes (bone), as well as synovial fluid to provide lubrication between the articular capsules. Together, the facets are primarily responsible for load transfer along the spinal column as it moves and are more pronounced in extension and axial rotation. Thus, the facets are important to consider when examining pathologies that may affect movement of the spine.
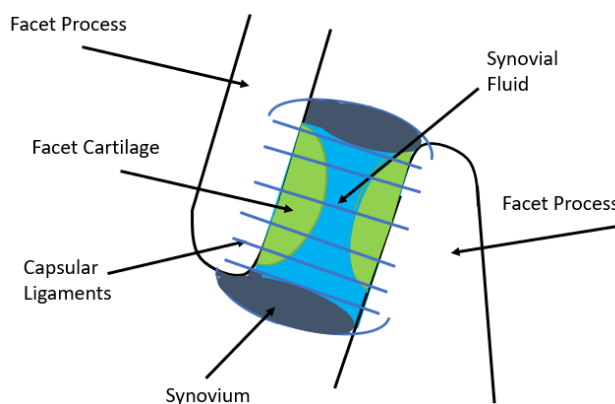
Figure 5-1: Facet joint.

Facet biomechanics have been studied in understanding potential causes for back pain, such as osteoarthritis (Pathria et al., 1987) or degenerative scoliosis (Wang et al., 2016), where contact between the facet pairs may degrade their lubricative properties

over time. In surgical applications, facetectomies are routinely conducted to provide flexibility gain in spines containing scoliosis (Ponte et al., 2018) or to treat patients with lumbar stenosis (Erbulut, 2014), or a clinical condition where the spinal canal narrows, to prevent spinal cord compression. The degree of intervertebral stability maintained during a facetectomy (Ahuja et al., 2020) or load transfer to surrounding soft tissues (Sharma, 1995) depends on how much of the facets are removed to achieve desired flexibility. Understanding facet behavior in advance may assist in enhancing surgical planning or clinical treatment related to spinal pathologies.

Three-dimensional Finite Element (FE) models have introduced various levels of details to represent the facet joint and their components, namely the cartilage and the synovial fluid. Due to the material and geometric complexity incorporated to characterize the bones and soft tissues within spinal FE models, the facet joint is typically represented simply using a frictionless contact algorithms incorporated within the FE code utilized (Du et al., 2016; Naserkhaki et al., 2018; Schmidt et al., 2008). Within these contact algorithms is where the variability of input parameters lies; facet joint representations in FE models make use of gap or contact thickness values between inferior and superior facets which may affect the quantitative forces transmitted between contact surfaces. Incompressibility within the facet joint is sometimes introduced through overclosure (Niemeyer et al., 2012; Shirazi-Adl and Drouin, 1987), or penetration, among contact surfaces, or direct contact of explicitly modeled facet capsules. Joint incompressibility has alternatively been supplemented through explicit modeling of the synovial fluid, based on the theory that opposing facet cartilage layers do not physically make contact during articulation (Kumaresan et al., 1998). Regardless, accurate representation of a

facet joint model is necessary to predict clinical outcomes and provide answers to clinical questions of interest. The following study examines the kinematic and load transfer effects of different modeling techniques of the facet joint, based on morphological features and as previously documented in literature.

5.3 METHODS

5.3.1 FE MODEL PREPARATION

An adult asymptomatic T7-T8 finite element model (Figure 5-2) was constructed using computer aided design (CAD) geometry and tessellated using Hypermesh (Altair Engineering, Troy, MI, USA). Using material properties listed in Tables 5-1 and 5-2, the cortical bone was characterized using triangular elements in the posterior and quadrilateral elements in the anterior of each vertebra. The posterior vertebral components (e.g., vertebral arches, spinous and transverse processes) were represented using tetrahedral elements, while the cancellous bone and components of the intervertebral disc (e.g., Annulus Fibrosus and Nucleus Pulposus) were represented using hexahedral elements. The annulus fibrosus contained cross-hatched fibers situated among 8 layers in the radial direction and 3 layers in the thickness direction. The volume fraction of the annulus fibers, characterized as cable elements, within the annulus fibrosus was approximately 16%. The transverse cross-sectional area and volume of the Nucleus Pulposus relative to the intervertebral disc were approximately 37% and 40% respectively. The stiffness properties of all ligaments, characterized as tension-only springs, were divided by the number of elements in each ligament group, and prescribed

using geometric and material parameters appropriate for the mid-thoracic region, as described in Table 5-3.
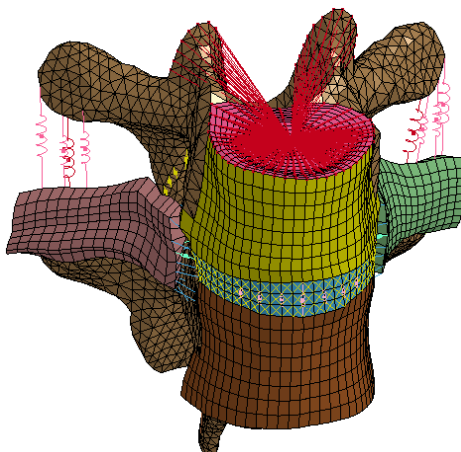
Figure 5-2: T7-T8 Finite element model with rigid body element (RBE) depicted in red.
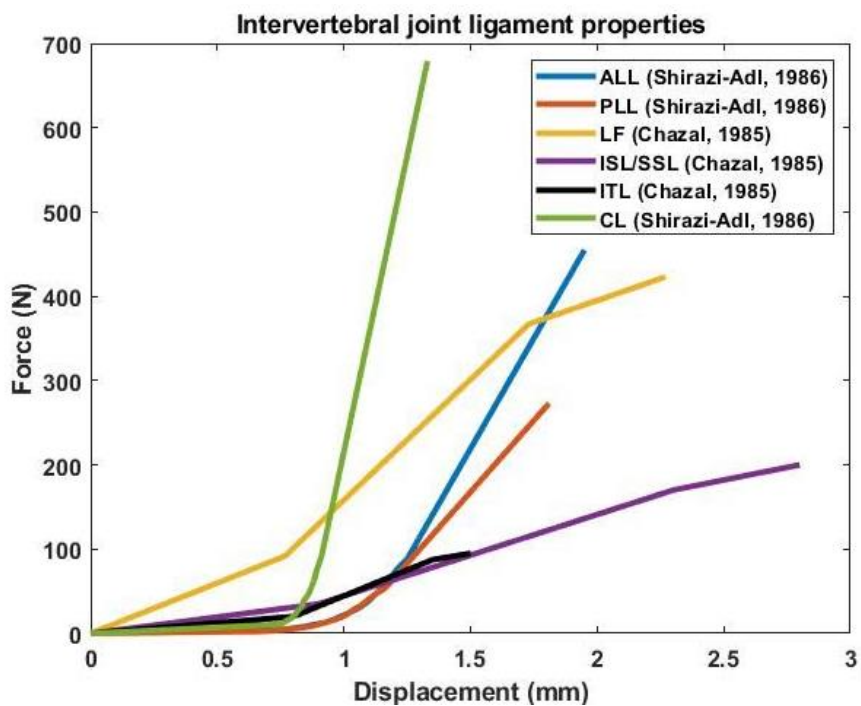
Figure 5-3: Intervertebral joint ligament properties.

Table 5-1: Vertebrae and Intervertebral Disc material properties.

Spinal Component	Material Property	Source
Cortical Bone	E=12 GPa, v=0.3	Naserkhaki et al., 2018
Cancellous Bone	E=200 MPa, v=0.315	Naserkhaki et al., 2018
Endplate	E=23.8 MPa, v=0.4, 1mm thickness	Schmidt et al., 2006
Annulus Fibrosus	C10=0.18 MPa, C01=0.045 MPa, v=0.45 Mooney-Rivlin	Schmidt et al., 2006
Nucleus Pulposus	C10=0.12 MPa, C01=0.03 MPa, v=0.499, Mooney-Rivlin	Schmidt et al., 2006
Annulus Fibers	Nonlinear Stress-Strain curve, all material and geometric scale factors adjusted based on layer position	Shirazi-Adl et al., 1986
Facet Cartilage	E=10.4 MPa, v=0.4	Mengoni et al., 2021
Synovial Fluid	ρ=1000 kg/m^3, K=1.67 GPa (elastic fluid)	Kumaresan et al., 1998

Table 5-2: Costovertebral Joint ligament properties.

Spinal Component	Material Property	Source
Lateral Costotransverse Ligament (LCTL)	Keff=126.5 N/mm	Aira et al., 2019
Superior Costotransverse Ligament (SCTL)	Keff=90.2 N/mm	Aira et al., 2019
Costotransverse Ligament (CTL)	Keff=54.9 N/mm	Aira et al., 2019
Radiate Ligament	A=10mm^2, E=42.1 MPa	Aira et al., 2019; Jiang et al., 1994
Intra-articular Ligament	Keff=20.9 N/mm	Aira et al., 2019

Table 5-3: Average model ligament lengths and cross-sectional areas.

Spinal Component	Average Length (mm)	Average Cross-Sectional Areas (mm^2)	Source
Anterior Longitudinal Ligament (ALL)	5.36	30	Chazal et al., 1985
Posterior Longitudinal Ligament (PLL)	4.929	17	Chazal et al., 1985
Ligamentum Flavum (LF)	24.832	26.7	Chazal et al., 1985
Interspinous Ligament (ISL)	5.541	30	Chazal et al., 1985
Supraspinous Ligament (SSL)	25.588	30	Chazal et al., 1985
Capsular Ligament (CL)	2.799 (over both sides)	36	Shirazi-Adl et al., 1986
Intertransverse Ligament (ITL)	18.359 (over both sides)	1.85	Chazal et al., 1985

5.3.2 ANALYSIS PROCEDURES

The facet joints were modeled using six different configurations intended to capture their physiological characterization (Figure 5-4). The first three configurations utilized a frictionless surface to surface penalty contact algorithm with minimum gaps of 0, 0.5, and 1mm set between inferior and superior facet surfaces; each gap was set by adjusting the contact thickness values of each surface to match each gap value. The fourth configuration utilized an explicitly modeled hexahedral facet cartilage layers with a frictionless penalty contact algorithm to represent the innermost cartilage surfaces, separated by an approximately 0.3mm gap bilaterally. The fifth and sixth configurations utilized one and three synovial fluid layers sandwiched between shell cartilage configurations directly bonded to the inferior and superior facet processes.

Using LS-DYNA implicit v971 R10.1, an external moment of 7.5 Nm was applied over the superior T7 endplate and facet processes in extension and left axial rotation for all configurations, while the inferior T8 endplate and facet processes were left fixed. The following assumptions were applied: as the facets exercise their role most prominently in extension and axial rotation, all functional unit rotations were restricted to those directions. Also, symmetry in both the left and right axial rotations justified a rotation only in one direction. Range of Motion as well as total force from the facets were output. Specifically, contact forces are reported for configurations incorporating the surface-to-surface contact algorithm, while the product of pressure and bond area for synovial fluid layers were utilized to generate force values for the synovial fluid. Due to the non-compatibility between the implicit scheme and fluid material models in LS-DYNA, facet joint configurations incorporating the synovial fluid utilized LS-DYNA explicit v971 R10.1 SMP. Using 4 CPUs, the termination times for all models amounted to 300ms, appropriately chosen to ensure quasi-static conditions. This was done by verifying that negligible kinetic energy in the FE model was calculated with respect to the total energy in the analyses.

(a)
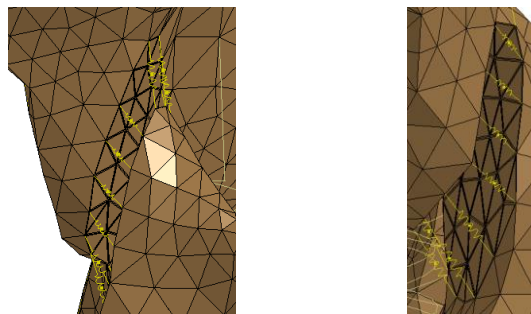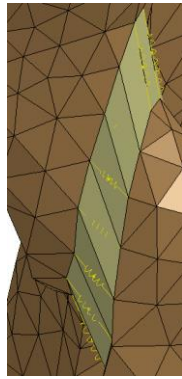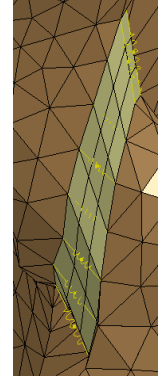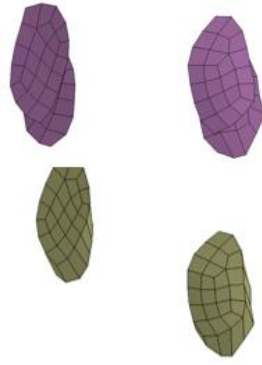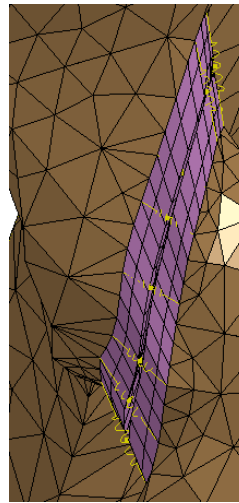
Figure 5-4: Facet Joint configurations. (a) Inferior and superior penalty contact surfaces. (b) Single synovial fluid layer with shell cartilage. (c) 3-layer synovial fluid with shell cartilage. (d) Discretized facet capsule.

5.4 RESULTS

5.4.1 RANGE OF MOTION

The penalty methods utilized in extension produced maximum RoM values ranging from 6° to 6.3° at the maximum applied moment directly increasing with the initial gap values from no gap (e.g., 0mm) to 1mm between facet surfaces. Incorporation

of the facet capsules without synovial fluid led to an approximate maximum RoM value of 5.8°. When the synovial fluid was explicitly modeled, the RoM had decreased to approximately 3.2° and 2.8° using one and three layers through the thickness respectively; the latter two were within the in-vitro data range presented. In flexion, the penalty methods produced maximum RoM movements at approximately 2.3° with negligible deviation between the configuration with no initial gap and those with nonzero gaps (approximately 0.01° difference). The facet capsule with frictionless contact yielded approximately the same RoM values. The synovial fluid configuration yielded between approximately 1.97° and 2.03° using 3 and 1 layer respectively. As the facet joints primarily facilitate sliding in flexion, little kinematic deviation was seen in the different results. In left axial rotation, the RoM values ranged from 3.9° to 4.2° with a direct increase in initial gap ranging from 0 to a 1mm gap within the contact algorithm. Use of the facet capsule led to a RoM value of approximately 3.97°, while use of the synovial fluid led to RoM values of approximately 2.6° and 2.4° using one and three layers respectively. In right lateral bending, the RoM values ranged between 5.55° and 5.75° when initial gap values between 0 and 1mm were prescribed; the initial gap value set to approximately 0.5mm produced 5.7° of RoM. The facet capsule characterization produced a rotation of approximately 5.4°. Incorporation of the synovial fluid produced approximately 3.9° and 4.5° using three layers and one layer respectively.
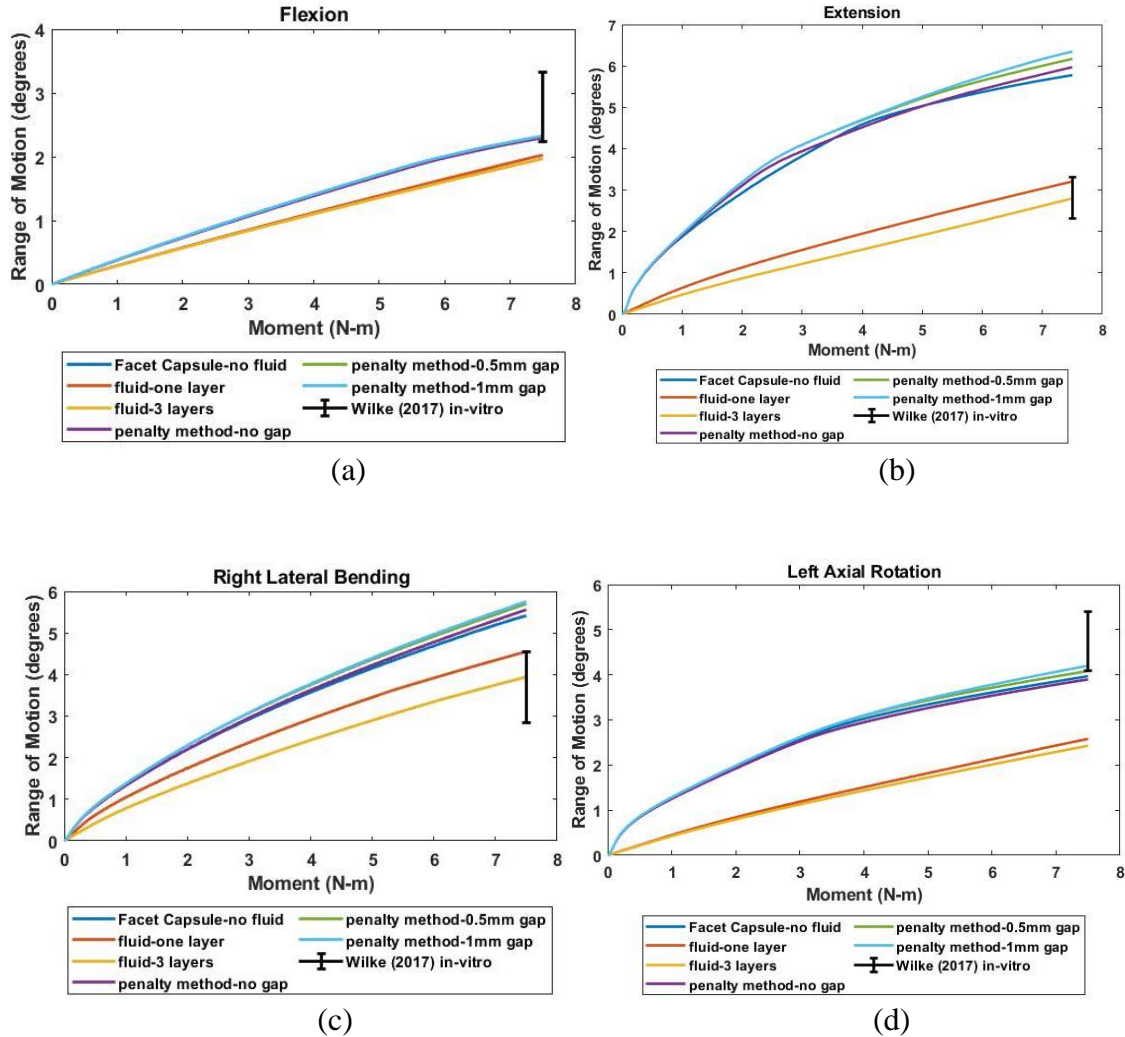
Figure 5-5: Range of Motion. (a) Extension. (b) Flexion. (c) Left Axial Rotation. (d) Right Lateral Bending.

5.4.2 FACET FORCE VALUES

In extension, the bilateral forces produced using penalty contact are 3.6, 44.3, and 102.1 Newtons using no initial gap, 0.5mm gap, and a 1mm gap respectively. The facet capsule produced total bilateral forces of approximately 134.8 Newtons. The synovial fluid configuration produced approximately 6 and 13.5 Newtons using 1- and 3-layer configurations respectively. In flexion, facet force values from penalty contact forces

range from 13.2 to 14.2 Newtons using the facet capsule configuration and the penalty formulation with no initial gap respectively. The facet forces incorporating a 0.5mm and 1mm gap produced no penalty forces. The synovial fluid incorporation produced 7.8 and 20 Newtons for the 3-layer and 1-layer configurations respectively. In left axial rotation, the forces produced on the right facet were 54.1 and 87.2 Newtons when a 0.5mm and no initial gap were introduced into the contact algorithm respectively. No force was produced using a 1mm initial gap. The facet capsule configuration produced approximately 52.8 Newtons. All the aforementioned configurations produced no forces on the left facet. The synovial fluid configuration produced approximately 132.7 and 152.1 Newtons on the right facet using 3 layers and 1 layer respectively through the thickness, while the left facet produced 169 and 209 Newtons on the left facet, attributed to tension within the fluid elements. In right lateral bending, no forces were produced when the penalty contact algorithms utilized a 0.5mm and 1mm initial gap; however, a 72.1 Newton force was produced on the right facet with no initial gap between surfaces. The right facet capsule produced approximately a 66.7 Newton force and no force in the left facet capsule. The synovial fluid configurations produced approximate forces of 87.5 and 101 Newtons in the right facet capsule and 37.2 and 46.1 in the left facet capsule, using the 3-layer and 1-layer configurations respectively. As with left axial rotation, the left facet capsule forces were generated from tension along the fluid elements. The stresses from the facet capsules (Figure 5-7), as well as pressure within the fluid elements (Figures 5-8 and 5-9) are shown to complement the force distribution within the facets. Computation times for all cases are shown in Table 5-4. All cases incorporating a direct

contact between inferior and superior facet surfaces showed a significantly smaller computation time compared with all cases incorporating fluid elements.
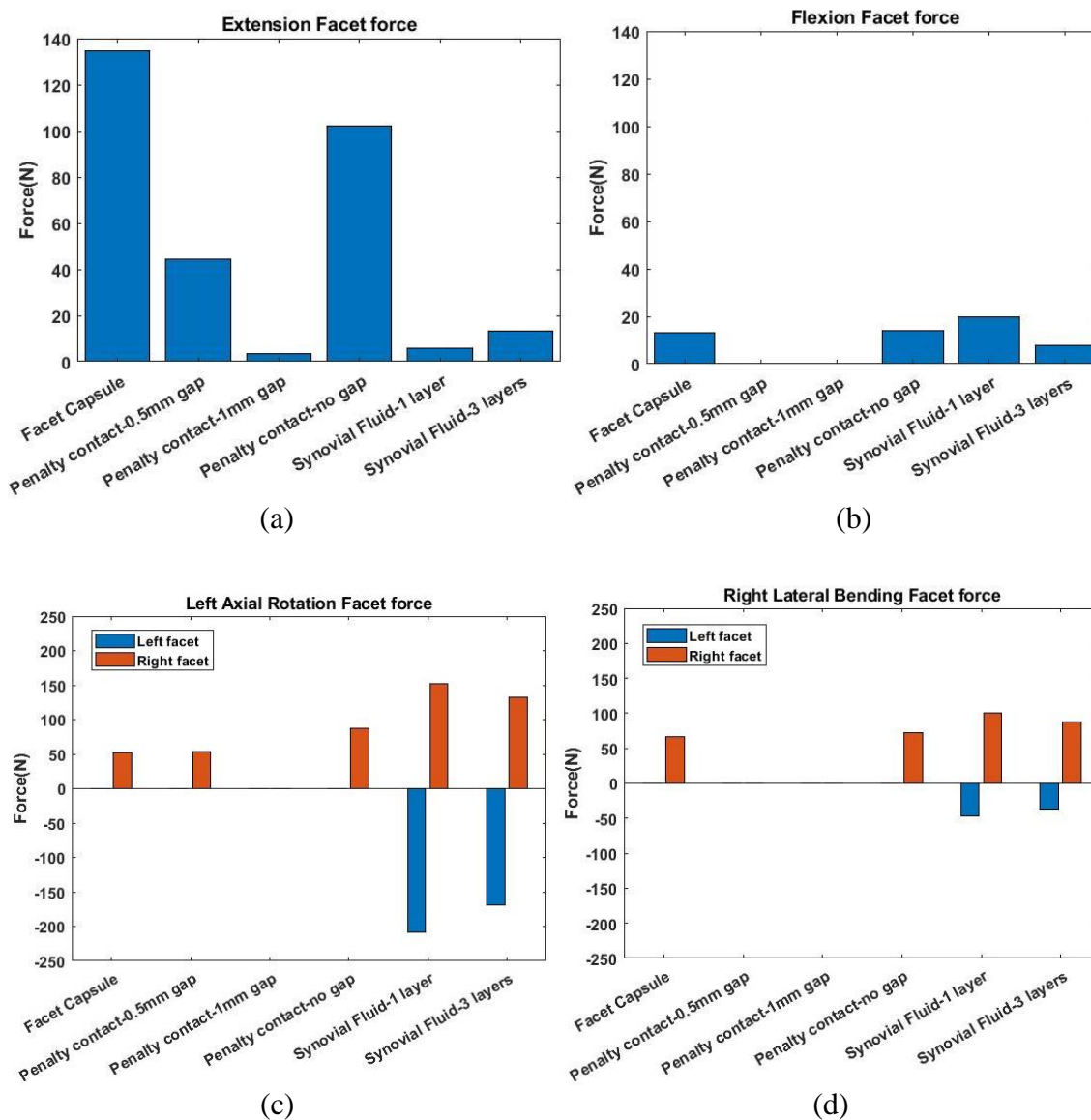
Figure 5-6: Facet joint forces. (a) Extension. (b) Flexion. (c) Left Axial Rotation. (d) Right Lateral Bending.
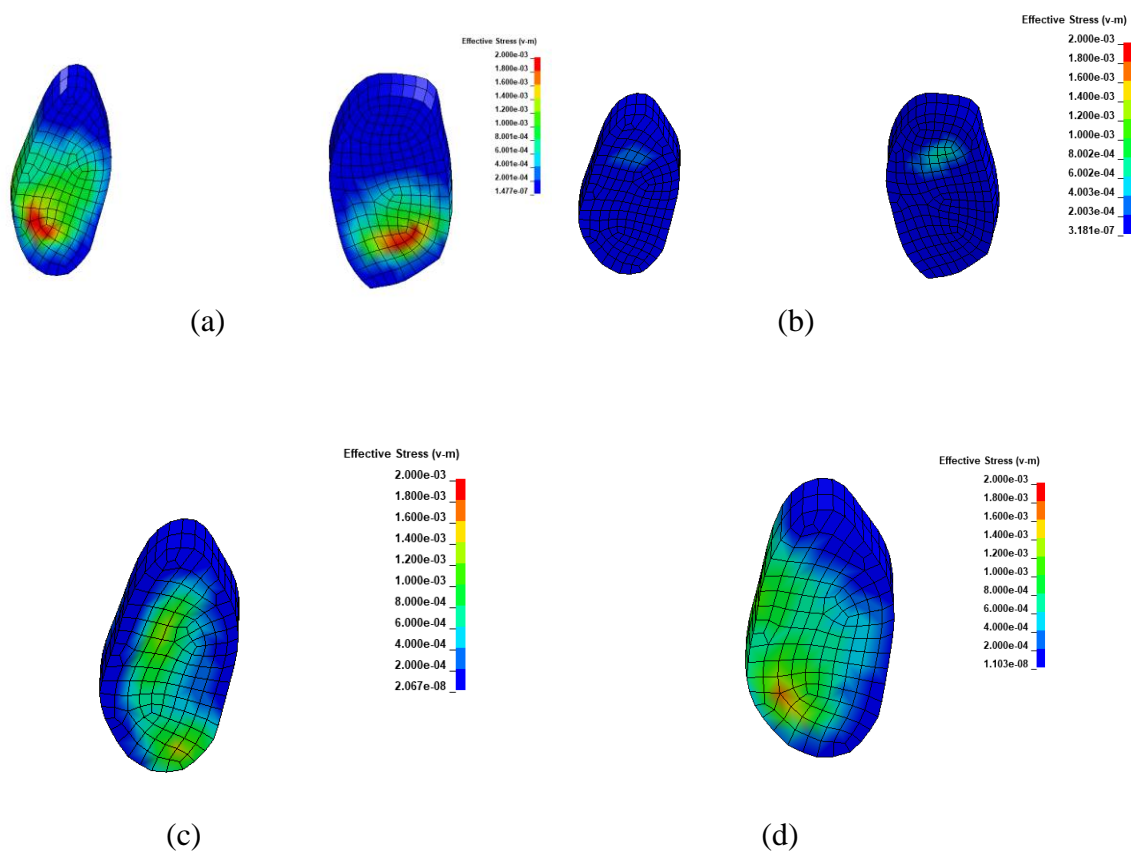
Figure 5-7: Stress distribution on facet capsules in GPa. (a) Inferior facets in extension. (b) Inferior facets in flexion. (c) Right inferior facet in left axial rotation. (d) Right inferior facet in right lateral bending.
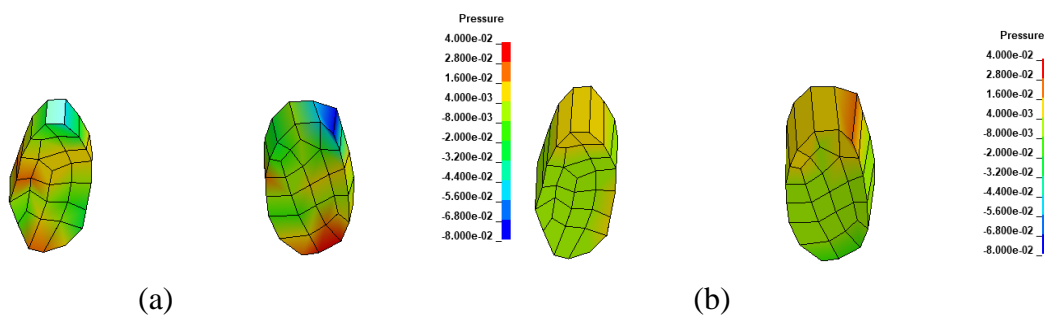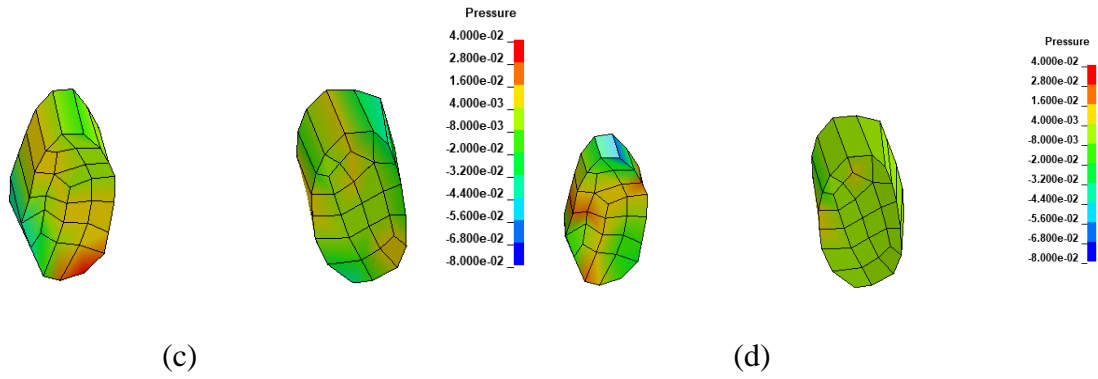
Figure 5-8: Synovial fluid pressure in GPa with 1 layer through thickness. (a) Extension. (b) Flexion. (c) Left Axial Rotation. (d) Right Lateral Bending.
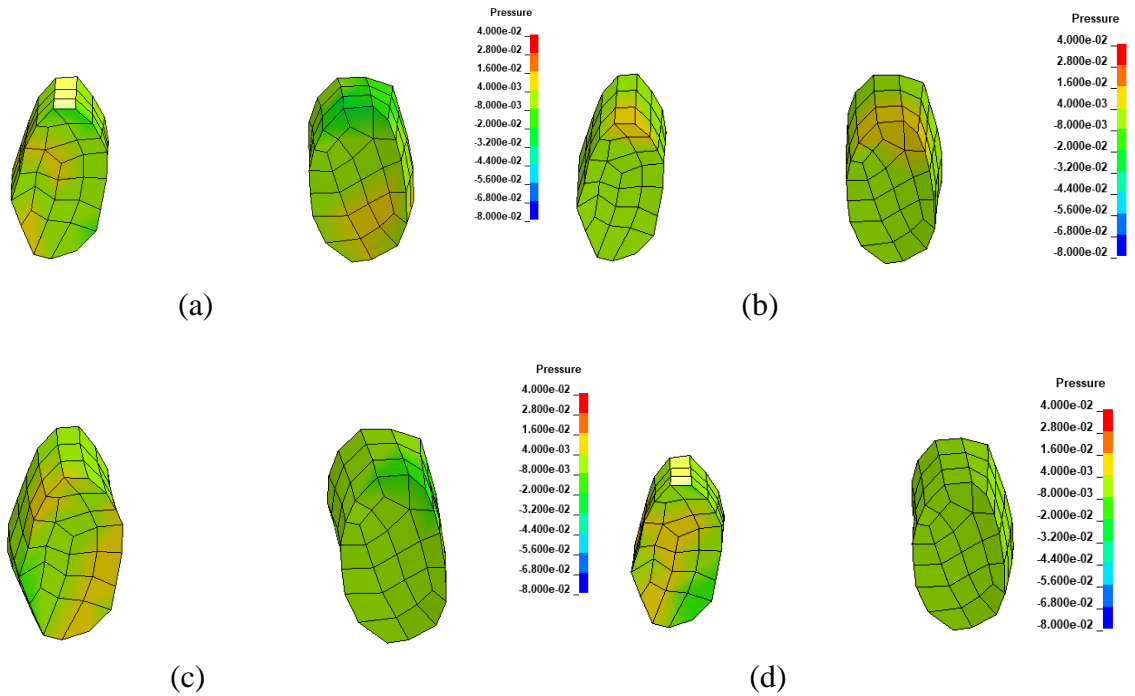
Figure 5-9: Synovial fluid pressure in GPa with 3 layers through thickness. (a) Extension. (b) Flexion. (c) Left Axial Rotation. (d) Right Lateral Bending.

Table 5-4. Computation times for each case in the HH:MM:SS Format

Facet configuration	Extension	Flexion	Left Axial Rotation	Right Lateral Bending
Penalty contact (no initial gap)	00:37:56	00:08:25	00:14:16	00:47:08
Penalty contact (0.5mm initial gap)	00:33:42	00:06:56	00:10:37	00:33:36
Penalty contact (1mm initial gap)	00:36:31	00:07:35	00:13:00	00:46:30
Facet capsule	00:47:30	00:09:35	00:15:14	00:43:35
Synovial Fluid-1 thickness layer	10:26:19	10:29:11	10:17:22	10:25:06
Synovial Fluid-3 layers through the thickness	10:17:56	10:24:38	10:22:38	10:21:23

5.5 DISCUSSION

The techniques employed to model facet joints in finite element models are shown to vary greatly. This study sought to investigate how these modeling approaches influenced the kinematics and facet forces within a thoracic spine functional unit. The surface contact algorithm is primarily used to model interaction between facet surfaces. The three distinct gap values were chosen to be representative of a range of values previously utilized to characterize the distance between the shell inferior and superior facet surfaces (Zander et al., 2017; Rohlmann et al., 2009; Shirazi-Adl and Drouin, 1987). Other studies explicitly model the facet cartilage using material properties from the literature (Mengoni et al., 2021), hence its inclusion in this study. The explicit representation of the synovial fluid, to the author's knowledge, has been explored once (Kumaresan et al., 1998), justified by the theory that articulating facet surfaces do not physically contact but instead are kept apart by the synovial fluid incompressibility.

Accordingly, this study incorporated synovial fluid layers to compare with other facet joint model methodologies.

Typically, utilizing a functional unit provides the simplest representation by which its mechanics may be realized and understood prior to use in fully integrated models. Thus, the effects resulting from model features as well as the time needed to obtain an analytical solution become more pronounced as the model size increases. As a first step in validating proper kinematic behavior of the T7-T8 functional unit, its RoM was assessed. When compared with in-vitro data (Wilke et al., 2017), RoM values varied depending on the features employed to model the facet joint. In flexion, all facet formulations incorporating a penalty contact algorithm were within the in-vitro standard deviations, but only those incorporating a non-zero gap along shell surfaces were within the standard deviation in left axial rotation. Likewise, the rotations were out of range when the functional unit was rotated in right lateral bending and extension. The incompressibility exhibited by the synovial fluid layers helped to decrease the RoM of the functional unit overall. Likewise, when the contact forces are assessed for all facets, the largest facet forces are transmitted in extension while the lowest are transmitted in flexion, where contact was engaged with both bilateral facets. The forces transmitted in the solid facet capsules were read the highest likely due to the contact area being more pronounced to calculate solid segment stiffness. The effect of the gap values is more pronounced in right lateral bending and left axial rotation; larger gap values (e.g., 1mm) lead to zero forces in both rotations while the 0.5mm only produces a zero force in right lateral bending, with contact only recorded in the right facet in both rotations. Presence of

the synovial fluid helps to exhibit bilateral facet forces in all cases but is more pronounced in left axial rotation.

The synovial fluid was run containing both one and three layers to assess the mesh sensitivity on both kinematics and pressure. Though the overall behavioral differences between the two configurations were small, as shown by the functional unit RoM, the coarser, one layer, configuration produced higher pressure and facet forces compared to the three-layer configuration, owing to concentrations in load distribution throughout the fluid. While the purpose of the synovial fluid is to provide both lubrication and incompressibility, its direct bond to facet processes by way of shell facet capsules likely stiffened the functional unit. The stiffer behavior exhibited may have been alleviated by adding a layer of incompressible fluid between two solid facet capsules to remove direct contact with the facet processes. A variation of this approach not presented here was tried but led to severe element distortion and lower time steps. A hydrostatic element formulation, similar to what was utilized in Kumaresan et al., (1998) and offered in commercial codes like ABAQUS (2014), may be most appropriate to characterize the facet. The study also confirms the need to have a sufficiently refined mesh to produce a reasonable pressure and force distribution throughout the fluid. Lastly, due to the vastly large time required to obtain a solution, direct utilization of fluid elements within the facet would not be an ideal configuration moving forward with larger FE models of the spine.

The commonly used surface contact algorithms require an understanding of how defined surfaces interact to generate force values when contact is detected. The utilization of the surface penalty algorithms in LS-DYNA relied on the shell elements situated on

the cortical bone to facilitate the contact between inferior and superior facet surfaces, whereas the modeling of solid facet capsules relied on the solid segments situated within each facet gap to engage in contact. During penalty contact, springs within the algorithm are utilized to counteract penetrating nodes in contact surfaces. The mortar option, utilized for these and subsequent studies, allows for the contact force in LS-DYNA (Livermore Software Technology, 2006) to be continuously and smoothly applied over all defined bodies in contact (Borvall, 2008). The stiffness equations for both solids and shells are listed below (Equations 1 and 2 respectively). As confirmed by different studies (Zander et al, 2017; Kumaresan et al, 1998; Mengoni et al, 2021; Niemeyer et al., 2012), the initial gaps defined within facet joints in FE models affect the forces transmitted and, consequently, may affect movement within the spine model. The results presented here make no exception to the varying facet forces presented, which generally increase with decreasing initial gap due to the time by which contact is initiated and engaged among the surfaces. As exhibited by stresses in the solid facet capsules, differences in RoM with and without the facet capsules could be attributed to strain energy imparted in the capsules when compared with facet configurations solely using the shell elements. Though little differences could be seen in the functional unit kinematics (e.g., less than 10%), the results suggest that penalty forces may not be enough to stiffen the functional unit, reinforcing the need to introduce additional parameters to account for the incompressibility of the synovial fluid to produce more accurate kinematic behavior. The specification of overclosure and pressure parameter values within contact algorithms should be chosen and specified to sufficiently capture behavior of the facet joints. Contrary to the linear equations used for penalty stiffness, exponential characterization of

the facet capsule stiffness, through a poroelastic (Hussain et al., 2010) or hyperelastic (Du et al., 2016) material, for example, may also help contribute to facet joint stiffness reinforcement.

$$k_{shell} = (f_s * K*A)/L_{shell\ diagonal,\ max} \qquad \text{(Equation 5-1)}$$

$$k_{solid} = (f_s * K*A^2)/V \qquad \text{(Equation 5-2)}$$

The following variables in the above equations are defined below:

k_{shell}-penalty stiffness for shell elements
k_{solid}-penalty stiffness for solid segments
fs-default stiffness scale factor
K-Bulk modulus
A-contact surface area
V-Volume of solid contact segments

Some limitations to the work presented are as follows. The capsular ligaments, which surround each facet joint, are an important contributor to spinal movement. However, as the focus of this study was investigation of modeling the fluid cavity within the facet, their effects were not examined. Secondly, the study only accounted for one functional unit within the spine. It is well documented that the facet orientations vary along the spinal column (Panjabi & White, Clinical Biomechanics of the Spine, pp.31-32,40); thus, future work may examine the effects of incorporating various facet joint configurations within different spinal regions. To the author's knowledge, no data exists to compare facet joint forces with data obtained from the literature and, thus, were approximated based on model comparison with kinematic in-vitro data. On that note, force data from the cervical (Kumaresan et al., 1998) and the lumbar spine (Du et al., 2016; Naserkhaki et al., 2018) exist, however, undergo different loading scenarios to produce the facet joint forces and kinematics produced. Thus, one must account for load

inputs and the spinal region of interest when considering the model methodology for facet joints. Also, the contact thicknesses and solid facet capsules assumed uniform thickness across each surface, which is a simplification considering their thickness can vary. As suggested in Mengoni et al. (2021), MRIs may increase the resolution, or image quantity, by which facet joints are captured to improve the fidelity by which facet morphology is represented in FE models during imaging conversion to CAD models. Regardless of these limitations, sufficient insight was provided on how facet joint model techniques may affect their mechanics and functional unit kinematics.

5.6 CONCLUSION

A comparison between approaches to representing the facet joint in an FE model was completed in this study. Utilizing a penalty surface contact algorithm within the solid facet capsules and where initial gap values were varied using shell-based facet surfaces led to significant increases in force values but negligible change in RoM, producing a comparable response overall with in-vitro data in left axial rotation and flexion. The explicit incorporation of the synovial fluid led to an increased presence of facet incompressibility which stiffened the functional unit response in flexion and left axial rotation but improved kinematically in extension and right lateral bending compared with in-vitro data. The latter approach led to increased run times due to its usability only using the explicit solver and would not be a good candidate for facet joint representation towards multi-segment FE models of the spine. Due to better computational efficiency and performance, utilization of the surface contact algorithms to characterize the facet joint remains a suitable choice to capture both force distribution and kinematics of the

spine. However, specification of and attention to contact algorithm parameters such as facet gap and pressure are needed to best capture the morphology and mechanics of the facet joint.

CHAPTER 6

A KINEMATIC COMPARISON OF AN ASYMPTOMATIC VS SCOLIOTIC ADOLESCENT SPINE FINITE ELEMENT MODEL

6.1 ABSTRACT

Spinal motion assessment is commonly used by clinicians to detect the presence of scoliosis in adolescent patients. The following study utilizes Finite Element (FE) analysis to assess the kinematic behavior of a spine with scoliosis compared to an asymptomatic one (e.g., Cobb angle of 0 degrees). A full thoracic and lumbar spine FE model with incorporated ribcage is utilized based on a computer-aided design (CAD) model of an adult spine. Using adolescent material scale factors appropriate for the anatomy of a 15-year-old, the asymptomatic spine is rotationally loaded along in flexion, extension, left and right lateral bending, and left and right axial rotation using a 2 N-m torque on the T1 superior endplate and facet processes. Next, scoliosis is induced in the asymptomatic model using asymmetric growth modulation conditions consistent with the Hueter-Volkmann law until the spine achieves a mild scoliosis condition; afterwards, the same loading conditions are applied as the asymptomatic case. Key findings from comparing the asymptomatic and scoliotic cases include: an increase in axial rotation coupling during sagittal rotations by as much as 2°-2.2° in flexion and extension respectively, as well as a decrease in global range of motion by as much as 5.5° in extension. Changes in intervertebral rotations were highest in the region of apex deformity, by as much as 0.95° in right axial rotation. Axial and coronal rotations of the scoliotic spine FE model produced asymmetric behavior when rotated in opposing directions. Using mechanical induction, the symptomatic FE model behavior matches

with clinical knowledge about the scoliotic spine and can provide invaluable insight toward future surgical planning studies.

6.2 INTRODUCTION

Adolescent Idiopathic Scoliosis (AIS) is a three-dimensional deformity of the thoracolumbar spine affecting approximately 2-4% of adolescents and is the most common spinal deformity (Wang et al., 2014). Scoliotic spines can be characterized as typically curved in the form of an S or C coronally, rotated in the axial plane, and decreased in curvature sagittally. To classify as a scoliotic spine, a Cobb angle must be at least 10 degrees. Measured from the coronal view of a radiograph (e.g., CT scan, X-ray, etc), a Cobb angle can be measured by clinicians to assess the extent to which the spine has deformed and, subsequently, decide what treatments are appropriate to correct the deformity. In the coronal plane, the largest of the deformities occurs, characterized by wedging of the intervertebral disc (IVD) and vertebrae (Stokes and Aronson, 2001; Modi et al., 2008; Scherer et al., 2013). The wedging is shown to be a large contributor to a stiffer spine (Wilke et al., 2015).

Spinal flexibility assessment techniques such as fulcrum bending (Hasler et al., 2010) and side bending in both supine (Polly et al., 1998) and standing positions (Lamarre et al., 2009) are utilized with radiographs to determine best methods to achieve desired surgical outcomes. Recent interest has been generated in further understanding the biomechanical behavior of scoliotic spines using clinical Range of Motion (RoM) (Mehkri et al., 2021) along with the coupling behavior of axial rotations with side bending during scoliosis assessments (Senkoylu et al., 2021). Segmental flexibility has

emerged in recently conducted studies to enhance the understanding of biomechanical behavior in patients with AIS (Little et al., 2016; Hasler et al., 2010). Thus far, no known study examines the effects of rotational coupling from both global and intervertebral levels as a function of Cobb angle. Understanding the biomechanical behavior of scoliotic versus asymptomatic spines is of emerging interest to clinicians and may further progress areas of surgical planning.

Finite element (FE) analysis has been utilized for non-invasive spinal biomechanics studies that allow for personalization of patient-specific anatomy through geometric and material property input. The FE method has been used by Lafon et al. (2010) to personalize the stiffness of thoracolumbar FE models of scoliotic patients. While they demonstrated the importance of intervertebral stiffness in producing accurate spinal behavior, only coronal and axial rotations were utilized to compare with side-bending radiographs (Lafon et al., 2010). The load distribution of a mobile lumbar spine with scoliosis has been assessed through FE analysis under rotations in three anatomic planes (Zhang et al., 2021). This study only focused on a Cobb angle of 43° and did not examine the thoracic spine.

While there is no known causation to AIS, the most accepted theory behind the scoliosis formation mechanism is the Hueter-Volkmann law (Stokes et al., 1996). The law expresses an inverse relationship between the amount of stress applied on localized growth plates within the spine and the amounts of bone growth on adjacent vertebrae. The nonuniform stress distribution within the growth plates is seen to contribute to asymmetric spinal growth in patients with scoliosis, describing a "vicious cycle" by which the deformity is further progressed. Previous FE model studies have made use of

the Hueter-Volkmann law to understand how various pathological variables affect scoliosis formation (Villemure et al., 2002; Huynh et al., 2007) while producing deformities matching radiographs of their patients (Shi et al., 2011). The following study assesses the global and intervertebral kinematic behavior of a thoracolumbar FE model with scoliosis induced through the Hueter-Volkmann law and compares its behavior to an asymptomatic model.

6.3 METHODS

6.3.1 FE MODEL SETUP

A volumetric thoracolumbar (T1-L5) FE model with ribcage (Figure 6-1) was constructed from an anatomist-drawn computer-aided design (CAD) model (CGHero Ltd., Manchester, UK) representative of an average asymptomatic adult and tessellated using Hypermesh (Altair Engineering, Troy, MI, USA). Each vertebra consists of posterior elements, cancellous bone, and cortical bone, comprised of tetrahedral, hexahedral, and a triangular/quadrilateral hybrid element formulations respectively. Three growth plate layers were situated inferior and superior to all intervertebral discs (IVDs) in the FE model (Figure 6-2). Each layer was given uniform thickness for a total thickness of 0.62mm (Abolaeha et al., 2012). The IVD consists of the nucleus pulposus and the annulus fibrosus, both of which were meshed using hexahedral elements. On average, the transverse cross-sectional area and volume of the nucleus pulposus relative to the IVD were approximately 33% and 40% respectively. Annulus fibers were also embedded within the annulus fibrosus of each disc using cables and were dimensioned to make up 16% of the total annulus fibrosus volume. Their stress-strain characterization

(Figure 6-3(a)) as well as cable cross-sections were assigned scale factors over 8 annulus fibrosus layers based on their position concentric to the nucleus pulposus (Shirazi-Adl et al., 1986). All the ribcage components were configured using hexahedral elements, with the exception of the intercostal muscles, which were charactered using shell elements. Material properties for the ribcage, all vertebrae and IVDs were acquired from literature (Table 6-1). Both intervertebral (Table 6-2) and costovertebral ligaments (Table 6-3) were characterized using cable elements. Accordingly, stress-strain curves were generated and assigned among four spinal regions: T1-T4, T5-T8, T9-T12, and L1-L5 (Figure 6-3b to 6-3e). Generating the strain required scaling displacement values by the average initial unstretched length of all FE model cables in each ligament group, while the stress required scaling force values by the cross-sectional area appropriate for each spinal region. The stress-strain values were divided by the number of elements in each ligament group. To map the spine from an adult to an adolescent, scale factors for the vertebrae, IVD, and ligaments were applied from derived factors acquired from Liu and Kang (2002) for a 15-year-old adolescent. Complete information on all aforementioned entities as well as the source for all ligament cross sections is found in Tables 1-3. The average element size of the entire model was 1.7mm. In total, the model contained 460,828 elements and 290,993 nodes. The study was then conducted in two phases.

6.3.2 SCOLIOSIS INDUCTION

To set up the asymptomatic spine model for scoliosis induction using LS-DYNA implicit v971 R10.1, a 6mm right lateral displacement was initially imposed on T8, a typical apex vertebra in a thoracolumbar scoliotic deformity. Next, a series of cables were

set up such that they were vertically positioned coronally, followed the spinal curve sagittally, and were rigidly connected using the sagittal and axial positions of all vertebrae centroids (Figure 6-4). The stress-strain curve for all cables (Figure 6-3f) was derived using a linear stiffness vs. force curve and scaled by the average cable length of 27.8 mm from the FE model and the physiological cross-sectional area of 1000 mm^2 for the rectus abdominis muscle as characterized in Brown and McGill (2005). An iterative approach was implemented to simulate vertebral body growth over the course of a year using three-month intervals. The boundary conditions for T1 allowed pin rotations and vertical translation only, while L5 was completely fixed. The first step in each iteration involves pretension of all cables. The amount of pretension in each cable uses the weight distribution summarized in Schultz et al., (1982) beginning with a 14% body weight applied on T1. Caudally, from T1 to L5, pretension was increased by a magnitude of approximately 2.6% body weight per vertebra. The weight listed in Liu and Kang (2002) for a 15-year-old adolescent (e.g., 527.8 Newtons) was utilized. Since the gender wasn't specified in the source, this weight value was verified with Center for Disease Control (CDC) weight-for-age percentile data and was within range between a 50th percentile female and male (CDC, 2000). Vertical element stresses on all growth plate sensitive layers were recorded and input into the Stokes' growth modulation equation (Stokes, 1990) (Equation 1) using MATLAB (Mathworks, Natick, MA, USA) to calculate growth within each adjacent newly formed layer. In applying vertebral growth, strain-based thermal expansion was applied normal to all vertebrae, or in local-z directions (Figure 6-4b),within all newly formed growth plate layers (Equation 2). After each preload and growth step, spinal deformity profiles were output and used as input for each subsequent

step. All soft tissue and vertebral stresses were reset to zero, assuming stress relaxation of soft tissues (Carrier et al., 2004). The input parameters for the aforementioned equations can be found in Table 6-1. Three extra iterations were performed to produce a mild scoliosis deformity.

$$G_i = G_m * (1-\beta*(\sigma_i-\sigma_m)) \qquad \text{(Equation 6-1)}$$
$$\varepsilon = (G_i*t)/L_{init} = \alpha*\Delta T \qquad \text{(Equation 6-2)}$$

6.3.3 ASYMPTOMATIC AND SCOLIOTIC KINEMATIC ANALYSES

Next, the asymptomatic and scoliotic spines were quasi-statically rotated within the three anatomic planes using an external moment of 2 N-m along the T1 superior facet processes and endplate. T1, in this case, was completely free while L5 remained fixed in all degrees of freedom. A follower preload was imposed using cables attached to all vertebral centroids and using the same load distribution profile to induce scoliosis as previously described. Flexion, extension, left and right lateral bending, and left and right axial rotations were imposed on both spine FE models. Translation data was taken from nodes on the spinous process tips of each vertebra to convert to sagittal and coronal rotations and superior growth plate transition layers of each vertebra to convert to axial rotations relative to a fixed coordinate system at L5. Global in-plane, global out of plane, and intervertebral in-plane rotations were output and compared between the asymptomatic and scoliotic spines.
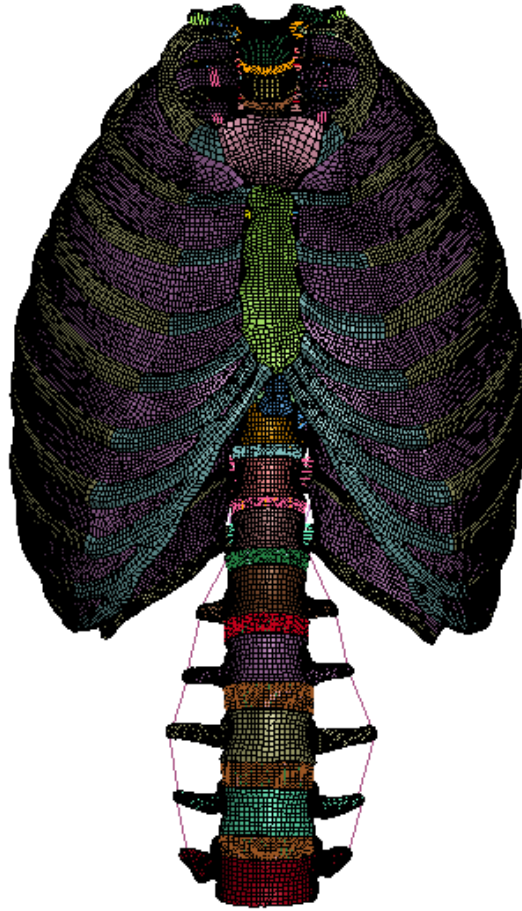
Figure 6-1: Asymptomatic thoracolumbar FE model.
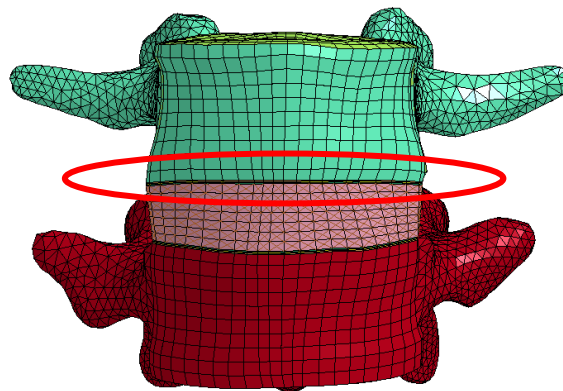
(a)
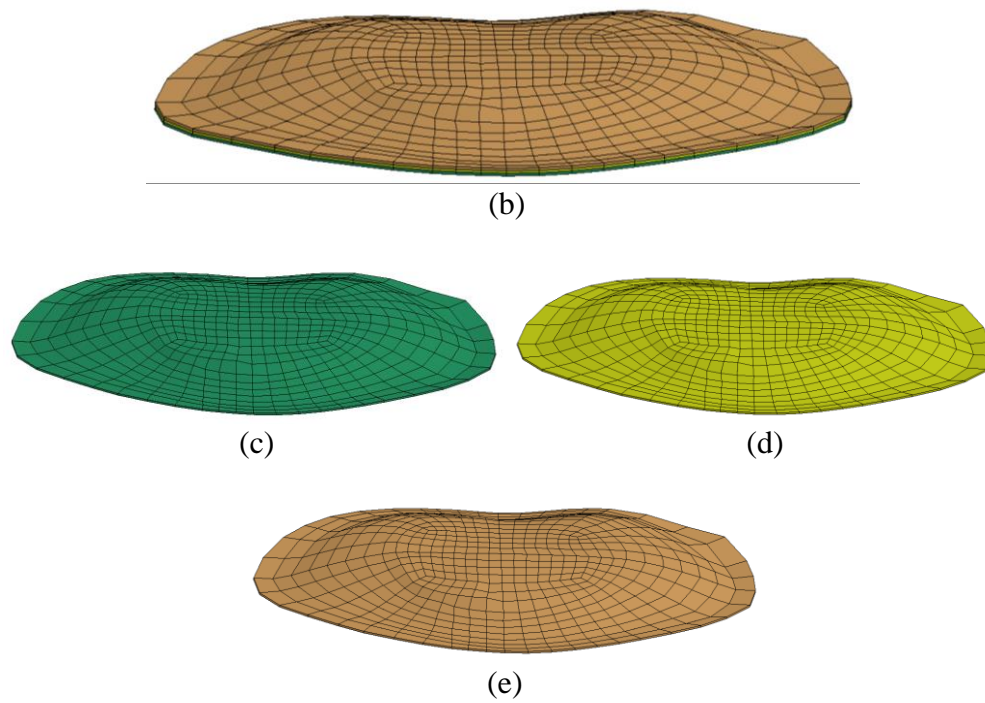
Figure 6-2: (a) Functional spinal unit. (b) Growth plate. (c) Sensitive layer. (d). Newly formed layer. (e) Transition layer. The sensitive layer sits adjacent to the IVD, the newly formed layer is sandwiched between the sensitive and transition layers, and the transition layer is adjacent to each vertebra.
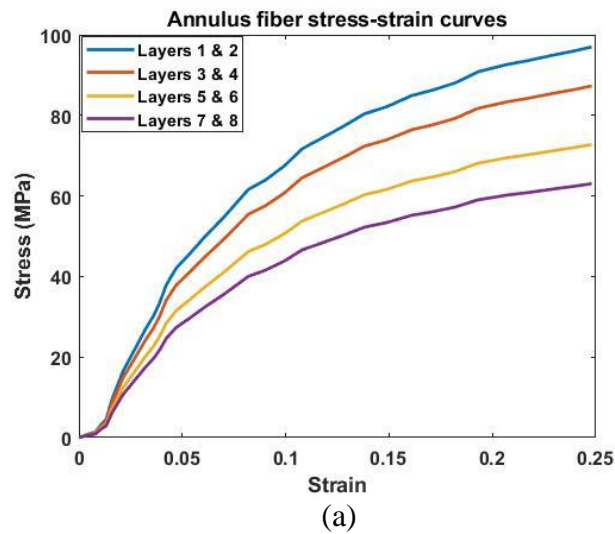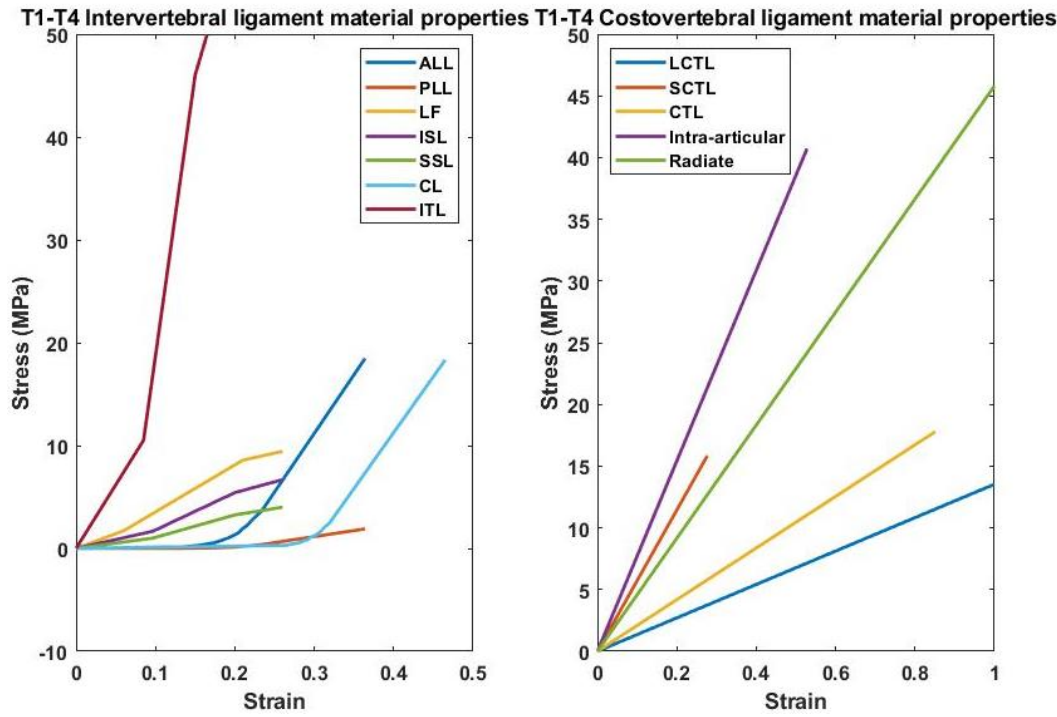
(b)
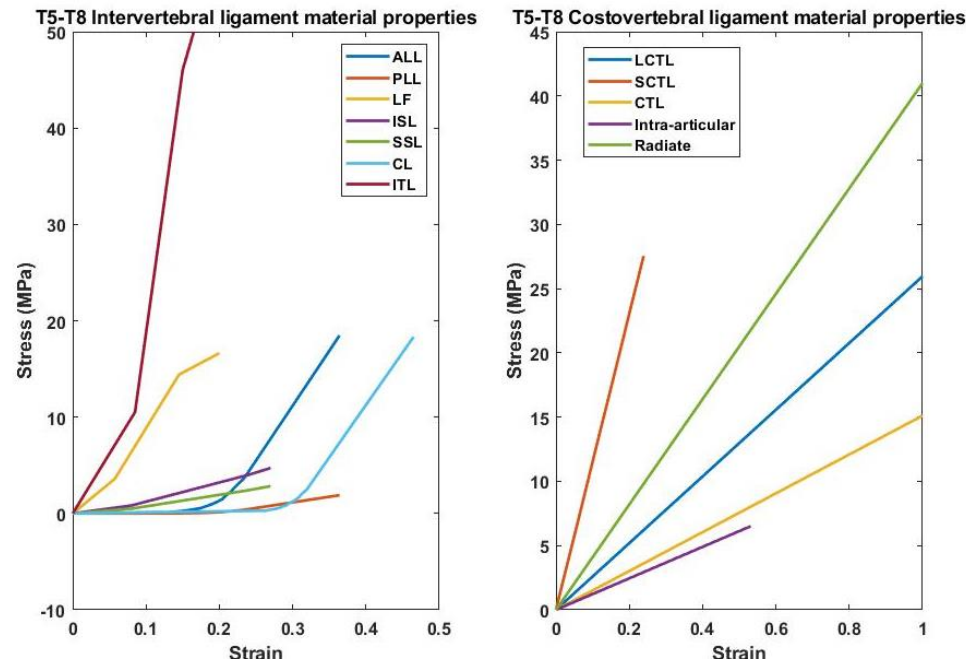
(c)
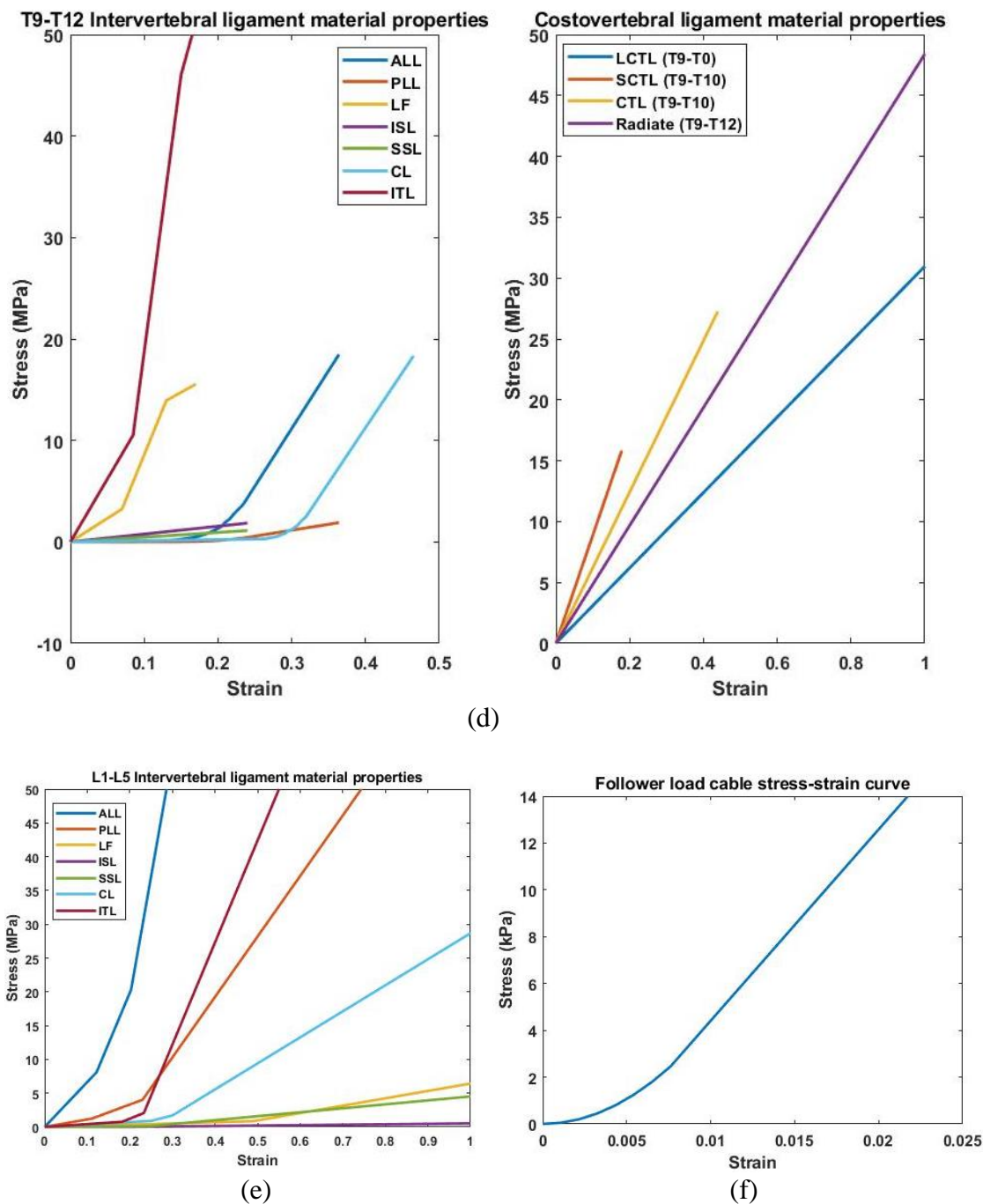
Figure 6-3: (a) Annulus Fiber stress-strain curves. (b) T1-T4 Intervertebral &
Costovertebral ligament stress-strain curves. (c) T5-T8 Intervertebral & Costovertebral
ligament stress-strain curves. (d) T9-T12 Intervertebral & Costovertebral ligament stress-
strain curves. Costotransverse ligaments are not present below T10. (e) L1-L5
Intervertebral ligament stress-strain curves. (f) Cable tension stress-strain curve.
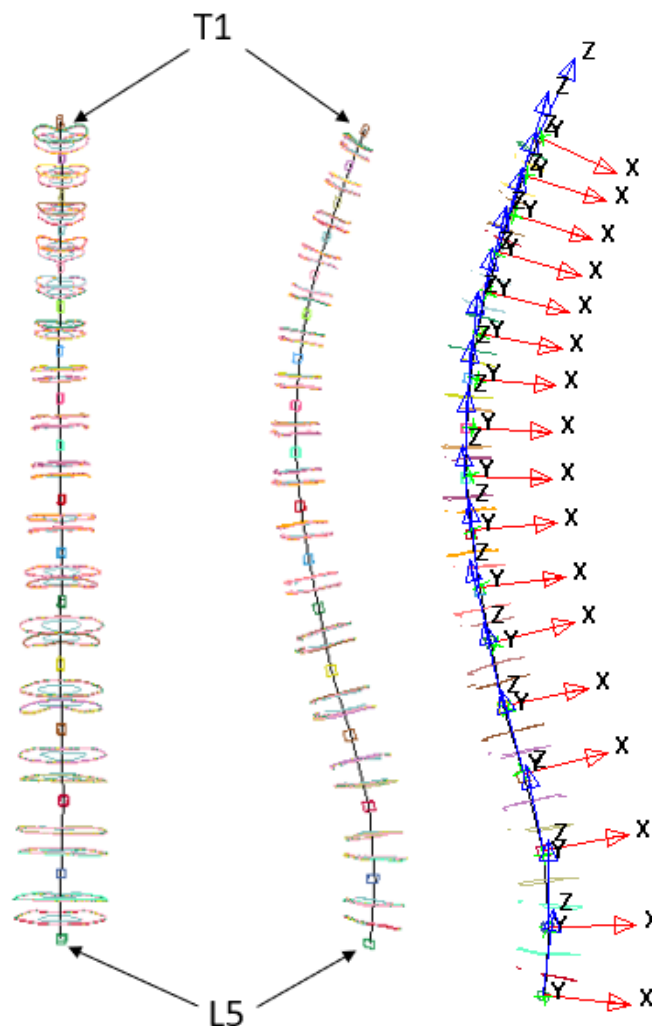
Figure 6-4: (a) Coronal view (left) and sagittal view (right) of cables (black) attached to rigid bodies in vertebral centers and tangent to spinal curve. (b) Sagittal view with vertebral coordinate systems.

Table 6-1. Vertebral, IVD, and ribcage material properties.

*Denotes properties incorporating scale factors appropriate for a 15-year-old (Liu & Kang, 2002).

	Material Properties	**Source**
Cortical Bone*	E=11.412 GPa, v=0.3	Naserkhaki et al., 2018
Cancellous Bone*	E=190.2 MPa, v=0.315	Naserkhaki et al., 2018
Annulus Fibrosus*	C10=0.1712 MPa, C01=0.0428 MPa, v=0.45	Schmidt et al., 2006

Table 6-1 continued.

Nucleus Pulposus	C10=0.12 MPa, C01=0.03 MPa, v=0.4999	Schmidt et al., 2006
Growth Plate-Sensitive Layer	E=12 MPa, v=0.3	Shi et al., 2011
Growth Plate-Newly Formed Layer	E=100 MPa, v=0.3	Shi et al., 2011
Growth Plate-Transition Layer	E=300 MPa, v=0.3	Shi et al., 2011
Intercostal Muscle	E=1.03 MPa, t=3mm	Kindig et al., 2015
Ribs*	E=11.4 GPa, v=0.35	Schlager et al., 2018
Costal Cartilage*	E=23.8 MPa, v=0.45	Meijer, 2011
Sternum*	E=2.38 GPa, v=0.3	Jansova et al., 2015

Table 6-2: Intervertebral ligament properties in FE Model.

^Denote force-displacement curves from Rohlmann (2006b) are used, but average cross-sectional areas from Goel (1995) were used to scale to stress and average length was used to scale to strain.

*The stress-strain curves from Shirazi-Adl (1986) were utilized, but the average cross-sectional areas from Chazal (1985) were used to scale the stress.

Ligament nomenclature is as follows: ALL-Anterior Longitudinal Ligament; PLL-Posterior Longitudinal Ligament; LF-Ligamentum Flavum; ISL-Interspinous Ligament; SSL-Supraspinous Ligament; CL-Capsular Ligament; ITL-Intertransverse Ligament.

Ligament	Vertebral levels	Average Length (mm)	Adolescent Scale factor	Cross-sectional area (mm^2)	Cross-sectional area source	No. of ligaments per segment
ALL	L1-L5	12.513	0.974	63.7	Goel (1995)^	13
	T9-T12	6.646	0.974	25	Shirazi-Adl (1986)*	7
	T7-T9	4.893	0.974	30	Shirazi-Adl (1986)*	7
	T5-T7	4.711	0.974	30	Shirazi-Adl (1986)*	5
	T1-T4	4.58	0.974	36	Shirazi-Adl (1986)*	5
PLL	L1-L5	7.787	0.974	20	Goel (1995)^	7
	T12-L1	4.533	0.974	19	Shirazi-Adl (1986)*	7
	T11-T12	4.2	0.974	19	Shirazi-Adl (1986)*	7
	T9-T11	4.643	0.974	19	Shirazi-Adl (1986)*	3
	T5-T8	4.07	0.974	17	Shirazi-Adl (1986)*	3
	T1-T4	3.511	0.974	10	Shirazi-Adl (1986)*	3

Table 6-2 continued.

LF	L1-L5	23.115	0.974	40	Goel (1995)^	3
	T9-T12	28.413	0.974	30	Chazal (1985)	3
	T5-T8	22.929	0.974	24.75	Chazal (1985)	3
	T1-T4	18.716	0.974	34	Chazal (1985)	3
ISL	L1-L5	7.155	0.974	40	Goel (1995)^	4
	T9-T12	12.144	0.974	29.5	Chazal (1985)	5
	T5-T8	5.516	0.974	29.5	Chazal (1985)	5
	T1-T4	8.145	0.974	8.333	Chazal (1985)	5
SSL	L1-L5	15.932	0.974	30	Goel (1995)^	3
	T9-T12	26.156	0.974	29.5	Chazal (1985)	3
	T5-T8	21.669	0.974	29.5	Chazal (1985)	3
	T1-T4	22.602	0.974	8.333	Chazal (1985)	3
CL	L4-L5	2.573	0.974	30	Goel (1995)^	16 (per side)
	L3-L4	3.348	0.974	30	Goel (1995)^	16 (per side)
	L2-L3	3.717	0.974	30	Goel (1995)^	16 (per side)
	L1-L2	2.712	0.974	30	Goel (1995)^	16 (per side)
	T12-L1	1.56	0.974	36	Shirazi-Adl (1986)*	12 (per side)
	T11-T12	2.139	0.974	36	Shirazi-Adl (1986)*	12 (per side)
	T10-T11	2.648	0.974	36	Shirazi-Adl (1986)*	16 (per side)
	T9-T10	3.239	0.974	36	Shirazi-Adl (1986)*	16 (per side)
	T8-T9	2.673	0.974	36	Shirazi-Adl (1986)*	13 (per side)
	T7-T8	2.562	0.974	36	Shirazi-Adl (1986)*	12 (per side)
	T6-T7	2.655	0.974	36	Shirazi-Adl (1986)*	12 (per side)
	T5-T6	1.91	0.974	36	Shirazi-Adl (1986)*	12 (per side)
	T4-T5	1.958	0.974	36	Shirazi-Adl (1986)*	11 (per side)
	T3-T4	1.708	0.974	36	Shirazi-Adl (1986)*	10 (per side)
	T2-T3	2.402	0.974	36	Shirazi-Adl (1986)*	12 (per side)
	T1-T2	2.842	0.974	36	Shirazi-Adl (1986)*	12 (per side)
ITL	L1-L5	26.839	0.974	1.8	Goel (1995)^	1 (per side)
	T1-T12	16.489	0.974	1.85	Chazal (1985)	1 (per side)

Table 6-3. Costovertebral ligament properties in FE Model.

^The force-displacement curves from Aira (2019) are utilized, but the cross-sectional areas from Meijer (2011) were used to scale to stress and the average length was used to scale to strain.

Ligament nomenclature is as follows: SCTL-Superior Costotransverse Ligament; LCTL-Lateral Costotransverse Ligament; CTL-Costotransverse Ligament; Intra-articular ligament, & Radiate Ligament.

Ligament	Vertebral levels	Average length (mm)	Adolescent Scale factor	Cross-sectional area (mm^2)	Cross-sectional area source	No. of elements per segment per side
SCTL	T1-T4	11.597	0.974	10	Meijer (2011)	3
	T5-T8	13.13	0.974	10	Meijer (2011)	3
	T9-T10	17.968	0.974	10	Meijer (2011)	3
LCTL						
	T1-T4	2.61525	0.974	10	Meijer (2011)	10
	T5-T8	2.105	0.974	10	Meijer (2011)	10
	T9-T10	3.1755	0.974	10	Meijer (2011)	10
CTL						
	T1-T2	4.383	0.974	10	Meijer (2011)	4
	T2-T3	2.067	0.974	10	Meijer (2011)	6
	T3-T4	3.018	0.974	10	Meijer (2011)	5
	T4-T5	2.116	0.974	10	Meijer (2011)	4
	T5-T6	1.941	0.974	10	Meijer (2011)	6
	T6-T7	2.555	0.974	10	Meijer (2011)	6
	T7-T8	3.074	0.974	10	Meijer (2011)	6
	T8-T9	3.736	0.974	10	Meijer (2011)	6
	T9-T10	6.221	0.974	10	Meijer (2011)	6
	T10-T11	4.988	0.974	10	Meijer (2011)	4
Intra-articular	T1-T4	5.38	0.974	10	Meijer (2011)	2
	T5-T8	6.005	0.974	10	Meijer (2011)	2
Radiate						
	T1-T2	4.693	0.974	10	Meijer (2011)	8
	T2-T3	2.645	0.974	10	Meijer (2011)	8
	T3-T4	3.635	0.974	10	Meijer (2011)	9
	T4-T5	3.792	0.974	10	Meijer (2011)	8
	T5-T6	3.645	0.974	10	Meijer (2011)	8
	T6-T7	3.07	0.974	10	Meijer (2011)	8
	T7-T8	3.427	0.974	10	Meijer (2011)	10
	T8-T9	2.72	0.974	10	Meijer (2011)	10

Table 6-3 continued.

	T9-T10	3.488	0.974	10	Meijer (2011)	10
	T10-T11	4.977	0.974	10	Meijer (2011)	10
	T11-T12	4.116	0.974	10	Meijer (2011)	10
	T12-L1	3.494	0.974	10	Meijer (2011)	12

Table 6-4: Definitions and assigned values to growth modulation equations 6-1 and 6-2.

Parameter name	Meaning	Value	Reference
G_i	Element growth rate	Derived from Matlab script	N/A
G_m	Growth rate for asymptomatic spine	0.8 mm/yr (thoracic) 1.1 mm/yr (lumbar)	Shi et al., 2011
β	Stress sensitivity factor	1.5 Mpa^{-1}	Stokes, 2007
σ_i	Growth plate stress on scoliotic spine	Derived from FE model	N/A
σ_m	Growth plate stress on asymptomatic spine	0.5 MPa	Shi et al., 2011
t	Elapsed time	0.25 yr (e.g., 3 mo)	N/A
L_{init}	Initial newly formed layer thickness per iteration	Derived from scoliotic FE model	N/A
α	Thermal expansion coefficient	27.5e-6 /°C	Fok et al., 2010
ΔT	Temperature difference	Derived from Matlab script	N/A

6.4 RESULTS

6.4.1 SCOLIOTIC SPINE FORMATION

After one year of modulated growth, a Lenke Type 1A (Lenke et al., 2003) right thoracic curve was produced with an approximately 22° Cobb angle (Figure 6-5). The kyphosis angle between the asymptomatic and scoliotic model was reduced from

approximately 52° to 47° respectively. A deformity apex was produced at T10-T11, with a maximum wedge angle of approximately 4.7° within the intervertebral disc. A small wedge angle less than 0.5° was produced in the apical vertebra of T10. Both measurements were taken from the inferior and superior endplates of both the disc and vertebra. The scoliotic FE model after 9 months of modulated growth is compared with a general CT scan of an adult with a right thoracic curve (Loeffler et al., 2020; Sekuboyina et al., 2020; Sekuboyina et al., 2021). The Cobb angles, measured between the T7 superior endplate and the L1 inferior endplate in both images, amounted to 14.6° in the CT scan and 13.7° in the FE model. The Cobb angle in CT scan was measured using 3D Slicer 5.0.2 (National Institutes of Health, Bethesda, MD, USA).

(a)   (b)   (c)

(d)

(e)

(f)

Cobb Angle=13.7°

(g)
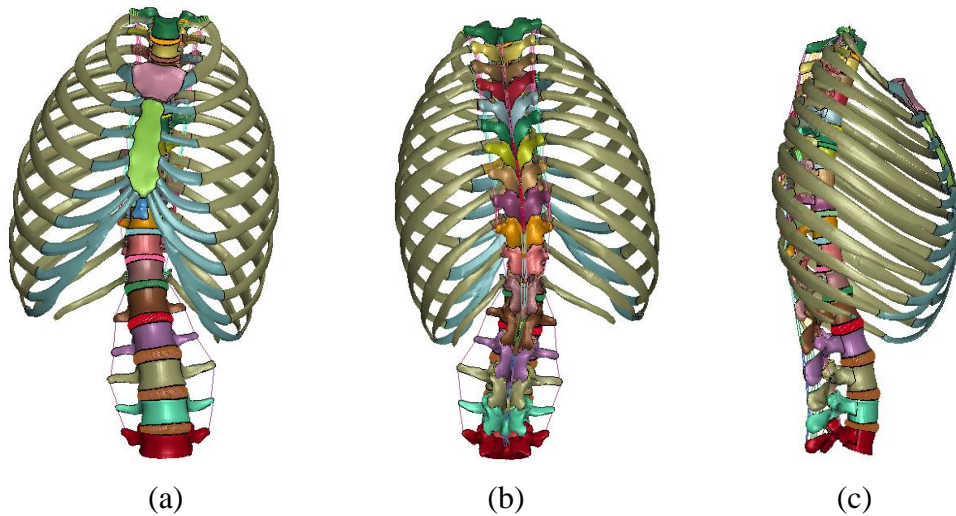
Figure 6-5: (a) Scoliotic FE model anterior view. (b) Scoliotic FE model posterior view. (c) Scoliotic FE model sagittal view. (d) Scoliotic FE axial view. (e) Wedged IVDs (T9-T10 to T12-L1). (f) Coronal adult scoliotic CT dataset (Sekuboyina et al., 2021). (g) FE model comparison after 9 months of growth with CT image.
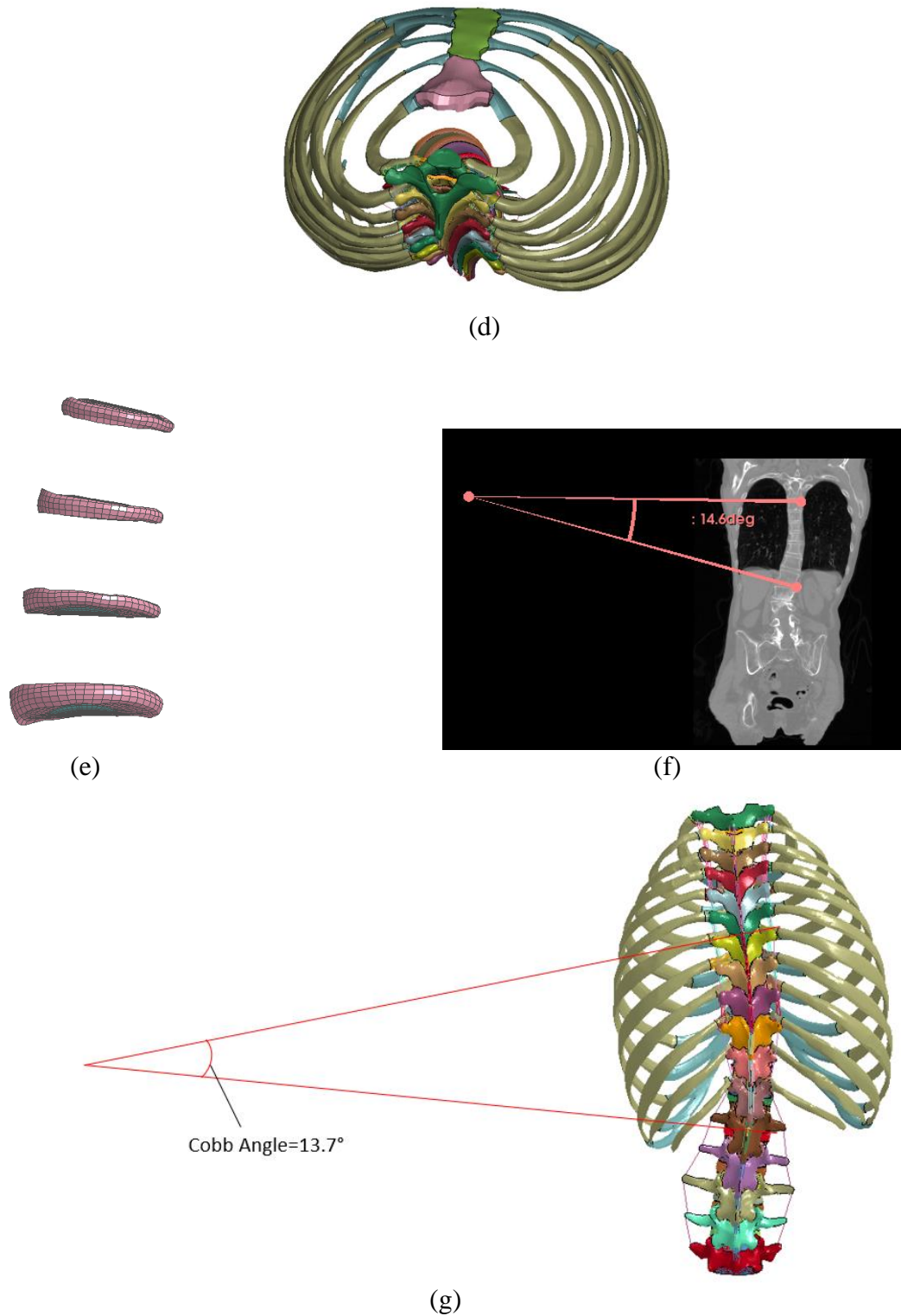
6.4.2 FLEXION & EXTENSION ROTATIONS

The asymptomatic global flexion rotations range between 0.2° and 10.5° between L4 and T1 respectively; left lateral bending and right axial rotations amount to no more than 0.4° and 1° respectively. The scoliotic global flexions range between 0.1° and 7° between L4 and T1; left lateral bending and right axial rotations amount to maximum values of 0.35° and 2.6° respectively. The maximum decrease in flexion of the scoliotic spine was approximately 3.5°; whereas the maximum decrease in left lateral bending and increase in right axial rotation are approximately 0.3° and 2° respectively. The asymptomatic intervertebral rotations during flexion range between 0.2° and 1.4°, the maximum occurring within the T12-L1 segment. The scoliotic intervertebral rotations ranged between 0.1° and 1°, with the maximum rotation occurring at T12-L1. The maximum decrease in intervertebral rotation in the scoliotic spine occurred at L1-L2 at approximately 0.43° relative to the asymptomatic condition.

The asymptomatic global extension rotations range between 0.25° and 14.8° between L4 and T1 respectively; right lateral bending and left axial rotation both amount to no more than 1.1°. The scoliotic global extensions range between 0.37° and 9.3°; right lateral bending and left axial rotation amount to maximum values of 0.67° and 2.6° respectively. The maximum decrease in extension of the scoliotic spine was approximately 5.5° compared to the asymptomatic condition; right lateral bending and left axial rotation saw a maximum decrease and increase of 0.7° and 2.2° respectively. The asymptomatic intervertebral rotations during extension range between 0.25° and 1.5°, the maximum occurring within the T12-L1 segment. The scoliotic intervertebral rotations ranged between 0.37° and 0.77°, the maximum value occurring at both T12-L1

and L1-L2. The maximum decrease in the scoliotic spine was approximately 0.75° at T12-L1 relative to the asymptomatic condition.
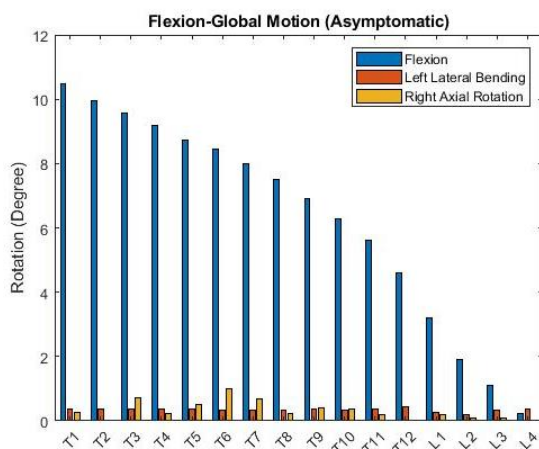
(a)
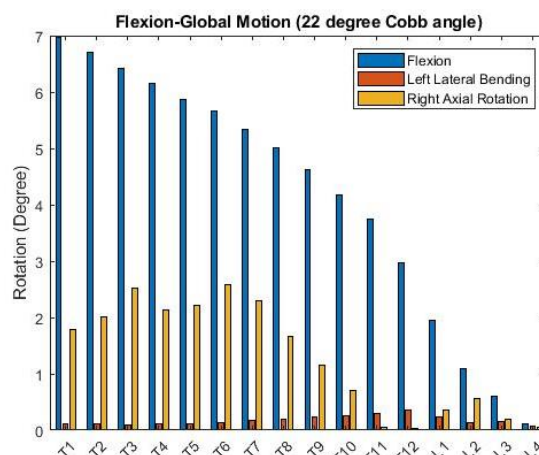
(b)
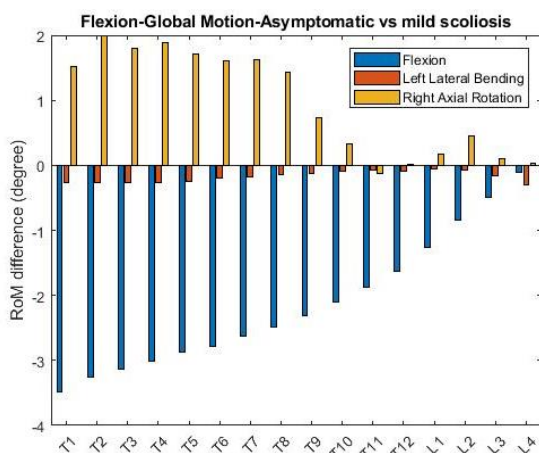
(c)
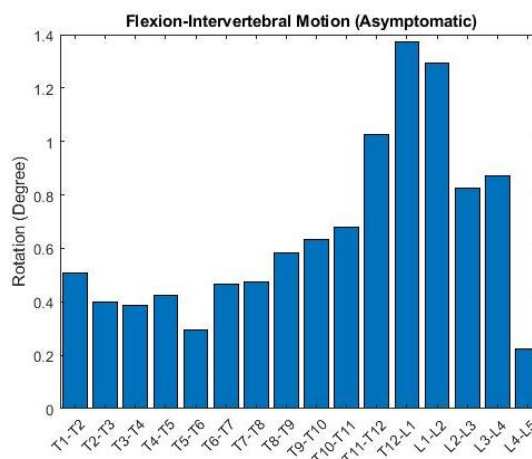
(d)
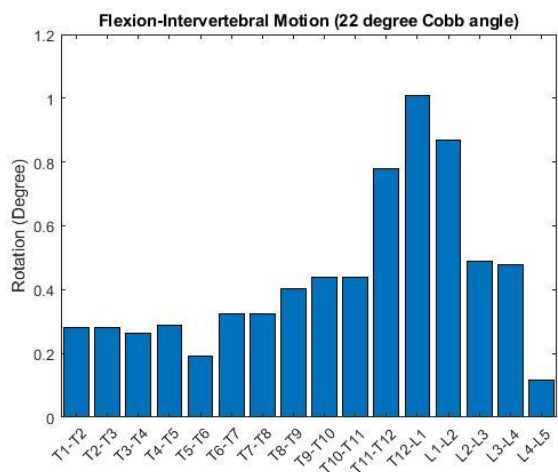
(e)
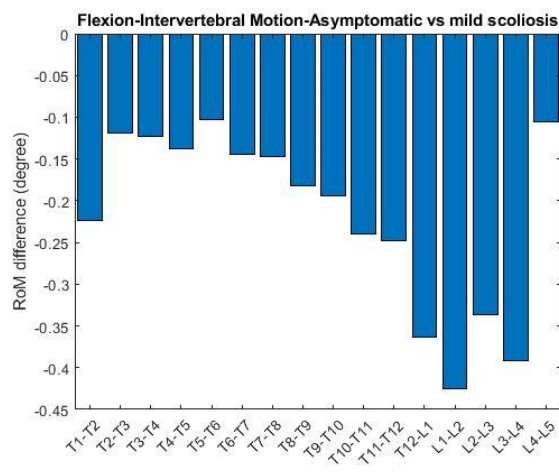
(f)

(g)
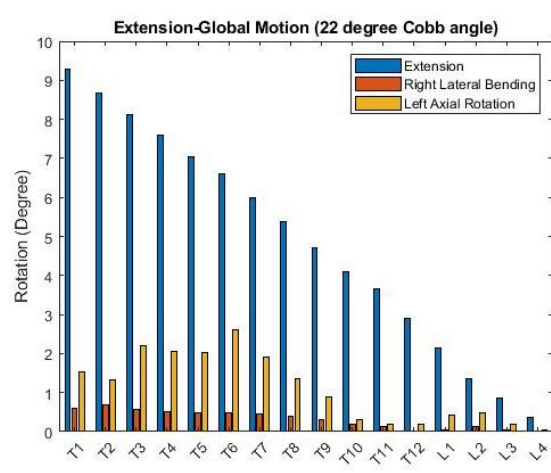
(h)

(i)

(j)

Figure 6-6: In-plane and out-of-plane kinematic segment behavior. (a) Asymptomatic global flexion. (b) Mild scoliotic global flexion. (c) Flexion global RoM differences between mild scoliotic and asymptomatic profiles. (d) Asymptomatic intervertebral flexion. I Mild scoliotic intervertebral flexion. (f) Flexion intervertebral RoM differences between mild scoliotic and asymptomatic profiles. (g) Asymptomatic global extension. (h) Mild scoliotic global extension. (i) Extension global RoM differences between mild scoliotic and asymptomatic profiles. (j) Asymptomatic intervertebral extension. (k) Mild scoliotic intervertebral extension. (l) Extension intervertebral RoM differences between mild scoliotic and asymptomatic profiles.

6.4.3 LEFT AND RIGHT LATERAL BENDING

The asymptomatic global left lateral bending rotations ranged between 0.3° and 12.2° between L4 and T1 respectively; maximum flexion and right axial rotations amount to approximately 0.8° and 3.2° respectively. The scoliotic global left lateral bending rotations ranged between 0.3° and 6.6° between L4 and T1 respectively; maximum flexion and right axial rotations amount to approximately 0.2° and 1.6° respectively. In the scoliotic spine, the maximum decrease in left lateral bending was 5.5°, 0.2° in flexion, and 1.8° in right axial rotation all relative to the asymptomatic condition. The asymptomatic intervertebral rotations range between 0.26° and 1.5°, with the maximum rotation occurring at T12-L1. The scoliotic intervertebral rotations ranged between 0.2°

and 0.8° with the maximum rotation occurring at L1-L2. The maximum decrease in intervertebral rotations was 0.76° in the scoliotic spine relative to the asymptomatic condition.

The asymptomatic global right lateral bending rotations ranged between 0.4° and 11.9° between L4 and T1 respectively; maximum flexion and left axial rotations amounted to approximately 0.8° and 2.6° respectively. The scoliotic global right lateral bending rotations ranged between 0.26° and 7.3° between L4 and T1; maximum flexion and left axial rotations ranged between 0.3° and 1.7° respectively. The maximum decrease in rotations within the scoliotic spines amount to 4.6° in right lateral bending, 0.63° in flexion, and 1.15° in left axial rotation relative to the asymptomatic condition. The asymptomatic intervertebral rotations range between 0.37° and 1.5°, the maximum rotation occurring at approximately L1-L2. The scoliotic intervertebral rotations ranged between 0.16° and 0.77°, with the maximum value occurring at T11-T12. The maximum decrease in intervertebral rotations was approximately 0.73° at both T12-L1 and L1-L2 within the scoliotic spine relative to the asymptomatic condition.
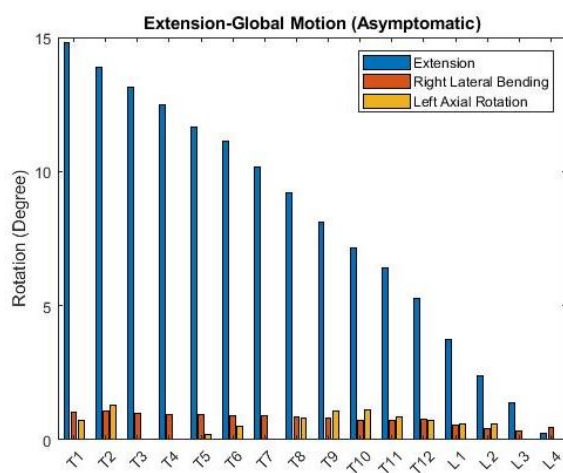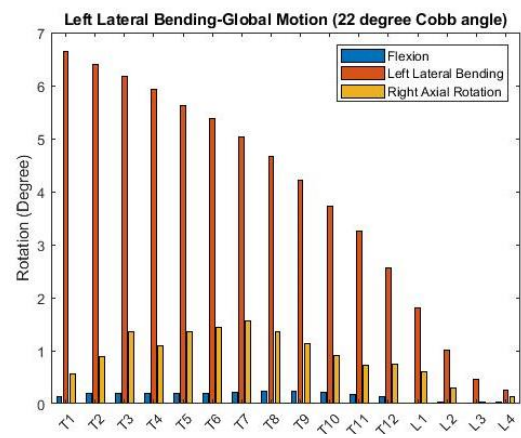

(a)   (b)
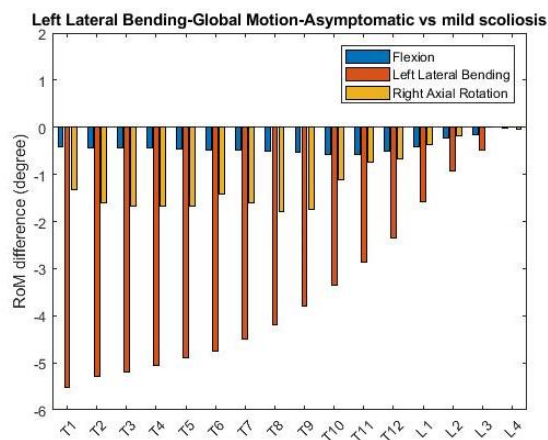
(c)
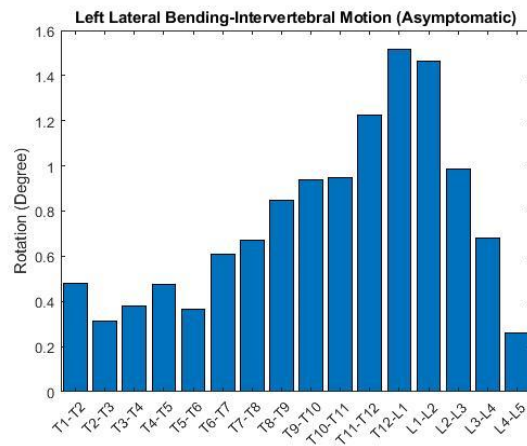
(d)

(e)
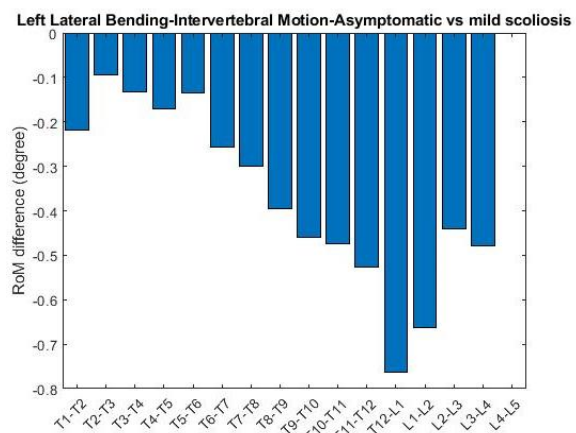
(f)
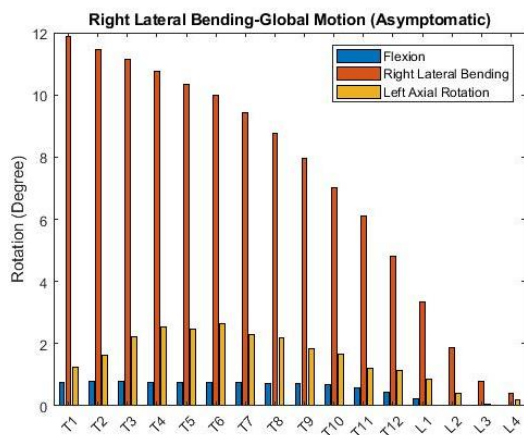
(g)
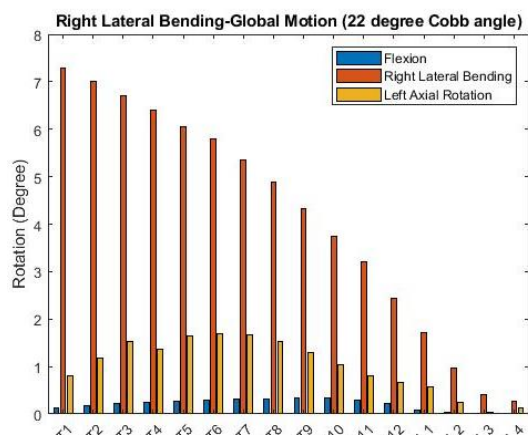
(h)
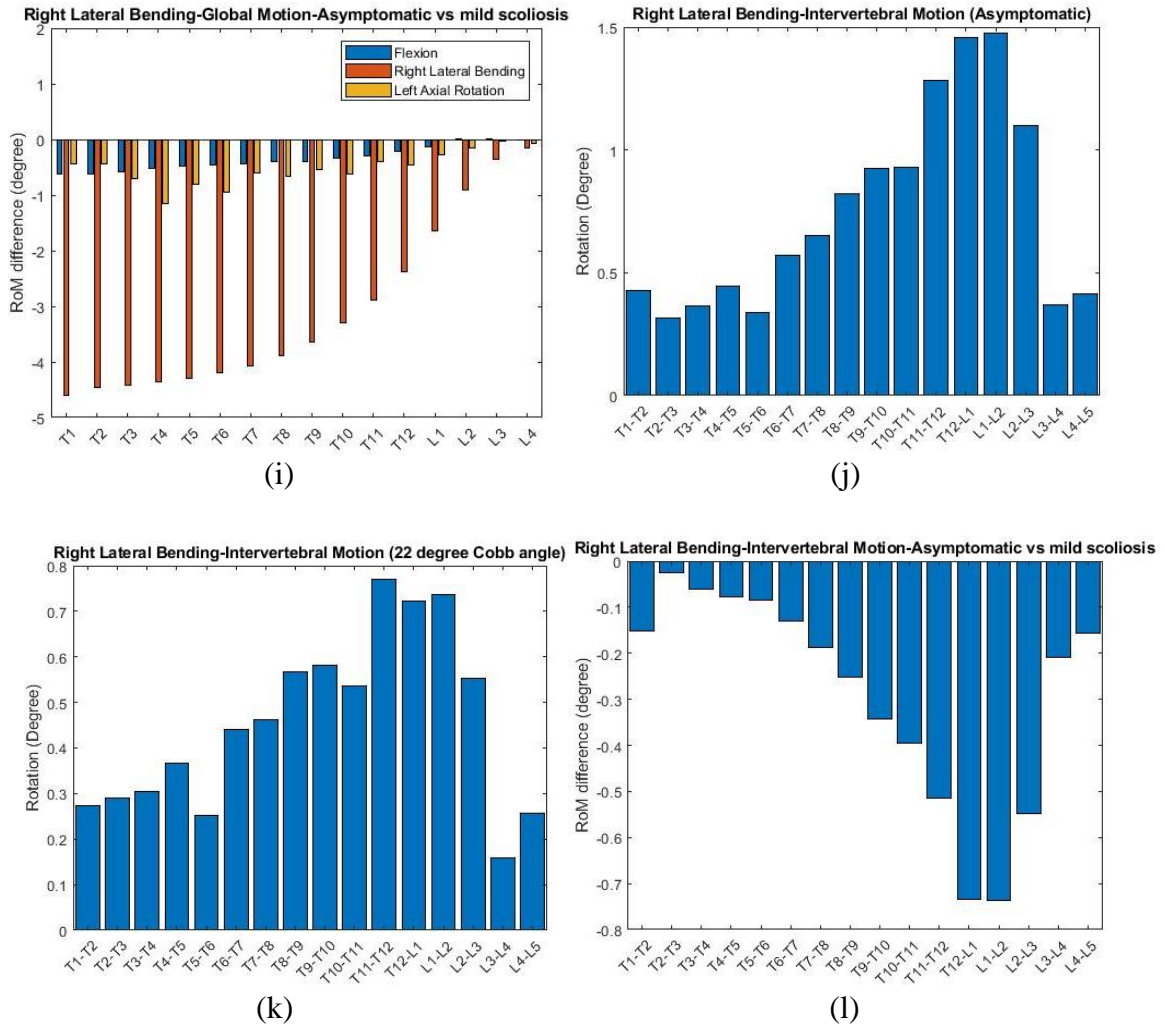
Figure 6-7: In-plane and out-of-plane kinematic segment behavior. (a) Asymptomatic global left lateral bending. (b) Mild scol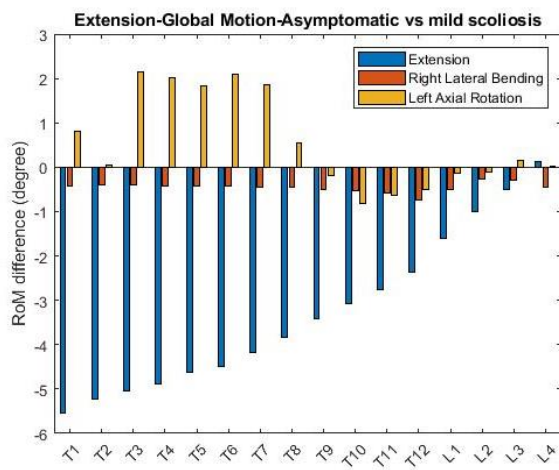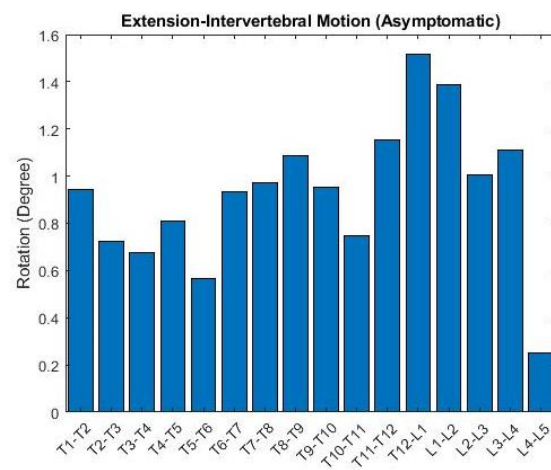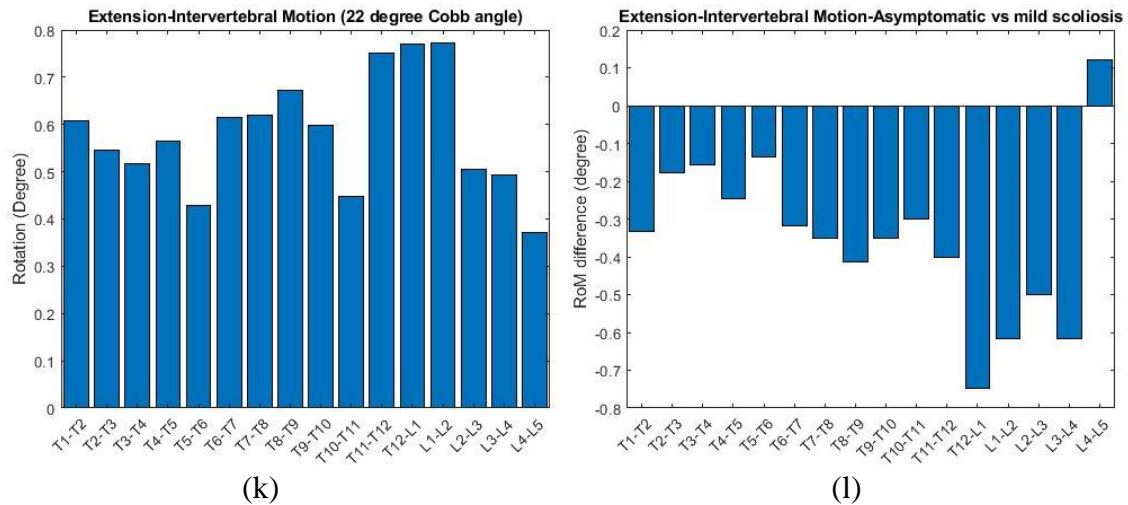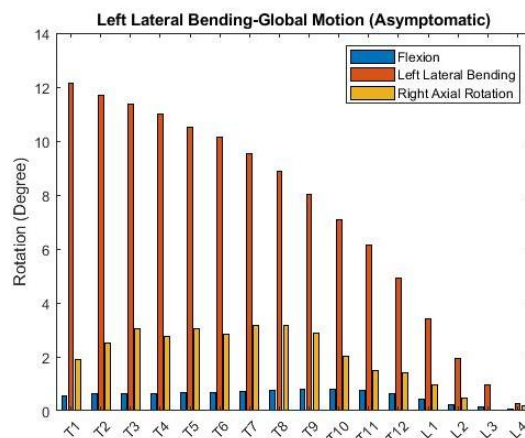iotic global left lateral bending. (c) Left lateral bending global RoM differences between mild scoliotic and asymptomatic profiles. (d) Asymptomatic intervertebral left lateral bending. (e) Mild scoliotic intervertebral left lateral bending. (f) Left lateral bending intervertebral RoM differences between mild scoliotic and asymptomatic profiles. (g) Asymptomatic global left lateral bending. (h) Mild scoliotic global left lateral bending. (i) Right lateral bending global RoM differences between mild scoliotic and asymptomatic profiles. (j) Asymptomatic intervertebral right lateral bending. (k) Mild scoliotic intervertebral right lateral bending. (l) Right lateral bending intervertebral RoM differences between mild scoliotic and asymptomatic profiles.

5.4.4 LEFT AND RIGHT AXIAL ROTATION

The asymptomatic global left axial rotation ranges between 0.95° and 13.9° between L4 and T1 respectively; the maximum flexion and right lateral bending rotations amounted to 1.6° and 2.3° respectively. The scoliotic global left axial rotation ranges between 0.45° and 10.9°; the maximum flexion and right lateral bending rotations were approximately 0.9° and 1.9° respectively. In the scoliotic spine relative to the asymptomatic spine, the maximum decrease in global left axial rotation was 3.1°, 1.3° in flexion and 0.87° in right lateral bending. The asymptomatic intervertebral rotations ranged between 0.15° and 1.6°, with the maximum rotations occurring at T1-T2 and T10-T11. The scoliotic intervertebral rotations ranged between 0.25° and 1.5°, with the maximum rotation occurring at T10-T11. The maximum decrease in intervertebral rotations within the scoliotic spine occurred at T1-T2 with 0.66°, however, a few increases in intervertebral rotations are present, the maximum occurring at T12-L1 with 0.48°.

The asymptomatic global right axial rotation ranges between 0.8° and 14.2° between L4 and T1 respectively; the maximum flexion and left lateral bending rotations amounted to 1.3° and 2.4° respectively. The scoliotic global right axial rotation ranges between 0.56° and 10° between L4 and T1 respectively; the maximum flexion and left lateral bending rotations amounted to 0.43° and 1.8° respectively. The maximum decrease in global right axial rotation was 4.2°, 1.1° in flexion, and 0.6° in left lateral bending. The asymptomatic intervertebral rotations ranged between approximately 0.2° and 1.7°, with the maximum rotation occurring at T1-T2. The scoliotic intervertebral rotations ranged between approximately 0.32° and 1.1°, with the maximum rotation

occurring at T12-L1. The maximum decrease in intervertebral rotations was 0.95° at T9-T10, however, a maximum increase of approximately 0.62° was present at T12-L1.
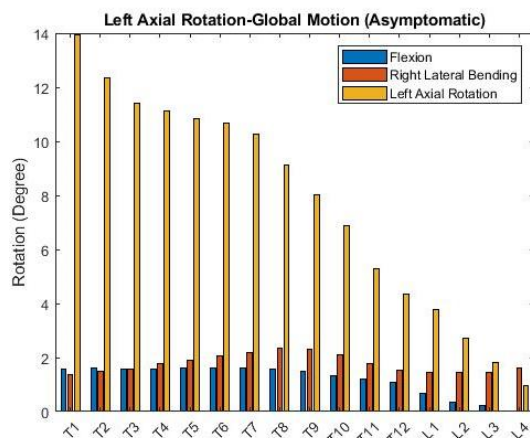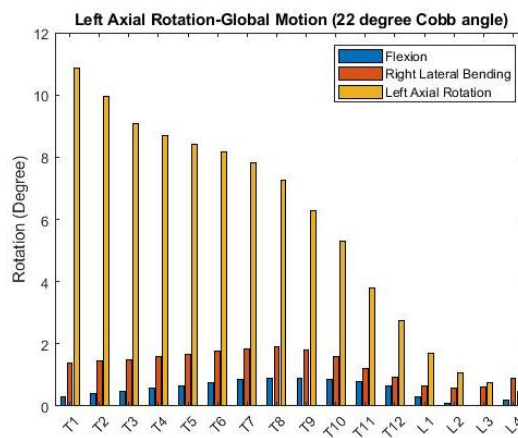
(a)   (b)
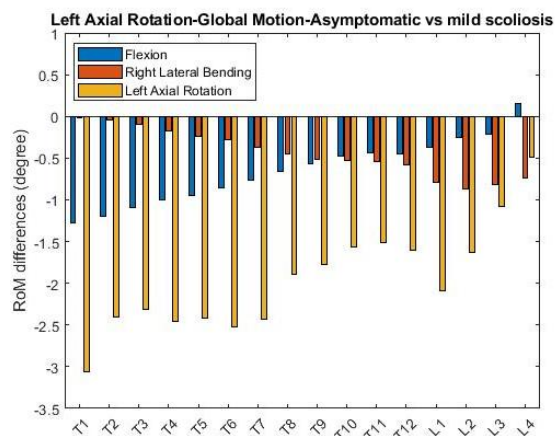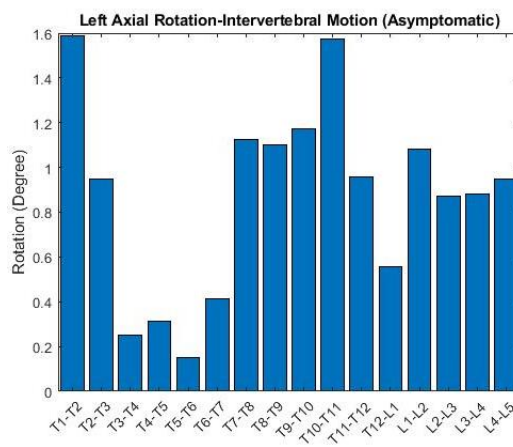
(c)   (d)
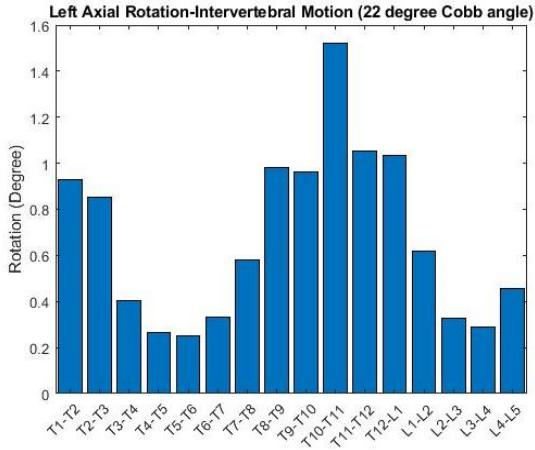
(e)
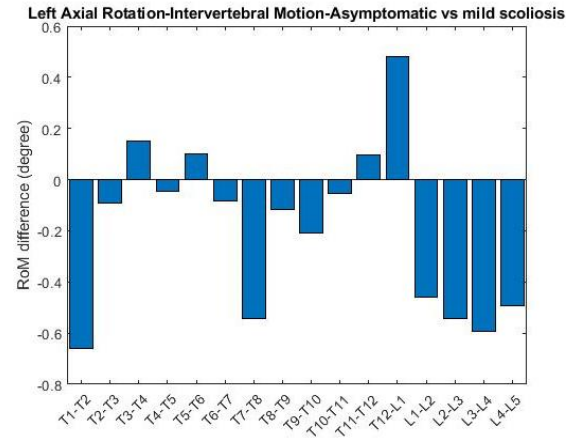
(f)
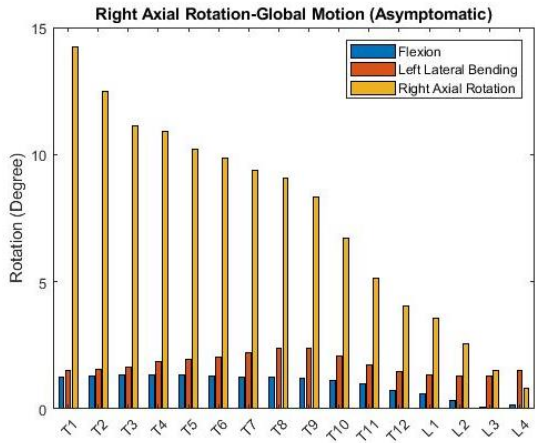
(g)
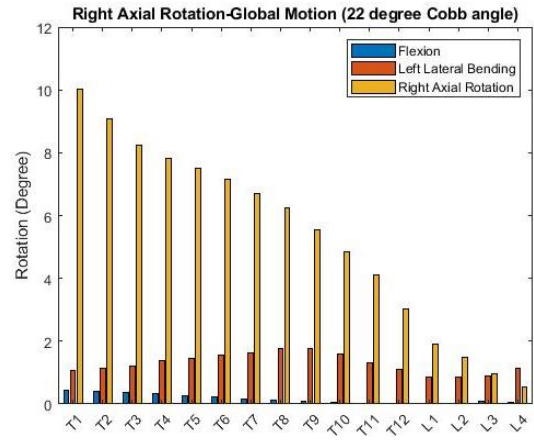
(h)
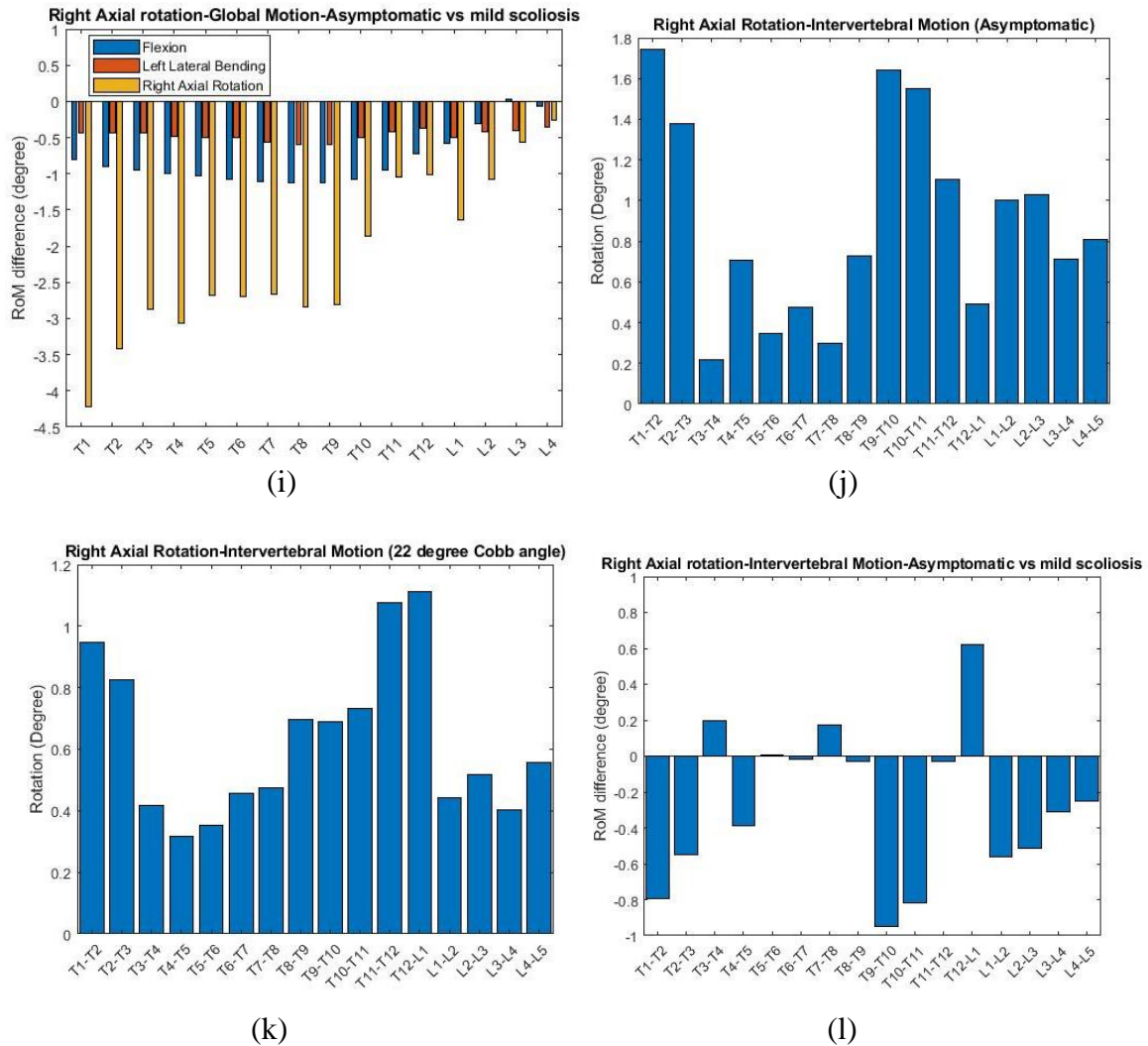
Figure 6-8: In-plane and out-of-plane kinematic segment behavior. (a) Asymptomatic global left axial rotation. (b) Mild scoliotic global left axial rotation. (c) Left axial rotation global RoM differences between mild scoliotic and asymptomatic profiles. (d) Asymptomatic intervertebral left axial rotation. (e) Mild scoliotic intervertebral left axial rotation. (f) Left axial rotation intervertebral RoM differences between mild scoliotic and asymptomatic profiles. (g) Asymptomatic global left axial rotation. (h) Mild scoliotic global left axial rotation. (i) Right axial rotation global RoM differences between 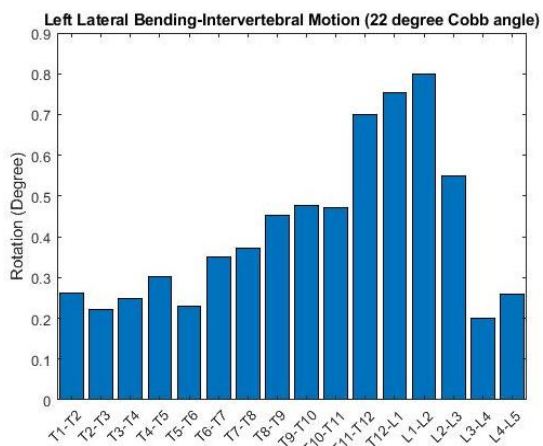mild scoliotic and asymptomatic profiles. (j) Asymptomatic intervertebral right axial rotation. (k) Mild scoliotic intervertebral right axial rotation. (l) Right axial rotation intervertebral RoM differences between mild scoliotic and asymptomatic profiles.

6.5 DISCUSSION

An assessment of kinematics within a scoliotic spine is needed to further understand the progression of the deformity within a patient as well as enhance decision making for treatment options, including for surgical correction. To the author's knowledge, a full kinematic assessment and comparison has not been performed with an asymptomatic, or healthy, spine using a thoracolumbar FE osseoligamentous model. The novelty of the study highlights both in-plane and out-of-plane rotations using sagittal, coronal, and axial torques imposed on T1 with a preload applied axial to the spinal columns.

6.5.1 SCOLIOSIS INDUCTION METHODOLOGY

Due to the absence of patient-specific anatomy, the scoliotic spine FE model was formed from the asymptomatic condition using iterative preload and growth modulation steps via the Hueter-Volkmann law to impose a mild deformity in the spine. Application of the preload required a path that followed the spinal curvature sagittally to maintain the FE model's structural stability during each iteration. The approach differs from previous model approaches relying on a gravitational field to impose preload (Clin et al., 2011); however, gravity is a pure vertical load that would have imposed instability into the model, hence the vertical orientation of the cables in the coronal plane. The resulting model produces axial rotations and slight reductions in kyphosis that are comparable with scoliotic deformities produced using similar methods (Villemure et al., 2002; Shi et al., 2011). A secondary comparison with an adult coronal CT image was performed to ensure validity of the induced deformity, coming within a degree of the Cobb angle measured

within a deformed FE model output. The adult dataset was chosen for comparison since the FE model is based off adult anatomy. The apical deformity was set at T10-T11 possibly due to its presence at the junction between false ribs and floating ribs, creating a difference in stiffness.

6.5.2 INTERPRETATION OF IN-PLANE AND OUT-OF-PLANE KINEMATICS

The ribcage presence in the FE model also seemingly played a large role in the kinematic behavior of both the asymptomatic and scoliotic spines. The coupled, or out-of-plane, kinematics reveal the effect the axial deformity has on axial rotation of the spine during sagittal rotation. The global rotations of the upper and mid-thoracic vertebra increase in a scoliotic spine versus an asymptomatic one. It is likely that the ribcage reinforcements in these regions of the spinal column contributed through direct costosternal connections between ribs and vertebrae. These connections also pronounce the kinematic differences present at the thoracolumbar junction (e.g., T12-L1), where the presence of floating ribs leads to major intervertebral decreases in flexion, extension, and lateral bending relative to other segments. The effects of disc wedging combined with floating rib attachments also produce intervertebral rotation increases in right axial rotation, where the wedge angle produced at T12-L1 was approximately 2.8°. A larger decrease in intervertebral rotation takes place in right axial rotation, at one above the apical segment (e.g., T9-T10 & T10-T11) within the scoliotic spine. Only one other study evaluated the kinematics of an asymptomatic, volumetric, thoracolumbar FE model with ribcage (Meijer, 2011). Using the same external moment of 2 N-m without preload, their intervertebral rotations saw increases at T11-T12 in extension, lateral bending, and axial

rotation, and again at L1-L2, mostly in lateral bending. While the results of this study are largely in agreement with these trends, rotations are lowest at T7-T8 or T8-T9, whereas the lowest rotations in this study are consistently present at T5-T6, potentially due to differences in ligament stiffnesses assigned between the upper thorax and mid-thorax. Also, magnitudes in this study are lower than in the publication either due to no applied preload or use of adolescent vertebrae and smaller ribcage in their studies.

6.5.3 LIMITATIONS

Due to limited data associated with the thoracolumbar scoliotic kinematics, assumptions were made regarding both the input loadings and the anatomy. Previous studies suggest that scoliotic bones are weaker and less stiff compared to their asymptomatic counterparts (Cheuk et al., 2015). To fairly compare the biomechanical behavior of deformed scoliotic models with asymptomatic ones, and to avoid applying loads past failure, an external moment of 2 N-m was chosen for all rotations. Another limitation presented was the use of adult anatomy to analyze adolescent biomechanics. To accurately model a young adolescent spine (e.g., 10-12 years old), it is not practical to linearly scale adult vertebrae down to size (Carman et al., 2022; Kumaresan et al., 2000). However, evidence shows that an adolescent can begin reaching skeletal maturity by age 15 (Jebaseelan et al., 2012). Thus, a compromise was made to map the adult spine to an older adolescent population through vertebral and soft tissue material property scale factors appropriate for a 15-year-old. Lastly, the study does not make use of patient-specific anatomy. Doing so may enhance the understanding of clinical options available

for treatment, as well as assign more accurate properties specific to the patient, such as anthropometry and weight.

6.6 CONCLUSION

Through application of the Hueter-Volkmann law, an asymptomatic osseoligamentous FE model was deformed to a scoliotic spine. Its output contains key pathological features similar to those identified in scoliosis patients. A biomechanical comparison was then conducted using FE models of an asymptomatic and a scoliotic spine. Both the influence of the ribcage and segment position within the main thoracic curve play a huge role in intervertebral rotational behavior. While the steps outlined need refinement to achieve a patient-specific platform towards surgical planning, the study presented offers general first steps for potential implementation in the future.

CHAPTER 7

CONCLUSION AND SUMMARY

The costs and risks of performing corrective surgery on adolescents with scoliosis continually rise and can be complicated by the variation in anatomy, spinal deformity and flexibility. The last two decades has seen an interest in computational analyses of the spine that resolve clinical questions that may prove difficult to answer through in-vivo or in-vitro means. The following dissertation outlines a building-block approach by which a volumetric finite element (FE) model of the thoracolumbar spine, through rigorous development and component validation primarily with in-vitro data, may be utilized for scoliosis surgical planning. Three distinct biomechanics studies are proposed and implemented in a fashion that may be pertinent to clinicians performing patient-specific surgical planning. While these studies have general application to the spine clinically, the procedures outlined represent first steps towards application within a patient-specific platform.

Since scoliosis is a three-dimensional deformity of both the thoracic and lumbar spines, it is crucial to accurately characterize the anatomy associated with both in an FE model to produce accurate biomechanical behavior. The literature offers little suggestions on how to appropriately characterize ligaments in the thoracic spine, driving a comparative kinematic study within a thoracic functional unit utilizing publicly available ligament stiffness properties. The functional unit with ligaments characterized using the traditional toe and linear stiffness regimes generally fared better than linear or overly stiff ligaments when compared to available in-vitro kinematic data. Though published

ligament properties are scarce and variable, choosing an appropriate set of ligament properties ideally requires one to look at demographic factors (e.g., age, gender) and physiological factors, such as ligament load regimes, spinal regions of interest, and pathological conditions of the spine, as all the aforementioned factors can affect how the spine behaves. Future work in this arena may explore the biomechanical effects of one or a combination of these variables in multi-segment FE models of the spine or developing unique ligament properties for adolescent patients.

The choice of soft tissue (e.g., ligaments & IVD) properties may also affect the desired outcomes clinicians face during surgical planning. Using the Ponte osteotomy as an example, a serial ligament resection procedure was implemented to demonstrate the differences in soft tissue load sharing after each step. Positional shifts in the Instant Center of Rotation (ICoR), used as a reference point to calculate ligament moment arms, were most pronounced when stiffer ligaments were removed sagittally, or when partial facetectomies were conducted, thus shifting the load sharing behavior among soft tissues still intact. The results, however, are valid for a specific sectioning sequence and were demonstrated on one asymptomatic joint. Future work should investigate the effects of ligament removal at different segments on soft tissue load sharing, as well as demonstrate on segments with scoliosis to enhance the pragmatism of the load sharing assessment during surgical resectioning. This work may also be extended to examining the kinematics and load sharing within spinal joints post-surgery, such as after a posterior spinal fusion.

One limitation of the functional unit models was its relative compliance in rotations dependent on facet rotations, such as extension. As shown in Chapter 5, the

penalty forces were not sufficient to resist motion of the joint. Future work may focus on implementing pressure-based contact either through a user-defined subroutine or incorporating pressure directly within other commercial finite element codes, all to enhance the behavior of the facet joint. It should be noted that while this result was primarily exhibited in the functional unit, the FE model incorporating the thoracic spine with ribcage did not have this issue pronounced in extension possibly due to costosternal-based reinforcement, as shown in Chapter 2.

Finally, the thoracolumbar FE model with ribcage, when mild scoliosis was induced, showed promising results when compared with a CT image and with physiological characteristics of scoliotic spines. In addition, the intervertebral behavior of the asymptomatic spines was mostly in agreement with similarly conducted work (Meijer, 2011), while the scoliotic spine did exhibit stiffer behavior compared with its asymptomatic counterpart. However, to further enhance the applicability of an FE model with induced scoliosis, future work should examine the biomechanical spinal behavior with Cobb angles appropriate for surgical intervention (e.g., 50 degrees or greater). Also, load bearing assessments of scoliotic spines, due to external loads or preloads, are becoming of interest to researchers; thus, future work should investigate the effects of different scoliotic deformities on the load bearing characteristics. Most importantly, this work may be enhanced by utilizing patient-specific anatomy to represent a true adolescent.

REFERENCES

ABAQUS (2014) Analysis User's Manual, Version 6.14. Dassault Systemes Simulia, Inc.

Abolaeha, O. A., Weber, J., & Ross, L.T. (2012). Finite element simulation of a scoliotic spine with periodic adjustments of an attached growing rod. Paper presented at the 34th Annual International Conference of the IEEE EMBS, San Diego, CA.

Adams, M. A., Hutton, W. C., & Stott, J. R. (1980). The resistance to flexion of the lumbar intervertebral joint. *Spine (Phila Pa 1976), 5*(3), 245-253.

Agency for Healthcare Research and Quality. (2011). Healthcare cost and utilization project. https://www.hcup-us.ahrq.gov/nisoverview.jsp.

Ahuja, S., Moideen, A. N., Dudhniwala, A. G., Karatsis, E., Papadakis, L., & Varitis, E. (2020). Lumbar stability following graded unilateral and bilateral facetectomy: A finite element model study. *Clin Biomech (Bristol, Avon), 75*, 105011.

Aira, J., Guleyupoglu, B., Jones, D., Koya, B., Davis, M., & Gayzik, F. S. (2019). Validated thoracic vertebrae and costovertebral joints increase biofidelity of a human body model in hub impacts. *Traffic Inj Prev, 20*(sup2), S1-S6.

American Association of Neurological Surgeons. http://www.aans.org/Patients/Neurosurgical-Conditions-and-Treatments/Scoliosis

Anderst, W., Baillargeon, E., Donaldson, W., Lee, J., & Kang, J. (2013). Motion path of the instant center of rotation in the cervical spine during in vivo dynamic flexion-extension: implications for artificial disc design and evaluation of motion quality after arthrodesis. *Spine (Phila Pa 1976), 38*(10), E594-601.

Asher, M. A., & Burton, D. C. (2006). Adolescent idiopathic scoliosis: natural history and long-term treatment effects. *Scoliosis, 1*(1), 2. doi:10.1186/1748-7161-1-2.

Ayturk, U. M., Puttlitz, C. M. (2011). Parametric convergence sensitivity and validation of a finite element model of the human lumbar spine. *Computer Methods in Biomechanics and Biomedical Engineering, 14*(8).

Barton, C., Noshchenko, A., Patel, V.V., Cain, C.M.J., Kleck, C., Burger, E.L. (2017). Different types of mechanical complications after surgical correction of adult spine deformity with osteotomy. *World J Meta-Anal, 5*(6), 132-149.

Betz, R. R., Harms, J., Clements III, D. H., Lenke, L. G., Lowe, T. G., Shufflebarger, H. L., ... & Beele, B. (1999). Comparison of anterior and posterior instrumentation for correction of adolescent thoracic idiopathic scoliosis. *Spine*, 24(3), 225-239.

Bilgic, S., et al. (2010). "Brace treatment in adolescent idiopathic scoliosis." Clinical and

Analytical Medicine.

Bogduk, N., Amevo, B., & Pearcy, M. (1995). A biological basis for instantaneous centres of rotation of the vertebral column. *Proc Inst Mech Eng H, 209*(3), 177-183.

Borvall, T. (2008). Mortar contact algorithm for implicit stamping analyses in LS-DYNA. Paper presented at the 10th International LS-DYNA User's Conference, Dearborn, MI.

Bridwell, K. H. (2006). Decision making regarding Smith-Petersen vs. Pedicle Subtraction Osteotomy vs. Vertebral Column Resection for spinal deformity. *Spine, 31*(19), S171-S178.

Brown, S. H., & McGill, S. M. (2005). Muscle force-stiffness characteristics influence joint stability: a spine example. *Clin Biomech (Bristol, Avon), 20*(9), 917-922.

Busscher, I., van der Veen, A.J., van Dieen, J.H., Kingma, I., Verkerke, G.J., Veldhuizen, A.G. (2010). In vitro biomechanical characteristics of the spine-a comparison between human and porcine spinal ligaments. *Spine, 35*(2), E35-E42.

Busscher, I., van Dieen, J. H., Kingma, I., van der Veen, A. J., Verkerke, G. J., & Veldhuisen, A. G. (2009). Biomechanical characteristics of different regions of the human spine. *Spine, 34*(26), 2858-2864.

Carman, L., Besier, T. F., & Choisne, J. (2022). Morphological variation in paediatric lower limb bones. *Sci Rep, 12*(1), 3251.

Carrier, J., Aubin, C. E., Villemure, I., & Labelle, H. (2004). Biomechanical modelling of growth modulation following rib shortening or lengthening in adolescent idiopathic scoliosis. *Med Biol Eng Comput, 42*(4), 541-548.

Center for Disease Control. (2000, May 30). Weight-for-age percentiles: Boys, 2 to 20 years. https://www.cdc.gov/growthcharts/data/set2/chart-03.pdf.

Center for Disease Control. (2000, May 30). Weight-for-age percentiles: Girls, 2 to 20 years. https://www.cdc.gov/growthcharts/data/set2/chart-04.pdf.

Chazal, J., Tanguy, A., Bourges, M., Gaurel, G., Escande, G., Guillot, M., & Vanneuville, G. (1985). Biomechanical properties of spinal ligaments and a histological study of the supraspinal ligament in traction. *J Biomech, 18*(3), 167-176.

Cheuk, K. Y., Zhu, T. Y., Yu, F. W., Hung, V. W., Lee, K. M., Qin, L., . . . & Lam, T. P. (2015). Abnormal bone mechanical and structural properties in Adolescent Idiopathic Scoliosis: A study with finite element Analysis and structural model index. *Calcif Tissue Int, 97*(4), 343-352.

Clin, J., Aubin, C. E., Lalonde, N., Parent, S., & Labelle, H. (2011). A new method to include the gravitational forces in a finite element model of the scoliotic spine. *Med Biol Eng Comput, 49*(8), 967-977.

Coogan, J. S., Francis, W. L., Eliason, T. D., Bredbenner, T. L., Stemper, B. D., Yoganandan, N., . . . & Nicolella, D. P. (2016). Finite element study of a lumbar intervertebral disc nucleus replacement device. *Front Bioeng Biotechnol, 4*, 93.

Cribb, M., Anderson, S., Martin, R., Parasidis, S., Martell, C., Polanco, M., Bawab, S., & Ringleb, S. (2020). Tensile testing of spinal ligaments. Poster session presented at: 2020 American Society of Biomechanics Conference; Aug 4-7; Atlanta, GA.

Dougherty, E. S. (2014). *Pediatric Human Spine-Growth Characterization and Finite Element Analysis.* (PhD), University of California-Davis, UMI Dissertation Publishing.

Dreischarf, M., Zander, T., Shirazi-Adl, A., Puttlitz, C. M., Adam, C. J., Chen, C. S., . . . & Schmidt, H. (2014). Comparison of eight published static finite element models of the intact lumbar spine: Predictive power of models improves when combined together. *Journal of Biomechanics, 47*(8), 1757-1766. doi:10.1016/j.jbiomech.2014.04.002.

Du, C. F., Yang, N., Guo, J. C., Huang, Y. P., & Zhang, C. (2016). Biomechanical response of lumbar facet joints under follower preload: a finite element study. *BMC Musculoskelet Disord, 17*, 126.

Duprey, S., Subit, D., Guillemot, H., & Kent, R. W. (2010). Biomechanical properties of the costovertebral joint. *Med Eng Phys, 32*(2), 222-227.

Ebrahimi, M., Mohammadi, A., Ristaniemi, A., Stenroth, L., & Korhonen, R. K. (2019). The effect of different preconditioning protocols on repeatability of bovine ACL stress-relaxation response in tension. *Journal of the mechanical behavior of biomedical materials*, *90*, 493–501.

Erbulut, D. U. (2014). Biomechanical effect of graded facetectomy on asymmetrical finite element model of the lumbar spine. *Turkish Neurosurgery*, *24*(6).

Fairhurst, H., Little, J. P., & Adam, C. J. (2009). The measurement of applied forces during anterior single rod correction of adolescent idiopathic scoliosis. In *Adelaide Centre for Spinal Research (ACSR)-Spinal Research Symposium VII*.

Fletcher, J. G. R., Stringer, M. D., Briggs, C. A., Davies, T. M., & Woodley, S.J. (2015). CT morphology of adult thoracic intervertebral discs. *Eur Spine J, 24*, 2321-2329.

Frost, B. A., Camarero-Espinosa, S., & Foster, E. J. (2019). Materials for the Spine: anatomy, problems, and solutions. *Materials (Basel), 12*(2). doi:10.3390/ma12020253.

Gillespie, K. A., & Dickey, J. P. (2004). Biomechanical role of lumbar spine segments in flexion and extension: Determination using a Parallel Linkage Robot and a Porcine Model. *Spine, 29*(11), 1208-1216.

Goel, V. K., Monroe, B. T., Gilbertson, L. G., & Brinckmann, P. (1995). Interlaminar shear stresses and laminae separation in a disc. Finite element analysis of the L3-L4 motion segment subjected to axial compressive loads. *Spine (Phila Pa 1976), 20*(6), 689-698.

Grealou, L., Aubin, C. É., & Labelle, H. (2002). Rib cage surgery for the treatment of scoliosis: a biomechanical study of correction mechanisms. *Journal of orthopaedic research*, *20*(5), 1121-1128.

Hasler, C. C., Hefti, F., & Buchler, P. (2010). Coronal plane segmental flexibility in thoracic adolescent idiopathic scoliosis assessed by fulcrum-bending radiographs. *Eur Spine J, 19*(5), 732-738.

He, C., & Wong, M. S. (2018). Spinal flexibility assessment on the patients with Adolescent Idiopathic Scoliosis: a literature review. *Spine (Phila Pa 1976), 43*(4), E250-E258.

Healy, A. T., Lubelski, D., Mageswaran, P., Bhowmick, D. A., Bartsch, A. J., Benzel, E. C., & Mroz, T. E. (2014). Biomechanical analysis of the upper thoracic spine after decompressive procedures. *Spine J, 14*(6), 1010-1016. doi:10.1016/j.spinee.2013.11.035.

Heuer, F., Schmidt, H., Klezl, Z., Claes, L., & Wilke, H. J. (2007). Stepwise reduction of functional spinal structures increase range of motion and change lordosis angle. *J Biomech, 40*(2), 271-280.

Holewijn, R. M., Schlosser, T. P. C., Bisschop, A., van der Veen, A. J., Stadhouder, A., van Royan, B. J., . . . de Kleuver, M. (2015). How Does Spinal Release and Ponte Osteotomy Improve Spinal Flexibility? The Law of Diminishing Returns. *Spine Deformity, 3*, 489-495.

Hortin, M. S. (2015). *Ligament model fidelity in finite element analysis of the human lumbar spine. Mechanical Engineering*. (Master's Thesis). BYU Scholars Archive, Brigham Young University-Provo.

Huitema, G., Willems, P. C., van Rhijn, L., Kleijnen, J., & Shaffrey, C. I. (2014). Anterior versus posterior spinal correction and fusion for adolescent idiopathic scoliosis. *Cochrane Database of Systematic Reviews*, (9).

Hukins, D. W., Kirby, M. C., Sikoryn, T. A., Aspden, R. M., & Cox, A. J. (1990). Comparison of structure, mechanical properties, and functions of lumbar spinal ligaments. *Spine (Phila Pa 1976), 15*(8), 787-795.

Hussain, M., Natarajan, R. N., An, H. S., & Andersson, G. B. (2010). Patterns of height changes in anterior and posterior cervical disc regions affects the contact loading at posterior facets during moderate and severe disc degeneration: a poroelastic C5-C6 finite element model study. *Spine*, *35*(18), E873-E881.

Huynh, A-M., Aubin, C-E., Rajwani, T., Bagnall, K.M., & Villemure, I. (2007). Pedicle growth asymmetry as a cause of adolescent idiopathic scoliosis: a biomechanical study. *Eur Spine J, 16*, 523-529.

Jansova, M., Cechova, H., Hyncik, L., & Toczyski, J. (2015). Evaluation of human thorax FE models in various impact scenarios. *Applied and Computational Mechanics, 9*, 5-20.

Jebaseelan, D. D., Jeberaj, C., Yoganandan, N., Rajasekaran, S., & Kanna, R. M. (2012). Validation efforts and flexibilities of an eight-year-old human juvenile lumbar spine using a three-dimensional finite element model. *Med Biol Eng Comput, 48*, 1223-1231.

Jiang, H. X., Raso, J. V., Moreau, M. J., Russell, G., Hill, D. L., & Bagnall, K. M. (1994). Quantitative morphology of the lateral ligaments of the spine - assessment of their importance in maintaining lateral stability. *Spine, 19*(23), 2676-2682.

Kim, H. J., Yagi, M., Nyugen, J., Cunningham, M. E., & Boachie-Adjei, O. (2012). Combined anterior-posterior surgery is the most important risk factor for developing proximal junctional kyphosis in idiopathic scoliosis. *Clinical Orthopaedics and Related Research®*, *470*(6), 1633-1639.

Kindig, M., Li, Z., Kent, R., & Subit, D. (2015). Effect of intercostal muscle and costovertebral joint material properties on human ribcage stiffness and kinematics. *Comput Methods Biomech Biomed Engin, 18*(5), 556-570. doi:10.1080/10255842.2013.820718.

Konieczny, M. R., Senyurt, H., & Krauspe, R. (2013). Epidemiology of adolescent idiopathic scoliosis. *Journal of children's orthopaedics*, *7*(1), 3–9.

Kumaresan, S., Yoganandan, N., & Pintar, F. A. (1998). Finite element modeling approaches of human cervical spine facet joint capsule. *J Biomech, 31*(4), 371-376.

Kumaresan, S., Yoganandan, N., Pintar, F. A., Maiman, D. J., & Kuppa, S. (2000). Biomechanical study of pediatric human cervical spine: a finite element approach. *J Biomech Eng, 122*(1), 60-71.

Kumaresan, S., Yoganandan, N., Pintar, F.A. (1999). Finite element analysis of the cervical spine: a material property sensitivity study. *Clinical Biomechanics, 14*, 41-53.

Lafon, Y., Lafage, V., Steib, J. P., Dubousset, J., & Skalli, W. (2010). In vivo distribution of spinal intervertebral stiffness based on clinical flexibility tests. *Spine (Phila Pa 1976), 35*(2), 186-193.

Lafon, Y., Steib, J. P., & Skalli, W. (2010). Intraoperative three-dimensional correction during in situ contouring surgery by using a numerical model. *Spine, 35*(4), 453-459.

Lamarre, M. E., Parent, S., Labelle, H., Aubin, C. E., Joncas, J., Cabral, A., & Petit, Y. (2009). Assessment of spinal flexibility in adolescent idiopathic scoliosis: suspension versus side-bending radiography. *Spine (Phila Pa 1976), 34*(6), 591-597.

Lee, S. W., Draper, E. R., & Hughes, S. P. (1997). Instantaneous center of rotation and instability of the cervical spine. A clinical study. *Spine (Phila Pa 1976), 22*(6), 641-647; discussion 647-648.

Lemosse, D., Le Rue, O., Diop, A., Skalli, W., Marec, P., Lavaste, F. (1998). Characterization of the mechanical behaviour parameters of the costovertebral joint. *Eur Spine J, 7*, 16-23.

Lenke, L. G., Edwards, C. C., & Bridwell, K. H. (2003). The Lenke classification of Adolescent Idiopathic Scoliosis: how it organizes curve patterns as a template to perform selective fusions of the spine. *Spine, 28*(20S), S199-S207.

Liebsch, C., Graf, N., Appelt, K., & Wilke, H. J. (2017). The rib cage stabilizes the human thoracic spine: An in vitro study using stepwise reduction of rib cage structures. *PLoS One, 12*(6).

Liebsch, C., Jonas, R., & Wilke, H. J. (2020). Thoracic spinal kinematics is affected by the grade of intervertebral disc degeneration, but not by the presence of the ribs: an in vitro study. *The Spine Journal*, *20*(3), 488-498.

Liebsch, C., & Wilke, H.J. (2020b). Rib presence, anterior rib cage integrity and segmental length affect the stability of the thoracic spine: An in vitro study. *Front Bioeng Biotechnol, 8*(46).

Little, J. P., & Adam, C. (2011a). Patient-specific computational biomechanics for simulating adolescent scoliosis surgery: Predicted vs clinical correction for a preliminary series of six patients. *International Journal for Numerical Methods in Biomedical Engineering, 27*, 347-356.

Little, J. P., & Adam, C. J. (2011b). Effects of surgical joint destabilization on load sharing between ligamentous structures in the thoracic spine-a finite element study. *Clin Biomech (Bristol, Avon), 26(9)*, 895-903.

Little, J. P., Pearcy, M.J., Izatt, M.T., Boom, K., Labrom, R.D., Askin, G.N., Adam, C.J. (2016). Understanding how axial loads on the spine influence segmental biomechanics for idiopathic scoliosis patients. *Clinical Biomechanics, 32*, 220-228.

Liu, X., & Kang, J. (2002). *Development of child pedestrian mathematical models and validation with accident reconstructions*. Paper presented at the IRCOBI.

Livermore Software Technology Corporation (2006). *LS-DYNA Theory Manual*.

Livermore Software Technology. (2003). *Quasistatic simulation.* Retrieved from https://www.dynasupport.com/howtos/general/quasistatic-simulation.

Löffler, M. T., Sekuboyina, A., Jacob, A., Grau, A. L., Scharr, A., El Husseini, M., ... & Kirschke, J. S. (2020). A vertebral segmentation dataset with fracture grading. *Radiology: Artificial Intelligence*, *2*(4).

Lotz, J. C., Fields, A. J., & Liebenberg, E. C. (2013). The role of the vertebral end plate in low back pain. *Global Spine J, 3*(3), 153-164.

Lubelski, D., Healy, A. T., Mageswaran, P., Benzel, E. C., & Mroz, T. E. (2014). Biomechanics of the lower thoracic spine after decompression and fusion: a cadaveric analysis. *Spine J, 14*(9), 2216-2223.

Mahaudens, P. & Detrembleur, C. (2015). "Increase of passive stiffness in adolescent idiopathic scoliosis." *Computer Methods in Biomechanics and Biomedical Engineering*, 18(S1), 1992-1993.

Majdouline, Y., Aubin, C. E., Sangole, A., & Labelle, H. (2009). Computer simulation for the optimization of instrumentation strategies in adolescent idiopathic scoliosis. *Med Biol Eng Comput, 47*(11), 1143-1154.

Mannen, E. M., Anderson, J. T., Arnold, P. M., & Friis, E. A. (2015). Mechanical Contribution of the Rib Cage in the Human Cadaveric Thoracic Spine. *Spine (Phila Pa 1976), 40*(13), E760-766.

Mattucci, S. F., Moulton, J. A., Chandrashekar, N., & Cronin, D. S. (2012). Strain rate dependent properties of younger human cervical spine ligaments. *J Mech Behav Biomed Mater, 10*, 216-226.

Matusik, E., Durmala, J., Olszanecka-Glinianowicz, M., Chudek, J., & Matusik, P. (2020). Association between bone turnover markers, leptin, and nutritional status in girls with Adolescent Idiopathic Scoliosis (AIS). *Nutrients*, *12*(9), 2657.

Mayurama, T. & Takeshita, K. (2008). Surgical treatment of scoliosis: a review of techniques currently applied. Scoliosis 3(6).

Mehkri, Y., Hernandez, J., McQueery, J., Carmona, J., & Ihnow, S. (2021). Global spine RoM in patients with AIS before and after corrective surgery. *Cureus*. doi:10.7759/cureus.19362.

Meijer, G. J. (2011). *Development of a non-fusion scoliosis correction device: numerical modelling of scoliosis correction.* (PhD), Universiteit of Twente Stichting Technologische Wetenschappen.

Meijer, G. J., Homminga, J., Veldhuizen, A. G., & Verkerke, G. J. (2011). Influence of interpersonal geometrical variation on spinal motion segment stiffness: implications for patient-specific modeling. *Spine (Phila Pa 1976), 36*(14), E929-935. doi:10.1097/BRS.0b013e3181fd7f7f

Menger R. P., Sin A. H. Adolescent and Idiopathic Scoliosis. [Updated 2022 Apr 9]. In: StatPearls [Internet]. Treasure Island (FL): StatPearls Publishing; 2022 Jan-. Available from: https://www.ncbi.nlm.nih.gov/books/NBK499908/

Mengoni, M. (2021). Biomechanical modelling of the facet joints: a review of methods and validation processes in finite element analysis. *Biomech Model Mechanobiol, 20*(2), 389-401.

Mitsuhashi, N., Fujieda, K., Tamura, T., Kawamoto, S., Takagi, T., & Okubo, K. (2009). BodyParts3D: 3D structure database for anatomical concepts. *Nucleic acids research*, *37*(suppl_1), D782-D785.

Modi, H. N., Suh, S. W., Song, H-R., Yang, J-H., Kim, H-J., & Modi, C.H. (2008). Differential wedging of vertebral body and intervertebral disc in thoracic and lumbar spine in adolescent idiopathic scoliosis – A cross sectional study in 150 patients. *Scoliosis, 3*(11).

Myklebust, J. B., Pintar, F., Yoganandan, N., Cusick, J. F., Maiman, D., Myers, T. J., & Sances, A., Jr. (1988). Tensile strength of spinal ligaments. *Spine (Phila Pa 1976), 13*(5), 526-531.

Naserkhaki, S., Arjmand, N., Shirazi-Adl, A., Farahmand, F., & El-Rich, M. (2018). Effects of eight different ligament property datasets on biomechanics of a lumbar L4-L5 finite element model. *J Biomech, 70*, 33-42.

Naserkhaki, S., Jaremko, J. L., Adeeb, S., & El-Rich, M. (2016). On the load-sharing along the ligamentous lumbosacral spine in flexed and extended postures: Finite element study. *J Biomech, 49*(6), 974-982.

Neumann, P., Keller, T. S., Ekstrom, L., Perry, L., Hansson, T. H., & Spengler, D. M. (1992). Mechanical properties of the human lumbar anterior longitudinal ligament. *J Biomech, 25*(10), 1185-1194.

Newell, N., Little, J. P., Christou, A., Adams, M. A., Adam, C. J., & Masouros, S. D. (2017). Biomechanics of the human intervertebral disc: A review of testing techniques and results. *Mechanical Behavior of Biomedical Materials, 69*, 420-434.

Niemeyer, F., Wilke, H-J., & Schmidt, H. (2012). Geometry strongly influences the response of numerical models of the lumbar spine-a probabalistic finite element analysis. *Biomechanics, 45*, 1414-1423.

Noshchenko, A., Hoffecker, L., Lindley, E. M., Burger, E. L., Cain, C. M., Patel, V. V., & Bradford, A. P. (2015). Predictors of spine deformity progression in adolescent idiopathic scoliosis: A systematic review with meta-analysis. *World journal of orthopedics*, *6*(7), 537.

Nolte, L. P., Panjabi, M., & Oxland, T.R. (1990). Biomechanical properties of lumbar spinal ligaments. *Clinical Implant Materials, Advances in Biomaterials, 9*, 663-668.

North American Spine Society. http://www.spine.org.

Oda, I., Abumi, K., Cunningham, B. W., Kaneda, K., & McAfee, P. C. (2002). An in vitro human cadaveric study investigating the biomechanical properties of the thoracic spine. *Spine (Phila Pa 1976), 27*(3), E64-70.

Panjabi, M. M., Brand, R. A., Jr., & White, A. A., 3rd (1976). Three-dimensional flexibility and stiffness properties of the human thoracic spine. *J Biomech, 9*(4), 185-192.

Panjabi, M. M., Krag, M. H., Dimnet, J. C., Walter, S. D., & Brand, R. A. (1984). Thoracic spine centers of rotation in the sagittal plane. *J Orthop Res, 1*(4), 387-394.

Panjabi, M. M., Oxland, T. R., & Parks, E. H. (1991). Quantitative anatomy of cervical spine ligaments. Part I. Upper cervical spine. *J Spinal Disord, 4*(3), 270-276.

Panzer, M., & Cronin, D. (2009). C4–C5 segment finite element model development, validation, and load-sharing investigation. *Biomechanics, 42*, 480-490.

Papadopoulos, E. C., Boachie-Adjei, O., Hess, W. F., Sanchez Perez-Grueso, F. J., Pellise, F., Gupta, M., . . . Complex Spine, N. Y. N. Y. (2015). Early outcomes and complications of posterior vertebral column resection. *Spine J, 15*(5), 983-991.

Pathria, M., Sartoris, D. J., & Resnick, D. (1987). Osteoarthritis of the facet joints: accuracy of oblique radiographic assessment. *Radiology*, *164*(1), 227-230.

Pearcy, M. J., & Bogduk, N. (1988). Instantaneous axes of rotation of the lumbar intervertebral joints. *Spine (Phila Pa 1976), 13*(9), 1033-1041.

Pintar, F. A., Yoganandan, N., Myers, T., Elhagediab, A., & Sances, A., Jr. (1992). Biomechanical properties of human lumbar spine ligaments. *J Biomech, 25*(11),

1351-1356.

Pizones, J., Sanchez-Mariscal, F., Zuniga, L., & Izquierdo, E. (2015). Ponte osteotomies to treat major thoracic adolescent idiopathic scoliosis curves allow more effective corrective maneuvers. *Eur Spine J, 24*(7), 1540-1546.

Polanco, M., Bawab, S., Ringleb, S., Audette, M., & Kakar, R. Examination of intervertebral ligament property sensitivity on a thoracic spine functional unit. *Available at SSRN 3990030*.

Polanco, M., Bawab, S., Ringleb, S., Audette, M., St Remy, C., & Bennett, J. 2020. "The use of porcine ligament properties as a substitute for human ligaments in a finite element model. Poster session presented at: 2020 American Society of Biomechanics Conference; Aug 4-7; Atlanta, GA.

Polly, D. W., & Sturm, P. F. (1998). Traction versus supine side bending-which technique best determines spine flexibility? *Spine, 23*(7).

Ponte, A., Orlando, G., & Siccardi, G.L. (2018). The true Ponte osteotomy-by the one who developed it. *Spine Deformity, 6*.

Qiu, T. X., Teo, E. C., Lee, K. K., Ng, H. W., & Yang, K. (2003). Validation of T10-T11 finite element model and determination of instantaneous axes of rotations in three anatomical planes. *Spine (Phila Pa 1976), 28*(24), 2694-2699.

Reamy, B. V. & Slakey, J. B. (2001). "Adolescent idiopathic scoliosis: review and current concepts." American Family Physician 64(1).

Riseborough, E. & Davies, R. (1973). "A genetic survey of idiopathic scoliosis in Boston, Massachusetts." Bone and Joint Surgery 55:974-982.

Rockenfeller, R., Muller, A., Damm, N., Kosterhon, M., Kantelhardt, S. R., Frank, R., & Gruber, K. (2021). Muscle-driven and torque-driven centrodes during modeled flexion of individual lumbar spines are disparate. *Biomech Model Mechanobiol, 20*(1), 267-279.

Rohlmann, A., Zander, T., Schmidt, H., Wilke, H-J., & Bergmann, G. (2006a). Analysis of the influence of disc degeneration on the mechanical behaviour of a lumbar motion segment using the finite element method. *Biomechanics, 39*, 2484-2490.

Rohlmann, A., Bauer, L., Zander, T., Bergmann, G., & Wilke, H. J. (2006b). Determination of trunk muscle forces for flexion and extension by using a validated finite element model of the lumbar spine and measured in vivo data. *Journal of Biomechanics, 39*(6), 981-989.

Rohlmann, A., Neller, S., Claes, L., Bergmann, G., & Wilke, H. J. (2001). Influence of a follower load on intradiscal pressure and intersegmental rotation of the lumbar spine.

Spine (Phila Pa 1976), 26(24), E557-561. doi:10.1097/00007632-200112150-00014.

Rohlmann, A., Zander, T., Rao, M., & Bergmann, G. (2009). Realistic loading conditions for upper body bending. *J Biomech, 42*(7), 884-890.

Salmingo, R. A. (2013). Biomechanical approach on corrective force acting on spine in scoliosis deformity surgery. Biomechanics and Robotics. Sapporo, Japan, Hokkaido University.

Samdani, A. F., Bennett, J. T., Singla, A. R., Marks, M. C., Pahys, J. M., Lonner, B. S., & Cahill, P. J. (2015). Do Ponte osteotomies enhance correction in Adolescent Idiopathic Scoliosis? An analysis of 191 Lenke 1A and 1B curves. *Spine Deformity, 3(5)*, 483-488.

Sangiorgio, S. N., Borkowski, S. L., Bowen, R. E., Scaduto, A. A., Frost, N. L., & Ebramzadeh, E. (2013). Quantification of increase in three-dimensional spine flexibility following sequential Ponte osteotomies in a cadaveric model. *Spine Deform, 1*(3), 171-178.

Scherer, S.-A., Begon, M., Leardini, A., Coillard, C., Rivard, C-H., & Allard, P. (2013). Three-Dimensional Vertebral Wedging in Mild and Moderate Adolescent Idiopathic Scoliosis. *PLoS One, 8*(8).

Schlager, B., Niemeyer, F., Liebsch, C., Galbusera, F., Boettinger, J., Vogele, D., & Wilke, H-J. (2018). Influence of morphology and material properties on the range of motion of the costovertebral joint – a probabilistic finite element analysis. *Computer Methods in Biomechanics and Biomedical Engineering, 21*(14)):731-739.

Schmidt, H., Heuer, F., Claes, L., & Wilke, H-J. (2008). The relation between the instantaneous center of rotation and facet forces-a finite element analysis. *Clinical Biomechanics, 23*, 270-278.

Schmidt, H., Heuer, F., Simon, U., Kettler, A., Rohlmann, A., Claes, L., & Wilke, H. J. (2006). Application of a new calibration method for a three-dimensional finite element model of a human lumbar annulus fibrosus. *Clin Biomech (Bristol, Avon), 21*(4), 337-344.

Schultz, A., Andersson, G., Ortengren, R., Haderspeck, K., & Nachemson, A. (1982). Loads on the lumbar spine - validation of a biomechanical analysis by measurements of intradiscal pressures and myoelectric signals. *Journal of Bone and Joint Surgery-American Volume, 64*(5), 713-720.

Sekuboyina, A., Husseini, M. E., Bayat, A., Löffler, M., Liebl, H., Li, H., ... & Kirschke, J. S. (2021). VerSe: A Vertebrae labelling and segmentation benchmark for multi-detector CT images. *Medical image analysis*, *73*, 102166.

Sekuboyina, A., Rempfler, M., Valentinitsch, A., Menze, B. H., & Kirschke, J. S. (2020). Labeling vertebrae with two-dimensional reformations of multidetector CT images: an adversarial approach for incorporating prior knowledge of spine anatomy. *Radiology. Artificial intelligence*, *2*(2).

Senkoylu, A., Ilhan, M. N., Altun, N., Samartzis, D., & Luk, K. D. (2021). A simple method for assessing rotational flexibility in adolescent idiopathic scoliosis: modified Adam's forward bending test. *Spine Deformity*, *9*(2), 333-339.

Shah, S. A., Dhawale, A. A., Oda, J. E., Yorgova, P., Neiss, G. I., Holmes, L., & Gabos, P. G. (2013). Ponte osteotomies with pedicle screw instrumentation in the treatment of adolescent idiopathic scoliosis. *Spine deformity*, *1*(3), 196-204.

Sharma, M., Langrana, N. A., & Rodriguez, J. (1995). Role of ligaments and facets in lumbar spinal stability. *Spine (Phila Pa 1976), 20*(8), 887-900.

Shi, L., Wang, D., Driscoll, M., Villemure, I., Chu, W. C., Cheng, J. C., & Aubin, C. E. (2011). Biomechanical analysis and modeling of different vertebral growth patterns in adolescent idiopathic scoliosis and healthy subjects. *Scoliosis, 6*(11), 11.

Shirazi-Adl, A., & Drouin, G. (1987). Load-bearing role of facets in a lumbar segment under sagittal plane loadings. *Journal of biomechanics*, *20*(6), 601-613.

Shirazi-Adl, A., Ahmed, A. M., & Shrivastava, S. C. (1986). Mechanical response of a lumbar motion segment in axial torque alone and combined with compression. *Spine (Phila Pa 1976), 11*(9), 914-927. doi:10.1097/00007632-198611000-00012

Sikoryn, T. A., & Hukins, D. W. (1990). Mechanism of failure of the ligamentum flavum of the spine during in vitro tensile tests. *J Orthop Res, 8*(4), 586-591.

Stokes, I. A. (1994). Three-dimensional terminology of spinal deformity. A report presented to the Scoliosis Research Society by the Scoliosis Research Society Working Group on 3-D terminology of spinal deformity. *Spine (Phila Pa 1976), 19*(2), 236-248.

Stokes, I. A. (2007). Analysis and simulation of progressive adolescent scoliosis by biomechanical growth modulation. *Eur Spine J, 16*(10), 1621-1628.

Stokes, I. A., & Aronsson, D. D. (2001). Disc and vertebral wedging in patients with progressive scoliosis. *J Spinal Disord, 14*(4), 317-322.

Stokes, I. A., Laible, J. P. (1990). Three-dimensional osseoligamentous model of the thorax representing initiation of scoliosis by asymmetric growth. *Biomechanics, 23*(6), 589-595.

Stokes, I. A., Spence, H., Aronsson, D. D., & Kilmer, N. (1996). Mechanical modulation of vertebral body growth: implications for scoliosis progression. *Spine*, *21*(10), 1162-1167.

Tapp, A., Payer, C., Schmid, J., Polanco, M., Kumi, I., Bawab, S., ... & Audette, M. (2021). Generation of patient-specific, ligamentoskeletal, finite element meshes for scoliosis correction planning. In *Clinical Image-Based Procedures, Distributed and Collaborative Learning, Artificial Intelligence for Combating COVID-19 and Secure and Privacy-Preserving Machine Learning* (pp. 13-23). Springer, Cham.

Troyer, K. L., Shetye, S. S., & Puttlitz, C. M. (2012). Experimental characterization and finite element implementation of soft tissue nonlinear viscoelasticity. *J Biomech Eng, 134*(11), 114501.

Tkaczuk, H. (1968). Tensile properties of human lumbar longitudinal ligaments. *Acta Orthop Scand*, Suppl 115:111+. doi:10.3109/ort.1968.39.suppl-115.01.

Urban, J. P., & Roberts, S. (2003). Degeneration of the intervertebral disc. *Arthritis research & therapy*, *5*(3), 120–130.

Vergari, C., Ribes, G., Aubert, B., Adam, C., Miladi, L., Ilharreborde, B., . . . & Skalli, W. (2015). Evaluation of a patient-specific finite element model to simulate conservative treatment in Adolescent Idiopathic Scoliosis. *Spine Deform, 3*(1), 4-11.

Vigneswaran, H. T., Grabel, Z. J., Eberson, C. P., Palumbo, M. A., & Daniels, A. H. (2015). Surgical treatment of adolescent idiopathic scoliosis in the United States from 1997 to 2012: an analysis of 20,346 patients. *J Neurosurg Pediatr, 16*(3), 322-328.

Villemure, I., Aubin, C.-E., Dansereau, J., & Labelle, H. (2002). Simulation of progressive deformities in Adolescent Idiopathic Scoliosis using a biomechanical model integrating vertebral growth modulation. *Biomechanical Engineering, 124*, 784-790.

Viviani, G. R., Ghista, D. N., Lozada, P. J., Subbaraj, K., & Barnes, G. (1986). Biomechanical analysis and simulation of scoliosis surgical correction. *Clin Orthop Relat Res, 208*(208), 40-47.

Watkins, R. T., Watkins, R., 3rd, Williams, L., Ahlbrand, S., Garcia, R., Karamanian, A., . . . & Hedman, T. (2005). Stability provided by the sternum and rib cage in the thoracic spine. *Spine (Phila Pa 1976), 30*(11), 1283-1286.

Wang, L., Zhang, B., Chen, S., Lu, X., Li, Z., & Guo, Q. (2016). A validated FEA of facet joint stress in degenerative lumbar scoliosis *World Neurosurgery, 95*, 126-133.

Wang, W., Baran, G. R., Betz, R. R., Samdani, A. F., Pahys, J. M., & Cahill, P. J. (2014). The use of finite element models to assist understanding and treatment for scoliosis: a review paper. *Spine Deform, 2*(1), 10-27.

Weiss, J. A., Gardiner, J. C., Ellis, B. J., Lujan, T. J., & Phatak, N. S. (2005). Three-dimensional finite element modeling of ligaments: technical aspects. *Med Eng Phys, 27*(10), 845-861.

Weiss, H.-R., & Goodall, D. (2008). Rate of complications in scoliosis surgery-a systematic review of the PubMed literature. *Scoliosis, 3*(9).

White, A. A., & Panjabi, M. M. (1990). *Clinical Biomechanics of the Spine* (2nd ed.). Philadelphia, PA: Lippincott, Williams and Wilkins. Pp. 9, 20-22, 29-33, 39-40, 86-87, 90-91, 98, 103, 107.

Wilke, H. J., Grundler, S., Ottardi, C., Mathew, C. E., Schlager, B., & Liebsch, C. (2020). In vitro analysis of thoracic spinal motion segment flexibility during stepwise reduction of all functional structures. *European Spine Journal, 29*(1), 179-185.

Wilke, H. J., Herkommer, A., Werner, K., & Liebsch, C. (2017). In vitro analysis of the segmental flexibility of the thoracic spine. *PLoS One, 12*(5), e0177823.

Wilke, H. J., Mathes, B., Midderhoff, S., & Graf, N. (2015). Development of a scoliotic spine model for biomechanical in vitro studies. *Clin Biomech (Bristol, Avon), 30*(2), 182-187.

Wilke, H. J., Wenger, K., & Claes, L. (1998). Testing criteria for spinal implants-recommendations for the standardization of in vitro stability testing of spinal implants. *Eur Spine J, 7*, 148-154.

Williams, P. L. (1995). Gray's anatomy: the anatomical basis of medicine and surgery. New York, NY: Churchill Livingstone, 512-514, 541-546.

Wu, G., Siegler, S., Allard, P., Kirtley, C., Leardini, A., Rosenbaum, D., Whittle, M., D'Lima, D., Cristofolini, L., Witte, H., Schmid, O., & Stokes, I. (2002). ISB recommendation on definitions of joint coordinate system of various joints for the reporting of human joint motion—part I: ankle, hip, and spine. *Biomechanics, 35*(4), 543-548.

Yao, J., Burns, J. E., Forsberg, D., Seitel, A., Rasoulian, A., Abolmaesumi, P., ... & Li, S. (2016). A multi-center milestone study of clinical vertebral CT segmentation. *Computerized Medical Imaging and Graphics*, *49*, 16-28.

Yoganandan, N., Kumaresan, S., & Pintar, F. A. (2000). Geometric and mechanical properties of human cervical spine ligaments. *J Biomech Eng, 122*(6), 623-629.

Zander, T., Dreischarf, M., Timm, A. K., Baumann, W. W., & Schmidt, H. (2017). Impact of material and morphological parameters on the mechanical response of the lumbar spine - A finite element sensitivity study. *J Biomech, 53*, 185-190.

Zhang, Q., Chon, T., Zhang, Y., Baker, J. S., & Gu, Y. (2021). Finite element analysis of the lumbar spine in adolescent idiopathic scoliosis subjected to different loads. *Comput Biol Med, 136*, 104745.

Zhong, W., Driscoll, S. J., Wu, M., Wang, S., Liu, Z., Cha, T. D., . . . Li, G. (2014). In vivo morphological features of human lumbar discs. *Medicine (Baltimore), 93*(28), e333.

Zhou, S. H., McCarthy, I.D., McGregor, A.H., Coombs, R.R.H., Hughes, S.P.F. (2000). Geometrical dimensions of the lower lumbar vertebrae – analysis of data from digitised CT images. *9*, 242-248.

VITA

MICHAEL A. POLANCO

Publications

- Polanco, M., Yoon, H., and Bawab, S. "Computational Assessment of Neural Probe and Brain Tissue Interface under Transient Motion," Journal of Biosensors, Volume 6, Issue 2, June 2016.
- Polanco, M., Yoon, H., and Bawab, S. "Micromotion-induced Dynamic Effects from a Neural Probe and Brain Tissue Interface," Journal of Micro/Nanolithography, MEMS, and MOEMS, Volume 13, Issue 2, June 2014.
- Polanco, M. and Littell, J., "Vertical Drop Testing and Simulation of Anthropomorphic Test Devices," Proceedings of the 67th American Helicopter Society Forum, Virginia Beach, VA, May 3-5, 2011.
- Polanco, M., "Use of LS-DYNA to assess the Energy Absorption performance of a Shell-Based Kevlar/Epoxy Composite Honeycomb," Proceedings of the 11th International LS-DYNA User's Conference, Dearborn, MI, June 6-8, 2010.

Conference Presentations

- Polanco, M., Bawab, S., Ringleb, S., Audette, M., St. Remy, C., Bennett, J. "The use of porcine ligaments as a substitute for human ligaments in a finite element model." American Society of Biomechanics Conference, Atlanta, GA. August 4-7, 2020.
- Polanco, M., Ringleb, S., Audette, M., St. Remy, C., Bennett, J., Bawab, S. "The effect of Costovertebral joints on the motion of a Thoracic Spine functional unit." American Society of Biomechanics Conference, August 3-6, 2021.
- Polanco, M., Ringleb, S., Audette, M., St. Remy, C., Bennett, J., Bawab, S. "Instantaneous Center of Rotation behavior during ligament removal in the Thoracic Spine." American Society of Biomechanics Conference, August 3-6, 2021.
- Polanco, M., Ringleb, S., Audette, M., St. Remy, C., Bennett, J., Bawab, S. "Load sharing assessment in a thoracic spine functional unit during surgical resection." North American Conference on Biomechanics, Ottawa, ON, August 22-26, 2022.

Education

Doctor of Philosophy in Mechanical Engineering   August 2022
Old Dominion University, Norfolk, VA

Master of Science in Aerospace Engineering   December 2013
Old Dominion University, Norfolk, VA
Thesis topic: Examination of Micromotion-Induced Transient Effects of Brain Tissue interfaced with a Neural Probe

Bachelor of Science in Mechanical Engineering   May 2007
The Pennsylvania State University, University Park, PA